To the Graduate Council:

I am submitting herewith a thesis written by Grady P. Saunders entitled "Scale Model Investigations of the Effects of Flow Conditioning Devices." I have examined the final paper copy of this thesis for form and content and recommend that it be accepted in partial fulfillment of the requirements for the degree of Master of Science, with a major in Mechanical Engineering.

Dr. Basil N. Antar, Major Professor

We have read this thesis
And recommend its acceptance:

Acceptance for the Council:

Vice Provost and Dean of
Graduate Studies

SCALE MODEL INVESTIGATIONS OF THE EFFECTS OF FLOW CONDITIONING DEVICES

A Thesis Presented for the
Master of Science Degree
The University of Tennessee, Knoxville

Grady P. Saunders
December, 2002

ACKNOWLEDGMENTS

The work reported herein was conducted in the aerodynamic laboratory of Sverdrup Technology, Inc. located in Tullahoma, TN. The experimental phases of the program were conducted during the fiscal years 01 and 02 under project numbers 90657 (FY 01) and 90701 (FY 02). The final analysis was performed under project number 90701 in FY 02.

The author gratefully acknowledges the assistance of Mr. Don A. Wagner whose years of experience in aerodynamic testing were invaluable in understanding the experimental results, Dr. Ed G. Duell, who aided with the performance of acoustic experiments, Mr. Jeff M. Hoffman and Mr. Richard A. Danforth, who aided with test conduction throughout the program, and Mr. Mike L. Mills of Sverdrup Technology's AEDC group, who supplied full-scale tunnel data and background information regarding past investigations into full-scale tunnel flow quality.

ABSTRACT

A scale model was constructed of a portion of a supersonic wind tunnel to perform experiments on various flow conditioning devices. The various devices researched were: swirl vanes, screens, honeycombs, and various combinations thereof. Each flow conditioning device was analyzed to show its effect on total pressure profiles, static pressure profiles, test section flow angularity, test section turbulence, and acoustic noise. Of most concern are the effects flow conditioning devices have on temporal fluctuation of previously mentioned parameters.

The data from these experiments were used as the basis for selecting a screen-honeycomb combination to be installed in the full-scale tunnel. The selected configuration consisted of two diffuser exit screens in combination with a long cell honeycomb in the stilling chamber. The selected configuration also included the existing screen across corner 4 and swirl vanes. It was concluded that these devices provide a net benefit and should not be removed. This configuration reduced test section flow angularity fluctuations to a very low level in the test section of the model; however, it did not eliminate transitory stall in the crossleg diffuser. Intermediate screens installed in the diffuser and, most likely, screens of some other treatment at the inlet of the diffuser would be required to completely eliminate unsteadiness in the diffuser. These treatments would involve both installation cost and an increase in operation

cost because of the associated increase in power requirements due to their location in high-speed flow. The experimental data, however, do show that intermediate screens in the diffuser are very effective at reducing flow unsteadiness downstream of the screen location.

This thesis presents a discussion on the methodology to conduct the experimental program and the results each combination of flow conditioning devices had on the various research parameters.

TABLE OF CONTENTS

Section		Page
I.	INTRODUCTION	1
II.	EXPERIMENTAL SETUP	
	2.1 Apparatus	4
	2.2 Test Procedures	9
	2.3 Instrumentation	11
	2.4 Data Reduction	22
III.	EXPERIMENTAL RESULTS	
	3.1 Flow Visualization	35
	3.2 Corner 3 Inlet Profile Conditioning	38
	3.3 Corner 3 Exit Total Pressure Profiles	39
	3.4 Corner 4 Inlet Total Pressure Profiles	41
	3.5 Stilling Chamber Total Pressure Profiles	42
	3.6 Test Section Flow Angularity Probe Data	47
	3.7 Hot-Wire Anemometer Turbulence Measurements	50
	3.8 Test Section "High-Response" Probe Measurements	52
	3.9 Test Section Total Pressure Profiles	55
	3.10 Acoustic Measurements	58
	3.11 Cross-Leg Diffuser Static Pressure Distribution	63
	3.12 Summary and Test Comparisons	64
	3.13 Impact on Compressor Power	66
IV.	CONCLUSIONS AND RECOMMENDATIONS	68
	REFERENCES	72

APPENDICES 75

APPENDIX A Tables 76

APPENDIX B Chapter II Figures 89

APPENDIX C Chapter III Figures 104

APPENDIX D Derivation of Axial Turbulence and Compressor Power Equations 168

VITA 177

LIST OF TABLES

Table		Page
A-1.	Approximate Deviation in Test Section Flow Angle of Full Scale Tunnel With And Without Swirl Vanes	77
A-2.	Materials of Construction	77
A-3.	Flow Conditioner Parameters and Diffuser Dimensions	78
A-4.	Configuration Codes	79
A-5.	Nominal Scale Model Test Conditions	80
A-6.	Cross-Leg Diffuser Pressure Tap Locations	80
A-7.	Stilling Chamber Rake Probe Spacing	81
A-8.	Corner 3 Inlet Rake Probe Spacing	82
A-9.	Sample of Test Log and Explanation of Data Type Code	83
A-10.	Summary of Test Parameter Values	84
A-11.	Summary of Core Region Data Normalized By the Baseline Configuration, C21	86
A-12.	Compressor Power Impact of Various Flow Conditioning Elements	88

LIST OF FIGURES

Figure		Page
B-1.	General Wind Tunnel Layout	90
B-2.	Setup A Scale Model Layout	91
B-3.	Setup B Scale Model Layout with Corner 3 Installed	92
B-4.	Setup B Scale Model Layout with Corner 3 Removed	93
B-5.	Model Details of Setup B with Corner 3 Installed	94
B-6.	Transducer Consistency Check	95
B-7.	Flow Angularity Probe Calibration Curve	95
B-8.	Flow Angularity Probe Response Test	96
B-9.	Frequency Response of Flow Angle Probe and High-Response Probe	96
B-10.	Instrumentation Setup for Corner 3 Inlet Rake and Cross-Leg Diffuser Static Survey	97
B-11.	Instrumentation Setup for Corner 3 Exit Rake	98
B-12.	Instrumentation Setup for Stilling Chamber and Corner 4 Inlet Rake	99
B-13.	Instrumentation Setup for Test Section Pitot-Static Probe	100
B-14.	Instrumentation Setup for Test Section High Response Probe	101
B-15.	Instrumentation Setup for Test Section Flow Angularity Probe	102
B-16.	Instrumentation Setup for Hot-Wire Anemometer	103
C-1.	Corner 3 Inlet Total Pressure and Temporal RMS Profiles: One Inlet Pipe Installed	105
C-2.	Corner 3 Inlet Total Pressure and Temporal RMS Profiles: Two Inlet Pipes Installed	106
C-3.	Corner 3 Inlet Total Pressure and Velocity Profiles: Configuration C04 & Full Scale Tunnel	107
C-4.	Corner 3 Exit Total Pressure and Temporal RMS Profiles: Configuration C04 & C07	108

C-5. Corner 3 Inlet & Exit Total Pressure 109
Profiles: Configurations C04 & C07

C-6. Corner 4 Inlet Total Pressure and Temporal 110
RMS Profiles: Configuration C04, C06, & C07

C-7. Stilling Chamber Core Region Total Pressure ... 111
Spatial Distribution and Temporal Fluctuation
With and Without Swirl Vanes

C-8. Stilling Chamber Total Pressure and RMS 112
Profiles, Corner 3 Installed: C05 & C04

C-9. Stilling Chamber Total Pressure and RMS 113
Profiles, Corner 3 Removed: C10 & C13

C-10. Stilling Chamber Core Region Total Pressure ... 114
Spatial Distribution and Temporal Fluctuation
Effects of Intermediate Screens

C-11. Stilling Chamber Total Pressure and RMS 115
Profiles, Corner 3 and Swirl Vanes
Installed: C05, C06, & C07

C-12. Stilling Chamber Total Pressure and RMS 116
Profiles, Swirl Vanes Installed, Corner 3
Removed: C10, C09, & C08

C-13. Stilling Chamber Core Region Total Pressure ... 117
Spatial Distribution and Temporal Fluctuation
Effects of Exit Screens

C-14. Stilling Chamber Total Pressure and RMS 118
Profiles: C13, C14, & C15

C-15. Stilling Chamber Total Pressure and RMS 119
Profiles: C19 & C24

C-16. Stilling Chamber Core Region Total Pressure ... 120
Spatial Distribution and Temporal Fluctuation
Effect of Honeycombs

C-17. Stilling Chamber Total Pressure and RMS 121
Profiles: C21 & C22

C-18. Stilling Chamber Total Pressure and RMS 122
Profiles: C19 & C23

C-19. Stilling Chamber Total Pressure & Velocity 123
Profiles: Baseline Configuration and
Full Scale Tunnel

C-20. Profiles of Yaw Angle Temporal Fluctuation 124
Corner 3 and Swirl Vanes Removed @ Y = -6 in.
Configurations C13 to C17

C-21. Temporal Fluctuation in Core Region of Yaw 124
Angle, Corner 3 and Swirl Vanes Removed
@ Y = -6 in. Configurations C13 to C17

C-22. Profiles of Yaw Angle Temporal Fluctuation 125
Corner 3 and Swirl Vanes Installed @ Y = -6 in.
Configurations C19 to C22, and C24

C-23. Temporal Fluctuation in Core Region of Yaw 125
Angle, Corner 3 and Swirl Vanes Installed
@ Y = -6 in. Configurations C19 to C22, and C24

C-24. Profiles of Yaw Angle Temporal Fluctuation 126
Corner 3 and Swirl Vanes Installed @ Y = 0 in.
Configurations C18 to C24

C-25. Temporal Fluctuation in Core Region of Yaw 126
Angle, Corner 3 and Swirl Vanes Installed
@ Y = 0 in. Configurations C18 to C24

C-26. Profiles of Pitch Angle Temporal Fluctuation .. 127
Corner 3 and Swirl Vanes Installed @ Z = 0 in.
Configurations C18 to C22, and C24

C-27. Temporal Fluctuation in Core Region of Pitch .. 127
Angle, Corner 3 and Swirl Vanes Installed
@ Z = 0 in. Configurations C18 to C22, and C24

C-28. Flow Angularity Probe Yaw Angle Time Trace 128
At Test Section Center, Configurations C21 & C19

C-29. Yaw Angle Fluctuation Profiles, With and 129
Without Swirl Vanes; Corner 3 Removed

C-30. Yaw Angle Fluctuation Profiles, Baseline 129
Configuration With and Without Corner 3

C-31. Yaw Angle Fluctuation Profiles, With and 130
Without 2/3 Screen; Corner 3 Installed

C-32. Yaw Angle Fluctuation Profiles, With and 130
Without 2/3 Screen; Corner 3 Removed

C-33. Hot Wire Anemometer Lateral Turbulence 131
Intensities of Core Region for Stilling
Chamber and Test Section

C-34. Hot Wire Anemometer Axial Turbulence 132
Intensities of Core Region for Stilling
Chamber and Test Section

C-35. Hot Wire Anemometer Spectral Density, v'/U 133
At Test Section Center,
Configurations C19 & C21

C-36. Hot Wire Anemometer Yaw Angle Time Trace at ... 134
Test Section Center, Configurations C19 and C21

C-37. Hot Wire Anemometer Spectral Density, u'/U 135
At Test Section Center,
Configurations C19 & C21

C-38. Temporal High Response Total Pressure 136
Fluctuation in Core Region, Corner 3 and
Swirl Vanes Removed

C-39. Temporal High Response Total Pressure 136
Fluctuation in Core Region, Corner 3 and
Swirl Vanes Installed

C-40. High Response Probe Calculated Turbulence 137
Intensity Time Trace at Test Section
Center, Configurations C21 and C19

C-41. High Response Probe Profiles on Test Section .. 138
Vertical Centerline, Configuration C24

C-42. High Response Probe Profiles on Test Section .. 139
Horizontal Centerline, Configuration C24

C-43. Test Section Total Pressure & RMS Profiles 140
Corner 3 Installed: C05 & C04

C-44. Test Section Total Pressure & RMS Profiles 141
Corner 3 Removed: C10 & C13

C-45. Test Section Total Pressure & RMS Profiles 142
Corner 3 Installed: C05, C06, & C07

C-46. Test Section Total Pressure & RMS Profiles 143
Corner 3 Removed: C10, C09, & C08

C-47. Test Section Total Pressure & RMS Profiles 144
Corner 3 and Swirl Vanes Removed:
C13, C14, & C15

C-48. Test Section Total Pressure & RMS Profiles 145
C19 and C24

C-49. Test Section Total Pressure & RMS Profiles 146
C21 and C22

C-50. Test Section Total Pressure & RMS Profiles 147
C19 and C23

C-51. Layout of Acoustic Instrumentation 148

C-52. Cross-Magnitude, Phase, and Coherence 149
Microphone Locations A & B, Setup A

C-53. Cross-Magnitude, Phase, and Coherence 150
Microphone Locations A & B, Configuration C19

C-54. Cross-Magnitude, Phase, and Coherence 151
Microphone Locations A & E, Configuration C19

C-55. Cumulative Sound Power and Power Spectra 152
From Acoustic Data in Test Section Floor
Configurations C05 and C04

C-56. Cumulative Sound Power and Power Spectra 153
From Acoustic Data in Test Section Floor
Configurations C05 and C19

C-57. Cumulative Sound Power and Power Spectra 154
From Acoustic Data at the Cross-Leg
Diffuser Exit, Configurations
C04, C05, C07, & C19

C-58. Power Spectral Density Comparison of Acoustic . 155
And Hot Wire Data, Baseline and C19

C-59. Cumulative Turbulence Intensity Comparison 156
Of Acoustic and Hot Wire Data, Baseline and C19

C-60. Cumulative Intensity Difference of Acoustic ... 157
And Hot Wire Data, Baseline and C19

C-61. Cross-Leg Diffuser Pressure Coefficient and ... 158
Temporal Fluctuation Distributions, Corner 3
Removed, 4/5 Screen Installed

C-62. Cross-Leg Diffuser Pressure Coefficient and ... 159
Temporal Fluctuation Distributions, Corner 3,
Swirl Vanes, 4/5 Screen Installed

C-63. Cross-Leg Diffuser Pressure Coefficient and ... 160
Temporal Fluctuation Distributions, 2 Exit
Screens and Long Cell Honeycomb Installed

C-64. Cross-Leg Diffuser Pressure Coefficient and Temporal Fluctuation Distributions Baseline Configuration ... 161

C-65. The Effect of Flow Conditioners on Test Section RMS Temporal Fluctuations of Total and Static Pressure 162

C-66. Effect of Flow Conditioners on the RMS Temporal Fluctuation in Flow Angle of the Flow Angularity Probe and Hot Wire Anemometer 163

C-67. Stilling Chamber and Test Section Core Region Total Pressure Spatial Distribution And Temporal Fluctuation Summary 164

C-68. Test Section to Stilling Chamber Core Region Total Pressure Spatial Distribution and Temporal Fluctuation Ratios .. 165

C-69. Test Section to Stilling Chamber Core Region Axial Turbulence Temporal Fluctuation Ratios .. 166

C-70. Test Section to Stilling Chamber Core Region Yaw and Pitch Angle Temporal Fluctuation Ratios .. 167

I INTRODUCTION

Force data exhibiting unacceptable levels of scatter were discovered during testing at a supersonic wind tunnel in March 1993. Investigation into the source of the scattered data revealed that temporal fluctuations of flow angle in the test section were responsible. Subsequently, it was found that flow angle fluctuations had always been present in the wind tunnel. However, in past testing these fluctuations were considered insignificant for the model types tested. More recently as aircraft designs have become more neutrally stable and instrumentation has become more sensitive, these effects have become significant. Modern instrumentation and data acquisition systems, for example, are able to better resolve time varying flows and resulting forces than in the past. Previous investigations led to the conclusion that intermittent flow separation in the crossleg diffuser was the source of the fluctuations. Hence, swirl vanes were installed at the diffuser inlet in 1995 in the full-scale tunnel to eliminate the intermittent separations. This modification reduced the temporal flow angle fluctuations in the test section, but not to the required levels.

Flow separations in the wind tunnel circuit were suspected as the cause of test section flow angle non-uniformity soon after the full-scale wind tunnel operation began in December 1960. The initial calibration of the wind tunnel reported that the spatial uniformity of flow angle was unsatisfactory. Flow separations were

investigated as the cause of the non-uniformity until vortex generators were installed in the crossleg diffuser inlet in 1967. However, efforts were focused on improving the time-averaged velocity profiles in the diffuser exit plane and stilling chamber, and spatial uniformity in the test section. The unsteady aspect of the separations was almost ignored until their effect became apparent during testing in March 1993 as mentioned above. This led to the installation of the swirl vanes in 1995.

A 60-degree cone probe was installed on the test section centerline to take flow angularity data before and after installation of the swirl vanes. The approximate values of deviation in test section pitch and yaw angle before and after swirl vane installation are shown in Table A-1.

Corner 3 inlet and stilling chamber velocity profile data taken after the swirl vanes were installed were provided to analysts in the Advanced Technology Segment group of Sverdrup Technology, Inc. for comparison with a set of comparable measurements taken in a scale model of the supersonic wind tunnel circuit. Full scale and model comparisons will be discussed later in this report.

The personnel of the Advanced Technology Segment (ATS) of Sverdrup Technology, Inc. have performed investigations on a 1-to-17.75 (5.63%) scale model of the full-scale supersonic wind tunnel circuit in its aerodynamic laboratory in Tullahoma, TN. This scale was selected to keep the scale model Reynolds numbers at approximately 10%

of full-scale Reynolds numbers with reasonable size and power requirements. The experimental efforts of the ATS focused on the effect of installing various flow conditioning devices at selected locations of the wind tunnel circuit on the test section flow unsteadiness. These flow conditioning devices included: swirl vanes installed as in full-scale tunnel; flow smoothing and damping screens at various locations along the crossleg diffuser; a short cell honeycomb (L/D=17) located in the stilling chamber; and a long cell honeycomb (L/D=52) located in the stilling chamber. Conclusions drawn from these experiments were used as the basis for recommending modifications to the full-scale tunnel to mitigate the high fluctuation levels in the wind tunnel test section. The primary recommendation made was to install two screens, each with a porosity of 54 percent, at the crossleg diffuser exit and a long cell honeycomb in the stilling chamber.

This thesis documents the investigation of the flow unsteadiness performed by the author, a member of the ATS in Tullahoma, TN, and presents a discussion on the methodology to conduct the experimental program and the results each combination of flow conditioning devices had on the various research parameters.

II EXPERIMENTAL SETUP

2.1 APPARATUS

A model scale of 1-to-17.75 (5.63%) was selected for the supersonic wind tunnel circuit bases on a literature survey of similar investigations and on practical considerations associated with model fabrication and facility operations. Many studies of wind tunnel flows have been conducted at 10 percent scale (e.g. Refs. 1-5), and at nominally 10 percent of full-scale tunnel Reynolds number. Since the full-scale tunnel operates nominally at a total pressure of one-half atmosphere and about 140°F total temperature, a model scale of about 5 percent provides 10 percent of full-scale Reynolds number by matching velocity and assuming ambient pressure in the subsonic portions of the full-scale tunnel. At 5.63 percent scale, the model size and power requirements were consistent with available space and building power. The final scale (5.63%) was arrived at by adjusting the diameter of corner 3, Figure B-1, to match the inside diameter of commercially available PVC pipe which was used for the air inlet ducting. This process resulted in a final diameter of 17.94 in. for corner 3 compared to the corresponding 26.54 ft in the full-scale tunnel. The corresponding diameters of corner 4 and the stilling chamber are 36.94 in. in the model and 54.64 ft in the full-scale tunnel.

Initial testing of the model was started before fabrication of the corner 3 and 4 turning vane sections was complete. The model was assembled without the corners and crossleg diffuser as illustrated in the layout sketch shown in Figure B-2. A temporary stilling chamber was constructed by reversing the inlet section of corner 4. A screen and a section of honeycomb were attached to the temporary stilling chamber to serve as an air inlet. This layout, designated Setup A, was used to validate instrumentation setups, check fan operation, and check facility acoustic levels. Acoustic data were acquired in the test section to define the fluctuating pressure level and peak frequencies that the downstream circuit components would impose on data to be taken later with the more complete facility.

The scale facility was then modified by including the crossleg diffuser upstream of corner 4 and was designated setup B, with the layout shown in Figures B-3 and B-4 with corner 3 installed and removed, respectively. The crossleg diffuser, corner 3, corner 4, the stilling chamber, and the contraction are the scaled components of the full-scale tunnel. Significant effort was made to duplicate the exact scaled geometry of the full-scale tunnel from the backleg duct to the end of the contraction. This included duplicating turning vane geometry, allowing for internal thermal insulation in setting the model air lines, and installing the screen across corner 4 identical to the screen installed in the full-scale tunnel. The duct diameter upstream of corner 3 was also scaled in diameter but not length.

The model facility operates by inducing inflow of atmospheric air through an inlet with suction provided by a 125 hp variable speed centrifugal fan. The contraction is connected to a 16 in. wide by 11.84 in. high Plexiglas test section. A "high speed" diffuser and acoustically treated corner are located downstream of the test section. The air inlet ducting upstream of corner 3 consists of one or more 20 ft sections of 18 in. inside diameter PCV pipe. The number of inlet sections was varied during the test program as a means of adjusting the velocity profile at corner 3. Inlet velocity profiles at corner 3 were varied to match full-scale wind tunnel data. The air inlet duct was fitted with a screened bellmouth inlet on the upstream end and was connected to corner 3 at the downstream end by sections of straight pipe, Fig. B-3.

The scale model does not have a supersonic nozzle or supersonic test section since the objective of the project was to simulate the subsonic flow that occurs upstream of the supersonic nozzle. Geometric scaling of full-scale tunnel components ends at the end of the fiberglass contraction. At this point the top and bottom walls in both the model and in the full-scale tunnel are parallel. The sidewalls in the full-scale tunnel continue to contract to the sonic throat and then expand to form the supersonic section of the nozzle. In the model the sidewalls are faired into the parallel walls of the test section.

The cross-leg diffuser, corner 3 and corner 4 were made of high quality plywood and polycarbonate sheets. The

cross-leg diffuser was made up of seven segments as shown in Figure B-5. The inlet and outlet diameters of the diffuser are 17.94 in. and 36.94 in., respectively, and the half-angle is 4.2 deg. The turning vanes in corners 3 and 4 are aluminum extrusions with the same profile as the full-scale wind tunnel vanes. The vanes in these corners have identical profiles with a chord of 3.95 in. Corner 3 contains 17 vanes set at a spacing interval of 1.41 in. and corner 4 contains 41 vanes spaced 1.24 in. apart. The gap to chord ratios are 0.357 and 0.314, respectively.

A 28 mesh x 0.0105 in. diameter wire screen was installed across the leading edge of the corner 4 turning vanes for most of the experiments.

Table A-2 lists the materials of construction for the various model components, and Table A-3 gives details on the screens and honeycombs used for flow conditioners. The crossleg diffuser was comprised of 7 segments and the dimensions of the segments are also included in this table.

The full-scale wind tunnel contains no flow conditioners other than crossleg diffuser swirl vanes and a 28-mesh screen upstream of and across the corner 4 turning vanes. Flow conditioning devices tested in the scale model included various combinations of screens in the crossleg diffuser between segments 2 and 3 (2/3 screen), between segments 4 and 5 (4/5 screen), and one and two screen combinations at the diffuser exit as listed in Table A-3.

Long cell and short cell honeycomb sections, with cell length-to-diameter ratios of 52.4 and 17.5 respectively, were tested in the stilling chamber. Both honeycombs have nominally hexagon shaped cells with an area-based equivalent diameter of 0.115 in. Both are made of 0.003 in. thick aluminum sheet.

The full-scale wind tunnel currently has a set of 12 swirl vanes installed at the crossleg diffuser inlet just downstream of the corner 3 turning vanes as shown in Figure B-4. The swirl vanes have a circular arc profile with a flat "bottom", and are set at an angle of attack of 14 degrees. The vanes have a 15 percent thickness ratio and a span of 19.75 percent of the duct diameter. Experiments with and without the swirl vanes were conducted in the scale model.

The scale model facility was generally operated at a nominal test section dynamic pressure of 69.2 psf (12.1 in. w.g.), which corresponds to a nominal Mach number of 0.21 and velocity of 240 ft/sec. This condition sets the velocity in corner 4 and the stilling chamber at nominally 40 fps. In the full-scale tunnel, the stilling chamber velocity varies with test section Mach number. The nominal range is 12 to 63 fps for the full-scale tunnel. The higher value corresponds to operation with a test section Mach number of 1.5 and the lower value to a test section Mach number of 3.5. Except for total pressure losses in the inlet ducting, the scale model operates at ambient pressure (2045 psf) and temperature (70 F). By comparison, the full-scale wind tunnel typically operates at a total

pressure of 1000 to 1200 psf and at nominally 140 F. These parameters correspond to a stilling chamber Reynolds number of 7.7×10^6 in the scale model a range of 1.7×10^7 to 9.3×10^7 in the full-scale tunnel.

2.2 TEST PROCEDURES

2.2.1 SETUP A

Setup A testing was done to ensure fan performance, verify instrument operation, quantify noise levels in the test area and to baseline tunnel noise propagations. Acoustic data was taken at the test section inboard wall, floor, outboard wall, and the high-speed diffuser wall.

2.2.2 SETUP B

Setup B was used to study the effects of different flow straightening and smoothing devices on pressure and velocity non-uniformities in the test section. It is this series of experiments from which conclusions are drawn concerning the effects of the different components on flow quality. Model components were added or removed one at a time to ensure direct comparisons of the test data. The flow conditioning elements examined include swirl vanes, screens, and honeycombs, and their various combinations and arrangements.

Individual configurations tested are referred to as C01, C02, etc. A key to the configurations is given in Table A-4. Numerical entries other than zero in table

columns indicate the presence and number of the item identified in the column headers. Configurations C01 through C04 were concerned with conditioning the velocity profile at corner 3 to match the profile observed in the full-scale tunnel. The number of lengths of the inlet pipe was varied and a screen was added at the inlet pipe at the air intake during these tests. The swirl vanes were first installed on configuration C05. Screens were added and removed from the cross-leg diffuser starting with C06. Corner 3 was removed from the circuit starting with C08 to verify that the corner 3 vanes did not induce the unsteady flow separation observed in the cross-leg diffuser. The corner and swirl vanes were reinstalled at C18. The evaluation of honeycomb in the stilling chamber started with C17. The corner 4 screen was removed for the last configuration tested (C24). Configurations C05 and C21 are repeat configurations and represent the current configuration of the full-scale wind tunnel crossleg diffuser and stilling chamber.

An array of tests was performed for each configuration for data acquisition and comparison. The following types of data were taken for various configurations; Acoustic data, Corner 3 inlet total pressure profile, corner 3 exit total pressure profile, cross-leg diffuser static pressure scan, corner 4 inlet total pressure profile, stilling chamber total pressure profile, test section total and static pressure profiles, test section flow angle fluctuation profile, and turbulence measurements in the stilling chamber and test section. A test log was created for the experimental program to record test conditions such

as ambient temperature, atmospheric pressure, and probe location for each data set. Also, a code was assigned to each data set to identify what type of data was taken to facilitate file distinction by the Fortran data reduction program.

The fan speed was adjusted for each test to attain a dynamic pressure, $q=1/2\rho u^2$, of approximately 69.2 psf (12.1 in. w.g.) in the test section. The nominal test conditions for various points of the scale model tunnel circuit are shown in Table A-5.

2.3 INSTRUMENTATION

The scale model fan speed was controlled using National Instruments Co. LabView™ software. Test probe pressure tubes were connected to MKS Model 698 differential pressure transducers. The transducer output signal was then filtered using a NEFF 470 signal conditioner and data acquisition system, and recorded using LabView™. Hot wire anemometer data was recorded and processed using a TSI IFA 300 Constant Temperature Anemometer System. In general, a minimum sampling frequency of 100 Hz and a test duration of 180 seconds was used to ensure that periodic fluctuations between 0.01 and 50 Hz could be captured. Details of pressure taps, probes, and rakes are listed in the following sections.

2.3.1 CROSSLEG DIFFUSER STATIC TAPS

Static pressure taps were installed along the centerline of the outboard side wall of the cross-leg diffuser. The taps were .063 inch diameter and spaced along the longitudinal axis in the plane of symmetry as shown in Table A-6. The taps were connected by tubing to a Scanivalve® switching unit; the pressure tubing was 0.063 inch ID urethane, with the shortest tube length being about 15 ft.

2.3.2 PITOT-STATIC PROBES

United Sensor® pitot-static probes were used to take total and static pressure measurements at the inlet to corner three, in the stilling chamber, and in the test section. The probes were 0.25 inch OD with a hemispherical head, 0.088 inches diameter total pressure orifice, and four diametrically opposed 0.033 inch diameter static pressure orifices located 1 inch aft of the probe nose. The probes' shank lengths (parallel to flow) were 3.5 inches (14 diameters). The test section probe height (normal to flow) was 12 inches; while the stilling chamber and corner 3 probe heights were 24 inches.

2.3.3 HIGH RESPONSE PITOT PROBE

A high response pitot probe was use to take total pressure measurements in the test section. The probe was fabricated out of 0.125 inch OD x .035 inch wall tubing. A 90 deg bend was located approximately 3 inches from the

probe tip. The remaining portion of the tubing was inserted into a section of 0.25 in. diameter tubing, which, in turn, passed through a compression fitting mounted on the test section wall. A 30 inch long length of flexible silicon tubing with an inside diameter of 0.10 inch was used to connect the probe to an MKS® transducer.

2.3.4 HIGH RESPONSE STATIC PROBE

A tubing configuration identical to the one described above for the high response total pressure probe was used to connect a test section wall static pressure tap to an MKS® transducer.

2.3.5 FLOW ANGULARITY PROBE

A United Sensor® 3-Dimensional Directional probe, P/N DA-250-24-CD, was used to measure flow angularity fluctuations in the test section. The primary sensing orifices are 0.031 inch diameter drilled through to a 0.032 inch diameter by 1.5 inch long passage. This passage then transitions to a 0.047 inch passage through the rest of the probe. The overall probe diameter is 0.25 inch and overall length is 24 inches. The primary sensing orifices are located in a small wedge machined into the 0.25 in. diameter body of the probe. The apex of the wedge is truncated so as to form a flat nosed wedge. A third sensing orifice is located in the nose of the wedge. During testing the primary sensing orifices, on opposite sides of the wedge, were each connected to the MKS® sensor and recorded simultaneously. The 0.25 in. body of the

probe was passed through a compression fitting mounted in the test section wall. Silicon tubing with an inside diameter of 0.010 in. was used to connect the probe to the two MKS® transducers. The transducers were referenced to local ambient pressure.

2.3.6 TOTAL PRESSURE RAKES

Total pressure rakes were installed at the corner 3 inlet, corner 3 exit, corner 4 inlet, and in the stilling chamber to obtain total pressure and total pressure fluctuation profiles at the respective locations. These data were used to extract velocity profiles as well.

2.3.6.1 STILLING CHAMBER RAKE

The stilling chamber rake could be installed on the horizontal or vertical centerline in the stilling chamber or on the horizontal centerline of the inlet to corner four. The rake consisted of twenty-nine (29) 0.063-inch diameter pitot probes. The probe spacing is shown in Table A-7. Care was taken to ensure that the length of tubing from each probe to the pressure transducer was the same to give equal response time for all rake probes. The tubing length was 15 feet. When a honeycomb was installed, the upstream end of the rake probes were 2 inches from the honeycomb face.

2.3.6.2 CORNER 3 INLET RAKES

Two eleven probe rakes were fabricated that could be installed back-to-back on the horizontal or vertical centerline at the inlet to corner 3 to achieve a twenty-two point cross sectional profile. Each rake length was equal to the inlet duct radius and consisted of eleven (11) 0.125 inch diameter pitot probes. The probe spacing is shown in Table A-8. Care was taken to ensure that the length of tubing from each probe to the pressure transducer was the same to give equal response time for all rake probes. The tubing length was 15 feet.

2.3.6.3 CORNER 3 EXIT SURVEY RAKE

The corner 3 exit rake consisted of three, 0.125 inch diameter probes, one inch apart. The rake was traversed manually to obtain profiles at the exit of corner 3.

2.3.7 DATA ACQUISITION HARDWARE

2.3.7.1 PRESSURE TRANSDUCERS

MKS® Model 698 differential pressure transducers were used to measure the gauge pressure of the total and static pressure probes. The transducers have a 0 to 100 torr range, a resolution of $1x10^{-6}$ of full scale, and a manufacturers listed accuracy of 0.05% of transducer reading.

An MKS® Model 690 absolute pressure transducer was used to measure ambient pressure. The absolute transducer has a 0 to 1000 torr range, a resolution of $1x10^{-6}$ of full scale, and a manufacturer's listed accuracy of 0.05% of transducer reading. Both transducer models have a 10 kHz low-pass filter.

2.3.7.2 SIGNAL CONDITIONER

A NEFF 470 signal conditioner was used prior to data recording. The signal conditioner has a total sampling rate of 10 kHz with a 16-bit Analog-to-Digital Converter (ADC) resolution. The following cards were installed in the system during testing:

- Calibration Card (470085)
- 3, 16-channel transformer coupled multiplexer cards (470056)
- 4-channel conditioner/multiplexer (470054)
- 16-bit isolated ac/dc input (470011)
- 2-channel frequency card (470012)
- 8-point relay output (470031)

2.3.7.3 HOT WIRE ANEMOMETER SYSTEM

A TSI® IFA 300 Constant Temperature Anemometer System was used to obtain the velocity components of the turbulence in the stilling chamber and the test section. The TSI® system utilizes constant temperature x-film probes. The samples were acquired at 1 kHz with a 300 Hz

analog low-pass filter. When a honeycomb was installed, the stilling chamber hot-wire probe tip was 6 inches from the honeycomb face.

2.3.8 CONSISTENCY AND RESPONSE CHECKS

Calibration tests were performed to confirm the accuracy and time response of the employed probes. Tests performed include: transducer and flow angularity probe accuracy, and response tests on the flow angularity probe, pitot-static probes, and the high response pitot and static probes.

2.3.8.1 TRANSDUCER CONSISTENCY

Transducer calibration was verified by applying a known pressure load to the transducers. A water manometer provided the source pressure, the magnitude of which was measured both by the transducer and an indicator on the water manometer. Figure B-6 shows that the measured pressure is exactly that of the applied pressure to within the uncertainty band of the water manometer.

The flow angularity probe calibration was verified using in-flow measurements. The flow angle probe was inserted in the test section and aligned with the mean flow by matching the pressure on each yaw port. Pressure measurements were then taken with the probe installed at various known angles relative to the mean flow. The calibration constant was calculated per the manufacturer using equation 1.

$$\beta = \frac{P_1 - P_2}{qSF} \tag{1}$$

where: P_i Port pressure

q Test section dynamic pressure

SF Calibration constant

β Flow angle

The calibration constant is the slope of the curve in Figure B-7, which agrees well with the manufacturer's SF of 0.046.

2.3.8.2 PROBE RESPONSES

Probe response tests were performed by applying a pressure load to the probe and subsequently releasing the load to create a step input to the measurement system. A second order polynomial regression curve was fit to the time-wise pressure decay data and the respective time derivatives. This approximates the system response as a second order system, and provides for the coefficients of the first and second derivatives as a function of time as shown in equation 2.

$$P = P_m + a_1 \frac{dP_m}{dt} + a_2 \frac{d^2 P_m}{dt^2} \tag{2}$$

where: $\alpha_{1,2}$ Function Coefficients

P Corrected (actual) pressure

P_m Measured pressure

t Time

Figure B-8 shows the time-wise data and the corrected pressure curves for the flow angularity probe.

The amplitude ratio can be found as a function of perturbation frequency as shown in equation 3.

$$\frac{P_m}{P} = \frac{1}{\sqrt{\left(1-\left(\frac{\omega}{\omega_n}\right)^2\right)^2 + 4\zeta^2\left(\frac{\omega}{\omega_n}\right)^2}} \qquad (3)$$

$$\omega_n = \frac{1}{\sqrt{a_2}} \qquad \zeta = \frac{a_1}{2\sqrt{a_2}}$$

$$\omega = 2\pi f$$

where: P Corrected (actual) pressure.

P_m Measured pressure.

ω_n Natural frequency, rad/sec.

ζ Damping coefficient.

ω Perturbation frequency, rad/sec.

f Perturbation frequency, Hz

Figure B-9 shows the frequency response of the flow angularity probe and the high response pitot probe.

2.3.8.3 ERROR ESTIMATION

The random error of calculation results by propagation of errors in measurement were found by the method outlined in chapter IV of Reference 13. Typical random error associated with various data reduction methods are discussed in Section 2.4.

2.3.9 ACOUSTIC INSTRUMENTATION

A Bruel and Kjaer® (B&K) acoustic measurement system was used to measure the acoustic pressure fluctuations in the circuit at multiple locations simultaneously. The system included a B&K Nexus 4 channel signal conditioner and power supply, Lemo cables, a calibrator, pre-amplifiers, and microphones. The microphones were B&K type 4193 low frequency response microphones with a B&K type 0211 adapter. The pre-amplifiers were B&K type 2669. The data acquisition system was laptop based with a 16-channel A/D card installed. LabView™ software was used to record the acoustic data. The B&K calibrator produced a 94 dB tone at 1000 Hz for calibration and a 114 dB tone at 1000 Hz as a system check.

2.3.10 TEST SETUP DIAGRAMMATICS

The corner 3 inlet total pressure rake probes were connected to ports seventeen (17) through thirty-seven (37) of a Scanivalve® which was used to step though each probe sequentially. A pitot-static probe was installed at the inlet to corner 3 to take comparative total and static

pressure measurements on Scanivalve® ports one (1) and two (2) respectively. The static pressure taps along the cross-leg diffuser axis were connected to Scanivalve® ports three (3) through sixteen (16). A pitot-static probe was also installed in the test section to record the test section dynamic pressure. A sketch of the test setup for the corner 3 inlet total pressure rake and diffuser static pressure scan is shown in Figure B-10.

The corner 3 exit rake was traversed manually across the horizontal centerline of the corner 3 exit plane. The rake probes were connected to ports thirty-eight (38) through forty (40) of the same Scanivalve® mentioned above. A sketch of the test setup for the corner 3 exit total pressure rake is shown in Figure B-11.

The pitot probes of the total pressure rake used in the stilling chamber and corner 4 inlet were connected to ports one (1) through twenty-nine (29) of a Scanivalve® which stepped through each probe sequentially. A pitot-static probe was installed in the stilling chamber and connected to Scanivalve ports thirty (30) and thirty-one (31) and in the test section connected to ports thirty-two (32) and thirty-three (33). A sketch of the test setup for the corner 4 inlet and stilling chamber total pressure rake is shown in Figure B-12.

The test section pitot-static, high response pitot and static, and flow angularity measurements were made by manually traversing the probes across the test section. Total and static pressures were taken simultaneously for

pitot-static and high response measurements, as were the static pressures on the flow angularity probe. Sketches of the test setup for the pitot-static probes, high response probes, and flow angularity probe are shown in Figures B-13 to B-15.

The hot-wire anemometer turbulence measurements were taken by inserting the probe assembly through the tunnel ceiling and traversed vertically across the stilling chamber or test section to acquire axial and pitch data, or through the tunnel wall and traversed horizontally to acquire axial and yaw data. The probe assembly was connected to the signal processor by coaxial cable. A sketch of the hot-wire anemometer test setup is shown in Figure B-16.

2.4 DATA REDUCTION

A Fortran program was written to reduce all data of a given type, while a MatLab™ code, from The Mathworks, Inc., was used to perform spectral analysis of turbulence data. A test log was created to assign nominal test conditions, probe position, and a data type code to each data file. Table A-9 shows a sample of the test log and an explanation of the test codes.

For all data files the average values and standard deviations of the sampled data were calculated as shown in equation 4.

$$RMS(X) = \sqrt{\frac{\sum_{i=1}^{n}(X_i - X_{ave})^2}{n}} \qquad (4)$$

$$X_{ave} = \frac{1}{n}\sum_{i=1}^{n} X_i$$

where: $RMS(X)$ Standard deviation of data file

n Number of samples of data file

X_i i^{th} sample argument value

X_{ave} Average argument value of data file

Data stationarity was tested by dividing a sample record into equal time intervals and computing the mean square of each interval. The variation between the maximum and minimum mean square value was less than 2 percent. Therefore the system can be considered stationary and the mean and mean square deviations of each data file can be considered in the temporal sense. From here forward, the point-wise deviations of a sample record will be referred to as temporal deviations.

Fan speed data was recorded for every data file. However, the data exhibited some amount of scatter due to electrical noise, causing high deviation levels. Therefore, this data was modified by applying a correction filter using a three-sigma test as shown in equation 5.

$$If\ |RPM_i - RPM_{ave}| > 3Rms(RPM)$$

$$Then\ RPM_i = RPM_{ave} \tag{5}$$

where:

RPM_i	Measured fan speed of i^{th} sample, rpm.
$Rms(RPM)$	Standard temporal deviation of raw data file, rpm.
RPM	Average fan speed of raw data file.

The average and temporal standard deviation of the new fan speed data set was then recalculated using equation 5 to obtain a more accurate prediction.

2.4.1 PITOT-STATIC PROBE SURVEYS

Total and static pressure measurements were taken with the pitot-static probe at 100 samples per second for 180 seconds to capture periodic fluctuations from 0.01 to 50 Hz. Each 180-second sample created one data file. The probe was then traversed across the test section to obtain profile data.

2.4.1.1 PROFILE DATA

The average total and static pressures of each point were referenced to their respective average value of the core flow, where the core flow is defined to be the region of flow from the test section center to 75% of the height and width of the test section. The core region typically consisted of 20 points for pitot-static surveys. These data were in turn normalized by both the average test

section dynamic pressure and average total pressure of the core flow as shown in equations 6.

$$DPt/q = \frac{Pt - Pt_{bar}}{q_{bar}} \qquad DPs/q = \frac{Ps - Ps_{bar}}{q_{bar}}$$

$$DPt/Pt = \frac{Pt - Pt_{bar}}{Pt_{bar} + P_{amb}} \qquad DPs/Pt = \frac{Ps - Ps_{bar}}{Pt_{bar} + P_{amb}} \tag{6}$$

where:

- Pt Average measured total gage pressure at one point
- Pt_{bar} Average total gage pressure of the core flow
- Ps Average measured static gage pressure at one point
- Ps_{bar} Average static gage pressure of the core flow
- P_{amb} Atmospheric pressure from test log
- q_{bar} Average dynamic pressure (Pt-Ps) of the core flow

The calculated random error of the above equations are as follows:

DP/q = +/- 1.25×10^{-3} DP/Pt = +/- 4.0×10^{-5}

The temporal standard deviation of the total and static pressures at each point were calculated by equation 4. This data was also normalized by the average test section dynamic pressure and average total pressure of the core flow as shown in equations 7.

$$RMS(DPt/q) = \frac{RMS(Pt)}{q_{bar}} \qquad RMS(DPs/q) = \frac{RMS(Ps)}{q_{bar}}$$

$$RMS(DPt/Pt) = \frac{RMS(Pt)}{Pt_{bar} + P_{amb}} \qquad RMS(DPs/Pt) = \frac{RMS(Ps)}{Pt_{bar} + P_{amb}} \tag{7}$$

where: *RMS(Pt)* Temporal standard deviation of *Pt*

RMS(Ps) Temporal standard deviation of *Ps*

2.4.1.2 SUMMARY DATA

The spatial deviation of the profiles and the deviation of the temporal variance of the profiles in the core flow region were calculated by equations 8.

$$RMS(DPt/q)_{Spatial} = \sqrt{\frac{1}{n}\sum_{i=1}^{n}\left[(DPt/q)_i - (DPt/q)_{ave}\right]^2}$$

$$RMS(DPt/Pt)_{Spatial} = \sqrt{\frac{1}{n}\sum_{i=1}^{n}\left[(DPt/Pt)_i - (DPt/Pt)_{ave}\right]^2} \tag{8}$$

$$RMS(DPt/q)_{Temporal} = \sqrt{\frac{1}{n}\sum_{i=1}^{n}\frac{RMS(Pt)^2}{q_{bar}}}$$

$$RMS(DPt/Pt)_{Temporal} = \sqrt{\frac{1}{n}\sum_{i=1}^{n}\frac{RMS(Pt)^2}{Pt_{bar} + P_{amb}}}$$

where: n Number of points in the core region

$(X)_{ave}$ Average parameter value across span

Deviations in static pressure are performed in a similar fashion.

2.4.2 FLOW ANGULARITY PROBE

The flow angularity probe was installed in the test section to obtain the temporal and spatial deviations in flow angle. This was accomplished by zeroing the probe at the test section centerline by equalizing the pressure on each static pressure port, then traversing the probe across the test section. The pressure measurements at each location were taken at 100 sample per second for 300 seconds. Each 300 second sample created one data file. Flow angle data was taken for 300 seconds to provide a sufficient sample length to detect any aperiodic changes in flow angle due to intermittent separation in the crossleg diffuser.

2.4.2.1 PROFILE DATA

The flow angle of each sample was calculated by equation 9.

$$\beta = \frac{P_1 - P_2}{qSF} \tag{9}$$

where: β Flow angle, degrees.

P_1 Average pressure of probe port 1 for data file

P_2 Average pressure of probe port 2 for data file

q Test section dynamic pressure from test log

SF Calibration coefficient, SF=0.046.

The calculated random error of the above equation is as follows:

$$\beta = +/- \ 0.045 \text{ deg}$$

The averages and temporal standard deviations of flow angle for each data file was then calculated by equations 4.0a. For the flow angularity data, the actual calculated flow angle is of little importance. The pertinent parameter here is the fluctuation level in flow angularity given by the temporal standard deviation.

2.4.2.2 SUMMARY DATA

The spatial deviations of the profiles and the deviations of the temporal variance of the profiles in the core flow region were calculated by equations 10.

$$RMS(\beta')_{Spatial} = \sqrt{\frac{1}{n}\sum_{i=1}^{n}[\beta_i - \beta_{ave}]^2}$$

$$RMS(\beta')_{Temporal} = \sqrt{\frac{1}{n}\sum_{i=1}^{n} RMS(\beta_i)^2} \qquad (10)$$

where: $RMS(\beta')_{Spatial}$ Spatial deviation of profile, degrees

β_i Mean flow angle of the i^{th} point

β_{ave} Mean flow angle of the core region

$RMS(\beta')_{Temporal}$	Deviation of profile variances, degrees
$RMS(\beta_i)$	Temporal deviation of the i^{th} point
n	Number of points in core region

2.4.3 TOTAL PRESSURE RAKES

Total pressure rakes were used to obtain total pressure profiles, temporal deviations in total pressure profiles, and spatial deviations in total pressure at the inlet to corner 3, the exit of corner 3, the inlet to corner 4, and in the stilling chamber.

Total pressure measurements were taken sequentially at each port at 100 samples per second for 180 seconds. Average total pressure and temporal standard deviation of each port were found using equations 4.0a. The average total pressure of each port was referenced to the average total pressure of the three central rake ports. These data were then normalized by both the local dynamic pressure and the local total pressure of the three central rake ports. Here the local dynamic pressure was calculated by dividing the dynamic pressure data taken in the test section by the local area ratio squared, $q_{loc} = q_{ts}/(A_{loc}/A_{ts})^2$. The total pressure rake data was calculated in the same manner as the pitot-static data as shown in equations 6, 7, and 8.

2.4.4 HOT WIRE ANEMOMETER TURBULENCE MEASUREMENTS

Hot wire anemometer measurements were taken in the stilling chamber and the test section. Velocity components

were acquired at 1 kHz (with a 300 Hz analog low-pass filter) for 262.144 seconds with a resolution of 0.02 m/s.

2.4.4.1 TURBULENCE INTENSITY

The overall turbulence intensity was found as shown in equation 11.

$$\frac{u'}{U} = \frac{\sqrt{\sum_{i=1}^{n}(u-U)^2}}{U} \qquad \& \qquad \frac{v'}{U} = \frac{\sqrt{\sum_{i=1}^{n}(v-V)^2}}{U} \tag{11}$$

where:

u,v	Instantaneous velocity components
u',v'	Average velocity deviations in velocity components
U,V	Mean velocity components
n	Number of sample in data set

2.4.4.2 FREQUENCY CONTENT

The original velocity signal can be approximated as the summation of weighted periodic functions, performed using a Discrete Fourier Transform (DFT). 2^n data point were taken for each data set so that a Fast Fourier Transform (FFT) could be utilized, which requires $n\log_{base2}(n)$ operations compared to n^2 required by the DFT.

This calculation yields the weight coefficients to the periodic functions, each of which represents the turbulent energy contained within a given frequency band. The magnitude of these coefficients represents the amount of energy within that frequency band. The summation of energy in the frequency domain equals the summation of energy in the time domain using the root-mean-square (RMS) as shown in equation 12.

$$RMS[X(t)] = \sqrt{\sum_{i=0}^{k} F(i)} \qquad (12)$$

where: i Index of the frequency band ($0 < k < n/2$)

n Number of samples in the data set

$F(i)$ Magnitude of the FFT coefficients

$X(t)$ Time dependent function

2.4.5 CROSS-LEG DIFFUSER STATIC PRESSURE RECOVERY

Static pressure taps were installed along the cross-leg diffuser to determine the effectiveness of the diffuser in recovering static pressure of the flow. Each static pressure measurement was taken at 100 samples per second for 60 seconds.

2.4.5.1 PROFILE DATA

The diffuser performance was gauged by the pressure coefficient, c_p, given by equation 13.

$$c_p = \frac{p_s - p_{s_in}}{q_{in}} \tag{13}$$

where:
- c_p Pressure coefficient
- p_s Local static pressure
- p_{s_in} Static pressure at diffuser inlet
- q_{in} Dynamic pressure at diffuser inlet

This can be compared to the ideal pressure coefficient, c_{p_ideal}, given by equation 14, to show the efficiency of the diffuser.

$$c_{p_ideal} = 1 - \left(\frac{A_{in}}{A}\right)^2 \tag{14}$$

where:
- c_{p_ideal} Ideal pressure coefficient
- A Local cross-sectional area
- A_{in} Diffuser inlet cross-sectional area

The diffuser efficiency can then be defined as:

$$\eta_d = \frac{c_p}{c_{p_ideal}} \tag{15}$$

2.4.6 ACOUSTIC DATA

Two microphones were mounted in two of the wind tunnel circuit locations for each acoustic data test. Programs written in both Matlab™ and TestView™ were used reduce the data. The Matlab™ program performed an auto spectral

correlation on each microphone location, returning the signal one-sided power spectrum, G_{xx}, as shown in equation 16.

$$G_{XX}(f) = \frac{2}{N\Delta t}\sum_{i=1}^{N} X_i(f,\Delta t)X_i^*(f,\Delta t) \qquad (16)$$

where: N Number of sample points in data block

Δt Time increment between sample points

X_i Fourier coefficients of the time trace, $x(t)$

X_i^* Conjugate of the Fourier coefficients

The overall power level, OPL, can then be found as the sum of the power spectrum magnitudes, which must be equal to the variance of the time trace as shown in Equation 17.

$$OPL = \sum G_{XX} = \sigma(t)^2 \qquad (17)$$

The LabView™ program was used to calculate the coherence, cross-spectral magnitude, and cross-spectral phase of two sets of simultaneous data. The coherence function is a normalized measure of the linear relationship between two signals in the frequency domain. If the two signals are perfectly related, the coherence will have a value of 1.0. Conversely, if there is no relationship between the signals, the coherence will be 0.0. The coherence is given by Equation 18.

$$\gamma_{XY}^{2}(f)=\frac{|G_{XY}(f)|^{2}}{G_{XX}(f)G_{YY}(f)} \tag{18}$$

where:

$\gamma_{XY}^{2}(f)$	The coherence function
$G_{XY}(f)$	The cross-correlation of *x(t)* and *y(t)*
$G_{XX}(f)$	The auto-correlation of *x(t)*
$G_{YY}(f)$	The auto-correlation of *y(t)*
f	Frequency

The cross-correlation, G_{xy}, returns complex coefficients containing magnitude and phase information given by Equations 19a and b.

$$G_{XY}(f)=\frac{2}{N\Delta t}\sum_{i=1}^{N}X_{i}^{*}(f,\Delta t)Y_{i}(f,\Delta t) \tag{19a}$$

$$G_{XY}(f)=|G_{XY}(f)|e^{j\theta_{XY}(f)} \tag{19b}$$

where:

N	Number of sample points in data block
Δt	Time increment between sample points
Y_i	Fourier coefficients of the time trace, *y(t)*
X_i^*	Conjugate of the Fourier coefficients of the time trace, *x(t)*
θ_{XY}	Phase angle between time traces *x(t)* and *y(t)*

III EXPERIMENTAL RESULTS

Experimental results are presented by test type. Model component phenomena shown by a particular test type are shown. Also, the experimental results presented herein are limited to data pertinent to the model component being discussed. Also, for the purposes of this report, the model configurations are referred to by their assigned codes, C01, C02, etc. Refer to Table A-4 for component installation details of each configuration.

3.1 FLOW VISUALIZATION

The ductwork from corner 3 to the end of the test section of the scale model was fabricated of either clear polycarbonate or acrylic. Tufts were installed on the turning vanes in corners 3 and 4, and on the duct walls in the cross-leg diffuser, contraction, and test section to enhance the visualization of the tunnel flow. Tufts attached to the end of a thin wand were also used to manually survey particular areas of interest. Also, when the diffuser exit screens were installed, lightweight foam particles were inserted into the diffuser to show intermittent flow separation in the crossleg diffuser.

The primary conclusions based on visual observations are summarized as follows.

1. The flow in the crossleg diffuser was found to be highly unsteady with and without corner 3, and with

and without the swirl vanes installed; thus, supporting the original hypothesis that the diffuser operates in the transitory stall mode.

2. Visual observations of the motion of tufts and lightweight foam particles showed that the separation regions in the diffuser move about in an apparent random aperiodic fashion. This motion covered approximately 80 percent of the length of the diffuser with or without corner 3 and the swirl vanes installed. Random flow reversal was observed over this entire length. Reversed flow was observed as far upstream as the middle of segment 2 in the scale model. These reversals appeared to the author and other observers to last for a few seconds with a variable period between reversals of a few seconds up to as much as 30 seconds. Flow reversal appeared on a more frequent basis in the downstream region of the diffuser.

3. Tuft motion appeared to the observer to be more intense and more chaotic with the corner removed from the circuit. With the corner installed, the separated flow region tended to favor the inside wall of circuit. The swirl vanes seemed to spread the flow more uniformly around the perimeter of the diffuser, but did not eliminate flow reversals.

4. The intermediate screens had a very decided calming effect on the flow downstream of the screens, but had

essentially no effect on the upstream flow. This was also true of the diffuser exit screens and honeycombs.

5. Tufts attached to the wall of the test section inlet contraction exhibited very noticeable motion with no flow conditioners installed in the stilling chamber or diffuser. Large groups of these tufts simultaneously executed "jerky" back and forth sideways motion in the same direction, but no complete reversals were observed. It is suspected that a region of flow separation existed at the bottom and top of the inlet contraction; however, the velocity there was probably not high enough to vigorously move the tufts. Tufts on the test section wall also showed the same kind of motion as observed in the contraction with an entire row of tufts sudden deflecting sideways.

6. The motion of tufts in the contraction and in the test section was barely visible with diffuser exit screens and stilling chamber honeycomb installed.

7. Reversed flow was observed in the outside vane passages in both corner 3 and 4. In corner 3, the flow in all vane passages appeared to be separated and unsteady with separation originating on the leading edge and extending along the pressure surface of the vanes. This flow appeared to be bi-stable and most intense in vanes rows on the inside of the turn. The same behavior was found in corner 4 when the 28-mesh screen was removed. The vane passages in this corner could not be accessed when the screen was in place.

More details of visual observations are given along with the presentation of data in the following sections. In general the visual observations agree in qualitative sense with the results of the experimental pressure and hot wire anemometer measurements.

3.2 CORNER 3 INLET PROFILE CONDITIONING

Four inlet configurations, C01 through C04, were studied to show the effects of different pipe inlet lengths, the effects of a pipe inlet screen, and to match the total pressure profile of the full-scale tunnel.

Two different inlet lengths to corner 3 were studied. Configurations C01 and C02 used one inlet pipe with an L/D of 13.9. Configurations C03 and C04 used two coupled pipes to create an inlet with an L/D of 26.5. Bellmouth inlets were placed on each pipe inlet. One was within a few inches of the building wall with the one pipe installed. Using two coupled pipes placed the bellmouth inlet outside the building. There was little difference in fluctuation levels whether one or two pipes were used to the inlet of corner 3. The total pressure profile did, however, exhibit a slightly more parabolic shape with the longer L/D.

The total pressure profile with one inlet pipe installed was somewhat asymmetric. The asymmetry was believed to be caused by the proximity of the inlet bellmouth to the building wall. The addition of a planar 1q (K_t=1) screen at the interface of the bellmouth exit and

the pipe inlet improved the profile symmetry as shown in Figure C-1. The shape of the profile with the screen installed suggests that when the flow reached the corner it was not fully developed. The inviscid core appears to extend outward to approximately y/R = 0.5.

With the two pipe inlet installed, the corner 3 inlet total pressure profiles appear fully developed in the sense that the influence of the wall extends inward to the centerline. There was slight asymmetry in the profile, however, with and without the screen installed, indicating flow at the corner 3 inlet station was still sensitive to some unknown asymmetry induced by the bellmouth inlet as shown in Figure C-2.

The corner 3 inlet total pressure profile with the two pipe inlet and the screen installed was judged to be an adequate match to the full-scale tunnel data as shown in Figure C-3. Further improvement by adding length and additional screening would have increased the total pressure loss of the inlet ducting, reducing the attainable test section speed. Therefore all subsequent testing was performed with the two pipe inlet and the 1q inlet screen installed.

3.3 CORNER 3 EXIT TOTAL PRESSURE PROFILES

Total pressure profiles were taken at the exit of corner 3 (cross-leg diffuser inlet) for configurations C04 and C07 with the corner 3 inlet rake removed. From this data, the loss coefficient, K_{c3}, of the corner-turning vane

assembly could be estimated by comparing to the corner 3 inlet data and the effect of the turning vanes shown.

Configuration C04 had no flow conditioning treatments installed. Configuration C07 had the swirl vanes, the 2/3 screen, and the 4/5 screen installed. The flow conditioning devices downstream of corner 3 had little effect on the corner 3 exit total pressure profile and temporal fluctuation profile, as shown in Figure C-4. The shape of the total pressure profiles, however, differs from the corner 3 inlet profiles on the outboard side of the duct.

The loss coefficient of corner 3 could be estimated by the difference in average total pressure between the inlet profiles mentioned in Section 3.2 and the exit profiles normalized by the average dynamic pressure of the corner as shown in equation 20.

$$K_t = \frac{P_{t_inlet} - P_{t_exit}}{q_{corner}} \qquad (20)$$

where:

K_t	-	Corner 3 loss coefficient
P_{i_inlet}	-	Average inlet total pressure
P_{i_exit}	-	Average exit total pressure
q_{corner}	-	Average dynamic pressure of the corner

Plots of the inlet and exit total pressure profiles normalized by the corner dynamic pressure are shown in Figure C-5. The loss coefficient found by equation 20 was

equal to the average difference in magnitude of the two profiles. The experimental loss coefficient of corner 3 was found to be on the order of 0.5 for both configurations C04 and C07 indicating that the loss coefficient is not dependant on the downstream flow conditioning. The loss coefficient of a corner with turning vanes of this type was expected be about 0.12 to 0.2 (Ref 6). This difference led to the investigation of the flow through the turning vanes.

The turning vanes in corner 3 were surveyed visually with a tuft wand to further investigate the high loss coefficient of the corner. The survey revealed highly aperiodic unsteady flow through all vane passages. The flow appeared to detach at the leading edge of the pressure surface of the vanes and remain detached throughout the vane passage. As a result of the high total pressure losses and flow separation in the vane rows, tests were performed with corner 3 removed to ensure that the turning vanes did not cause unsteady flow separation in the crossleg diffuser. Pertinent test results with and without corner 3 installed are presented in the following sections.

3.4 CORNER 4 INLET TOTAL PRESSURE PROFILES

Corner 4 inlet (cross-leg diffuser exit) total pressure profiles were taken for configurations C04, C06, and C07. Figure C-6 shows the total pressure and temporal RMS profiles of these configurations. Configuration C04 is the baseline for these tests without swirl vanes and flow conditioners. Configuration C06 has the swirl vanes and 4/5 screen installed and configuration C07 adds the 2/3

screen. These data show the improvement in spatial distribution and temporal fluctuation by the addition of swirl vanes and flow conditioning screens installed in the cross-leg diffuser. Profiles were not taken with the swirl vanes alone because the swirl vanes induce a large degree of flow angularity that result in inaccurate total pressure measurements.

The total pressure profile of configuration C04 is highly skewed suggesting a large separation in the inboard side of the cross-leg diffuser. The temporal RMS levels, however, are much higher on the outboard side than the inboard side. This difference indicates that the unsteady disturbances sensed by the rake probes are convected with the flow instead of being transmitted like acoustic plane waves. If the unsteadiness had been propagated as a acoustic wave, the temporal fluctuations in the flow separation region would have also been high.

The combination of swirl vanes and the 4/5 screen (configuration C06) greatly improves the spatial uniformity and reduces the temporal fluctuations across the entire profile. The addition of the 2/3 screen further improves the spatial uniformity and temporal fluctuations.

3.5 STILLING CHAMBER TOTAL PRESSURE PROFILES

Stilling chamber total pressure profiles were taken for all configurations except C01, C18, and C20. These data shows the effects of the swirl vanes, screens installed in the cross-leg diffuser, and honeycombs

installed in the stilling chamber on the total pressure spatial profiles and temporal total pressure fluctuations.

3.5.1 EFFECT OF SWIRL VANES

Comparison tests were performed on the swirl vanes with corner 3 installed (configurations C04 and C05) and with corner 3 removed (configurations C10 and C13). As can be seen in Figure C-7, the spatial distribution and temporal fluctuation of the core region were reduced by the same order of magnitude regardless of whether corner 3 was installed or not. This can be shown by defining an attenuation ratio as the ratio of the average spatial distribution or temporal fluctuation of the core region with swirl vanes to the corresponding value without swirl vanes. The attenuation ratios for the swirl vanes are as follows:

Attenuation of spatial distribution: C05/C04 = 0.86
C10/C13 = 0.74

Attenuation of temporal fluctuation: C05/C04 = 0.45
C10/C13 = 0.66

The spatial and temporal RMS total pressure profiles for configurations C04 and C05 are shown in Figure C-8. The swirls vanes reverse the skewness of the total pressure profile in the stilling chamber. Figure C-9 shows the total pressure and temporal RMS profile for configurations C10 and C13 with corner 3 removed. Without the swirl

vanes, the total pressure profiles have a high level core region as reported in Ref 8. With the swirl vanes installed, the high core region total pressure is forced toward the walls. It should be mentioned here that in addition to swirl vane effects, the profiles show that the installation of corner 3 adds to the asymmetry of the spatial profile while reducing the temporal fluctuation levels.

3.5.2 EFFECT OF INTERMEDIATE CROSS-LEG DIFFUSER SCREENS

Screens were installed in two intermediate locations in the cross-leg diffuser. These locations were between segments two and three (2/3 screen) and between segments four and five (4/5 screen) of the cross-leg diffuser. The 4/5 screen was added to a baseline configuration. The 2/3 screen was then added in conjunction with the 4/5 screen. This was done with and without corner 3 installed. Spatial and temporal statistics are summarized in bar chart format in Figure C-10. Total pressure and temporal RMS profiles are shown in Figures C-11 and C-12.

Both spatial distribution and temporal fluctuation of the core region were improved with the addition of each screen as shown in Figure C-10. The most profound effect of the screens was the improvement of the spatial distribution by adding the 4/5 screen with corner 3 installed (C06). With the corner removed, the improvement was not a great. This can be attributed to the large degree of asymmetry of the profile imposed by corner 3. This can readily be seen in Figures C-11 and C-12. Adding

the 2/3 screen did little to the spatial distribution and temporal fluctuations when corner 3 was installed (C07). With the corner removed, however, the addition of the 2/3 screen (C08) reduced both the spatial distribution and temporal fluctuation level to approximately ½ that of configuration C09. It is also interesting to note that while the baseline spatial distribution is much worse with corner 3 installed, the temporal fluctuation is actually better, indicating that the turning vanes tend to act as a subtle flow conditioning device even though the turn creates an asymmetric profile.

3.5.3 EFFECT OF CROSS-LEG DIFFUSER EXIT SCREENS

Diffuser exit screens were added to the array of flow conditioning elements starting with configuration C14. The swirl vanes and corner 3 were already removed to investigate their effect on the flow separations in the cross-leg diffuser. Therefore, the cross-leg diffuser exit screen comparison testing was performed with the swirl vanes and corner 3 removed. One exit screen was added to a baseline configuration, and then an identical screen was added creating back-to-back screens, ¾ inch apart at the diffuser exit.

As with the intermediate screens, both spatial distribution and temporal fluctuation of the core region in the stilling chamber were improved with the addition of each screen as shown by the profiles in Figure C-13. With both exit screens installed, the spatial and temporal attenuation ratios were 0.60 and 0.51 respectively as

defined in Section 3.5.1. A comparison of the total pressure and RMS profiles is shown in Figure C-14.

3.5.4 EFFECT OF CORNER 4 SCREEN

The full-scale tunnel has a screen attached to the leading edge of the corner 4 turning vanes. The screen was removed for one test to check the impact, if any, on tunnel flow quality. This test was done with the long cell honeycomb and two diffuser exit screens installed. Figure C-15 shows the total pressure and RMS profiles with and without the corner 4 screen. As shown, the corner 4 screen does improve the spatial distribution and temporal fluctuations.

3.5.5 EFFECT OF STILLING CHAMBER HONEYCOMBS

A long cell honeycomb (configuration C22) was compared directly to the full-scale tunnel baseline configuration (C21). A short cell honeycomb was installed with two diffuser exit screens installed (configuration C23) and compared to a similar configuration with the long cell honeycomb installed (configuration C19).

A summary of the spatial distribution and temporal fluctuation effects of the honeycombs is shown in Figure C-16. The long cell honeycomb spatial distribution and temporal fluctuation attenuation ratios versus the baseline configuration were 0.41 and 0.71 respectively. The short cell honeycomb showed little effect on the temporal fluctuation level. It did, however, increase the spatial

distribution level. Figure C-17 shows the total pressure and temporal RMS profiles for the baseline configuration (C21) and with the long cell honeycomb installed (configuration C22). The long cell honeycomb flattens the total pressure profile and substantially reduces the temporal fluctuation levels. Figure C-18 shows the total pressure and temporal RMS profiles with two diffuser exit screens installed with the long cell honeycomb (configuration C19) and with the short cell honeycomb installed (configuration C23). It is evident that the total pressure distortion level increases with the short cell honeycomb installed as indicated by the higher total pressure near the outboard wall.

3.5.6 COMPARISON TO FULL-SCALE TUNNEL PROFILE

The total pressure and velocity profiles in the stilling chamber of the baseline model configuration (C21) and the full-scale tunnel are shown in Figure C-19. The model profiles do not match the full-scale profiles. It is believed that this is caused by differences in the duct Reynolds numbers and different characteristic in the flow through the turning vane passages in the scale model. Also, the sample frequency and length of the full-scale data was unknown.

3.6 TEST SECTION FLOW ANGULARITY PROBE DATA

Test section yaw angle fluctuation data was taken at y = -6 in. for configurations C04 to C11, C13 to C17, C19 to C22, and C24, and at y = 0 in. for configurations C18 to

C24. Test section pitch angle data was taken at z = 0 in. for configurations C18 to C22, and C24.

Figure C-20 shows yaw angle fluctuation profiles for configurations C13 to C17 at y = -6 in. This figure compares the effect of various flow-conditioning devices with corner 3 and the swirl vanes removed. Configuration C13 is the baseline with no flow conditioners. As can be seen in the figure, the temporal yaw angle fluctuation decreases with each element addition. Figure C-21 summarizes the temporal fluctuation in the core region of the flow for the same configurations.

Figure C-22 shows yaw angle fluctuation profiles for configurations C19 to C22, and C24 at y = -6 in. This figure compares the effect of various flow-conditioning devices with corner 3 and the swirl vanes installed. Configuration C21 is the full-scale tunnel baseline. As before, the temporal yaw angle fluctuation level decreases with each element addition. Figure C-23 summarizes the temporal fluctuation in the core region of the flow for the same configurations.

Similar results were found for yaw angles at y = 0 in. and for pitch angles at z = 0 in. as shown in Figures C-24 to C-27. One notable exception is that there was no discernable difference between configurations C18 and C19 for either pitch or yaw indicating that the addition of the 4/5 screen in conjunction with two diffuser exit screens and the long cell honeycomb had little effect. Also presented is a 40 second sample of a time trace comparison

of configurations C19 and C21 in Figure C-28 to show the profound effect the flow conditioning elements have on the time signal of the flow angle.

Figure C-29 shows the yaw angle fluctuation profiles with (configuration C10) and without (configuration C13) swirl vanes. The profile of configuration C10 is limited to approximately half of the test section width in this case. It appears that the swirl vanes do little to reduce the temporal fluctuation in flow angle. The peak in fluctuation level is simply shifted to another location in the test section.

Figure C-30 shows the yaw angle fluctuation profiles of the full-scale tunnel baseline configuration with (C05 and C21) and without (C10) corner 3 installed. While only a one-half profile was obtained with the corner removed, the data shows that the corner improves the temporal fluctuation level in the core region while levels near the wall are largely unaffected.

Figures C-31 and C-32 show the effect of the 2/3 screen installed in the cross-leg diffuser with and without corner 3 installed. The yaw angle fluctuations were reduced by the 2/3 screen only when corner 3 was installed. This parallels the total pressure data taken in the stilling chamber as reported in Section 3.5.2.

3.7 HOT-WIRE ANEMOMETER TURBULENCE MEASUREMENTS

Hot wire anemometer turbulence measurements were taken in the stilling chamber for configurations C18 to C24 and in the test section for configurations C17 to C24. Tests were performed in both the pitch and yaws planes. The hot wire measurements agree well with the flow angularity data because the fluctuation level is attenuated for each flow-conditioning element added. The fluctuation levels, however, are slightly higher than those measured by the flow angularity probe due to the much faster response of the hot wire probe.

Figure C-33 shows the summary of the lateral turbulence intensities for pitch and yaw plane measurements in the core region of the stilling chamber and test section for configurations C18 to C24. Likewise, Figure C-34 shows the axial turbulence intensities for the same configurations.

It is believed that the turbulence intensity measurements for the highly conditioned flows such as configuration C18 and C19 are overestimated due to mechanical vibration of the probe itself. Figure C-35 shows the cumulative turbulence intensity and power spectral density of the lateral turbulence in the yaw plane at the test section center for configurations C19 and C21. For configuration C19, the large peak in spectral density at approximately 26 Hz is the response at the first mode natural frequency of the probe. The peaks at 155 and 310 Hz are harmonic frequencies of probe system. This can also

be evidenced by the sudden increase in cumulative turbulence intensity at these frequencies. The turbulence measurements for the unconditioned flows such as configuration C21 do not show this phenomenon. The unconditioned flow exhibits a smooth decrease in intensity with increasing frequency. The power, however, is approximately two orders of magnitude higher across the entire spectrum. This indicates that the large peaks associated with mechanical vibrations seen in the highly conditioned flows are simply of the same order as the turbulence intensity of the unconditioned flow and do not contribute significantly to overall turbulence intensity. Therefore, lateral turbulence intensity levels for the unconditioned flow are believed to be accurate. Figure C-36 shows a two second sample of the lateral turbulence time traces for configurations C21 and C19 for comparison. The amplitude of the 26 Hz peaks of Figure C-37(b) readily shows the strong dependence of highly conditioned flow lateral turbulence measurements on the probe vibration. The acoustic pressure fluctuations should have very little impact on the lateral turbulence measurements. This can be inferred because acoustic plane waves should not affect lateral turbulence measurements, and the geometry of the scale model dictates that the acoustic frequencies must be greater than approximately 180 Hz to create any cross modes in the ducting. Also, the acoustic energy levels above 180 Hz are very low relative to the turbulence measurements.

Figure C-37 shows the cumulative and power spectral density of the axial turbulence at the test section center for configurations C19 and C21. There is discrete peak at

approximately 7 Hz associated with plane wave propagation upstream from the high-speed diffuser. The sharp peak at 25 Hz occurs due to the plane wave propagation of the fan noise upstream. The axial turbulence measurements will include plane wave acoustic pressure fluctuations caused by the scale facility. Further details on this subject are included in Section 3.10.1.

It should be noted that the spectral densities presented are the averages of 32 blocks of the time sample for clarity. This allowed better identification of spectral peaks. Without block averaging, peaks in the spectrum were difficult, if not impossible, to identify. Block averaging does, however, create a deficit in total energy, especially when there is a substantial proportion of low frequency energy, because blocking acts as a low pass filter at a frequency equal to the number of averaging blocks divided by the total sample time. Therefore, the overall turbulence intensities reported are the actual intensities, given by the root-mean-square of the data time sample. Cumulative intensity plots, when averaging is performed, are for the purpose of showing trends only.

3.8 TEST SECTION "HIGH-RESPONSE" PROBE MEASUREMENTS

Test section high response probe total and static pressure measurements were taken for configurations C14 to C24. The total pressure was taken at the test section center to measure temporal fluctuations for configurations C18 to C23, and profiles were taken for configurations C14

to C17 and C24. The static pressure was taken in the center of the test section floor.

The total pressure fluctuation levels with corner 3 and the swirl vanes removed are shown in Figure C-38. These data agree with the stilling chamber total pressure fluctuations, decreasing with each flow-conditioning element added. Similar results appear with corner 3 and the swirl vanes installed as shown in Figure C-39. Again, there is little attenuation associated with the addition of the 4/5 screen (configuration C18) with respect to the two diffuser exit screens and long-cell honeycomb of configuration C19.

The test section center total pressure and wall static pressure data was obtained simultaneously, allowing an approximation of the axial turbulence intensity to be made. The axial velocity fluctuation can be found by equation 21.

$$\frac{u'}{U_{ave}} = \frac{1}{\gamma M^2}\left[\frac{\delta Pt}{Pt_{ave}} - \frac{\delta Ps}{Ps_{ave}}\right] \qquad (21)$$

where:

u'	Axial velocity fluctuation ($U - U_{ave}$)
U_{ave}	Average axial velocity
γ	Fluid specific heat ratio
M	Mach number
Pt	Total pressure of sample
Pt_{ave}	Average total pressure
Ps	Static pressure of sample
Ps_{ave}	Average static pressure

Equation 21 was derived by taking the log of the isentropic compressible pressure relationship, and then differentiating and solving for u'/U. The derivation an be found in Appendix D.

The time traces of this data for configurations C21 and C19 are shown in Figure C-40. The overall axial turbulence intensity was found by taking the root-mean-square of the new velocity fluctuation time trace. The relative intensity levels found agree well with the hot wire anemometer data.

During testing, a flow visualization tuft was introduced in the contraction and it appeared that the viscous layers on the top and bottom walls (vertical layers) were much thicker and unstable than those on the sidewalls (horizontal layers). This led to the modification of the high response total pressure probe to enable it to measure closer to the wall. Figure C-41 shows the vertical profiles of total pressure and fluctuation for configuration C24. The figure shows that the near wall viscous layer is approximately 10% of the test section height, and that the fluctuation levels are an order of magnitude larger near the wall than in the core region. Figure C-42 shows the horizontal profiles of the same configuration. Here, the near wall viscous layer was less than 5% of the test section width, and the fluctuation levels near the wall were approximately 2 times the levels in the core region. It is believed that this indicated a flow separation in the large angle contraction in the

vertical plane. This may not be indicative of the full-scale tunnel, however, because the separation phenomenon is influenced by the Reynolds number and the model Reynolds number is approximately one-tenth that of the full-scale tunnel.

3.9 TEST SECTION TOTAL PRESSURE PROFILES

Test section horizontal total pressure profiles were taken for configurations C04 to C11 and C13 to C24. Vertical profiles were taken for configurations C13 to C24. This data shows the effect of the swirl vanes, screens installed in the cross-leg diffuser, and honeycombs installed in the stilling chamber on the total pressure spatial profile and temporal total pressure fluctuations.

The general trend in the spatial distributions and temporal fluctuations of the test section data parallels that of the stilling chamber. Of interest here is the effect flow-conditioning elements have on the thickness of the near wall viscous layers.

3.9.1 EFFECT OF SWIRL VANES

Comparison tests were performed on the swirl vanes with corner 3 installed (configurations C04 and C05) and with corner 3 removed (configurations C10 and C13). The spatial and temporal RMS total pressure profiles are shown in Figures C-43 and C-44. With corner 3 installed and no swirl vanes, the thickness of the viscous layer was indeterminable and appears to extend to the center of the

test section, while with the swirl vanes the inviscid core extended to a value of y/width/2 = 0.6 as shown in Figure C-43. With corner 3 removed, the swirls vanes increased the invisid core from y/width/2 = 0.4 to 0.6 as shown in Figure C-44.

3.9.2 EFFECT OF INTERMEDIATE CROSS-LEG DIFFUSER SCREENS

The effect of the intermediate cross-leg diffuser screens was tested as summarized in Section 3.5.2. The intermediate screens increased the invisid core from y/width/2 = 0.6 to approximately 0.8 for all tests regardless of corner 3 installation. For both cases, however, there was a slightly more profound effect near the inboard wall. Profiles with corner 3 installed are shown in Figure C-45, and with corner 3 removed in Figure C-46.

3.9.3 EFFECT OF CROSS-LEG DIFFUSER EXIT SCREENS

The cross-leg diffuser exit screen comparison testing was performed with the swirl vanes and corner 3 removed. One exit screen was added to a baseline configuration, and then an identical screen was added creating back-to-back screens at the diffuser exit.

The baseline profile with corner 3 and the swirl vanes removed was asymmetric with the invisid core offset toward the outboard wall. The addition of diffuser exit screens had little effect near the outboard wall. However, the screens increased the invisid core near the inboard wall

from y/width/2 = 0.4 to 0.8. Total pressure profiles for these test are shown in Figure C-47.

3.9.4 EFFECT OF CORNER 4 SCREEN

The full-scale tunnel has a screen attached to the leading of the corner 4 turning vanes. The screen was removed for one test to check the impact, if any, on tunnel flow quality.

Figure C-48 shows the total pressure and RMS profiles with and without the corner 4 screen. As shown, the corner 4 screen has little impact on the profile of conditioned flow.

3.9.5 EFFECT OF STILLING CHAMBER HONEYCOMBS

A long cell honeycomb (configuration C22) was compared directly to the full-scale tunnel baseline configuration (C21). A short cell honeycomb was installed with two diffuser exit screens installed (configuration C23) and compared to a similar configuration with the long cell honeycomb installed (configuration C19).

The addition of the long cell honeycomb to the baseline configuration nearly eliminated the viscous layer over the measured region with slight evidence of transition at y/width/2 = 0.8 near the outboard wall as shown in Figure C-49. With the long cell honeycomb and two diffuser exit screens installed, the transition moved further out to y/width/2 = 0.9 as shown in Figure C-50. The profiles of

Figure C-50 also showed that there was little effect if a short cell honeycomb is used in lieu of the long cell honeycomb. However, the temporal fluctuation levels did increase by a factor of 1.28 when the short cell honeycomb was installed.

3.10 ACOUSTIC MEASUREMENTS

Acoustic measurements were made for setup A, and for configurations C04 to C07, and C19 of setup B. Measurements were made at the test section inboard wall (location A), floor (location B), outboard wall (location C), high-speed diffuser wall (location D), corner 3 outboard wall 8" downstream of the turning vanes (location E), cross-leg diffuser exit outboard wall (location F), and cross-leg diffuser inboard wall (location G) as shown in Figure C-51. Acoustic data were taken at two locations simultaneously to identify the direction of acoustic pressure fluctuation sources.

Acoustic data was taken for setup A to identify fluctuating pressure sources unique to the scale model apparatus. In general, pressure fluctuations generated above 1 Hz was propagated upstream from the high-speed diffuser and fan. Below 1 Hz fluctuations propagated downstream from the stilling chamber. Figure C-52 shows the cross-spectral magnitude and phase for microphone locations A and B. The magnitude peak in the 3 to 8 Hz range with a negative phase indicated sound pressure generated at the high-speed diffuser exit which propagated upstream. The fan noise can be identified in a like manner

denoted by the sharp magnitude peak at 20 Hz (1200 rpm). Conversely, below 1 Hz, the magnitude increased with a positive phase indicating pressure fluctuations generated in the stilling chamber and propagating downstream.

Figure C-53 shows the cross-spectral magnitude and phase for microphone locations A and B for configuration C19 of setup B. The magnitude and phase results were consistent with those for setup A. Note that the fan was run at a higher speed to match the test section dynamic pressure for setup B because of the extra total pressure associated with the added inlet ducting, the cross-leg diffuser, and the flow conditioners. This shifted the peak in magnitude associated with fan speed up to approximately 25 Hz (1500 rpm). Also, the very low frequency magnitudes were greatly reduced. It can be seen that very low frequency pressure fluctuations were generated in the cross-leg diffuser and propagated downstream as shown in Figure C-54 for microphone locations A and E, because the cross-phase below 1 Hz was positive. It should be noted that the coherence between signals was near 1.0 for the spectral data presented indicating a strong linear relationship between signals.

Once the fluctuating pressure sources were identified, the effect of flow conditioning on the fluctuating pressure levels was reviewed. Figure C-55 shows the sound pressure level (SPL) spectra and the cumulative SPL at the test section floor with (configuration C05) and without (configuration C04) swirl vanes. The swirl vanes actually increased the pressure fluctuation level at the test

section floor approximately 10% over the entire frequency band. Figure C-56 shows the SPL spectra and the cumulative SPL at the test section floor for the baseline configuration (C05), and with two diffuser exit screens and a long cell honeycomb installed (configuration C19). The screens and honeycomb reduced the pressure fluctuations below 3 Hz between 20% and 40%, and increased the fluctuations 10% to 15% above 7 Hz. Figure C-57 shows the SPL spectra and the cumulative SPL at the cross-leg diffuser inlet for the baseline configuration (C05), with the swirl vanes removed (configuration C04), with crossleg diffuser screens installed at segments 2/3 and 4/5 (configuration C07), and with two diffuser exit screens and a long cell honeycomb installed (configuration C19). The pressure fluctuations with the swirl vanes installed (C05) are substantially reduced over the entire frequency range contrary to the data from the test section. This indicated that the swirl vanes did aid in preventing flow separations in the cross-leg diffuser. However, this did not translate into reduced fluctuations on the test section walls. The addition of the intermediate crossleg diffuser screens (C07) further reduced the fluctuations across the frequency range. Comparing to the baseline (C05), the addition of the exit screens and honeycomb (C19) had little impact below 4 Hz and increased the fluctuating pressure levels above 4 Hz. The attenuation of the acoustic levels by the flow conditioning element was much less that determined by the axial turbulence measurements.

3.10.1 EFFECT OF ACOUSTIC NOISE ON AXIAL TURBULENCE

The potential exists for the axial turbulence measurements acquired with the hot wire anemometer system to be effected by acoustic noise unique to the scale model, resulting in inaccurate representation of the turbulence attenuation of flow conditioning elements. A quick check of the largest characteristic cross-sectional dimension of the scale model revealed that the sound pressure waves must exist only as plane waves below approximately 180 Hz. Therefore, an acoustic velocity perturbation may be calculated by equation 22, Ref 7.

$$u' = \frac{p'}{\rho a} \tag{22}$$

Hence, the axial turbulence, u'/U, can be found from the acoustic microphone data which is given in p'. Figure C-58 shows the power spectral density of the axial turbulence for the baseline configuration and configuration C19 for both the hot-wire anemometer and acoustic data. In the baseline configuration, the hot-wire data clearly picked up the acoustic plane waves associated with the high-speed diffuser in the 3 to 8 Hz range, thus somewhat increasing the level of turbulence as measured by the hot-wire. For highly conditioned flows as in configuration C19, the hot-wire data converged toward the acoustic plane wave curve. Here, the high-speed diffuser acoustic propagation appeared, as did a sharp peak at the fan speed (25 Hz). These peaks increased the overall value of the turbulence for the highly conditioned flows significantly.

The acoustic curves for both configurations were very similar in magnitude and shape, indicating that the flow conditioners had little effect on the acoustic pressure fluctuations. The reversal in trends in the very low frequencies ($f < 1$ Hz) supported the conclusion of Section 3.4 that the separation energy was propagated primarily by convection of the flow and not plane waves.

The 25 Hz peak in the axial turbulence measurements is not to be confused with the 26 Hz peak in the lateral turbulence measurements discussed earlier. It was concluded that the effect of the probe vibration, if any, was negligible with regard to axial turbulence measurements. It is by pure coincidence that these peak frequencies are similar.

Figure C-59 shows the cumulative turbulence intensity for the same configurations mentioned above. Notice the jumps in the turbulence intensity at 7 and 25 Hz. The acoustic plane waves were filtered from the data by taking the difference of the hot-wire and acoustic curves as shown in Figure C-60. This is a very useful tool to quantify the attenuation of the flow conditioning elements, especially if hot-wire and acoustic data were taken simultaneously. Because the hot-wire anemometer and acoustic data were not taken simultaneously, there is obviously some error associated with the curves of Figure C-60 because of non-repeatability. For the data presented here, the un-filtered hot-wire data returns an attenuation ratio of 0.55, while the "filtered difference" method returns an attenuation ratio of 0.38.

3.11 CROSS-LEG DIFFUSER WALL STATIC PRESSURE DISTRIBUTION

A static pressure scan of the cross-leg diffuser was performed for all test configurations to measure to pressure recovery coefficient, Cp, and efficiency of the diffuser. The addition of flow conditioning devices had little effect on the efficiency of the static pressure recovery of the diffuser. When the intermediate cross-leg diffuser screens were added, there was a noticeable drop in calculated efficiency as expected due to the total pressure loss incurred across the screen. This, however, is not indicative of the diffuser performance.

Most notable was the effect the flow conditioners had on the temporal fluctuations in the diffuser wall static pressure. Figure C-61 shows the pressure coefficient and temporal fluctuation distribution along the diffuser with the 4/5 screen installed and corner 3 removed (configuration C17). The reduction in temporal fluctuation levels is very apparent downstream of the screen. Figure C-62 shows the distributions with the 4/5 screen, corner 3, and the swirl vanes installed (configuration C18). The corner and swirl vanes substantially reduced the temporal fluctuations in the diffuser.

The temporal fluctuations in static pressure were also reduced by the addition of the diffuser exit screens. Figure C-63 shows the pressure coefficient and temporal fluctuation distribution along the diffuser with the exit screens installed (configuration C19). Figure C-64 shows

the distributions without any diffuser treatments (configuration C21).

The loss coefficient, K_{c3}, of corner 3 was also calculated for tests where the corner 3 inlet total pressure was recorded in conjunction with the cross-leg diffuser scan and agreed well with the coefficient found in Section 3.3. The calculated loss coefficients for configurations C04 and C07 were 0.48 and 0.41 respectively, compared to 0.49 and 0.53 as outlined in Section 3.3.1.

3.12 SUMMARY AND TEST COMPARISONS

Table A-10 shows a summary of the pertinent parameters of the core region for different tests of configurations C04 through C24. Table A-11 normalizes the data of Table A-10 by the baseline configuration, C21. This a quick reference to gauge the effectiveness of each configuration change.

Figure C-65 shows the effect of flow conditioners on the test section RMS temporal fluctuations of total and static pressure for the pitot-static probe and the high response pitot and static probes. The overall levels measured by the high response probe were higher than those of the pitot-static probe due to its enhanced frequency response. As shown in the figure, the trend of the two test types was similar.

Figure C-66 compares the temporal fluctuation in flow angle as measured by the flow angularity probe and the hot

wire anemometer for both pitch and yaw. Again, the overall levels were higher for the hot wire anemometer as its frequency response was much higher than that of the flow angularity probe. Note that there was no flow angularity probe data taken for configuration C23 and no hot-wire data taken in the pitch plane for configuration C18.

Figure C-67 shows the total pressure fluctuations in the stilling chamber measured by a total pressure rake and in the test section measured by the pitot-static probe. Again, the general trend was a decrease in spatial distribution and temporal fluctuation with the addition of each flow conditioning element. Note that stilling chamber total pressure rake data was not taken for configurations C18 and C20.

The ratio of test section to stilling chamber parameters is of interest as it can give some insight into the departure of the contraction from ideal. If one assumes an ideal contraction with constant total pressure streamlines, the ratio of the total pressure fluctuations should be 1.0 and the ratio of axial turbulence (u'/U) should be equal to 1/CR (Ref 12), where CR is the contraction ratio. Figures C-68 and C-69 show the test section to stilling chamber ratio of total pressure fluctuations and axial turbulence respectively. The total pressure fluctuation ratios remain near 1.0 as expected, the axial turbulence ratios; however, tended to increase as more flow conditioning elements were added. This indicates that the departure of the contraction from ideal becomes

apparent as the flow quality in the stilling chamber increases.

The test section to stilling chamber ratio of lateral turbulence should be equal to $1/(CR)^{1/2}$ (Ref 12) for an ideal contraction. Figure C-70 shows the test section to stilling chamber ratio of the lateral turbulence. Here, the ratios remained relatively constant as expected. This indicated that the departure of the contraction from ideal had a more profound effect on axial fluctuation than lateral fluctuations.

3.13 IMPACT ON COMPRESSOR POWER

The additional power required by the full-scale tunnel compressor drive system was identified as an additional criterion for flow conditioning recommendations. The impact of the addition of flow conditioning elements to the full-scale tunnel compressor power was assessed by equation 23.

$$\frac{\delta \dot{E}}{\dot{E}} = \frac{\gamma - 1}{\gamma} \frac{\lambda_c^{o\,\frac{\gamma-1}{\gamma}}}{\lambda_c^{o\,\frac{\gamma-1}{\gamma}} - 1} \frac{\lambda_T \; q_{sc}}{\lambda_c^o \; p_{t0}} K_{tk} \left(\frac{A_{sc}}{A_k} \right)^2 \tag{23}$$

where:

$\delta \dot{E}$ Change in compressor power by the addition of a loss element

$\dot{E}$ Compressor power required in baseline configuration

γ Fluid specific heat ratio

λ_c^o Compressor pressure ratio in baseline configuration

λ_T Total pressure ratio of test-leg

q_{sc} Dynamic pressure in stilling chamber

p_{t0} Total pressure in stilling chamber

K_{tk} Loss coefficient of added flow conditioning element

A_{sc} Stilling chamber cross-sectional area

A_k Cross-sectional flow area of added flow conditioning element

Equation 23 was derived similarly to equation 21. The logarithm was taken of the isentropic compressor power equation, and then it was differentiated to find the effect of the additional loss element in terms of compressor power required. The derivation of equation 23 can be found in Appendix D.

The impact of the flow conditioning elements on compressor power is shown in Table A-12.

IV CONCLUSIONS AND RECOMMENDATIONS

Experiments on controlling or damping the flow angularity fluctuations in the test section by installing various combinations of screens and honeycomb resulted in several configurations that reduced the test section fluctuation by an order of magnitude. The data from these experiments were used as the basis for selecting a screen-honeycomb combination to be installed in the full-scale tunnel. Details of the selection process are not discussed here except to note that configuration C19, consisting of two diffuser exit screens in combination with a long cell honeycomb in the stilling chamber, was selected. Configuration C19 also included the existing screen across corner 4 and swirl vanes. It was concluded that these devices provide a net benefit and should not be removed. This configuration reduced test section flow angularity fluctuations to a very low level in the test section of the model; however, it did not eliminate transitory stall in the crossleg diffuser. Intermediate screens installed in the diffuser and, most likely, screens of some other treatment at the inlet of the diffuser would be required to completely eliminate unsteadiness in the diffuser. These treatments would involve both installation cost and an increase in operation cost because of the associated increase in power requirements due to their location in high-speed flow. The experimental data, however, do show that intermediate screens in the diffuser are very effective at reducing flow unsteadiness downstream of the screen location.

Specific observations and conclusions concerning flow in the experimental facility are enumerated below.

1. Tufts attached to the diffuser, contraction, and test section walls, and seeding the flow with lightweight foam particles proved to be very effective flow diagnostic tools. Both techniques provided clear evidence of transitory stall in the diffuser.

2. Unsteady flow was also found in the corner 3 turning vane passages. Flow separation appeared to originate at the vane leading edge and extend along the pressure surface in the flow direction and did not appear to reattach.

3. Experiments with and without corner 3 installed showed that transitory stall occurred in the diffuser with or without the corner, thus, verifying that the corner and its turning vanes do not cause the transitory stall in the diffuser.

4. With corner 3 installed, horizontal total pressure profiles at the diffuser exit (corner 4 inlet) and in the stilling chamber showed an extensive flow separation region on the inboard side of the turn. This region was much greater at the diffuser exit indicating that the corner 4 screen provides a significant degree of flow smoothing.

5. Flow angularity measurements using the flow angularity probe and the hot wire anemometer both showed that the combination of two diffuser exit screens and a honeycomb in the stilling chamber resulted in more than an order of magnitude reduction in flow angularity fluctuation level in the model test section, while the levels with the long cell honeycomb installed were 10 to 20 percent less than with the short cell honeycomb installed.

6. Axial turbulence measurements indicated that the differences among various combinations were not large. The flow conditioners were not highly effective in damping axial velocity fluctuation. This same result was seen in total pressure and static pressure measurements.

7. Total pressure surveys in the test section revealed very thick viscous layers near the walls. Total pressure temporal fluctuations were very pronounced in the thick viscous layer compared to the level seen near the center of the test section; however, static pressure fluctuations in the layer were about the same as at the centerline. The foregoing observations may be of special significance to the full-scale tunnel. If the boundary of the viscous layer is alternately moving toward the wall and away from the wall it will induce time varying flow angularity in the inviscid core. In a low Mach number subsonic flow, this effect might be expected

to damp out exponentially with distance measured from the wall. In contrast, in a supersonic flow the disturbance will propagate from the "edge" of the viscous layer along Mach lines into the inviscid core with virtually no damping.

REFERENCES

1. Murthy, S. V., Kmak, F. J., Boone, A. R., and Muzzio, D. E., "Test Data Summary Report on the Simulation Tests in BLASTANE for Design and Validation of Flow Conditioning Systems for Annular and Wide Angle Diffusers in NASA Ames 11 FT TWT," NASA Ames Research Center, Moffett Field, CA., March 1995.

2. Canacci, Victor A., Spera, David A., and Gonsalez, Jose C., "Flow Quality Studies of the Scale Model Icing Research Tunnel and Projections to the Full-Scale Modified IRT," AIAA Paper No. 99-0307, January 1999.

3. Canacci, V. A., Gonsalez, J. C., Spera, J. C., and Weaver, H. L., "Scale Model Icing Research Tunnel Validation Studies," AIAA-98-0706, 1998.

4. Ditshuizen, J. C. A. van, "Design and Calibration of the 1/10th-Scale Model of the NLR Low Speed Wind Tunnel LST 8 x 6," NLR MP 75031 U, 1975.

5. Chitamani, Seetharam H., "Design Features and Flow Qualities of the Boeing Research Aerodynamic Icing Tunnel," AIAA-94-0540, January 1994.

6. Idelchik, I. E., "Handbook of Hydraulic Resistance," 3rd edition, CRC Press, 1994.

7. Beranek, L. L., and Ver, I. L., "Noise and Vibration Control Engineering," John Wiley and Sons, Inc., 1992.

8. Ozimek, L. G., Azad, R. S., and Derksen, R. W., "An Experimental Investigation of Turbulence Parameters in an Eight Degree Conical Diffuser," Symposium on Thermal Anemometry, January 1987.

9. Taylor, G. I, and Batchelor, G. K., "The Effect of Wire Gauze on Small disturbances in a Uniform Stream", Quarterly Journal of Mechanics and Applied Mathematics, Vol. 2, No. 1, 1947, p.1.

10. Loehrke, R. I., and Nagib, H. M., "Experiments on Management of Free-Stream Turbulence," AGARD Report No. 598., 1984.

11. Dolan, Francis X. and Runstadler Peter W, Jr., "Pressure Recovery Performance of Conical Diffusers at High Subsonic Mach Numbers," NASA CR-2299, August 1973.

12. Uberoi, M.S., "Effect of Wind-Tunnel Contraction on Free-Stream Turbulence," Journal of the Aeronautical Sciences, August 1956.

13. Young , H.D., "Statistical Treatment of Experimental Data," McGraw-Hill Book Company, Inc., 1962.

APPENDICES

APPENDIX A

TABLES

Table A-1. Approximate Deviation in Test Section Flow Angle of Full Scale Tunnel With and Without Swirl Vanes.

	Pitch Angle Deviation, deg		Yaw Angle Deviation, deg	
Test Section Mach Number	Pre Swirl Vanes	Post Swirl Vanes	Pre Swirl Vanes	Post Swirl Vanes
1.6	0.150	0.170	0.175	0.170
1.8	0.125	0.115	0.161	0.158
2.0	0.140	0.090	0.160	0.117

Table A-2. Materials of Construction

Component	**Material**
Inlet Pipe	Poly Vinyl Chloride (PVC)
Corner 3 Ducting	Polycarbonate (Lexan)
Corner 3 Turning Vanes	Extruded Aluminum
Cross-Leg Diffuser Ducting	Polycarbonate (Lexan)
Corner 4 Ducting	Polycarbonate (Lexan)
Corner 4 Turning Vanes	Extruded Aluminum
Contraction	Fiberglass
Test Section	Acrylic (Plexiglass)
High Speed Diffuser	Birch plywood
Corner 1 Duct	Birch plywood (w/ acoustic treatment)
Screens	Stainless Steel
Honeycomb	Aluminum

Table A-3. Flow Conditioner Parameters and Diffuser Dimensions

Screens

Screen	Mesh	Wire Diameter	Percent Open
Air Inlet	18 x 18	.0130"	58.7%
2/3	18 x 18	.0145"	54.6%
4/5 (Pre C14)	20 x 20	.0145"	50.4%
4/5 (Post C14)	16 x 16	.0165"	54.2%
7/C4	16 x 16	.0165"	54.2%
C4	28 x 28	.0105"	49.8%

Honeycombs

Honeycomb	Cell Hydraulic Diameter	Cell Depth	Cell L/D_h	Foil Thickness	Percent Open
Long Cell	.1146"	6"	52.36	.003"	89.9%
Short Cell	.1146"	2"	17.45	.003"	89.9%

Cross-leg Diffuser at Flanges

Flange Upstr/Downstr	Length from Inlet	Diameter at Flange	A_{flange}/A_{inlet}
1/2	18.95"	20.8"	1.33
2/3	34.95"	23.1"	1.65
3/4	48.95"	25.2"	1.96
4/5	73.45"	28.8"	2.56
5/6	93.95"	31.8"	3.12
6/7	111.95"	34.4"	3.65
7/C4	128.45"	36.8"	4.18

Table A-4. Configuration Codes

Conf. No.	Inlet Screen	Inlet Pipes	Corner 3	Swirl Vanes	Screen 2/3	Screen 4/5	Screen 7/C4	Bauer Trips	Long Honey-comb	Short Honey-comb	C4 Screen
C01	0	1	1	0	0	0	0	0	0	0	1
C02	1	1	1	0	0	0	0	0	0	0	1
C03	0	2	1	0	0	0	0	0	0	0	1
C04	1	2	1	0	0	0	0	0	0	0	1
C05	1	2	1	1	0	0	0	0	0	0	1
C06	1	2	1	1	0	1	0	0	0	0	1
C07	1	2	1	1	1	1	0	0	0	0	1
C08	1	2	0	1	1	1	0	0	0	0	1
C09	1	2	0	1	0	1	0	0	0	0	1
C10	1	2	0	1	0	0	0	0	0	0	1
C11	1	2	0	1	0	0	0	1	0	0	1
C12	1	2	0	0	0	0	0	1	0	0	1
C13	1	2	0	0	0	0	0	0	0	0	1
C14	1	2	0	0	0	0	1	0	0	0	1
C15	1	2	0	0	0	0	2	0	0	0	1
C16	1	2	0	0	0	1	2	0	0	0	1
C17	1	2	0	0	0	1	2	0	1	0	1
C18	1	2	1	1	0	1	2	0	1	0	1
C19	1	2	1	1	0	0	2	0	1	0	1
C20	1	2	1	1	0	0	2	0	0	0	1
C21	1	2	1	1	0	0	0	0	0	0	1
C22	1	2	1	1	0	0	0	0	1	0	1
C23	1	2	1	1	0	0	2	0	0	1	1
C24	1	2	1	1	0	0	2	0	1	0	0

Table A-5. Nominal Scale Model Test Conditions*.

Location	A / A_{ts}	Mach #	Dynamic Pressure, in w.g	Axial Velocity, ft/sec	Reynolds Number
Test Section	1.00	0.210	12.1	240	$1.6x10^7$
Stilling Chamber	6.13	0.034	0.32	39	$7.7x10^6$
Cross-Leg Diffuser, Segment 4/5	3.58	0.058	0.94	67	$1.0x10^7$
Cross-Leg Diffuser, Segment 2/3	2.31	0.091	2.27	104	$1.25x10^7$
Diffuser Inlet	1.40	0.150	6.14	171	$1.58x10^7$

* Nominal conditions based on 14.2 psia atmospheric pressure in and U.S. Standard Temperature of 59 °F.

Table A-6. Cross-Leg Diffuser Pressure Tap Locations

Static Tap	Inches from diffuser inlet, x	Normalized by diffuser inlet diameter, x/D
1	4.76	0.2644
2	9.31	0.5172
3	14.17	0.7873
4	26.76	1.4868
5	41.78	2.3214
6	56.93	3.1628
7	65.16	3.6199
8	83.61	4.6499
9	102.74	5.7080
10	120.01	6.6672

Table A-7. Stilling Chamber Rake Probe Spacing

Stilling Chamber Rake Port Number	Inches from Center of Rake, y Outboard Positive	Normalized by Stilling Chamber Radius, y/R
Port 1	18.000	0.975
Port 2	17.375	0.941
Port 3	16.750	0.907
Port 4	16.125	0.873
Port 5	15.375	0.832
Port 6	14.500	0.785
Port 7	13.500	0.731
Port 8	12.500	0.677
Port 9	11.250	0.609
Port 10	9.750	0.528
Port 11	8.000	0.433
Port 12	6.000	0.325
Port 13	4.000	0.217
Port 14	2.000	0.108
Port 15	0.000	0.000
Port 16	-2.000	-0.108
Port 17	-4.000	-0.217
Port 18	-6.000	-0.325
Port 19	-8.000	-0.433
Port 20	-9.750	-0.528
Port 21	-11.250	-0.609
Port 22	-12.500	-0.677
Port 23	-13.500	-0.731
Port 24	-14.500	-0.785
Port 25	-15.375	-0.832
Port 26	-16.125	-0.873
Port 27	-16.750	-0.907
Port 28	-17.375	-0.941
Port 29	-18.000	-0.975

Table A-8. Corner 3 Inlet Rake Probe Spacing

Rake Port Number	Inches from Pipe Wall, y	Normalized by Pipe Radius, y/R
Port 1	0.188	0.979
Port 2	0.438	0.951
Port 3	0.750	0.917
Port 4	1.250	0.861
Port 5	1.875	0.792
Port 6	2.500	0.722
Port 7	3.250	0.639
Port 8	4.250	0.528
Port 9	5.563	0.382
Port 10	6.875	0.236
Port 11	8.250	0.083

Table A-9. Sample of Test Log and Explanation of Data Type Code

Config.	Test Filename	Data Type	Fan Set Point, rpm	Fan Spd Act., rpm	Patm, kPa	q_ts, in w.c	Tatm, C	y, in	z, in
C19	B187_11	4	1510	1484	98.341	12.1	12.3	-6.37	0.00
C19	B187_12	4	1510	1484	98.340	12.1	12.3	-6.87	0.00
C19	B187_13	4	1510	1484	98.338	12.1	12.3	-7.37	0.00
C19	B187_14	4	1510	1484	98.333	12.1	12.8	-1.38	0.00
C19	B188_01	4	1510	1484	98.325	12.1	13.6	1.38	0.00
C19	B188_02	4	1510	1484	98.329	12.1	13.7	1.87	0.00
C19	B188_03	4	1510	1485	98.329	12.1	13.8	2.37	0.00
C19	B188_04	4	1510	1484	98.335	12.1	14.0	2.87	0.00
C19	B188_05	4	1510	1485	98.338	12.1	14.2	3.37	0.00
C19	B188_06	4	1510	1483	98.341	12.1	14.1	3.87	0.00
C19	B188_07	4	1510	1485	98.337	12.1	14.2	4.37	0.00

Data Type	Explanation
0	(None)
1	Test Conditions
2	Stilling Chamber
3	Crossleg+C3 Inlet
4	Test Section Pt Horizontal
5	Test Section Pt Vertical
6	Hi-Response Pt and Pstatic
7	Alpha-Probe Vertical (Yaw Ports)
8	Alpha-Probe Horizontal (Yaw Ports)
9	Alpha-Probe (Pitch Ports)
10	C3 Exit Survey
11	C4 Inlet Profile
12	Flow angularity probe response test
13	Turbulence (Test section, Pitch)
14	Turbulence (Test section, Yaw)
15	Turbulence (Stilling chamber, Pitch)
16	Turbulence (Stilling chamber, Yaw)

Table A-10. Summary of Test Parameter Values

Configuration	α probe (RMS, deg)			TS turbulence (RMS, deg)		SC turbulence (RMS, deg)		High response probe	
	Pitch	Yaw (y=0)	Yaw (y=-6)	Pitch	Yaw	Pitch	Yaw	RMS(dPt/Pt)%	RMS(dPs/Pt)%
C01	-	-	-	-	-	-	-	-	-
C02	-	-	-	-	-	-	-	-	-
C03	-	-	-	-	-	-	-	-	-
C04	-	-	0.6116	-	-	-	-	-	-
C05	-	-	0.4509	-	-	-	-	-	-
C06	-	-	0.1549	-	-	-	-	-	-
C07	-	-	0.0633	-	-	-	-	-	-
C08	-	-	0.1243	-	-	-	-	-	-
C09	-	-	0.1235	-	-	-	-	-	-
C10	-	-	1.0857	-	-	-	-	-	-
C11	-	-	1.1151	-	-	-	-	-	-
C12	-	-	0.6708	-	-	-	-	-	-
C13	-	-	0.8145	-	-	-	-	-	-
C14	-	-	0.3456	-	-	-	-	0.0261	0.0346
C15	-	-	0.1759	-	-	-	-	0.0198	0.0281
C16	-	-	0.0980	-	-	-	-	0.0178	0.0242
C17	-	-	0.0371	0.1398	0.1215	-	-	0.0169	0.0229
C18	0.0343	0.0353	-	0.0968	0.1117	0.4086	0.3682	0.0156	0.0211
C19	0.0302	0.0460	0.0495	0.1383	0.1351	0.4668	0.3906	0.0158	0.0219
C20	0.2706	0.2603	0.2493	0.5944	0.4913	2.1748	1.7030	0.0224	0.0281
C21	0.4701	0.6891	0.6839	1.2466	1.1508	3.9675	2.9513	0.0344	0.0429
C22	0.0945	0.2128	0.1738	0.3133	0.3085	0.8803	0.6950	0.0193	0.0244
C23	-	0.0595	-	0.1567	0.1652	0.4481	0.3888	0.0185	0.0227
C24	0.0499	0.0930	0.0693	0.1917	0.1944	0.6383	0.4956	0.0169	0.0230

Table A-10. Concluded

Configuration	Horiz SC Rake, RMS(dPt/Pt)%		Horiz TS PS Probe, RMS(dPt/Pt)%		Horiz TS PS Probe, RMS(dPs/Pt)%	
	Temporal	Spatial	Temporal	Spatial	Temporal	Spatial
C01	-	-	-	-	-	-
C02	0.0107	0.0469	-	-	-	-
C03	0.0178	0.0442	-	-	-	-
C04	0.0144	0.0522	0.0236	0.0364	0.0242	0.0422
C05	0.0124	0.0234	0.0193	0.0186	0.0299	0.0226
C06	0.0099	0.0101	0.0139	0.0116	0.0199	0.0174
C07	0.0094	0.0092	0.0122	0.0137	0.0216	0.0234
C08	0.0067	0.0065	0.0104	0.0138	0.0188	0.0139
C09	0.0115	0.0118	0.0158	0.0161	0.0278	0.0187
C10	0.0188	0.0146	0.0265	0.0234	0.0356	0.0219
C11	0.0219	0.0126	0.0294	0.0181	0.0380	0.0208
C12	0.0181	0.0379	-	-	-	-
C13	0.0255	0.0220	0.0391	0.0496	0.0404	0.0203
C14	0.0153	0.0172	0.0225	0.0204	0.0394	0.0195
C15	0.0131	0.0132	0.0185	0.0183	0.0272	0.0235
C16	0.0091	0.0079	0.0182	0.0207	0.0235	0.0135
C17	0.0093	0.0066	0.0149	0.0089	0.0200	0.0116
C18	-	-	0.0104	0.0106	0.0168	0.0109
C19	0.0147	0.0052	0.0124	0.0098	0.0174	0.0127
C20	-	-	0.0146	0.0096	0.0250	0.0219
C21	0.0206	0.0193	0.0318	0.0107	0.0429	0.0230
C22	0.0147	0.0079	0.0158	0.0106	0.0230	0.0173
C23	0.0141	0.0067	0.0158	0.0118	0.0251	0.0208

Table A-11. Summary of Core Region Data Normalized by Configuration C21

Configuration	α probe			TS turbulence		SC turbulence		High response probe	
	Pitch	Yaw (y=0)	Yaw (y=-6)	Pitch	Yaw	Pitch	Yaw	Pt	Ps
C04	-	-	0.894	-	-	-	-	-	-
C05	-	-	0.659	-	-	-	-	-	-
C06	-	-	0.226	-	-	-	-	-	-
C07	-	-	0.093	-	-	-	-	-	-
C08	-	-	0.182	-	-	-	-	-	-
C09	-	-	0.181	-	-	-	-	-	-
C10	-	-	1.588	-	-	-	-	-	-
C11	-	-	1.631	-	-	-	-	-	-
C12	-	-	0.981	-	-	-	-	-	-
C13	-	-	1.191	-	-	-	-	-	-
C14	-	-	0.505	-	-	-	-	0.759	0.806
C15	-	-	0.257	-	-	-	-	0.574	0.654
C16	-	-	0.143	-	-	-	-	0.516	0.564
C17	-	-	0.054	0.112	0.106	-	-	0.492	0.534
C18	0.073	0.051	-	0.078	0.097	0.103	0.125	0.453	0.491
C19	0.064	0.067	0.072	0.111	0.117	0.118	0.132	0.459	0.511
C20	0.576	0.378	0.365	0.477	0.427	0.548	0.577	0.650	0.654
C21	1.000	1.000	1.000	1.000	1.000	1.000	1.000	1.000	1.000
C22	0.201	0.309	0.254	0.251	0.268	0.222	0.235	0.561	0.567
C23	-	0.086	-	0.126	0.144	0.113	0.132	0.536	0.528
C24	0.106	0.135	0.101	0.154	0.169	0.161	0.168	0.492	0.535

Table A-11. Concluded

Configuration	Horiz SC Rake		Horiz TS PS Probe, Pt		Horiz TS PS Probe, Ps	
	Temporal	Spatial	Temporal	Spatial	Temporal	Spatial
C04	2.706	0.701	0.743	3.412	0.564	1.833
C05	1.214	0.602	0.606	1.743	0.696	0.983
C06	0.522	0.480	0.439	1.091	0.463	0.755
C07	0.477	0.457	0.386	1.288	0.504	1.019
C08	0.335	0.325	0.329	1.289	0.440	0.604
C09	0.610	0.560	0.499	1.506	0.648	0.811
C10	0.759	0.915	0.834	2.197	0.830	0.954
C11	0.654	1.064	0.924	1.694	0.885	0.903
C12	1.965	0.879	-	-	-	-
C13	1.143	1.240	1.231	4.648	0.942	0.882
C14	0.891	0.741	0.707	1.912	0.918	0.848
C15	0.683	0.638	0.583	1.711	0.633	1.020
C16	0.410	0.440	0.572	1.936	0.549	0.586
C17	0.342	0.450	0.470	0.834	0.466	0.504
C18	-	-	0.329	0.988	0.392	0.475
C19	0.270	0.713	0.390	0.915	0.406	0.550
C20	-	-	0.460	0.898	0.582	0.953
C21	1.000	1.000	1.000	1.000	1.000	1.000
C22	0.408	0.712	0.498	0.993	0.537	0.751
C23	0.349	0.686	0.497	1.108	0.585	0.904
C24	0.332	0.694	0.417	1.107	0.390	0.675

Table A-12. Compressor Power Impact of Various Flow Conditioning Elements

Element	Screen Percent Open	Loss Coefficient, Kt	Element Area ft2	Stilling Chamber to Element Area Ratio	Additional Compressor Power
Stilling Chamber					
Screen, 56.85% open	56.85	1.14	2345	1.00	0.64
Honeycomb, L/D = 16	na	0.78	2345	1.00	0.44
Honeycomb, L/D = 50	na	2.15	2345	1.00	1.21
Corner Screen, 49.8% open	49.8	1.67	3316	0.71	0.47
Crossleg					
Diffuser Exit Screen, 54% open	54	1.32	2345	1.00	0.78
Seg 4/5 Screen, 54% open	54	1.32	1447	1.62	2.05
Seg 2/3 Screen, 54% open	54	1.32	932	2.51	4.95

Note: Power Impact Calculated with Test Section Mach Number of 1.6.

Element Combination	Combination dEdot, Mw	Total Edot, Mw	Total Edot, hp
Short honeycomb plus 2 stilling chamber screens	1.71	161.71	216858
+2 diffuser exit screens	3.27	163.27	218953
+ Seg 4/5 screen	5.32	165.32	221705
+ Seg 2/3 screen	10.27	170.27	228344
Long honeycomb, no stilling chamber screens	1.21	161.21	216193
+2 diffuser exit screens	2.77	162.77	218288
+ Seg 4/5 screen	4.83	164.83	221040
+ Seg 2/3 screen	9.78	169.78	227678

Note: Test Facilities Handbook Quotes Motor Drive Power of 226000 hp

APPENDIX B

CHAPTER II FIGURES

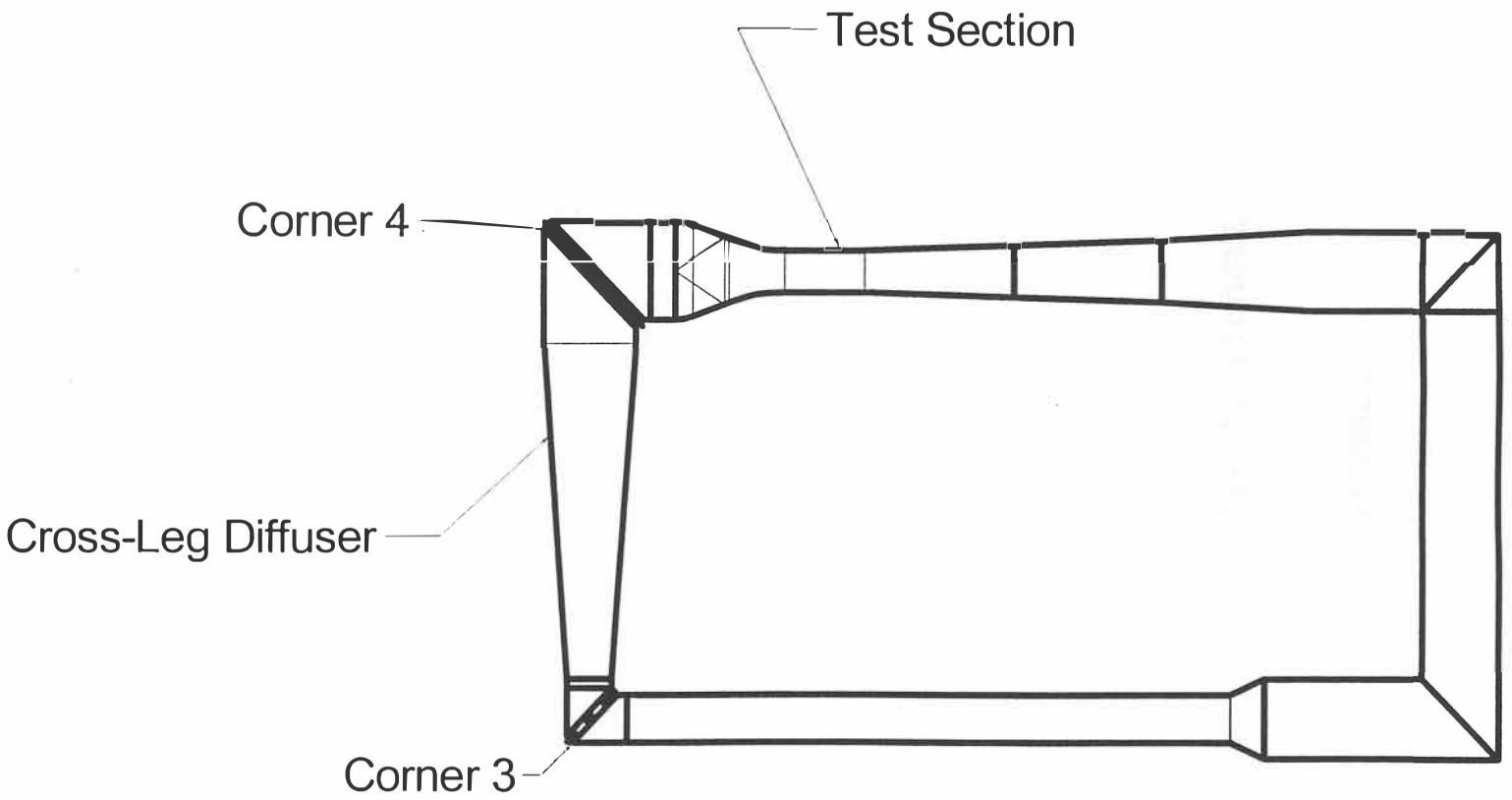


Figure B-1. General Wind Tunnel Layout

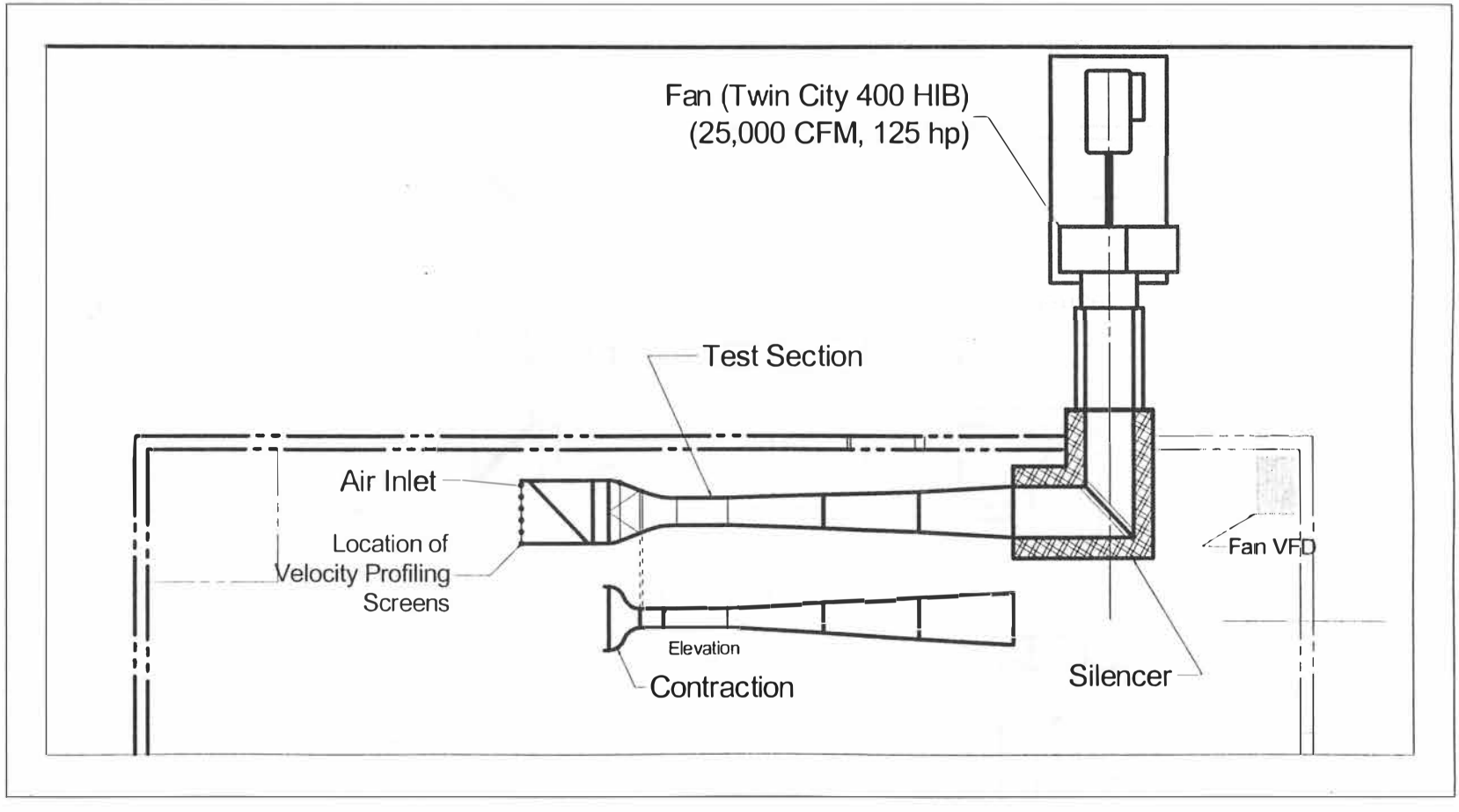


Figure B-2. Setup A Scale Model Layout

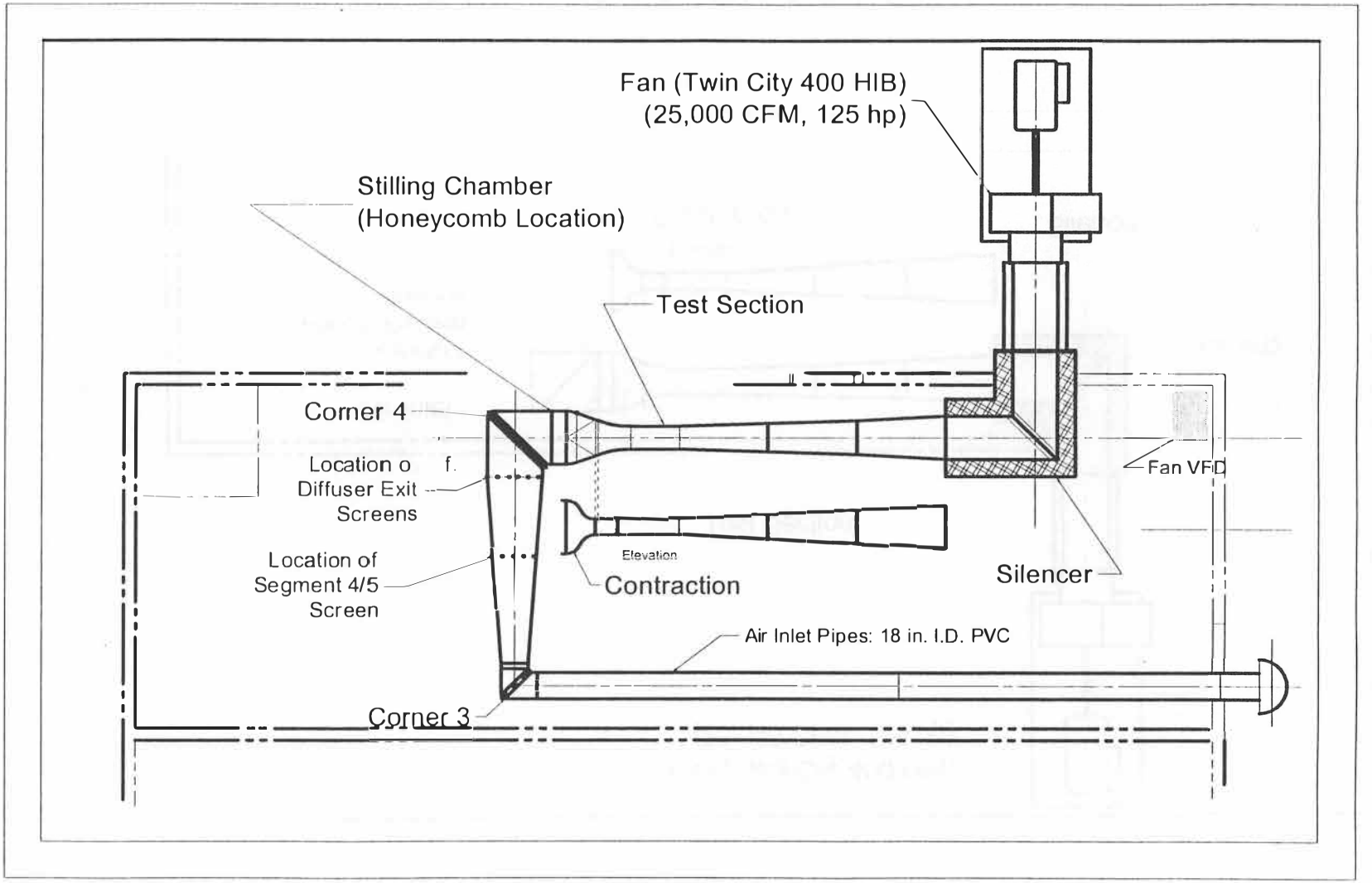


Figure B-3. Setup B Scale Model Layout with Corner 3 Installed

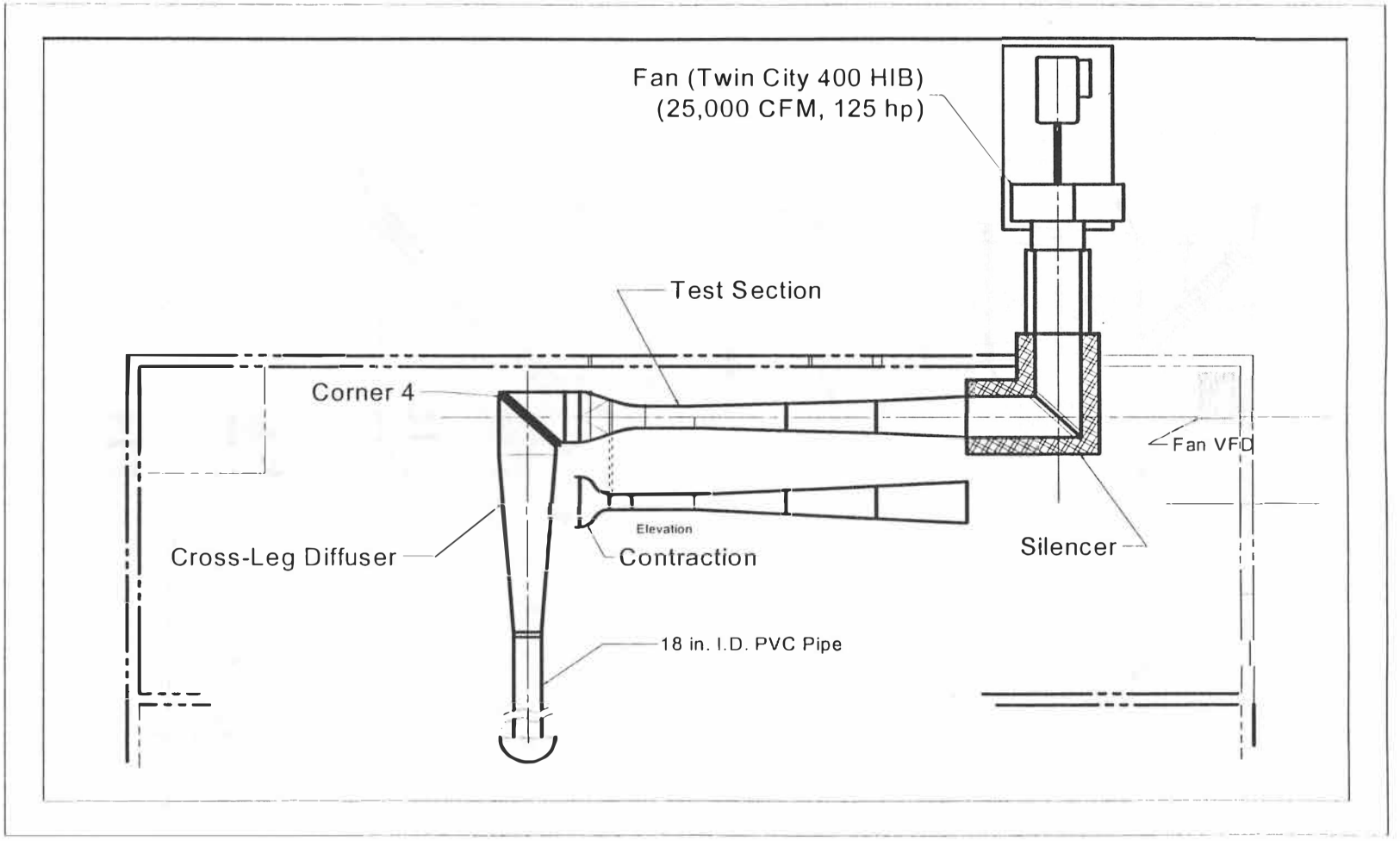


Figure B-4. Setup B Scale Model Layout with Corner 3 Removed

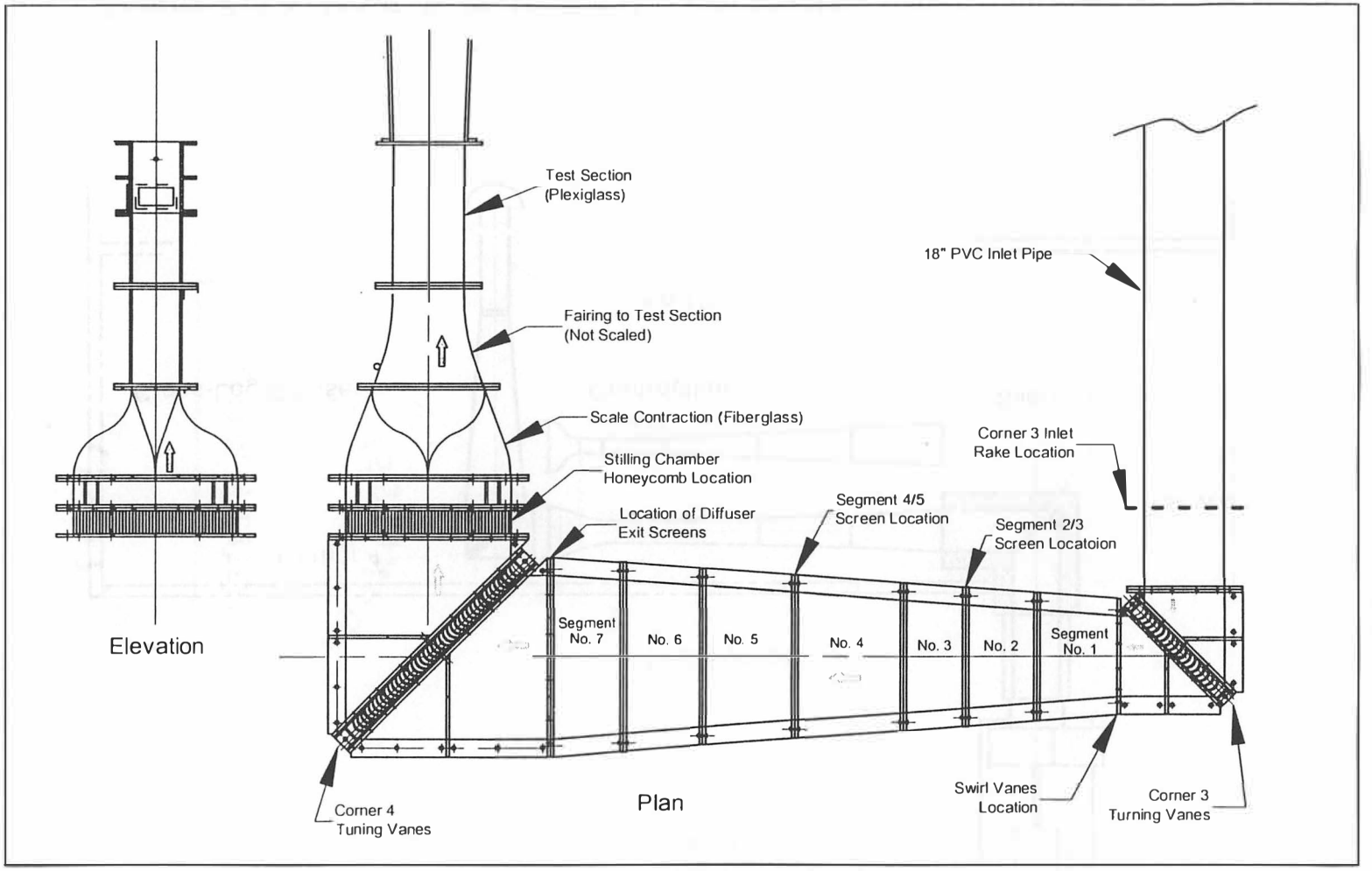


Figure B-5. Model Details of Setup B with Corner 3 Installed

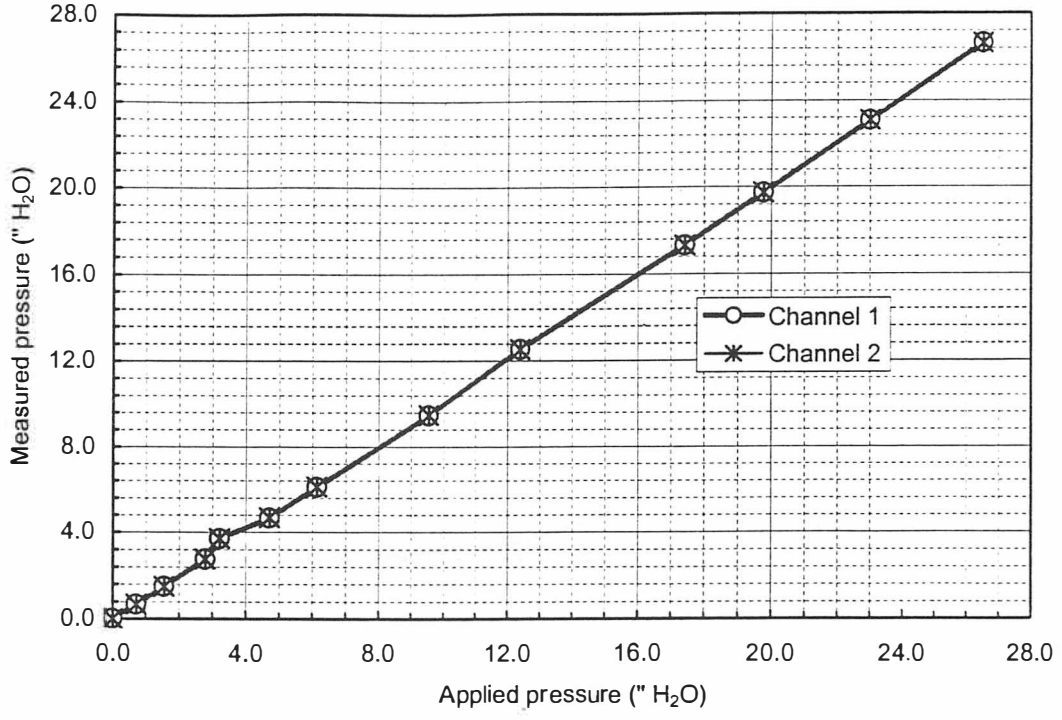


Figure B-6. Transducer Consistency Check

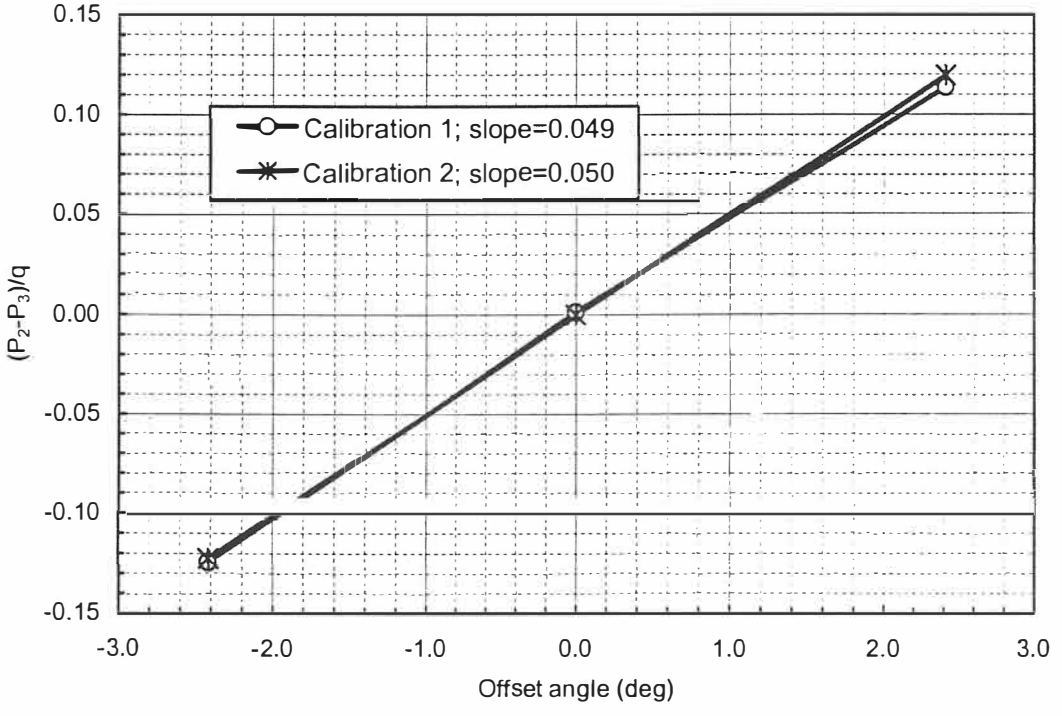


Figure B-7. Flow Angularity Probe Calibration Curve.

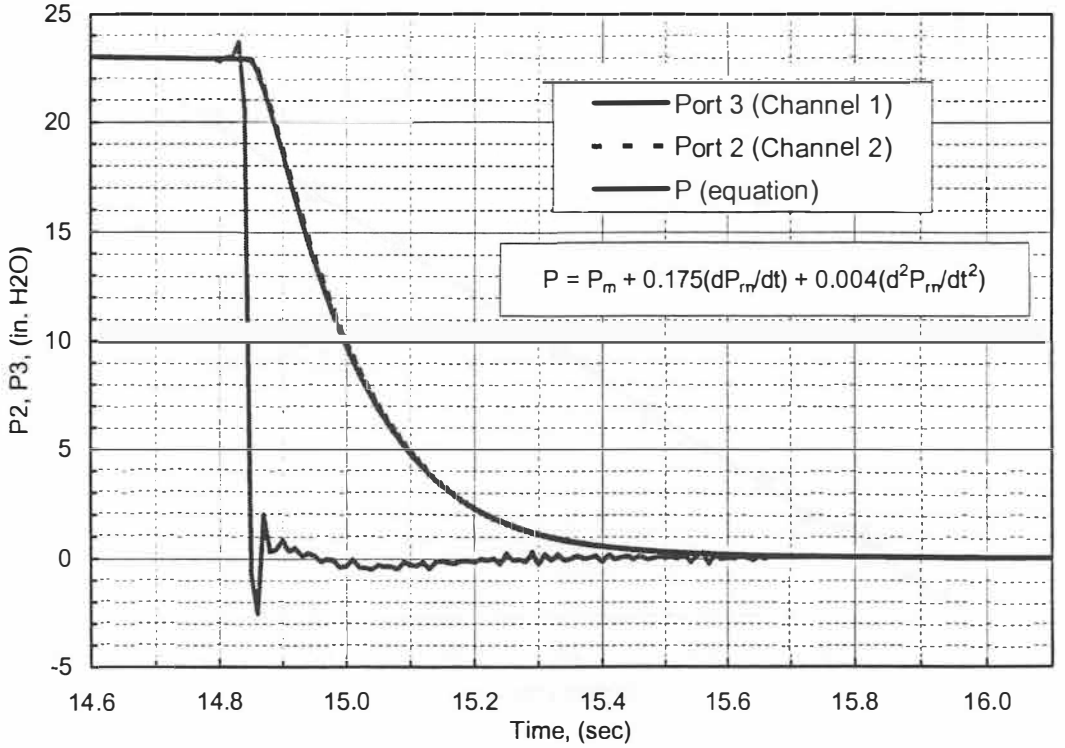


Figure B-8. Flow Angularity Probe Response Test.

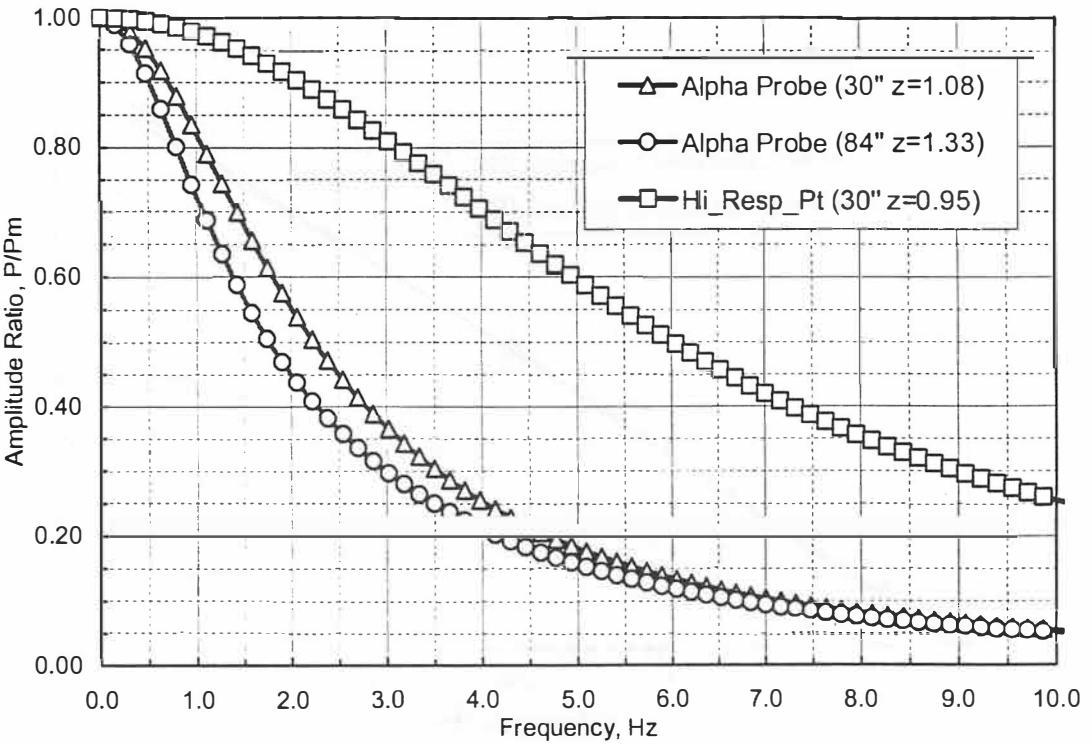


Figure B-9. Frequency response of flow angle probe and high-response probe (Derived from experimental response to a step input).

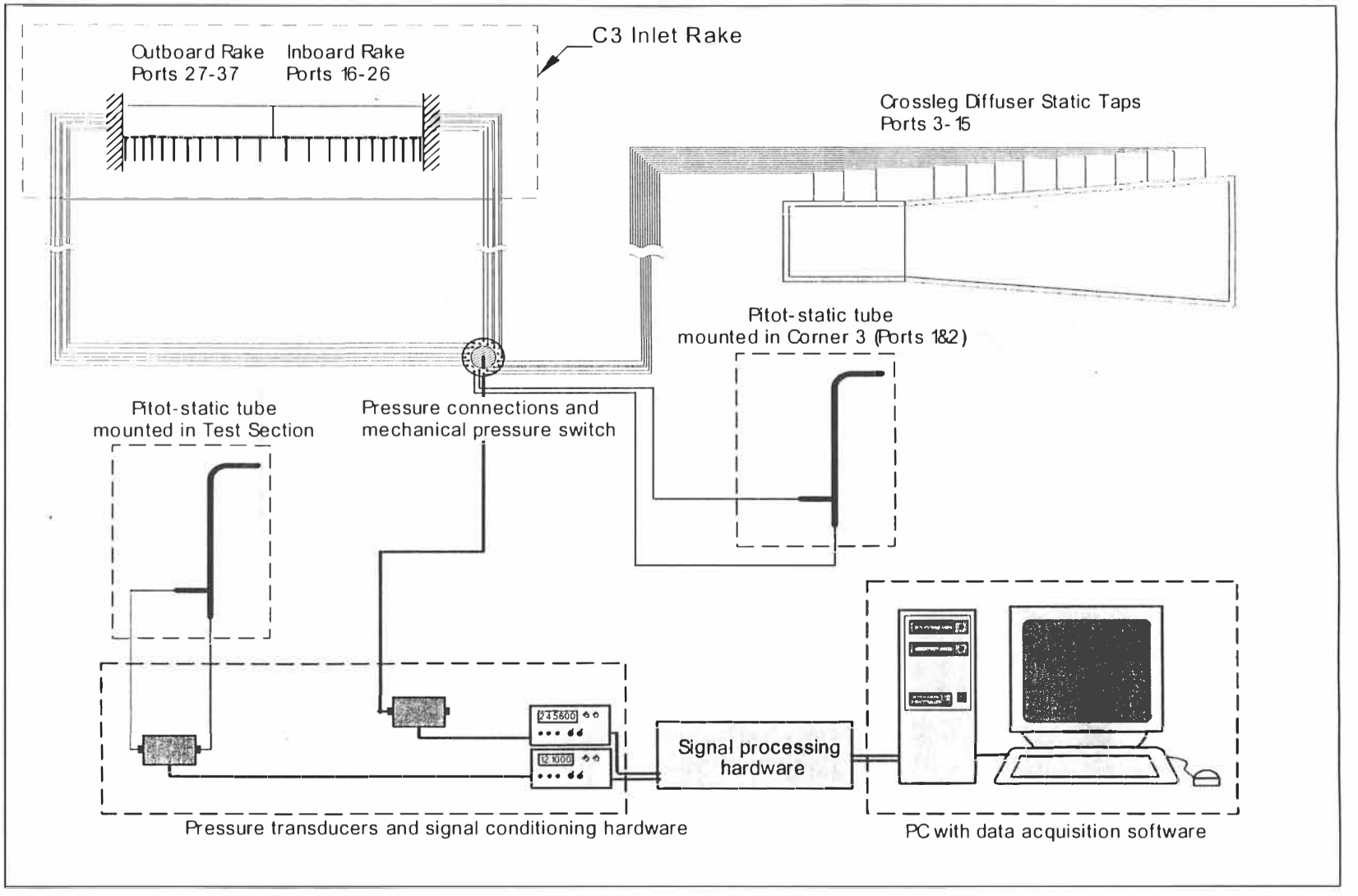


Figure B-10. Instrumentation Setup for Corner 3 Inlet Rake and Cross-Leg Diffuser Static Survey

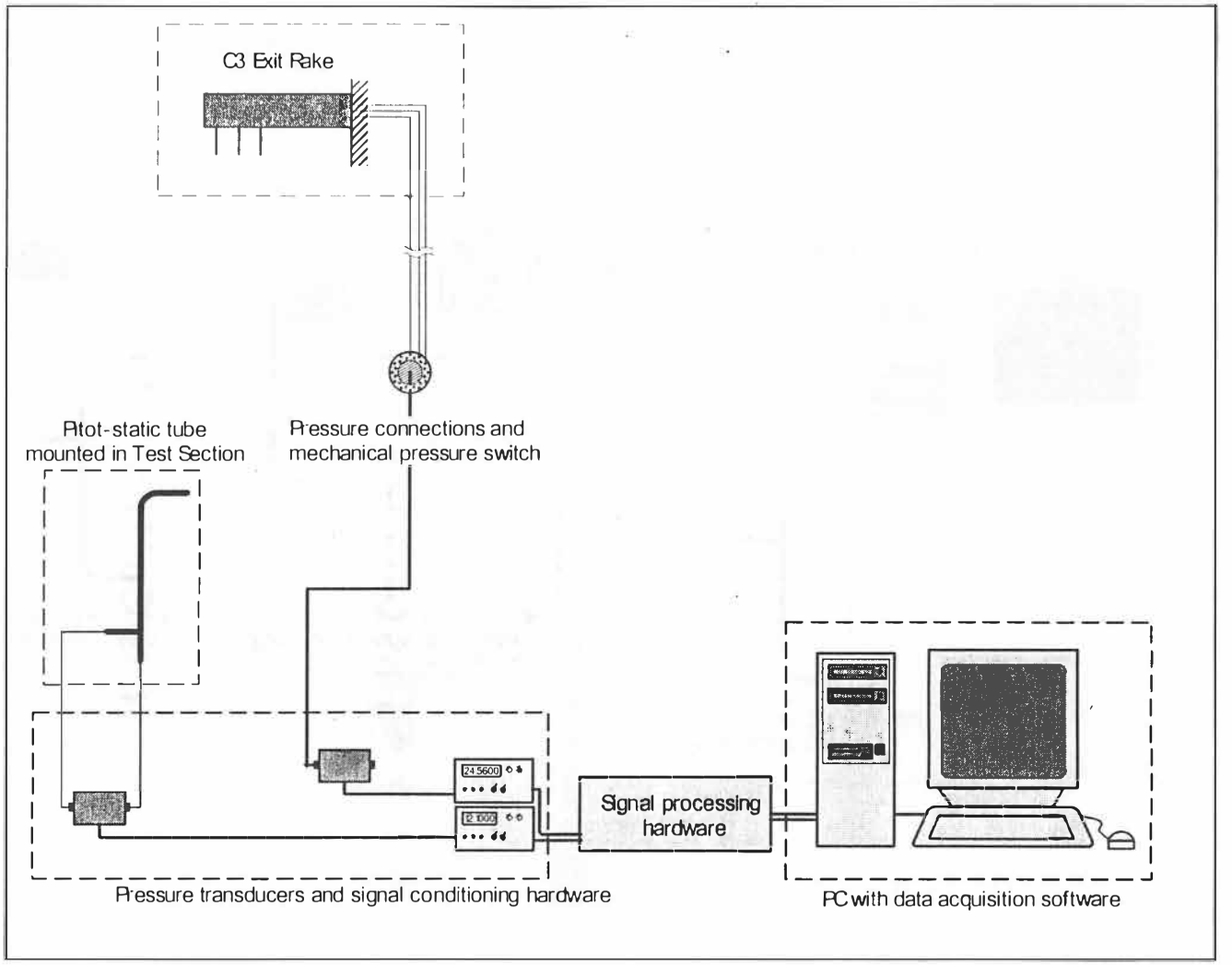


Figure B-11. Instrumentation Setup for Corner 3 Exit Rake

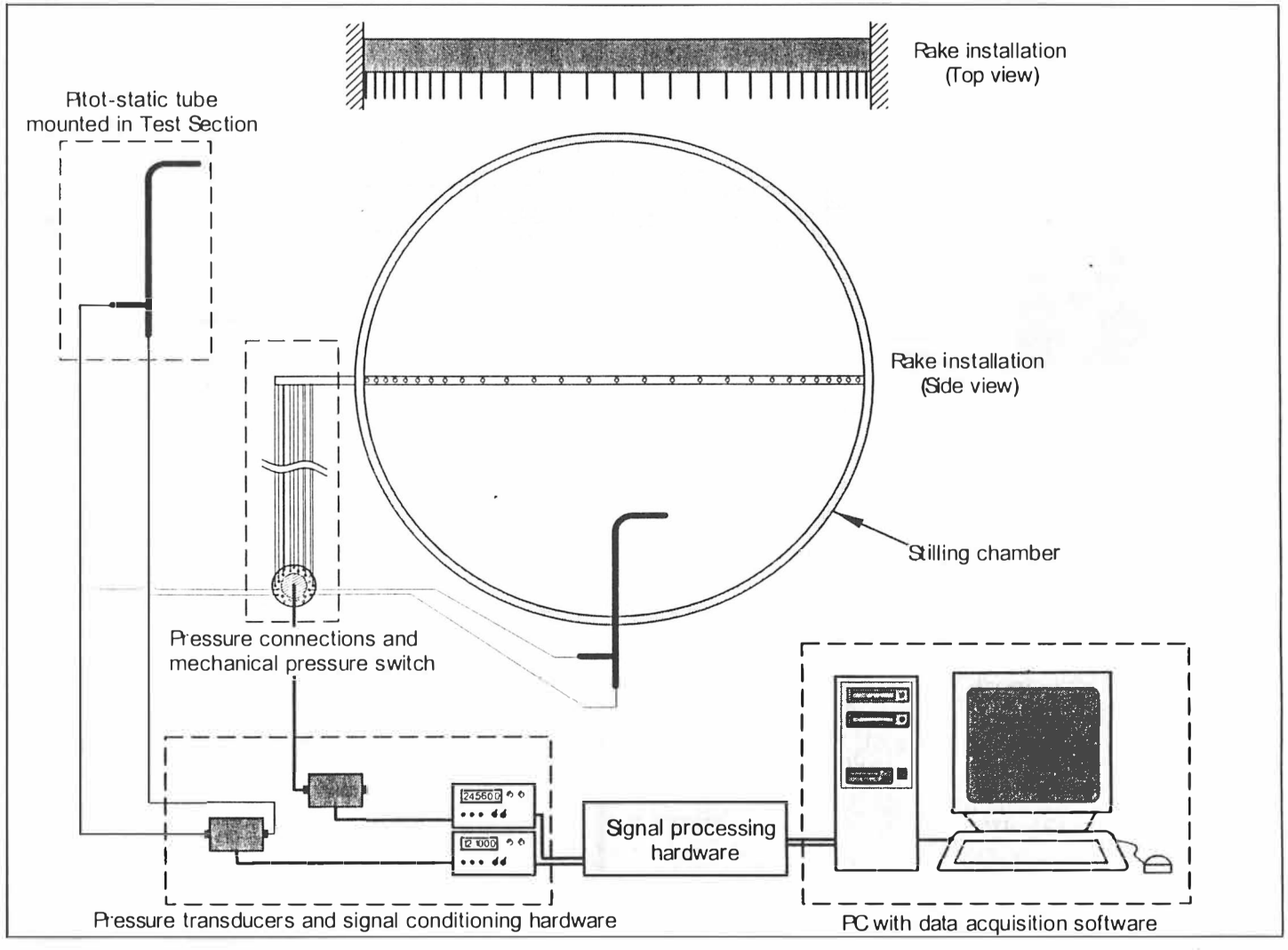


Figure B-12. Instrumentation Setup for Stilling Chamber and Corner 4 Inlet Rake

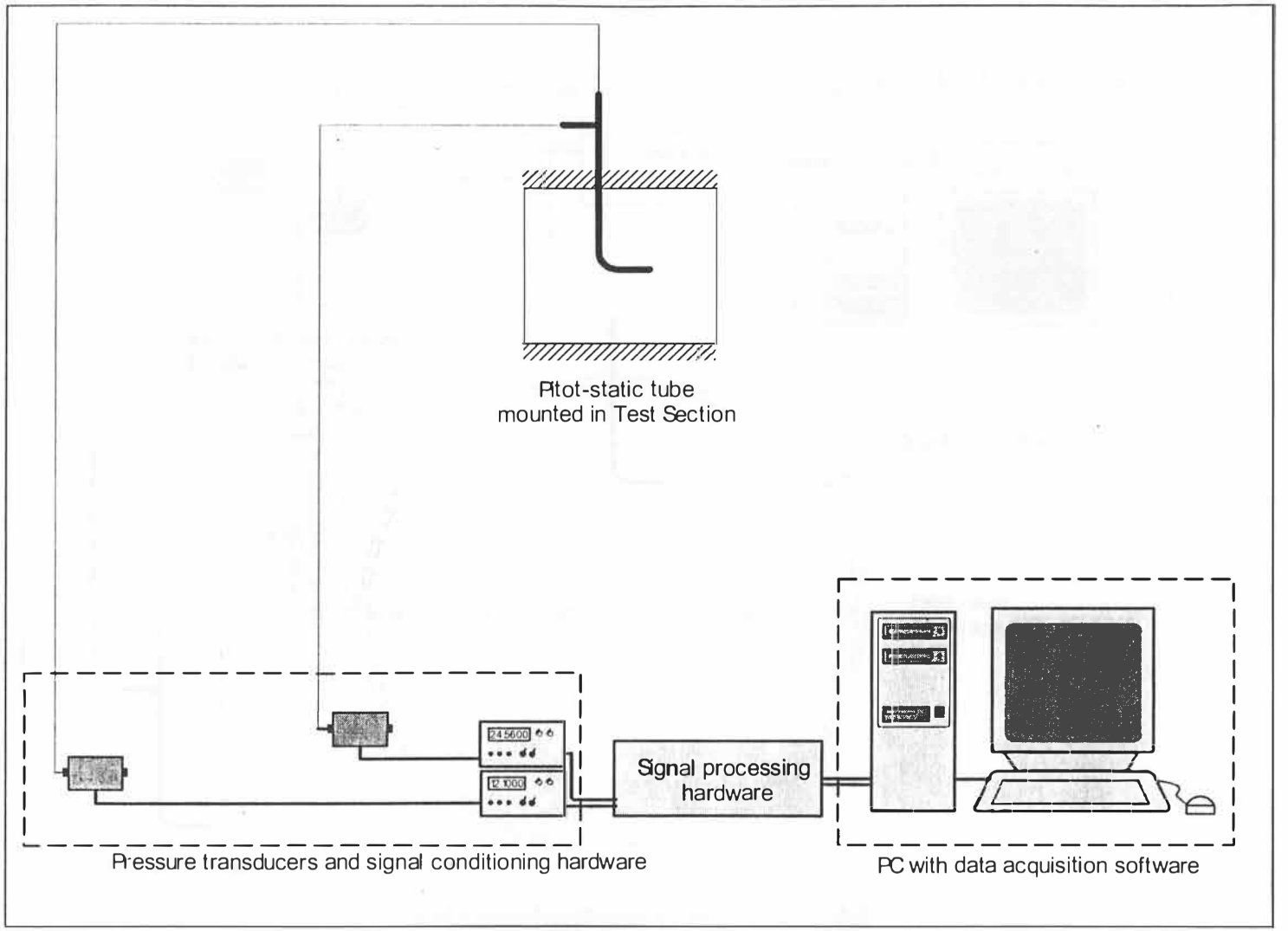


Figure B-13. Instrumentation Setup for Test Section Pitot-Static Probe

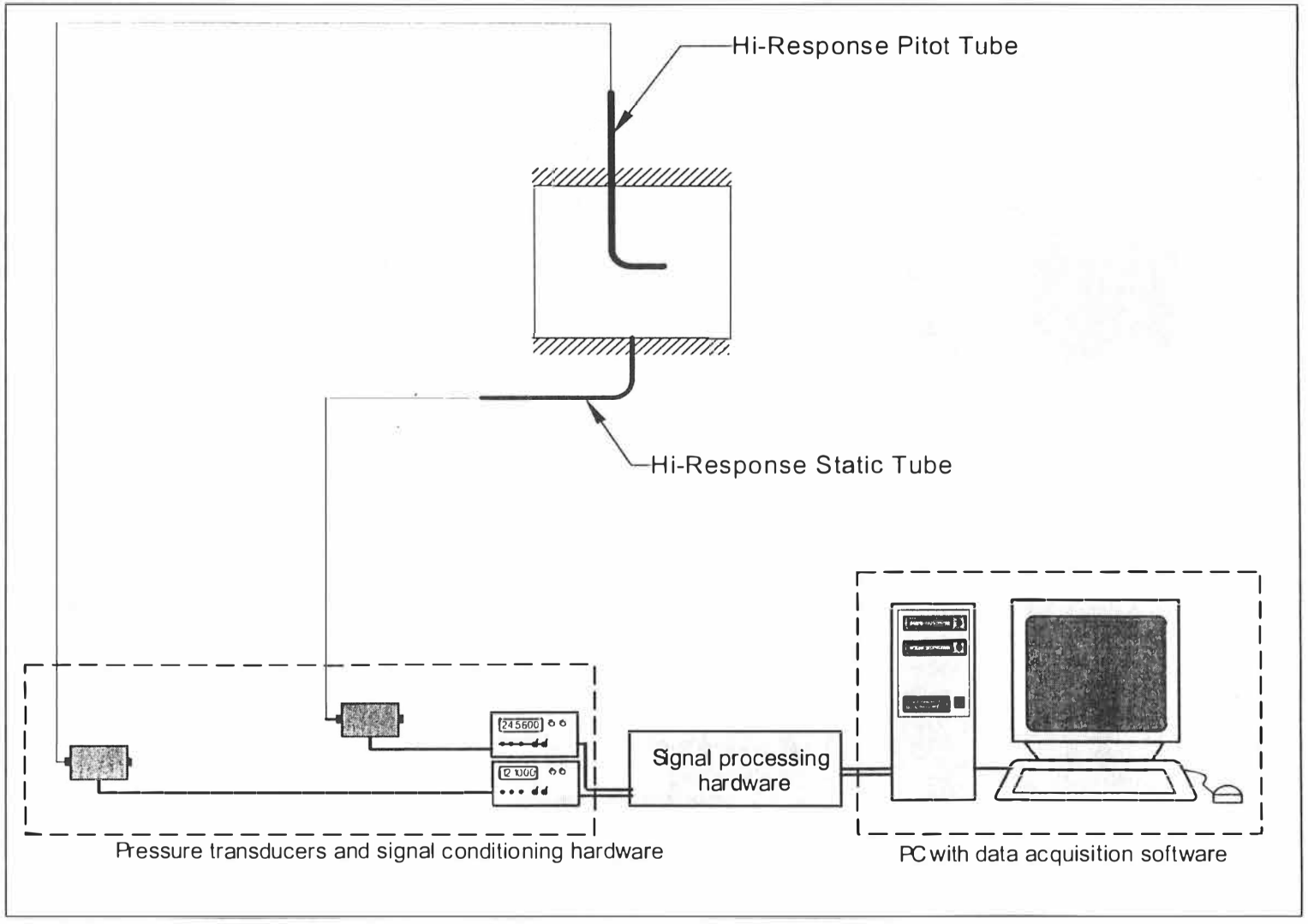


Figure B-14. Instrumentation Setup for Test Section High Response Probe

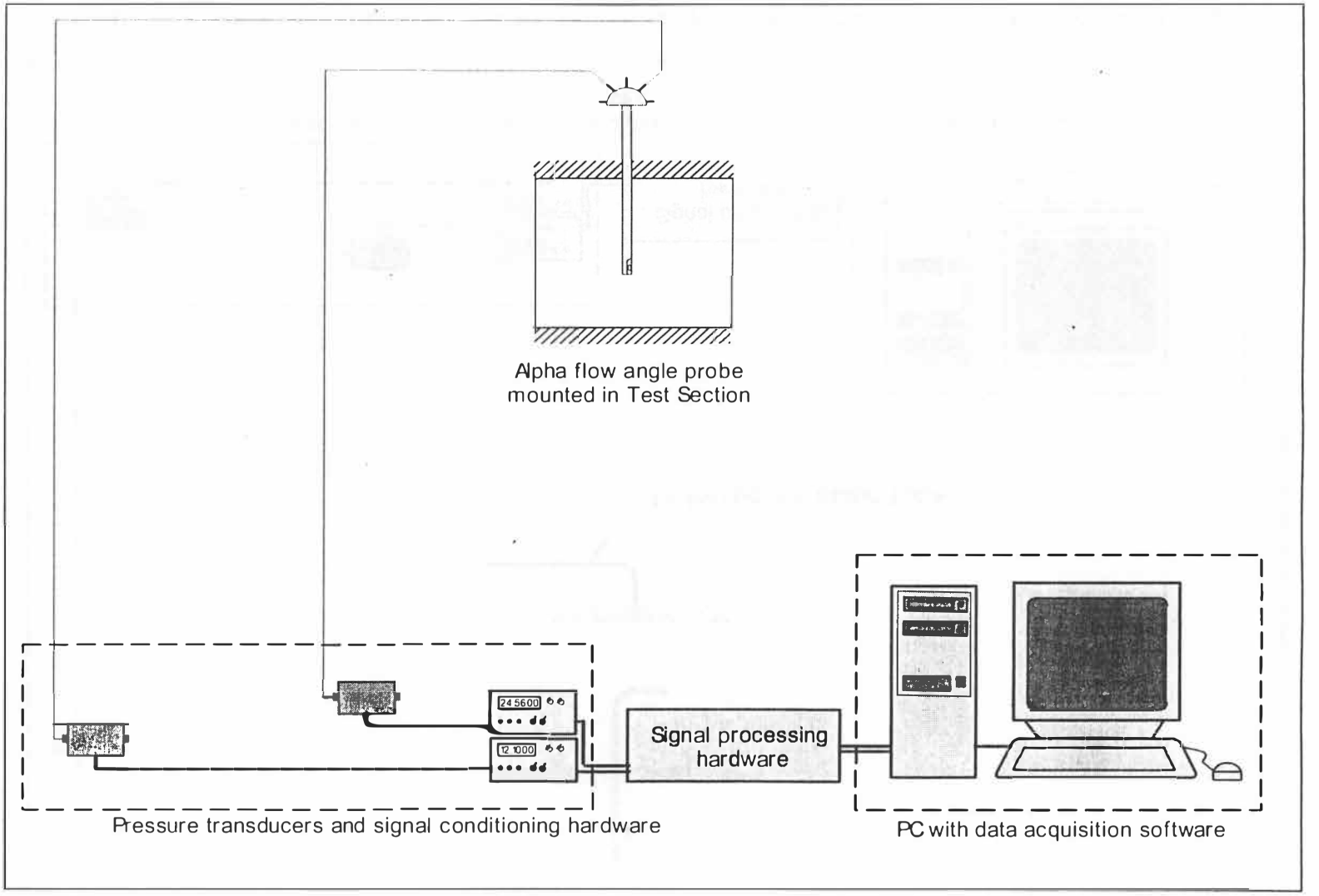


Figure B-15. Instrumentation Setup for Test Section Flow Angularity Probe

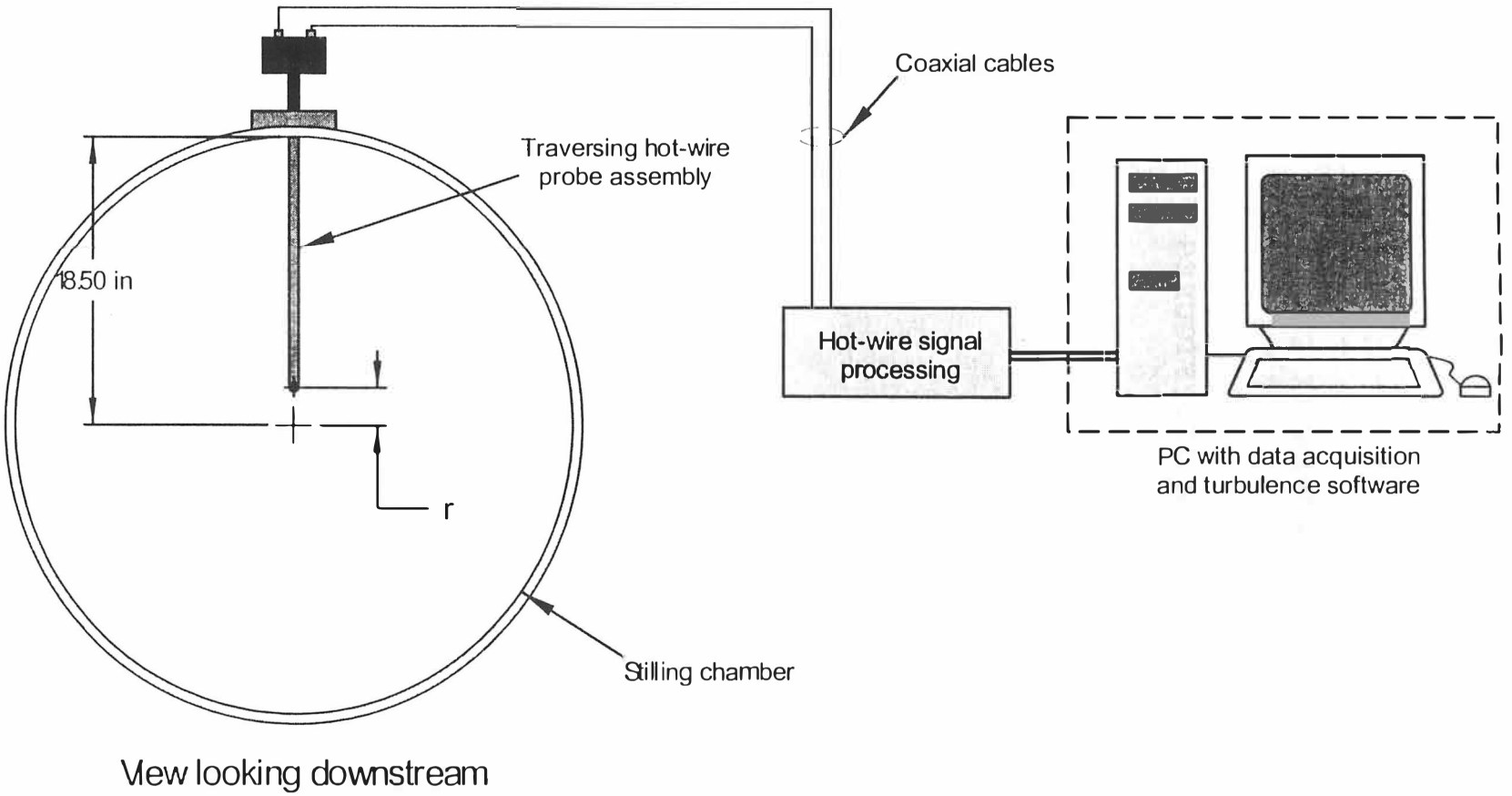
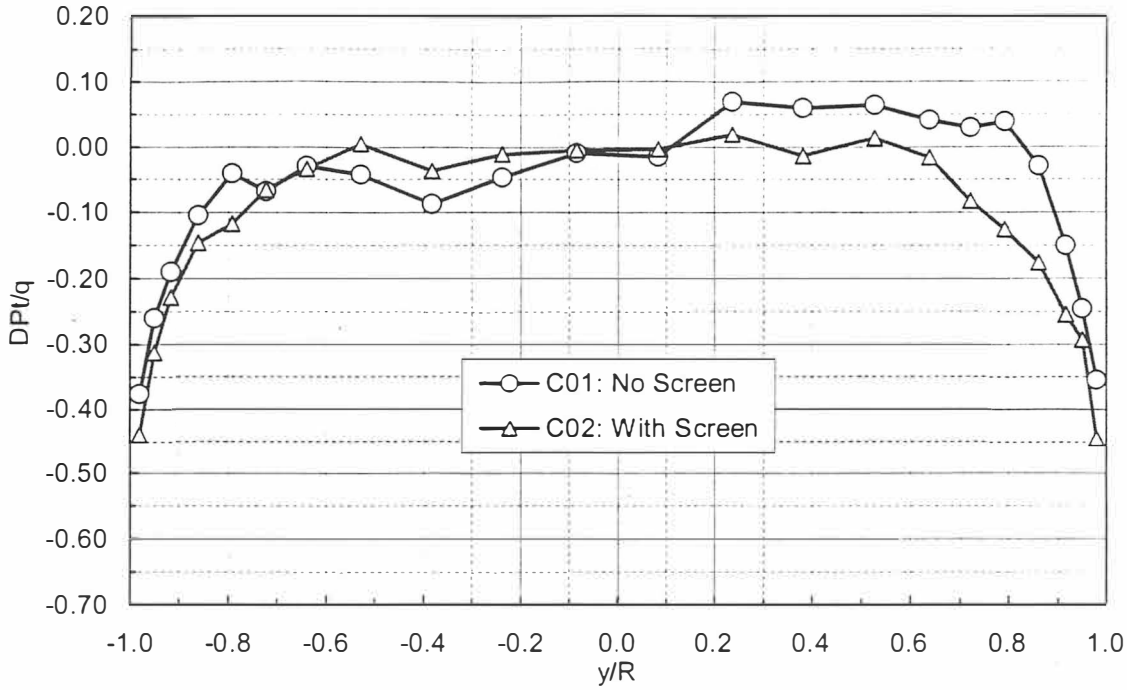


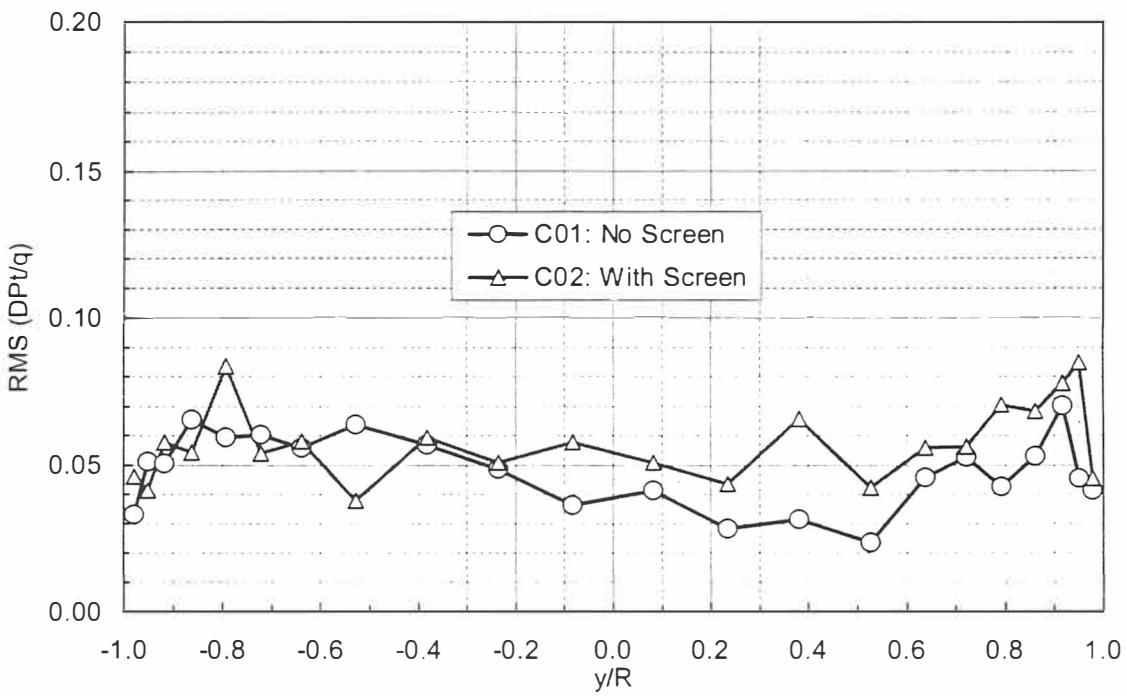
Figure B-16. Instrumentation Setup for Hot-Wire Anemometer (Stilling Chamber Shown)

APPENDIX C

CHAPTER III FIGURES

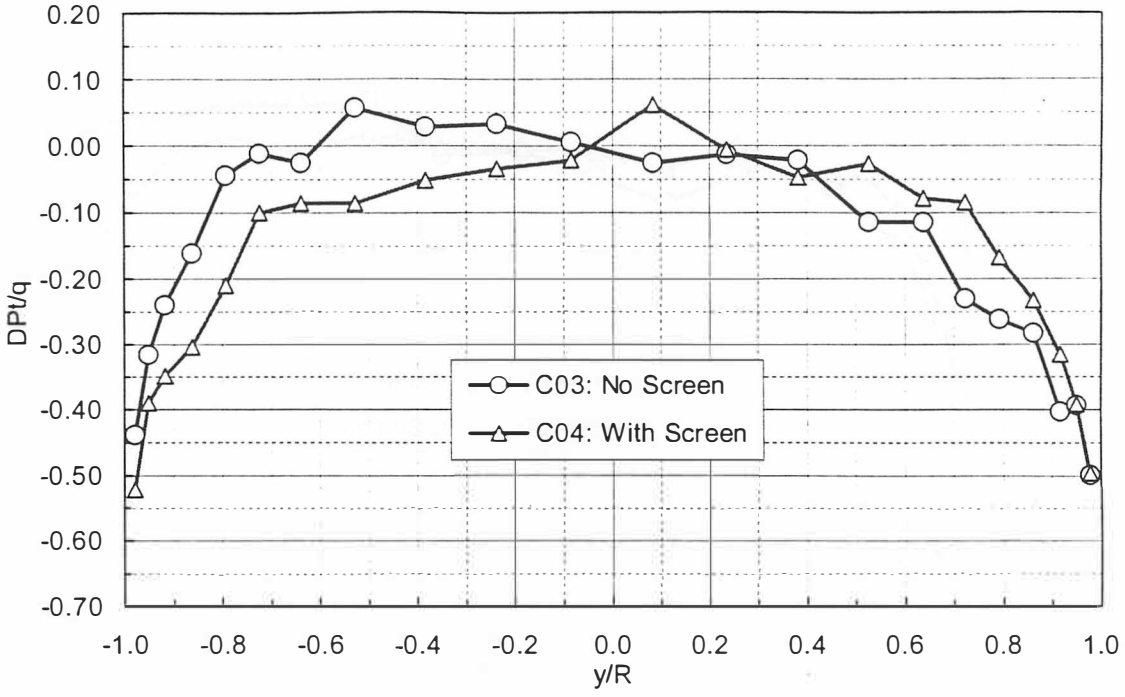


a) Total Pressure Profiles

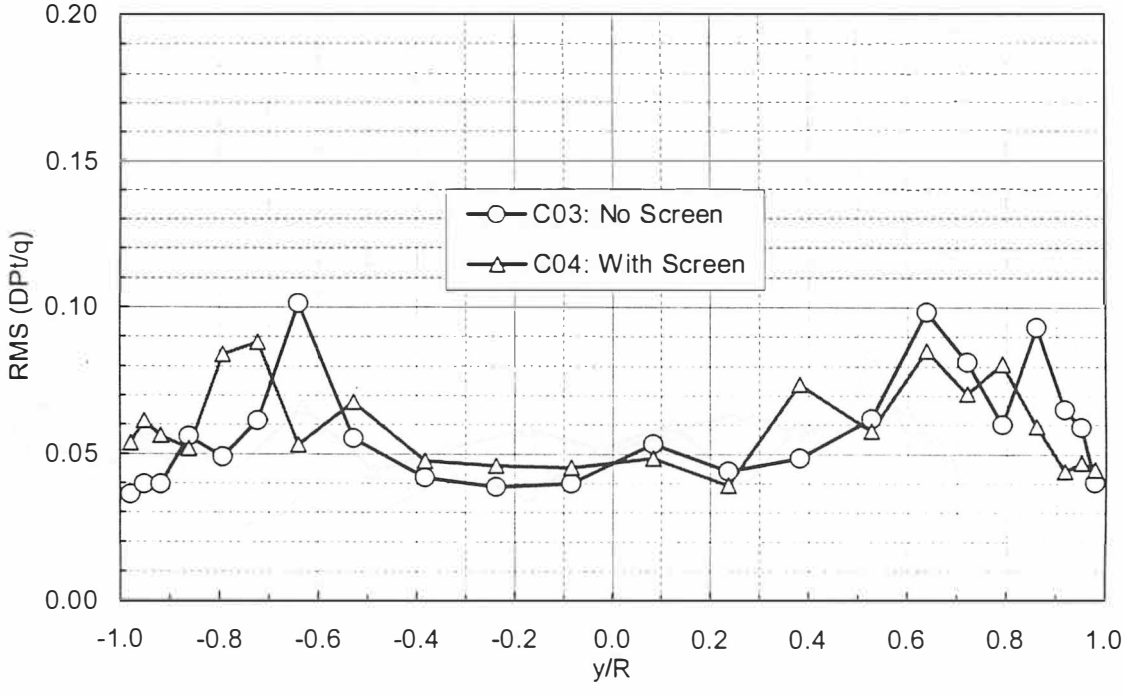


b) Temporal RMS Profiles

Figure C-1. Corner 3 Inlet Total Pressure & Temporal RMS Profiles, One Inlet Pipe Installed (L/D = 13.9), With (C02) and Without (C01) Inlet Screen.

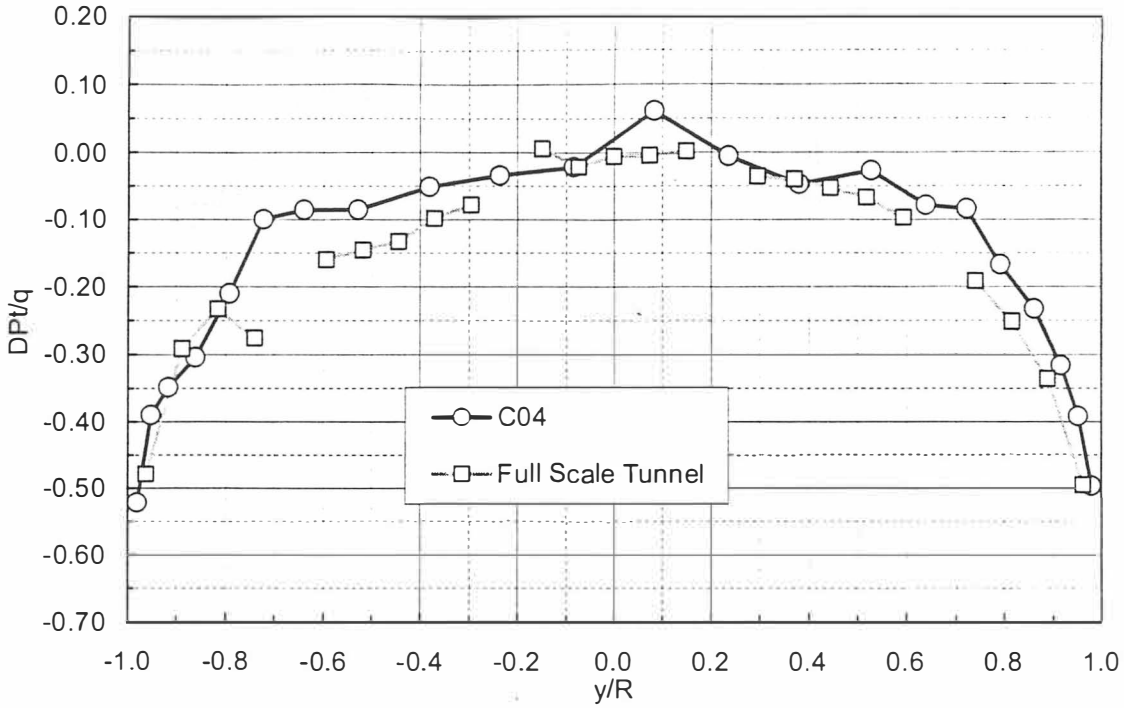


a) Total Pressure Profiles

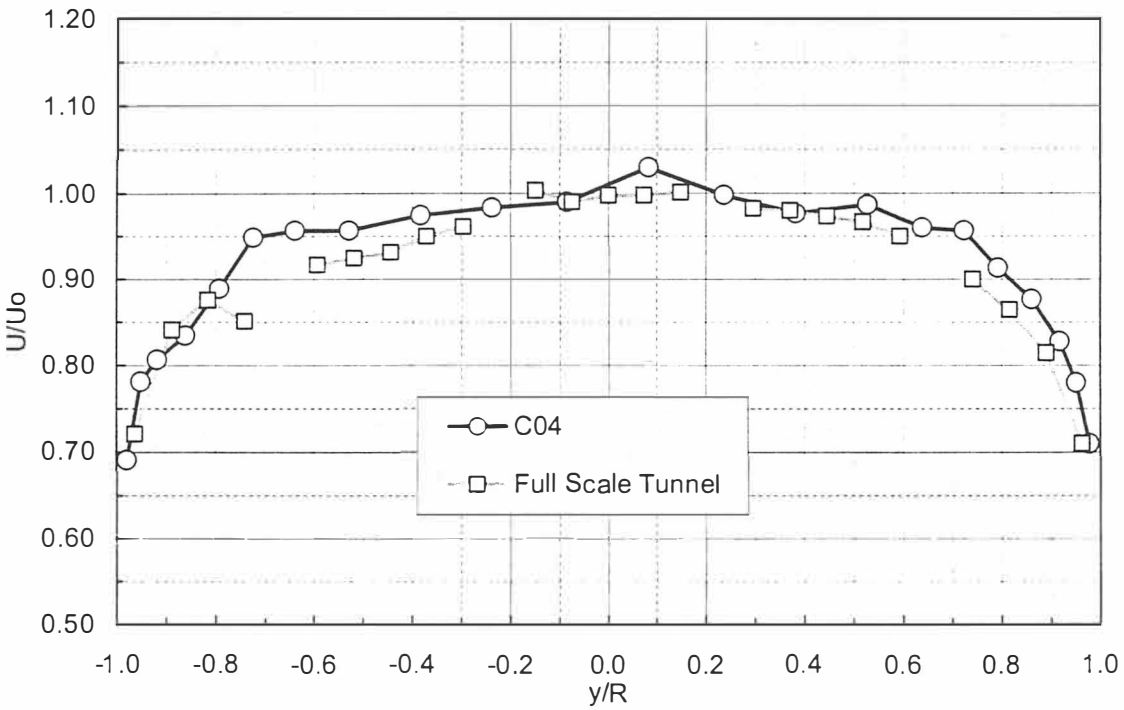


b) Temporal RMS Profiles

Figure C-2. Corner 3 Inlet Total Pressure & Temporal RMS Profiles, Two Inlet Pipes Installed (L/D = 26.5), With (C04) and Without (C03) Inlet Screen.

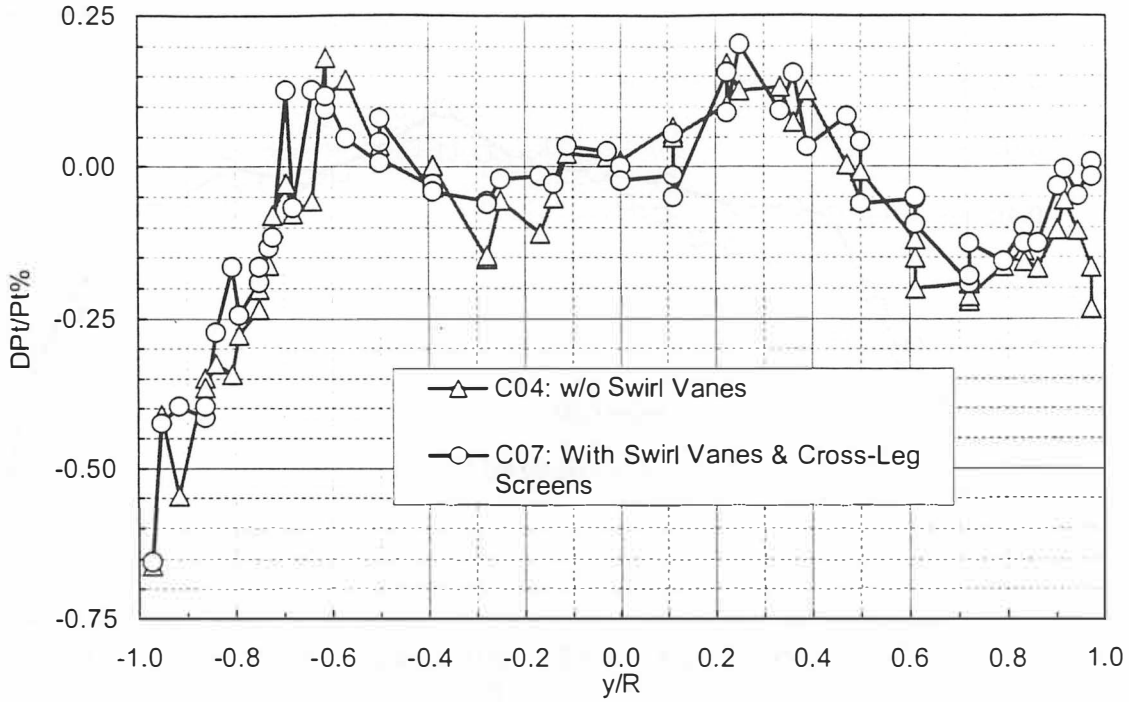


a) Total Pressure Profiles

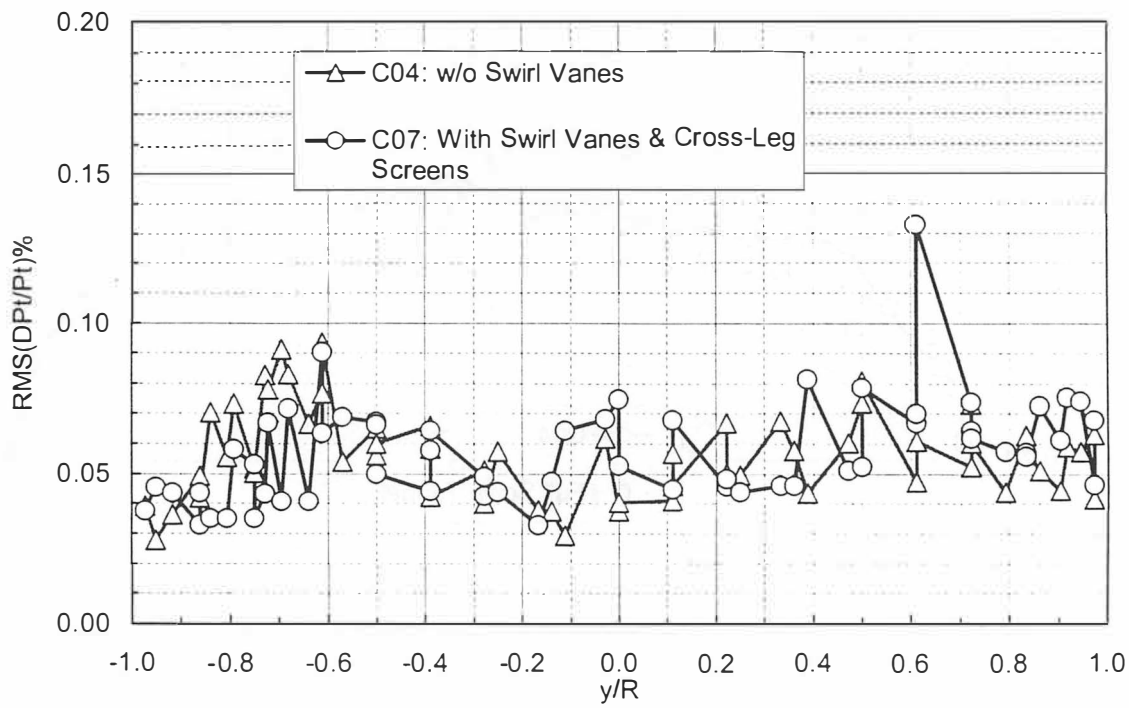


b) Velocity Profiles

Figure C-3. Corner 3 Inlet Total Pressure and Velocity Profiles: Configuration C04 & Full Scale Tunnel.

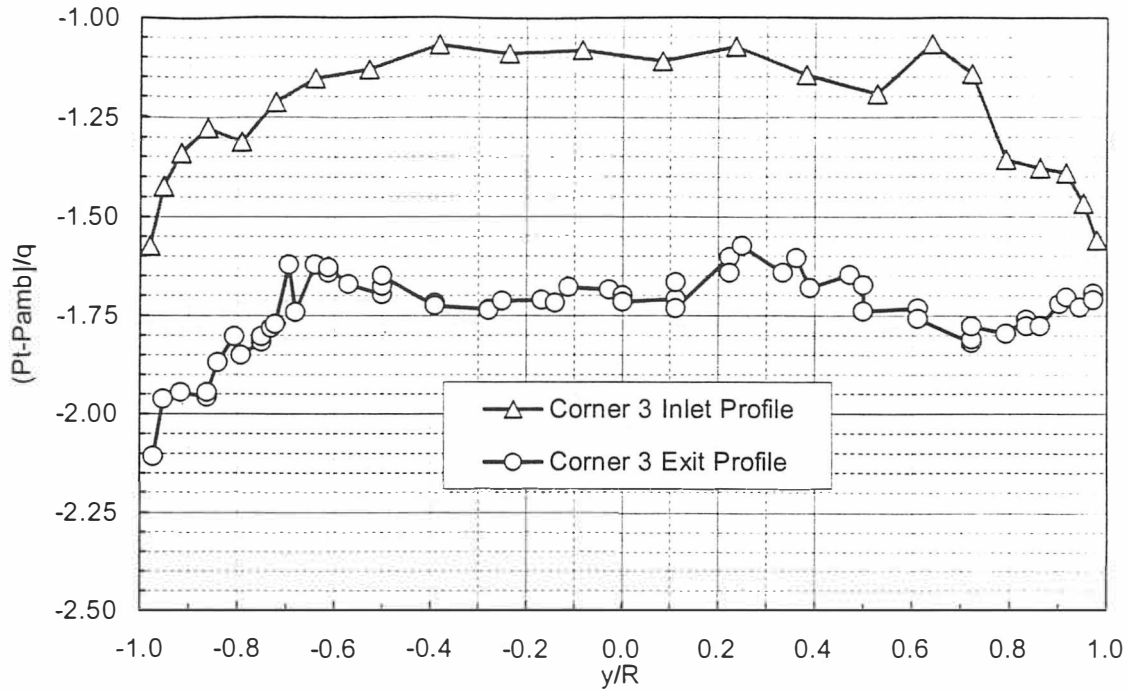


a) Total Pressure Profiles

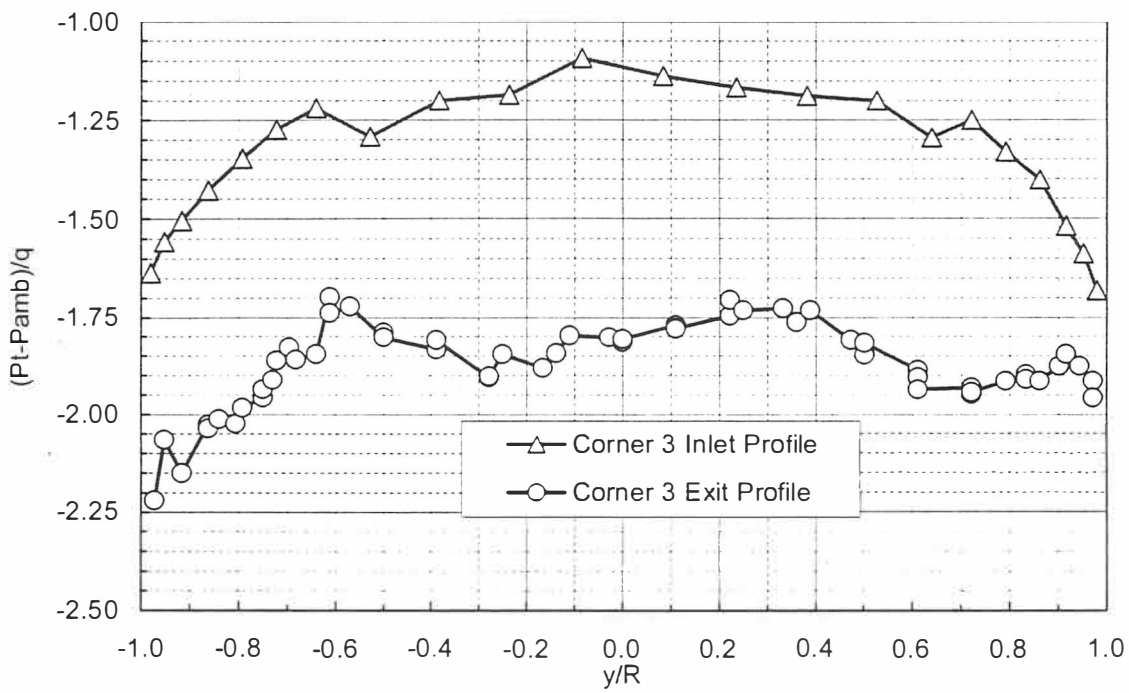


b) Temporal RMS Profiles

Figure C-4. Corner 3 Exit Total Pressure and Temporal RMS Profiles: Configurations C04 (without Swirl Vanes) & C07 (with Swirl Vanes & Cross-Leg Screens).

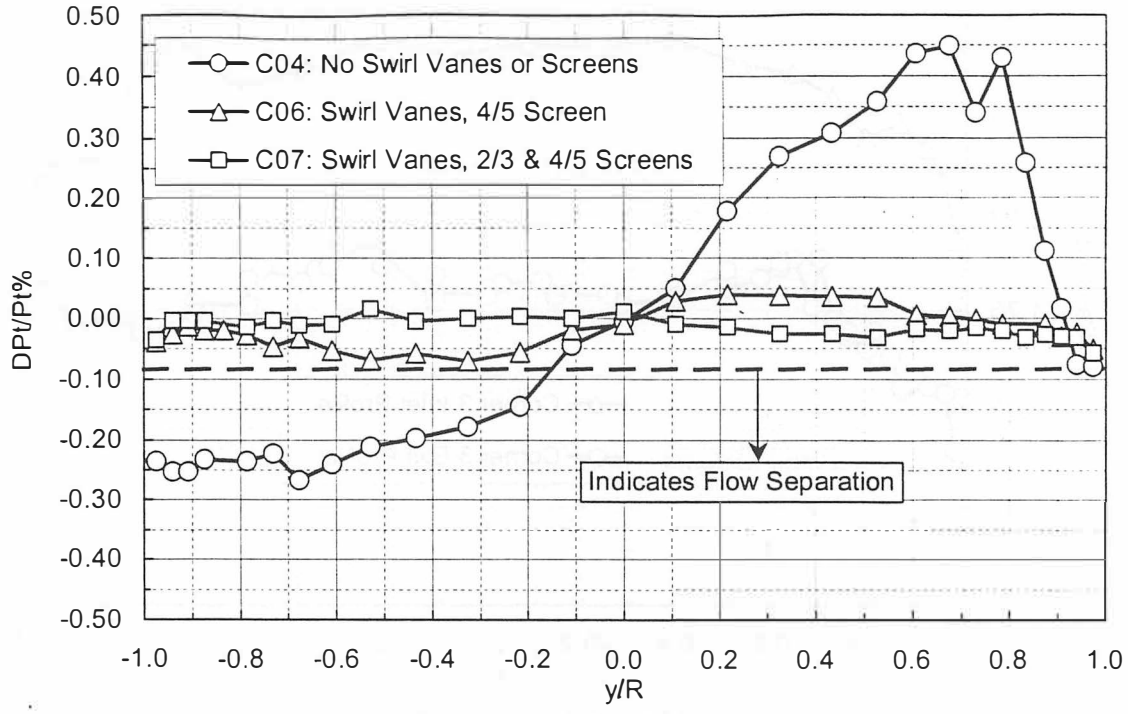


a) Configuration C04. Kt = 0.49

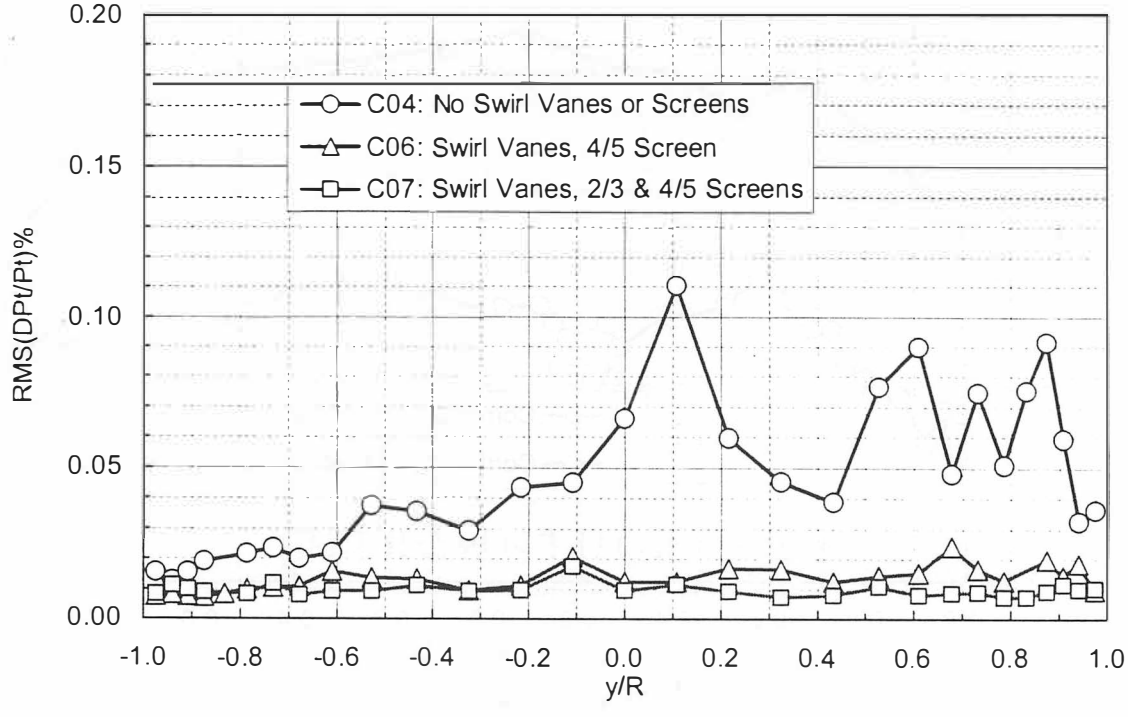


b) Configuration C07. Kt = 0.53

Figure C-5. Corner 3 Inlet & Exit Total Pressure Profiles: Configurations C04 (without Swirl Vanes) & C07 (with Swirl Vanes & Cross-Leg Screens).



a) Total Pressure Profiles



b) Temporal RMS Profiles

Figure C-6. Corner 4 Inlet Total Pressure and Temporal RMS Profiles, Configurations C04, C06, and C07.

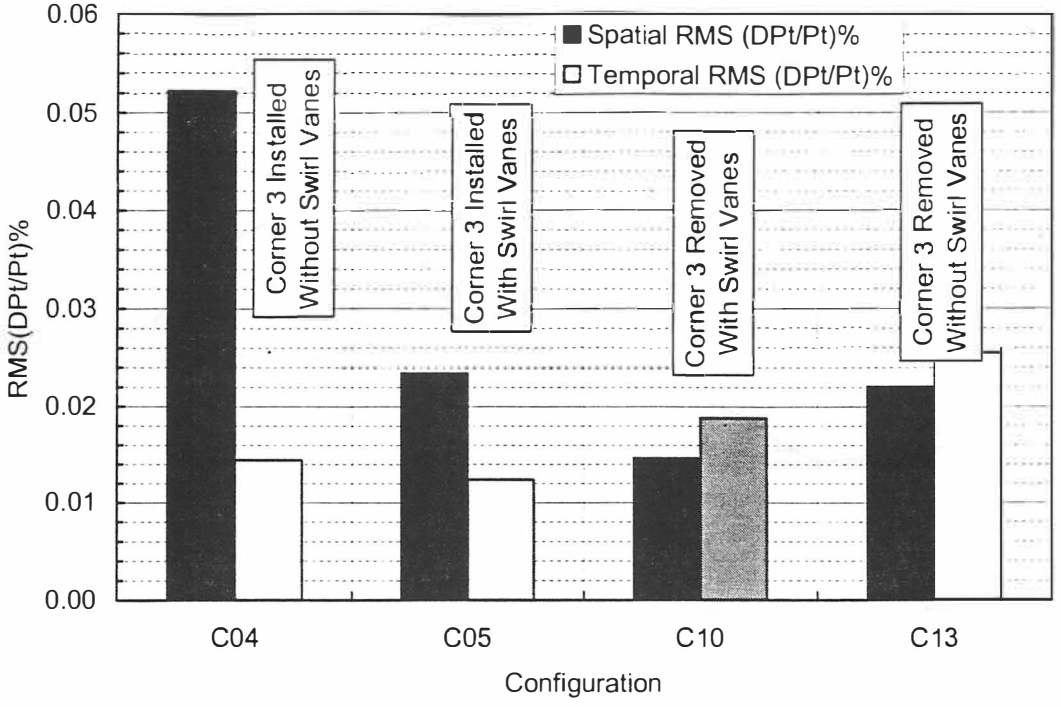
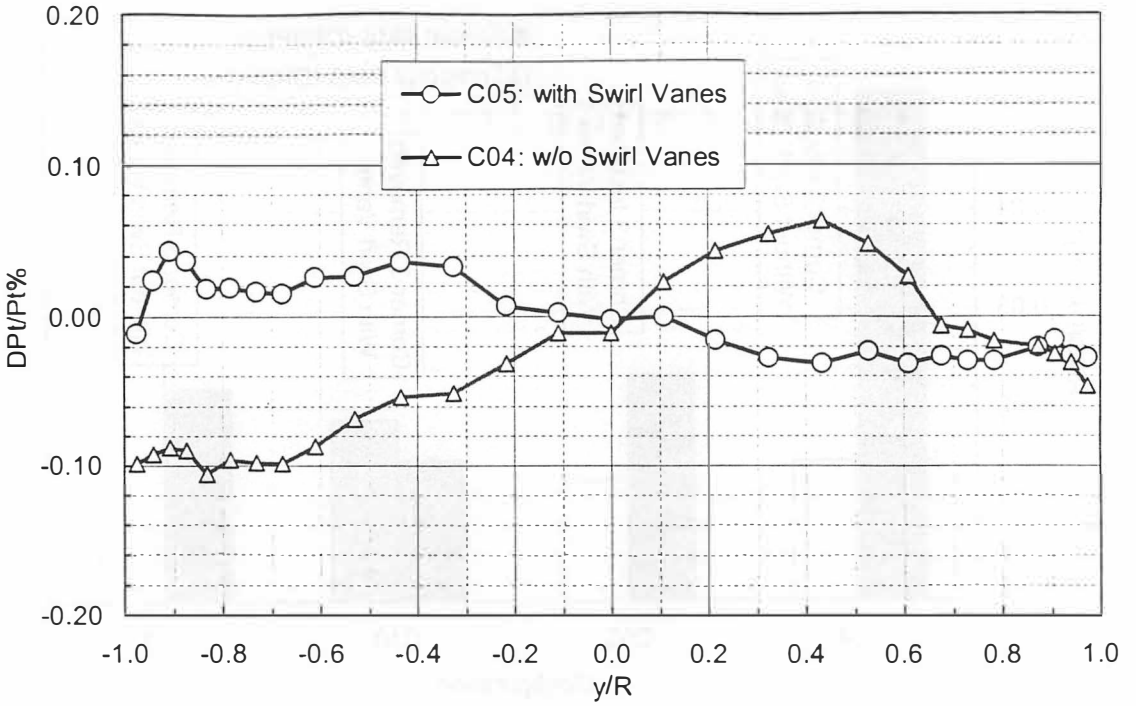
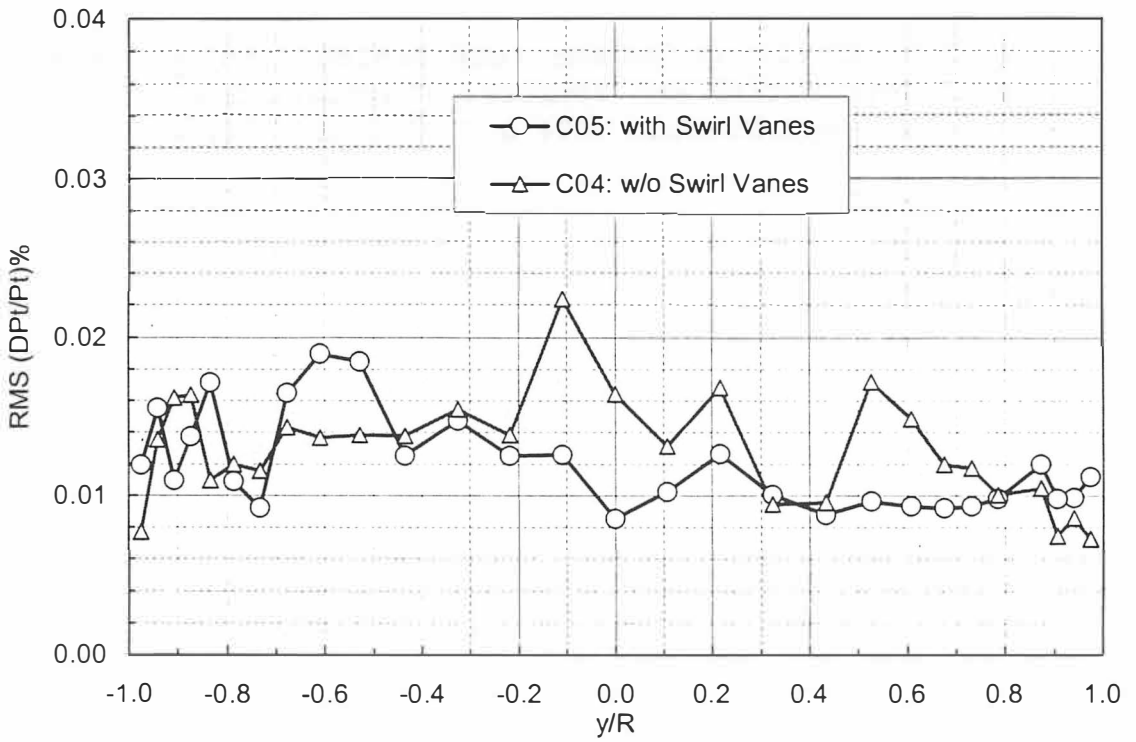


Figure C-7. Stilling Chamber Core Region Total Pressure Spatial Distribution and Temporal Fluctuation With (C05 & C10) and Without (C04 & C13) Swirl Vanes.

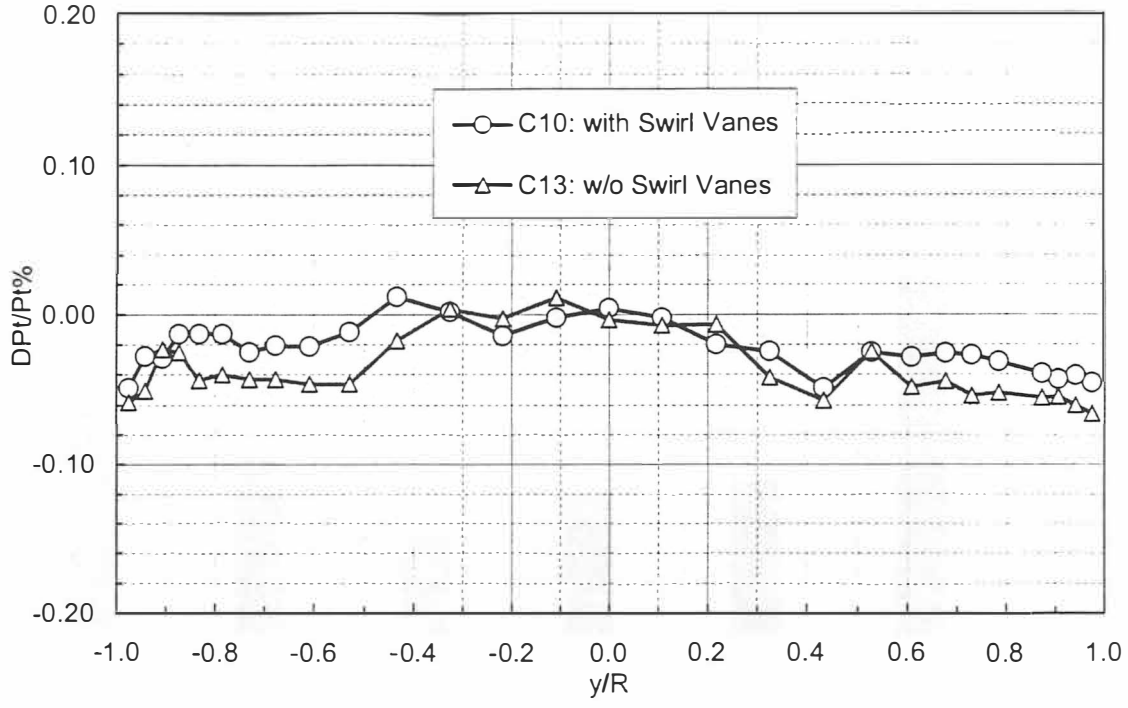


a) Spatial Total Pressure Profile

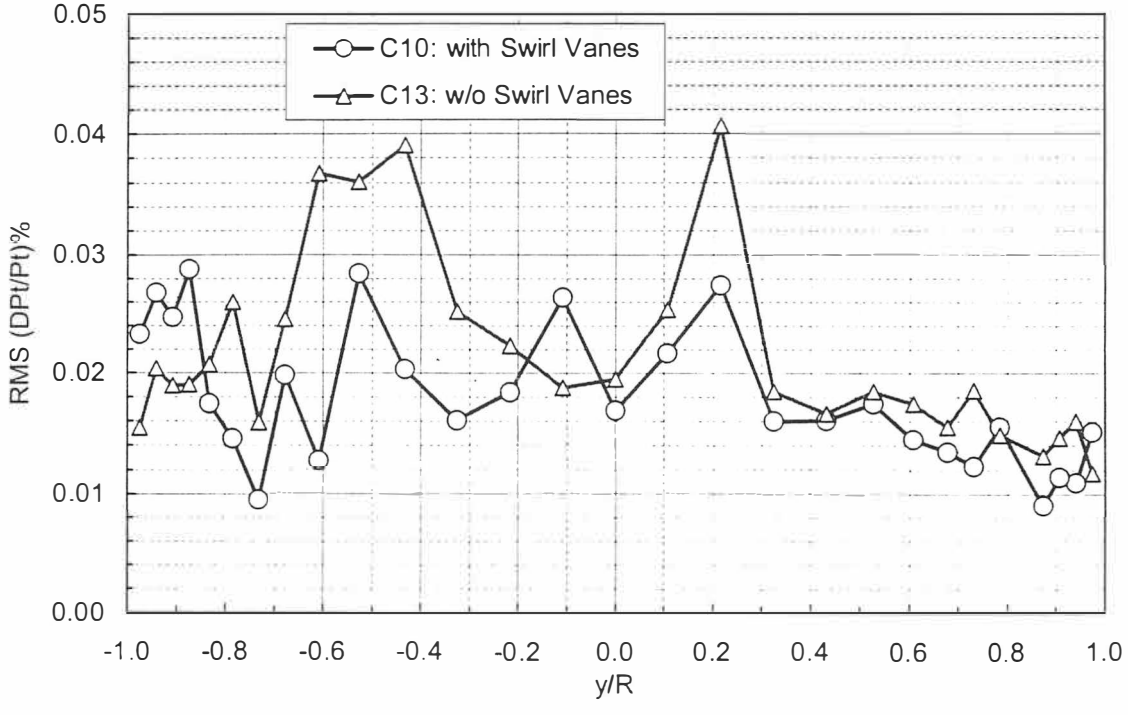


b) Temporal RMS Profiles

Figure C-8. Stilling Chamber Total Pressure & RMS Profiles, Corner 3 Installed: C05 (with swirl vanes) & C04 (without swirl vanes)



a) Total Pressure Profile



b) Temporal RMS Profiles

Figure C-9. Stilling Chamber Total Pressure & RMS Profiles, Corner 3 Removed: C10 (with swirl vanes) & C13 (without swirl vanes)

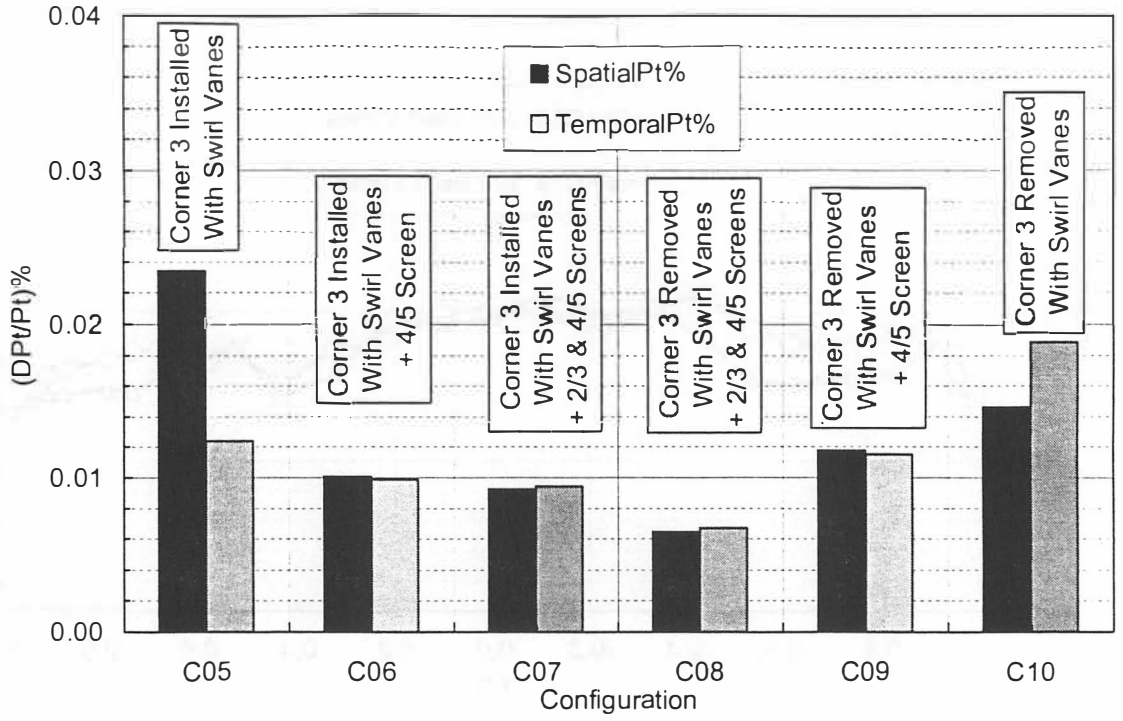
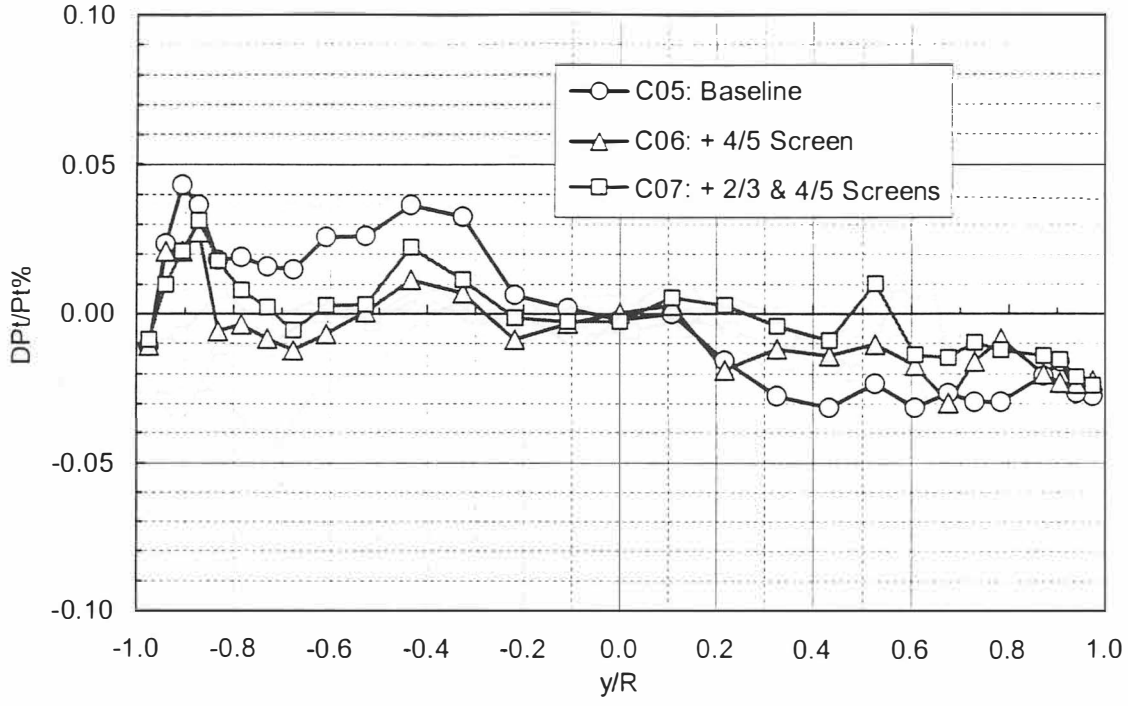
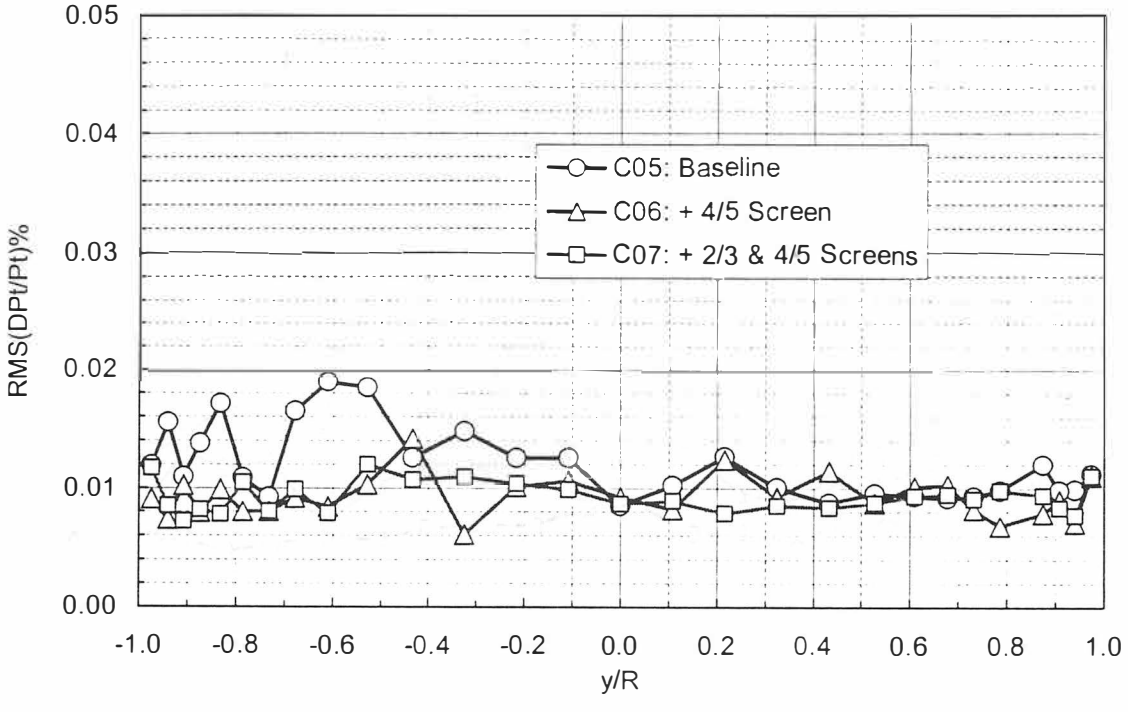


Figure C-10. Stilling Chamber Core Region Total Pressure Spatial Distribution and Temporal Fluctuation Effects of Intermediate Sreens.

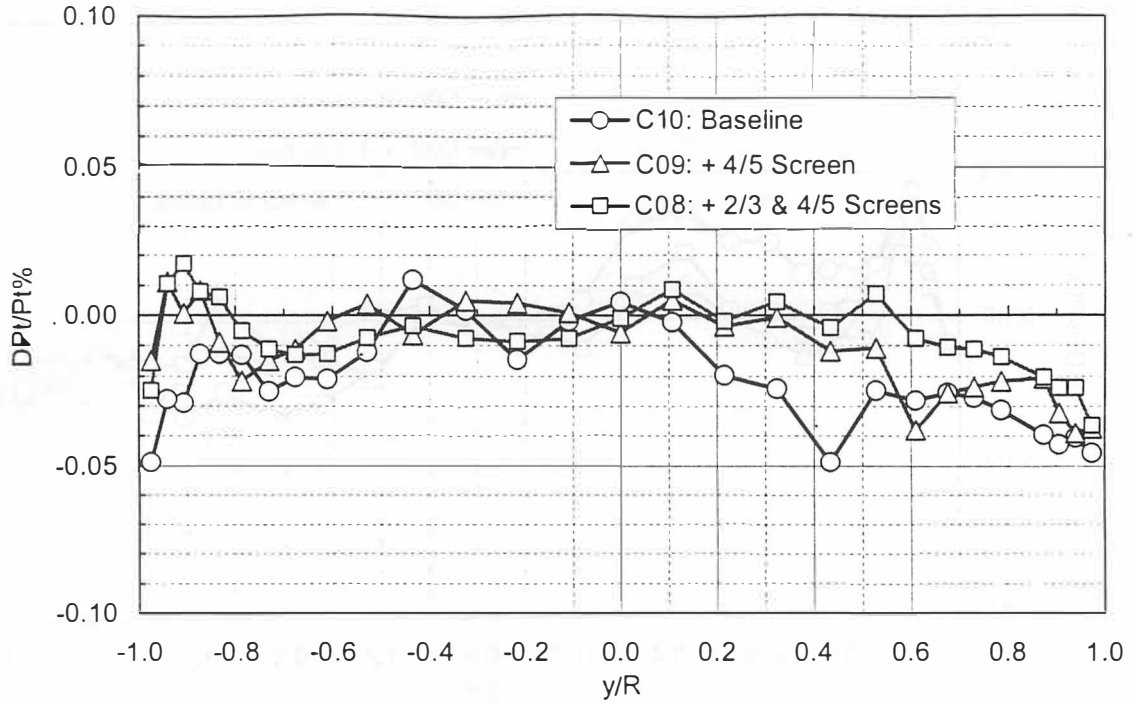


a) Total Pressure Profile

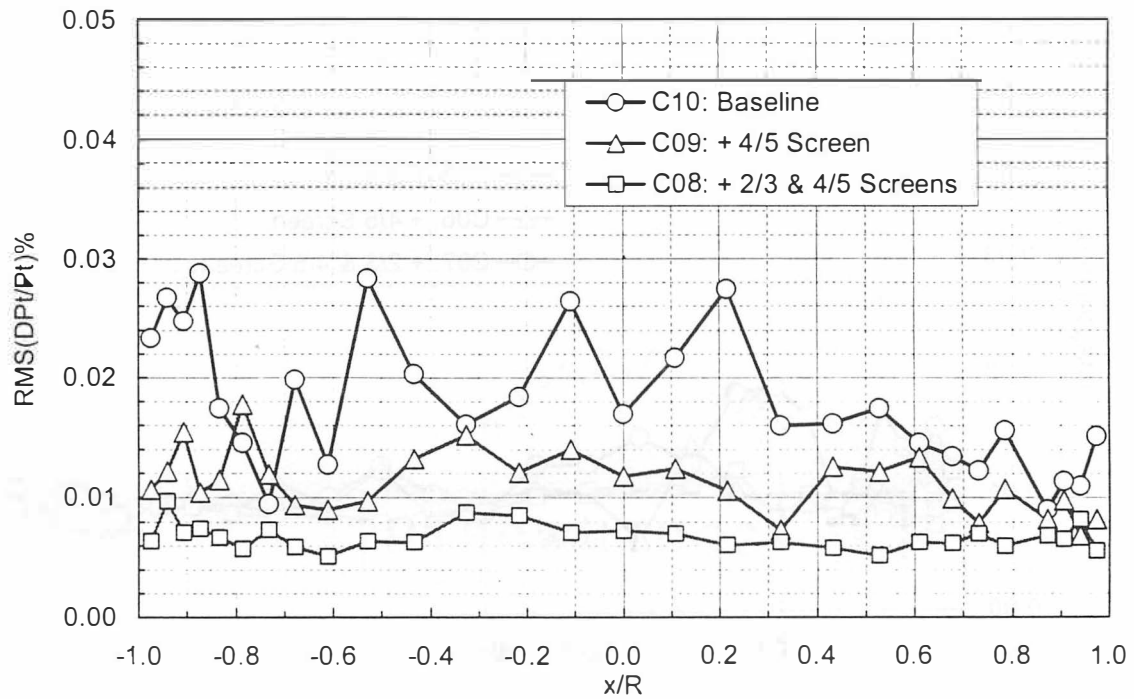


b) Temporal RMS Profiles

Figure C-11. Stilling Chamber Total Pressure & RMS Profiles, Corner 3 & Swirl Vanes Installed: C05 (baseline), C06 (with 4/5 screen), & C07 (with 4/5 & 2/3 screens)



a) Total Pressure Profile



b) Temporal RMS Profiles

Figure C-12. Stilling Chamber Total Pressure & RMS Profiles, Swirl Vanes Installed, Corner 3 Removed: C10 (baseline), C09 (with 4/5 screen), & C08 (with 4/5 & 2/3 screens)

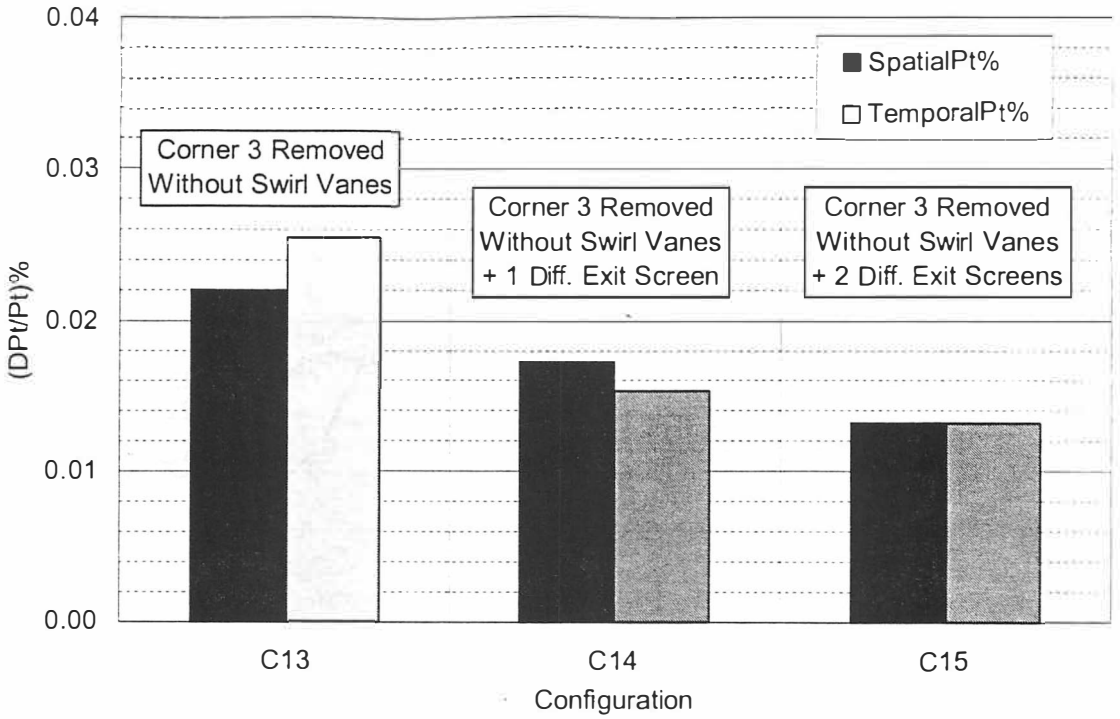
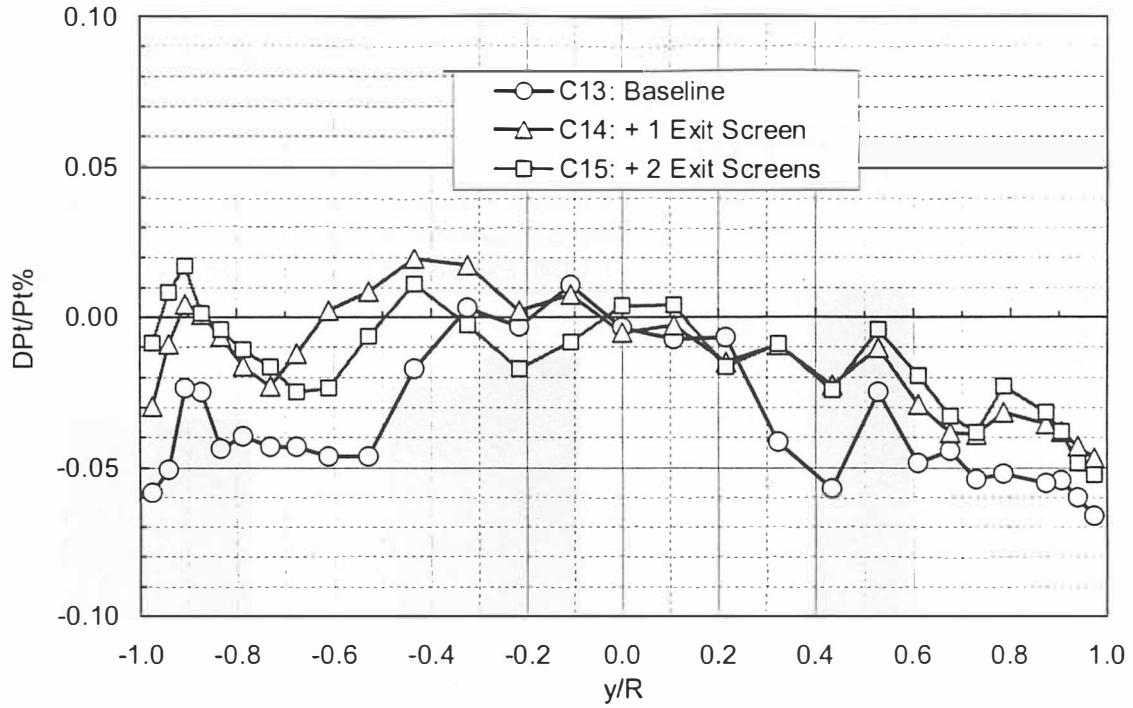
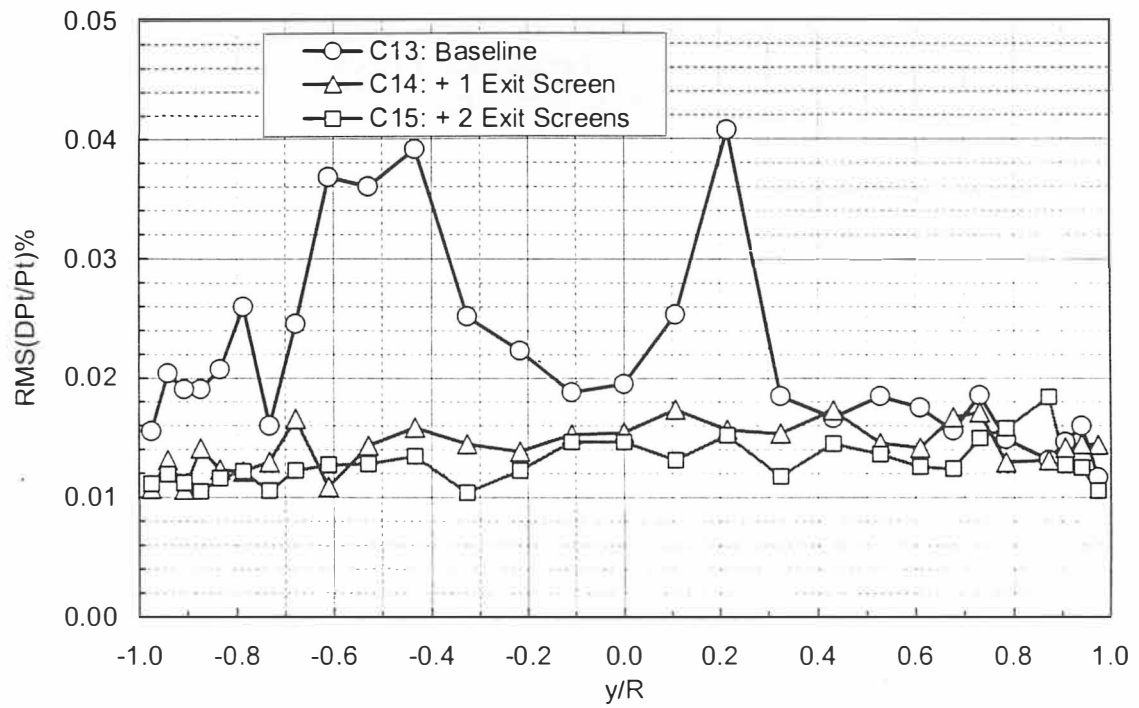


Figure C-13. Stilling Chamber Core Region Total Pressure Spatial Distribution and Temporal Fluctuation Effects of Exit Screens.

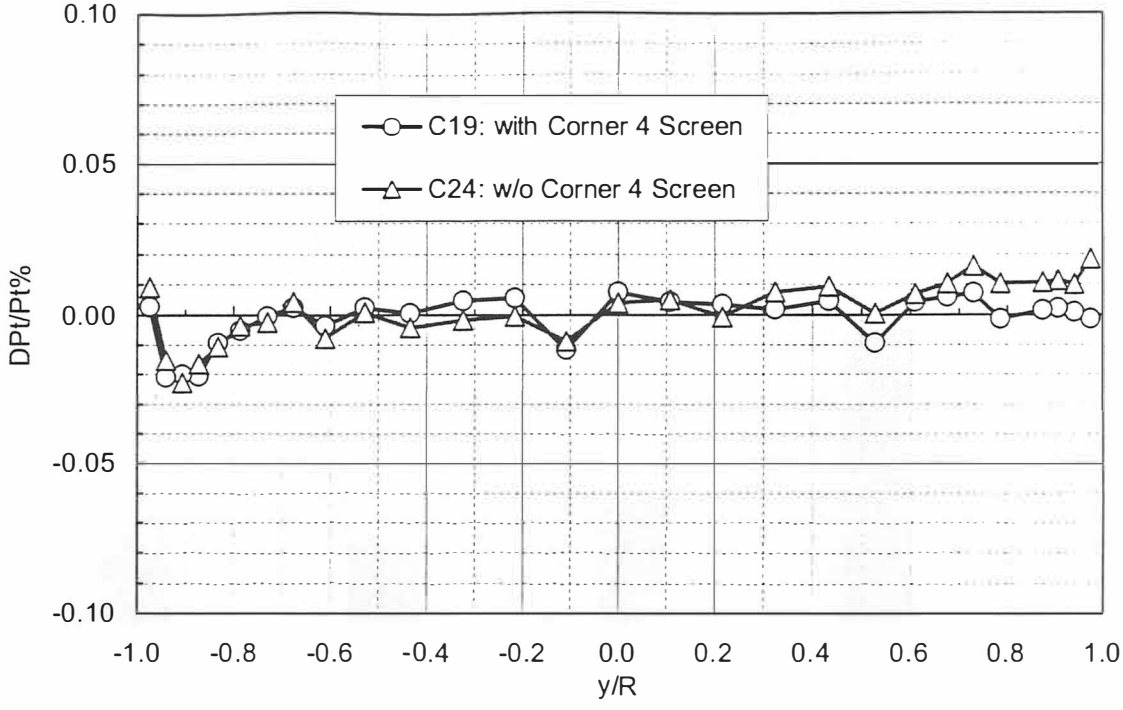


a) Total Pressure Profile

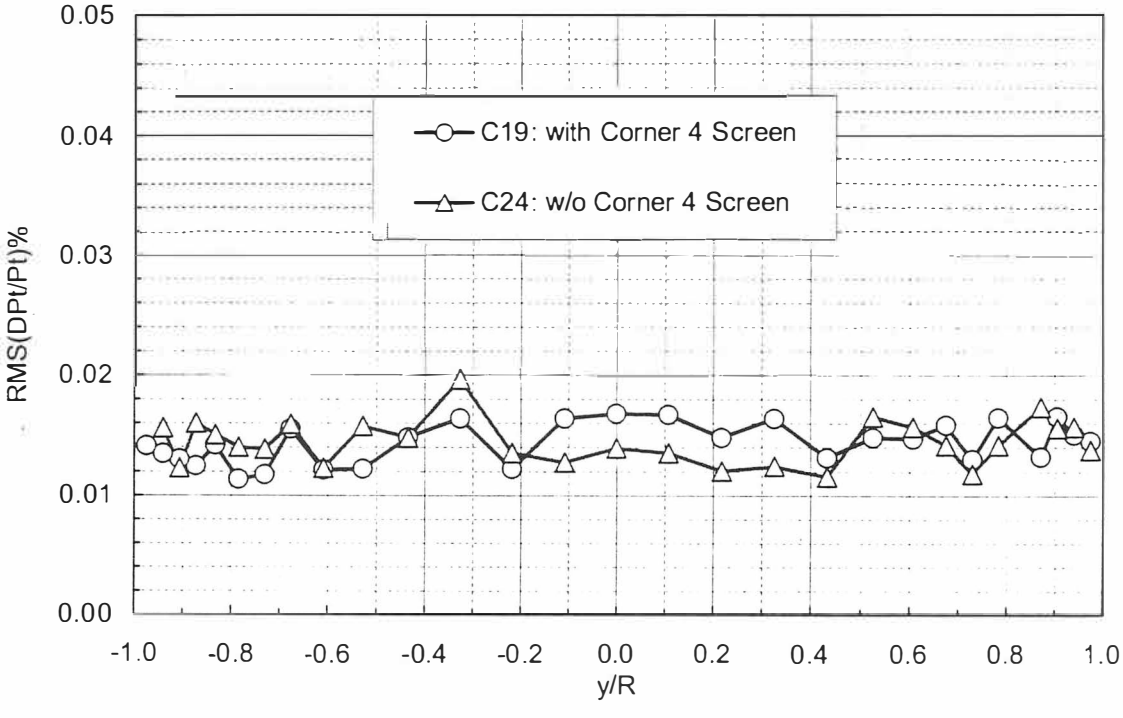


b) Temporal RMS Profiles

Figure C-14. Stilling Chamber Total Pressure & RMS Profiles, C13 (baseline), C14 (one exit screen), & C15 (two exit screens)



a) Total Pressure Profile



b) Temporal RMS Profiles

Figure C-15. Stilling Chamber Total Pressure & RMS Profiles, C19 (with C4 screen) & C24 (without C4 screen).

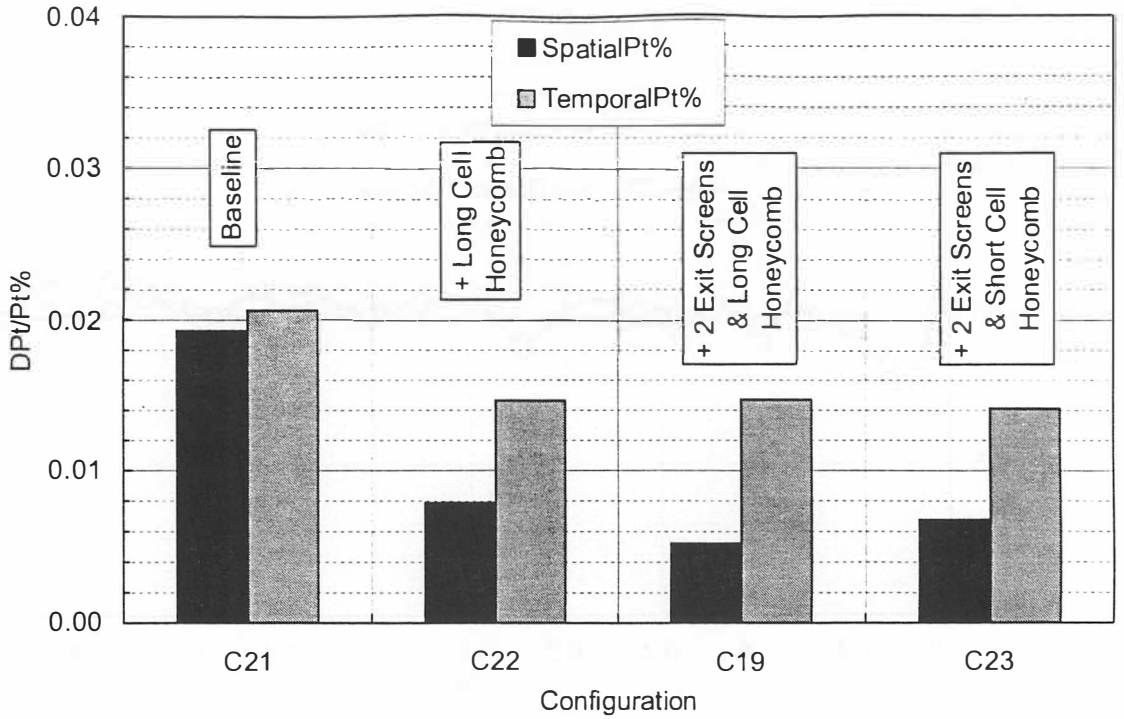
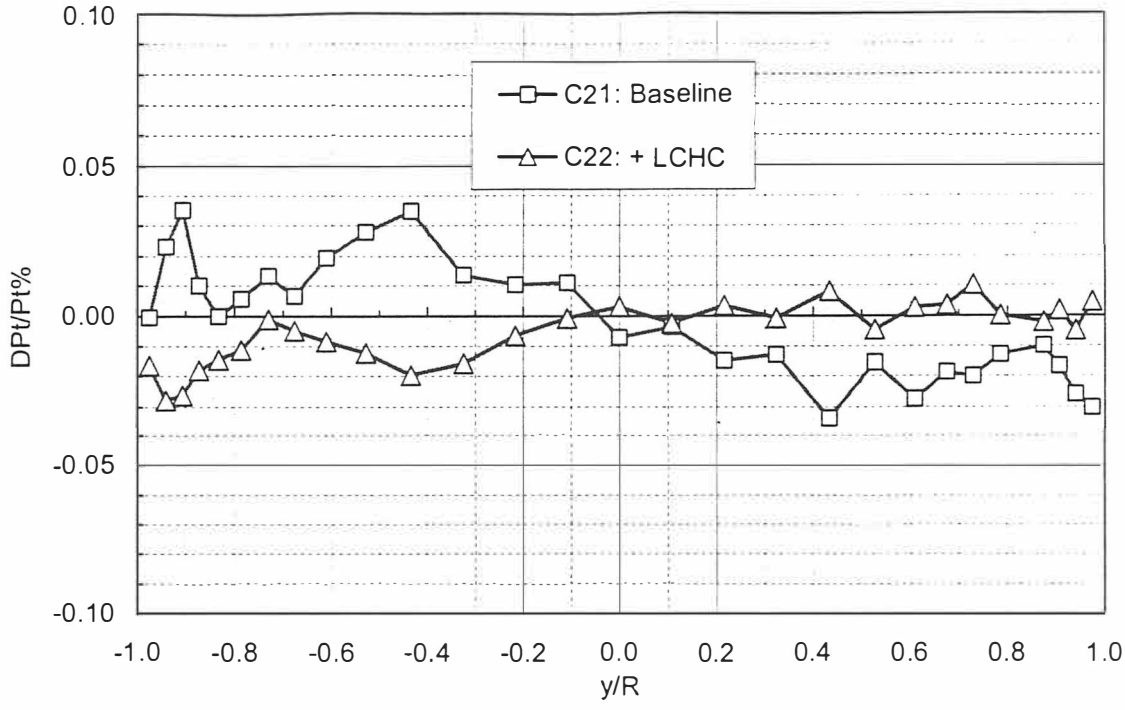
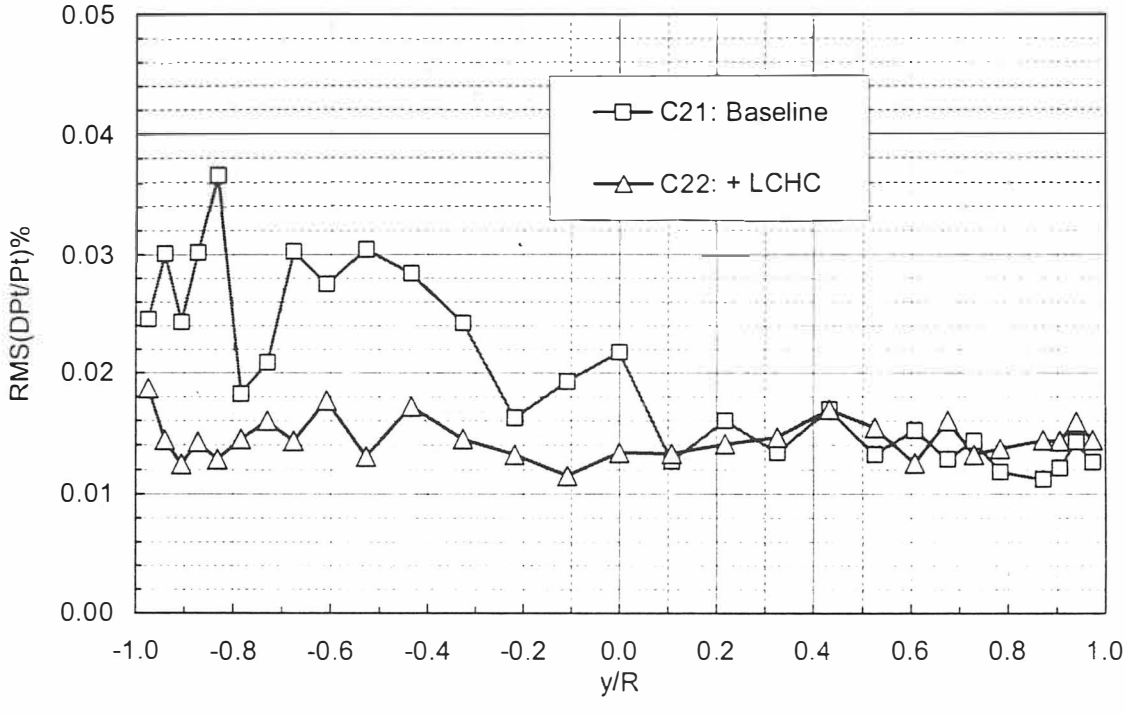


Figure C-16. Stilling Chamber Core Region Total Pressure Spatial Distribution and Temporal Fluctuation Effects of Honeycombs.

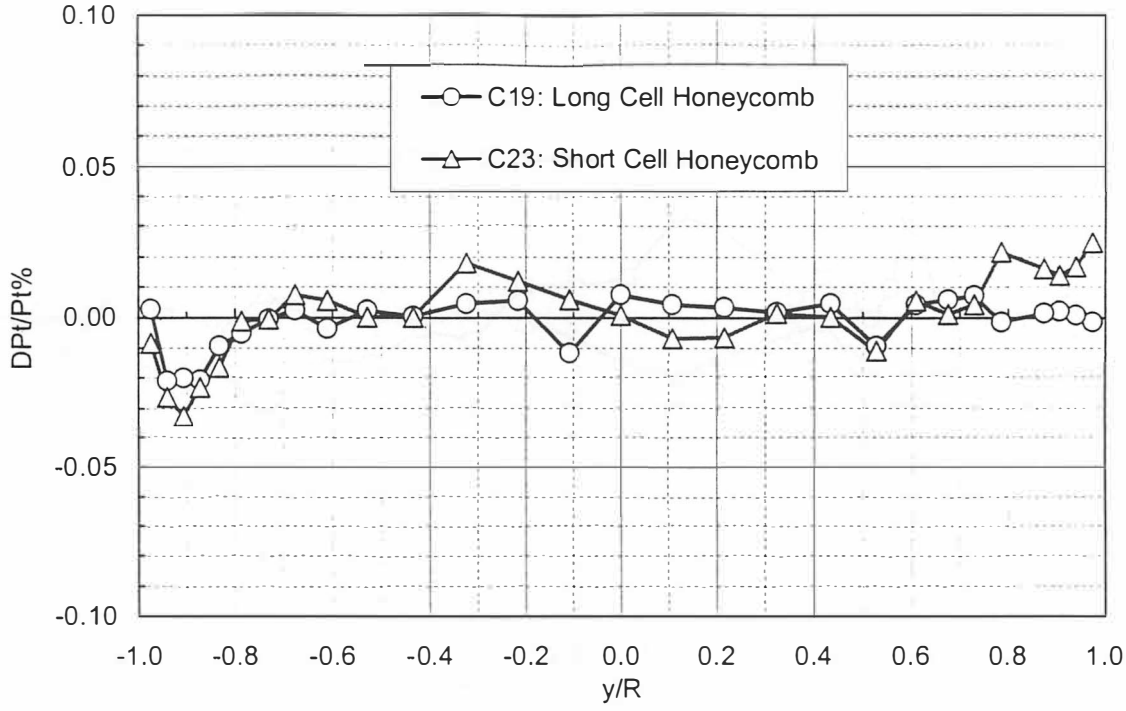


a) Total Pressure Profile

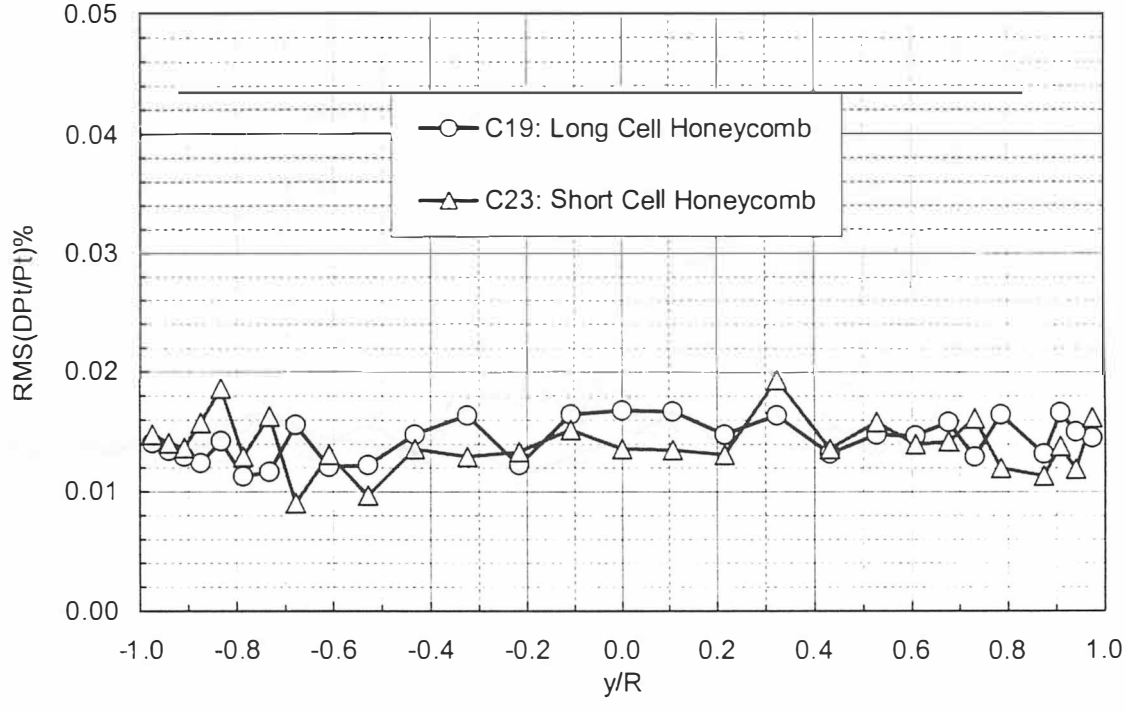


b) Temporal RMS Profiles

Figure C-17. Stilling Chamber Total Pressure & RMS Profiles, C21 (Baseline) & C22 (Long Cell Honeycomb).

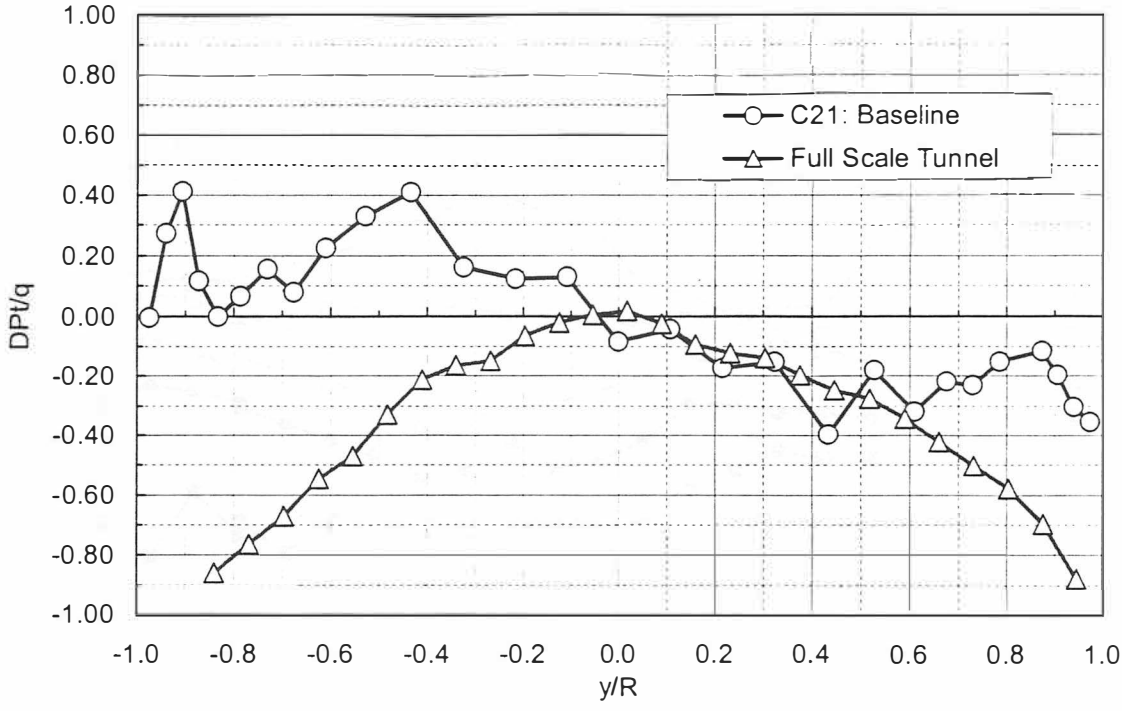


a) Total Pressure Profile



b) Temporal RMS Profiles

Figure C-18. Stilling Chamber Total Pressure & RMS Profiles, C19 (Long Cell Honeycomb) & C23 (Short Cell Honeycomb).



a) Total Pressure Profile



b) Velocity Profiles

Figure C-19. Stilling Chamber Total Pressure & Velocity Profiles, Baseline Configuration (C21) and Full Scale Tunnel

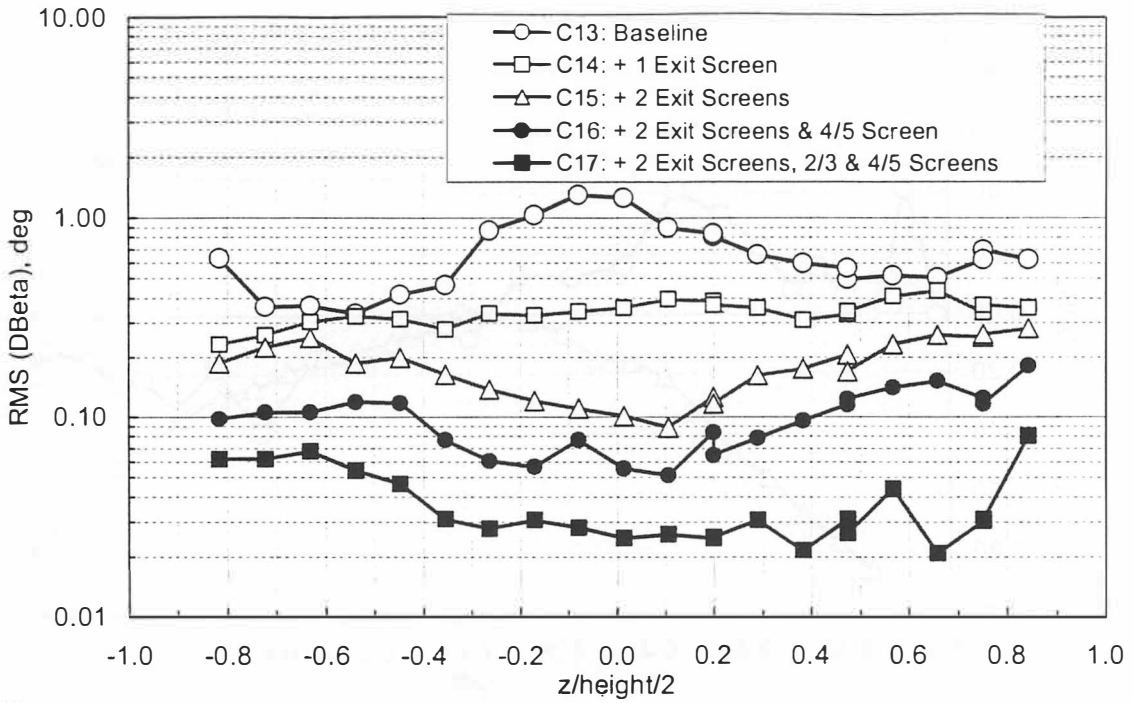


Figure C-20. Profiles of Yaw Angle Temporal Fluctuation, Corner 3 and Swirl Vanes Removed @ Y = -6 in., Configurations C13 to C17.

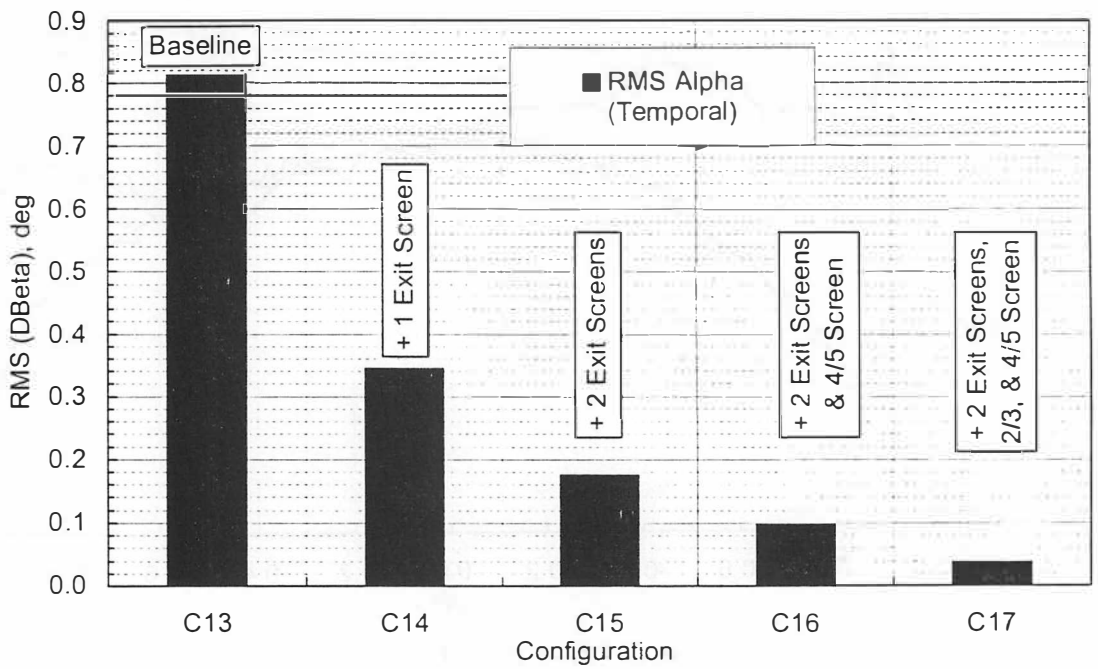


Figure C-21. Temporal Fluctuation in Core Region of Yaw Angle, Corner 3 and Swirl Vanes Removed @ Y = -6 in., Configurations C13 to C17

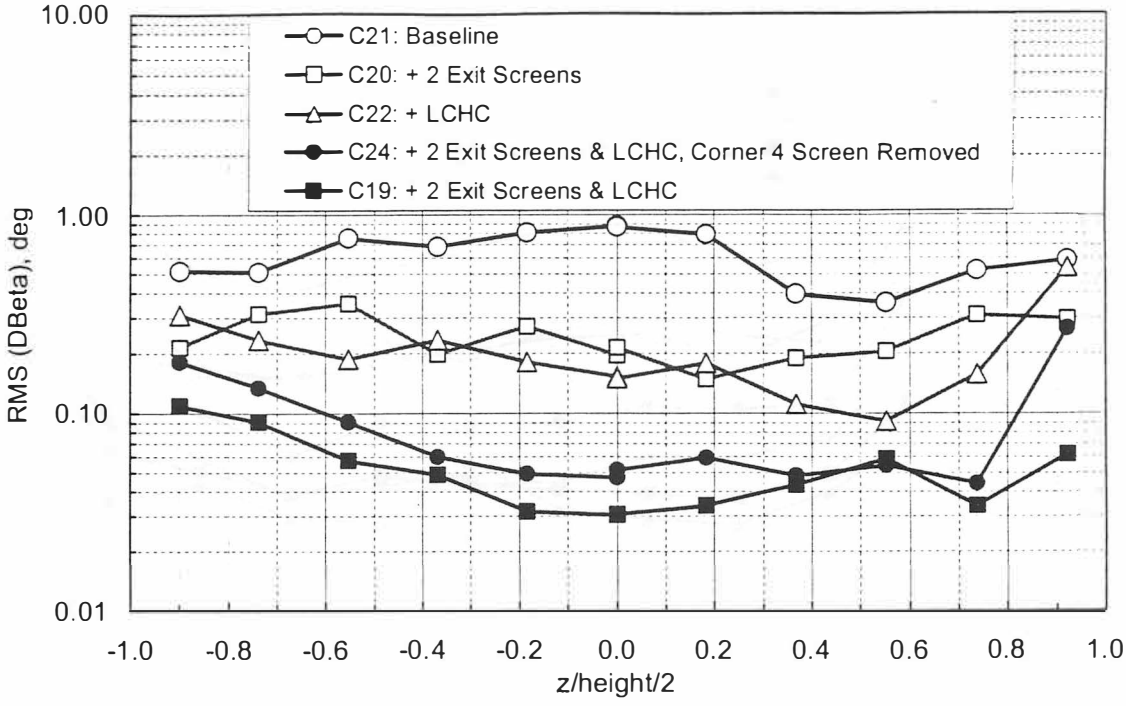


Figure C-22. Profiles of Yaw Angle Temporal Fluctuation, Corner 3 and Swirl Vanes Installed @ Y = -6 in., Configuration C19 to C22, and C24.

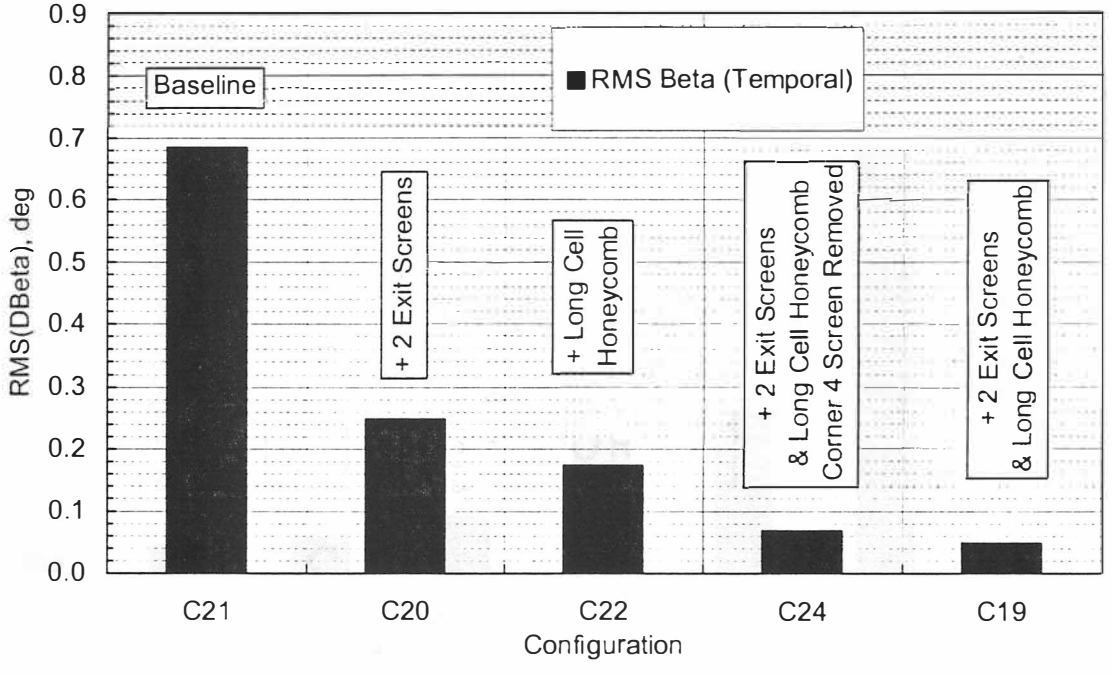


Figure C-23. Temporal Fluctuation in Core Region of Yaw Angle, Corner 3 and Swirl Vanes Installed @ Y = -6 in., Configurations C19 to C22, and C24.

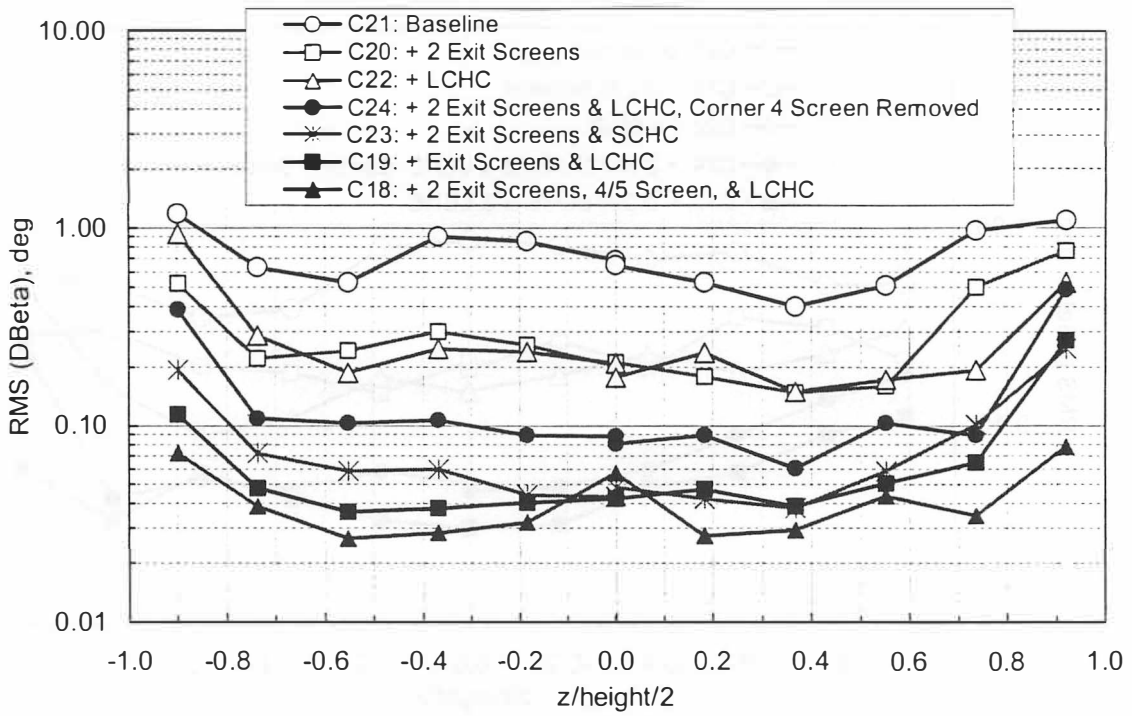


Figure C-24. Profiles of Yaw Angle Temporal Fluctuation, Corner 3 and Swirl Vanes Installed @ Y = 0 in., Configurations C18 to C24.

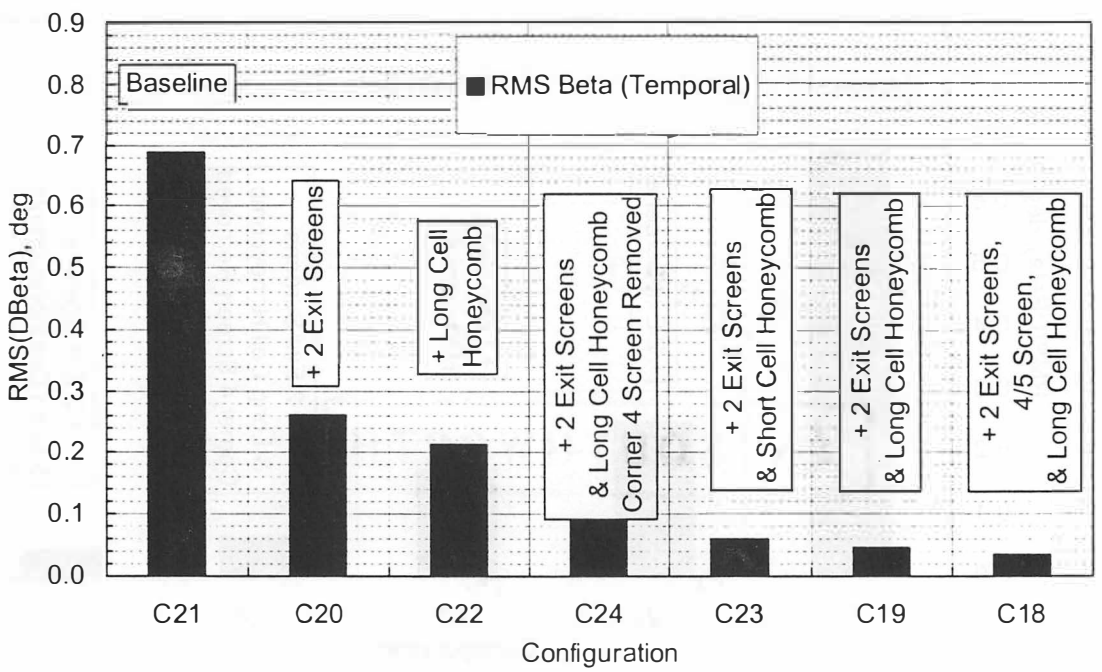


Figure C-25. Temporal Fluctuation in Core Region of Yaw Angle, Corner 3 and Swirl Vanes Installed @ Y = 0 in., Configurations C18 to C24.

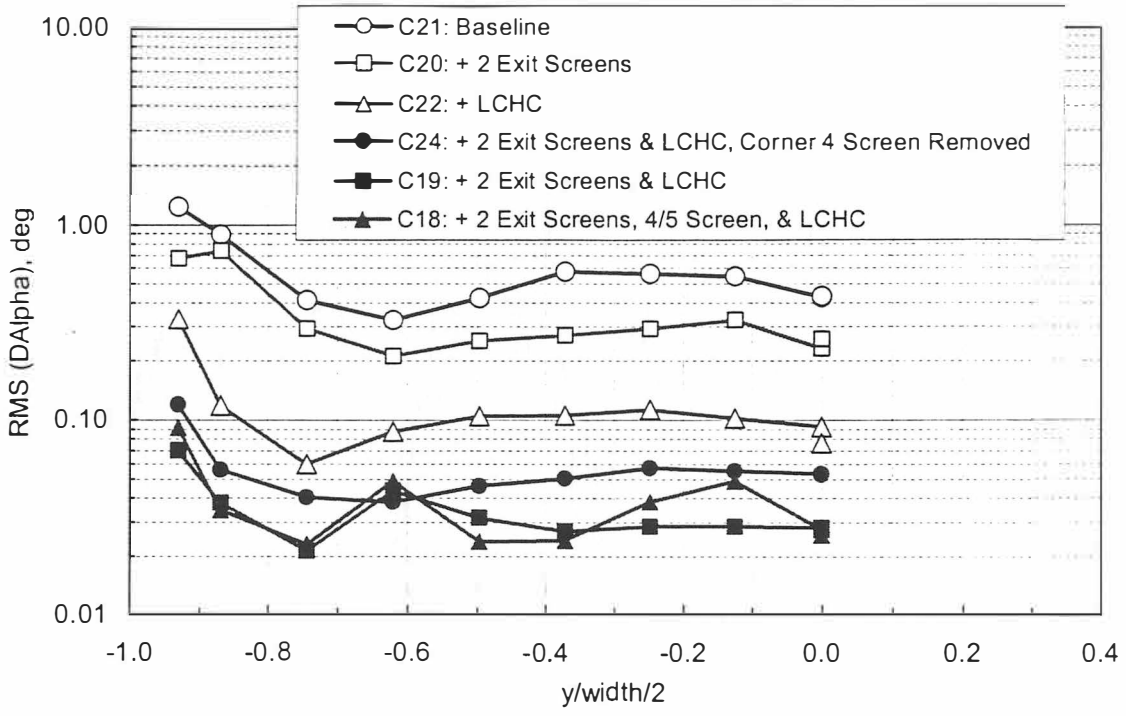


Figure C-26. Profiles of Pitch Angle Temporal Fluctuation, Corner 3 and Swirl Vanes Installed @ Z = 0 in., Configurations C18 to C22, and C24.

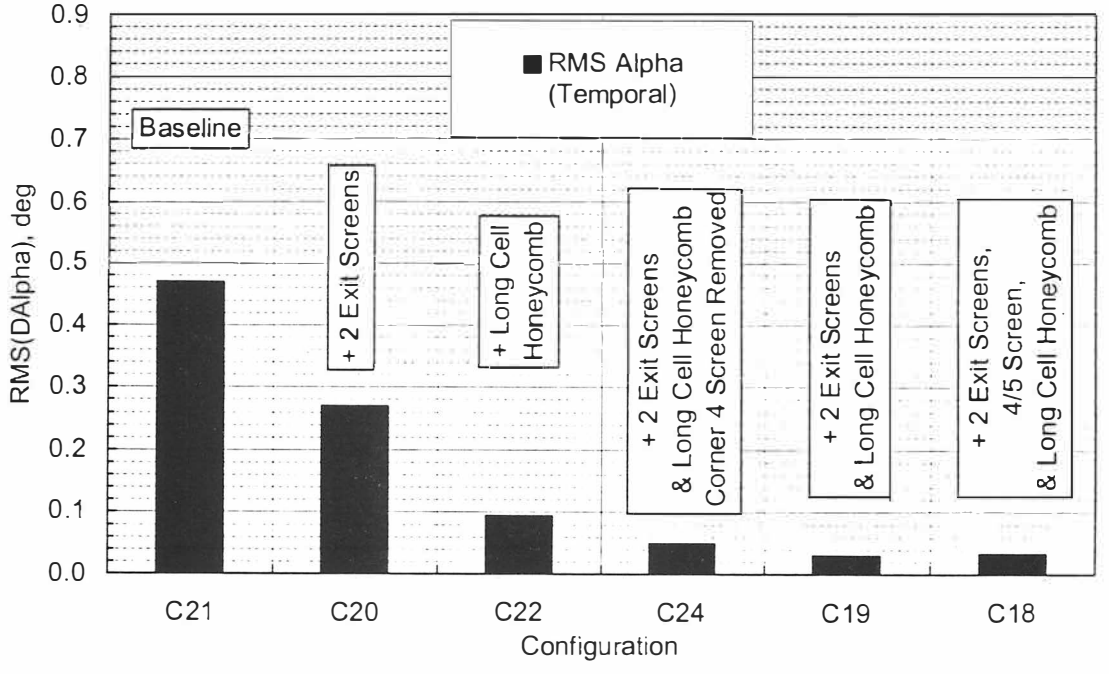
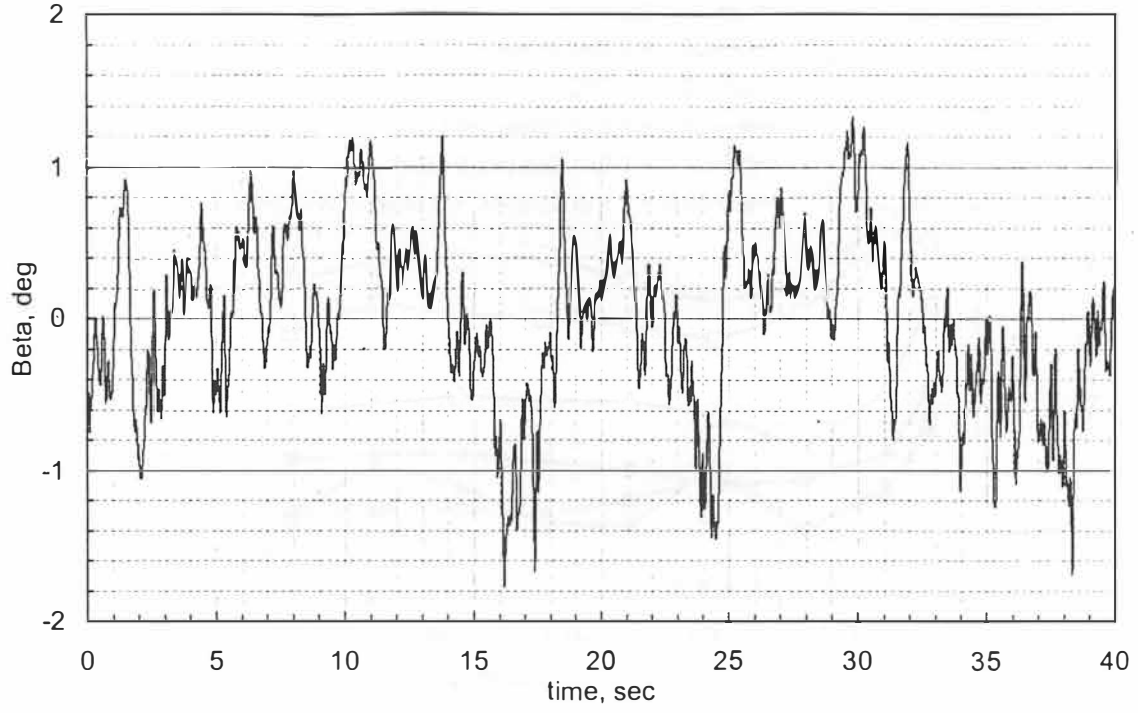
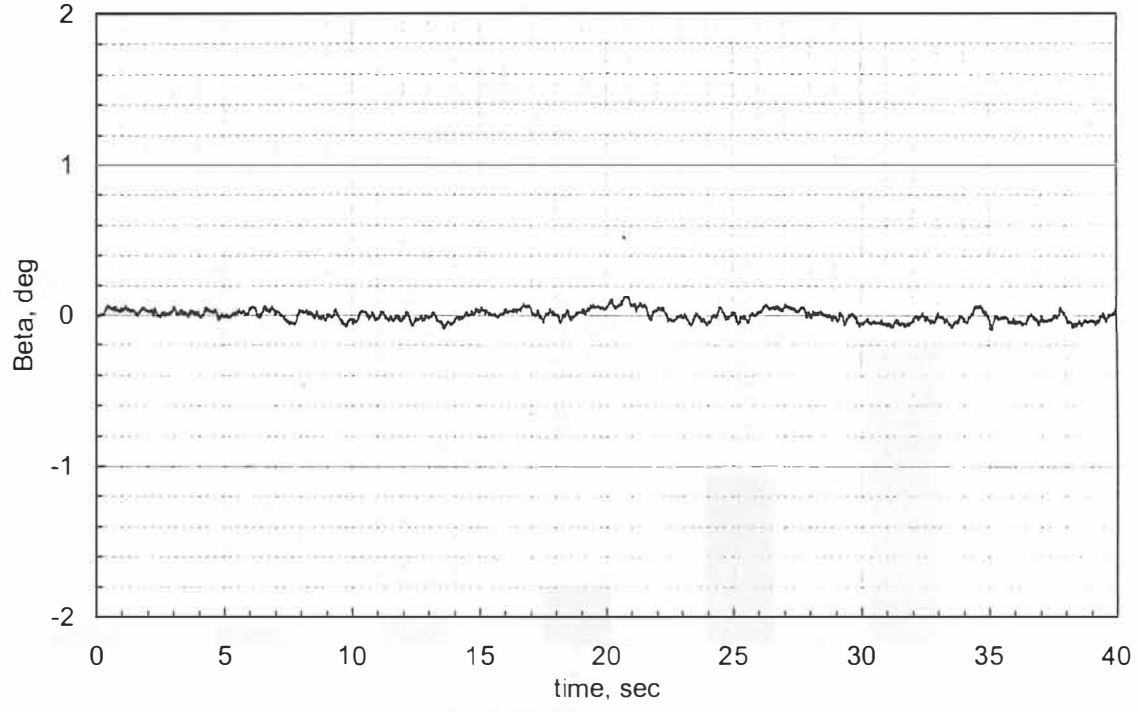


Figure C-27. Temporal Fluctuation in Core Region of Pitch Angle, Corner 3 and Swirl Vanes Installed @ Z = 0 in., Configurations C18 to C22, and C24



a) Configuration C21, RMS(Beta) = 0.69 deg



b) Configuration C19, RMS(Beta) = 0.046 deg

Figure C-28. Flow Angularity Probe Yaw Angle Time Trace at Test Section Center, Configurations C21 and C19.

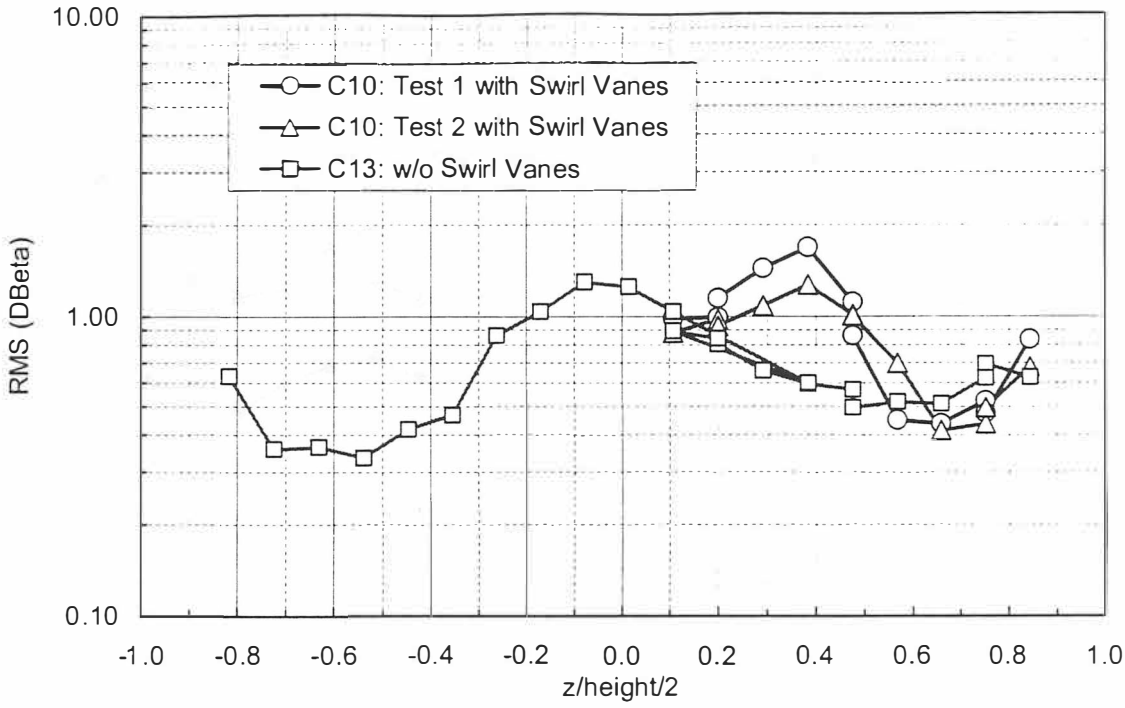


Figure C-29. Yaw Angle Fluctuation Profiles, With (C10) and Without (C13) Swirl Vanes; Corner 3 Removed.

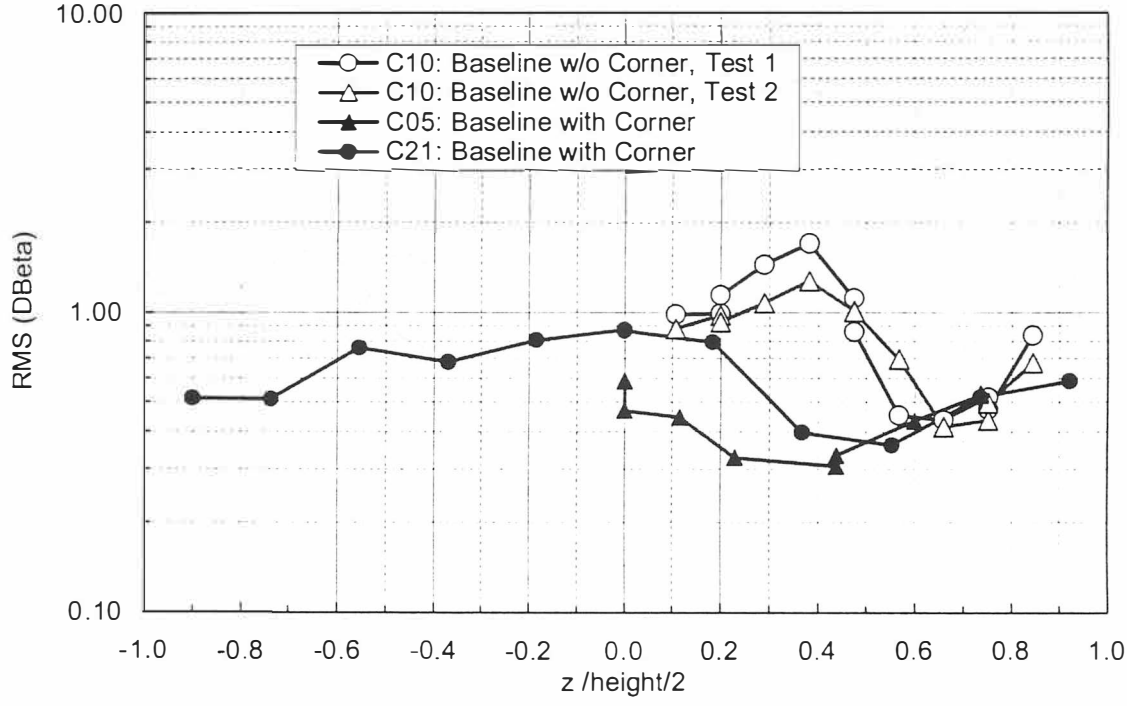


Figure C-30. Yaw Angle Fluctuation Profiles, Baseline Configuration With (C05,C21) and Without (C10) Corner 3.

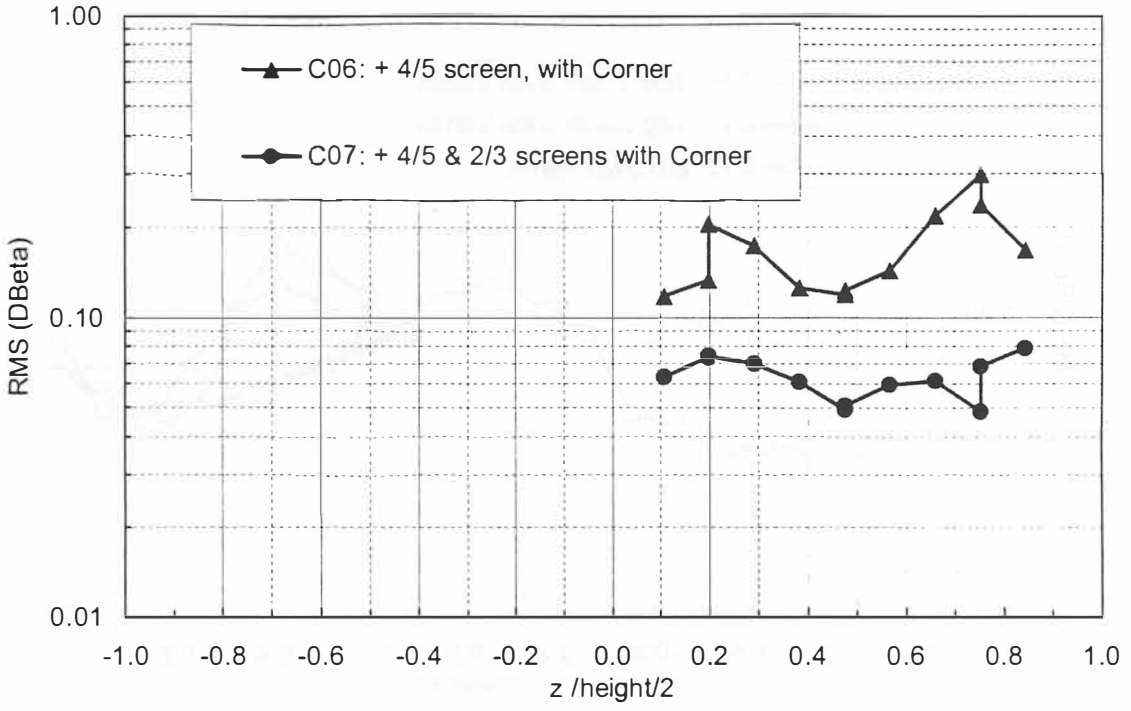


Figure C-31. Yaw Angle Fluctuation Profiles, With (C08) and Without (C09) 2/3 Screen; Corner 3 Installed.

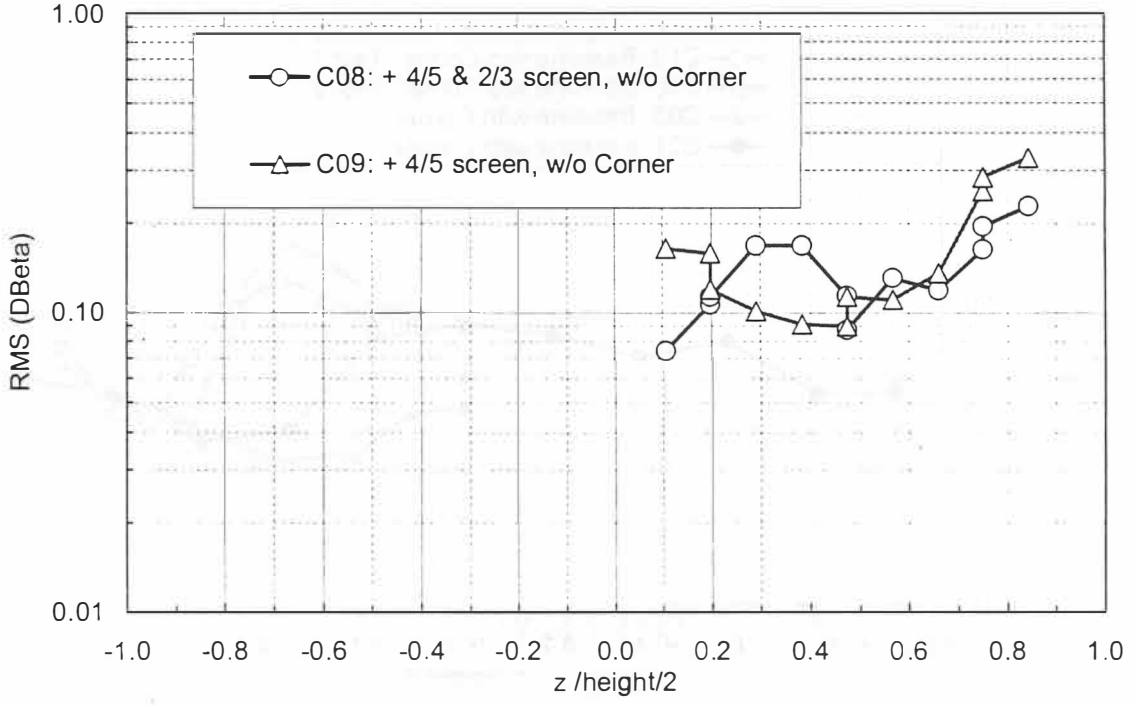
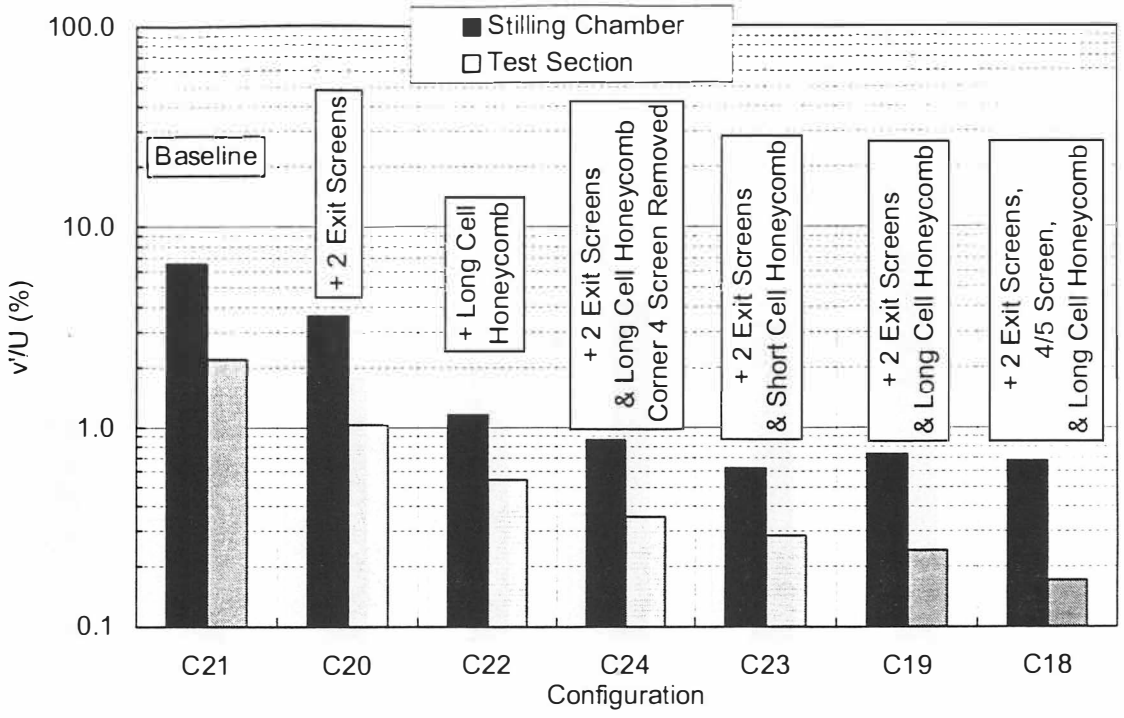
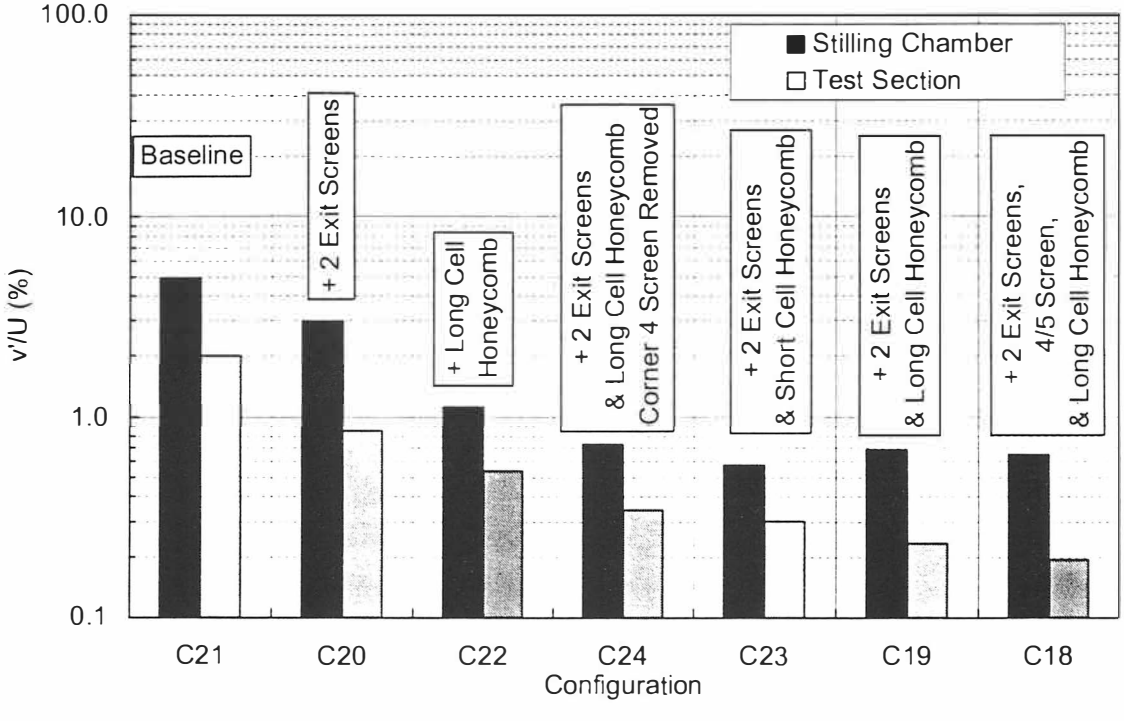


Figure C-32. Yaw Angle Fluctuation Profiles, With (C07) and Without (C06) 2/3 Screen; Corner 3 Removed.



a) Pitch Plane



b) Yaw Plane

Figure C-33. Hot Wire Anemometer Lateral Turbulence Intensities of Core Region for Stilling Chamber and Test Section.

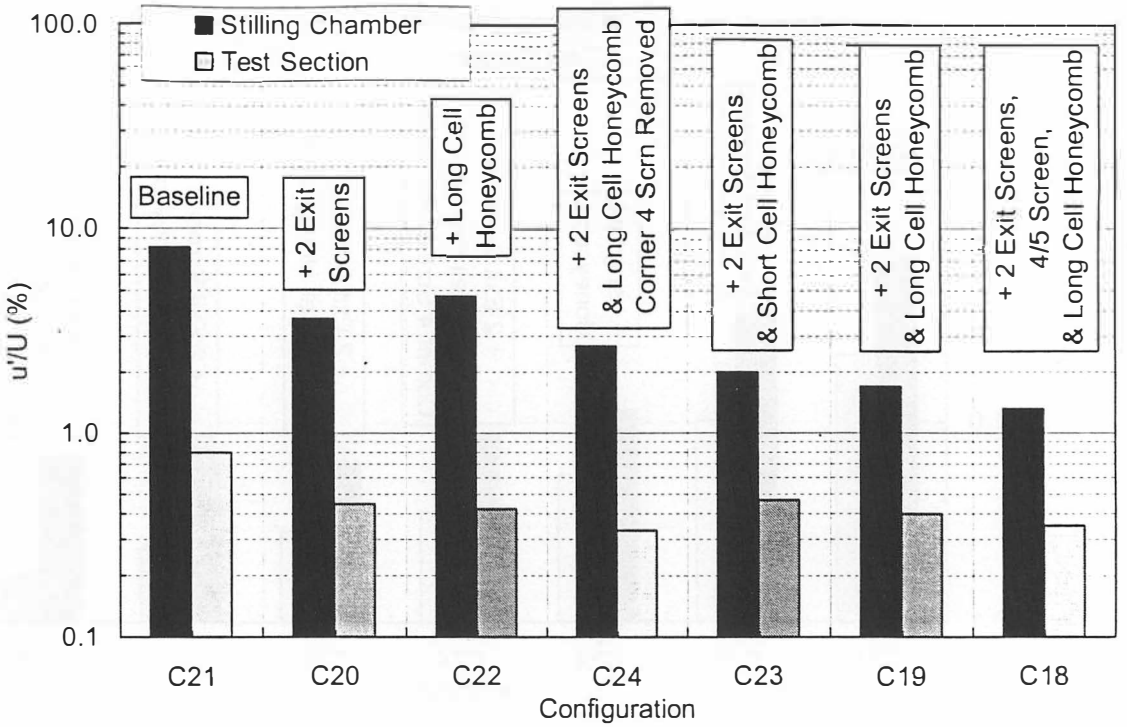
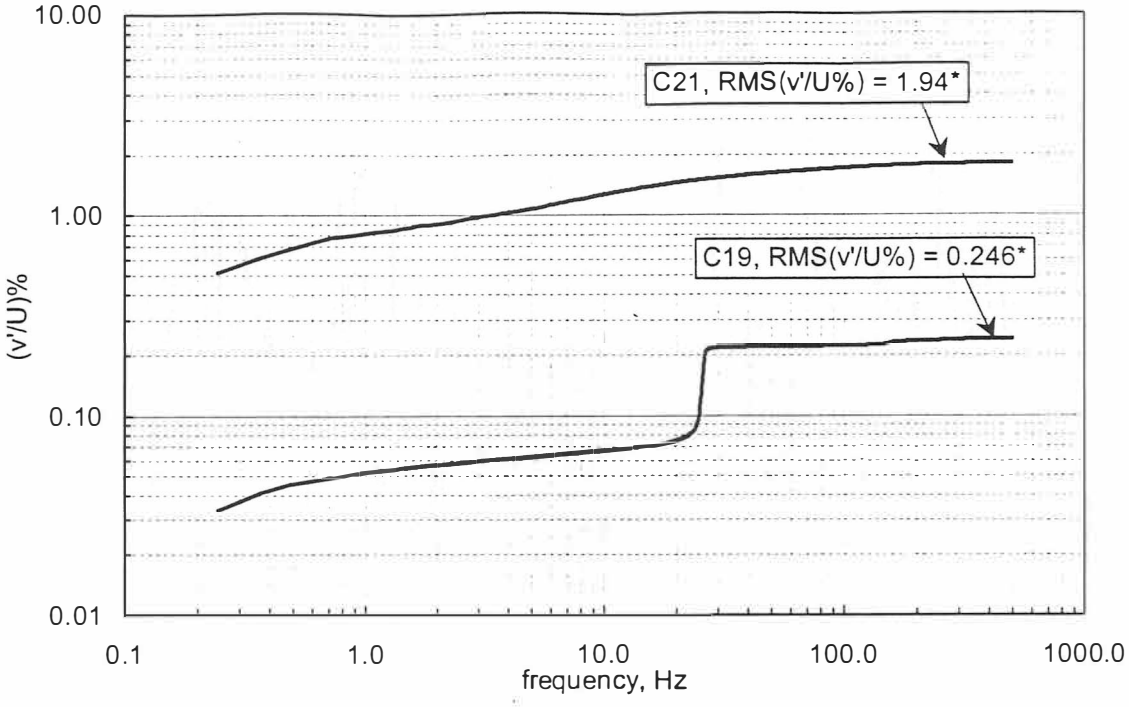
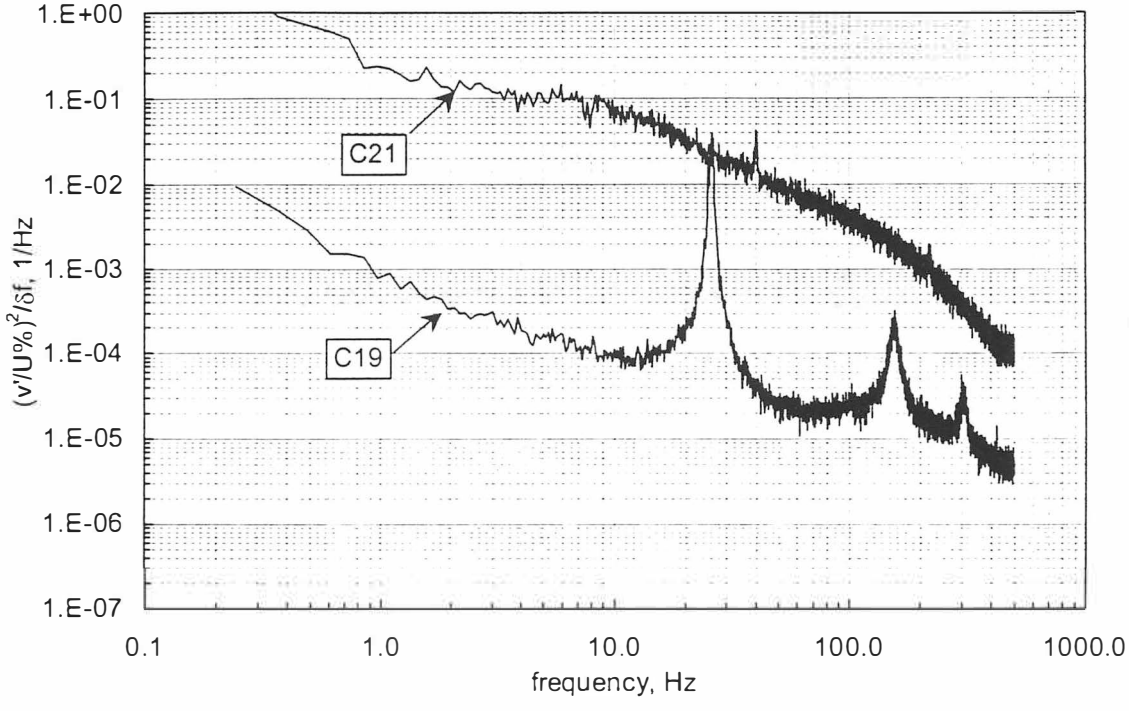


Figure C-34. Hot Wire Anemometer Axial Turbulence Intensities of Core Region for Stilling Chamber and Test Section.

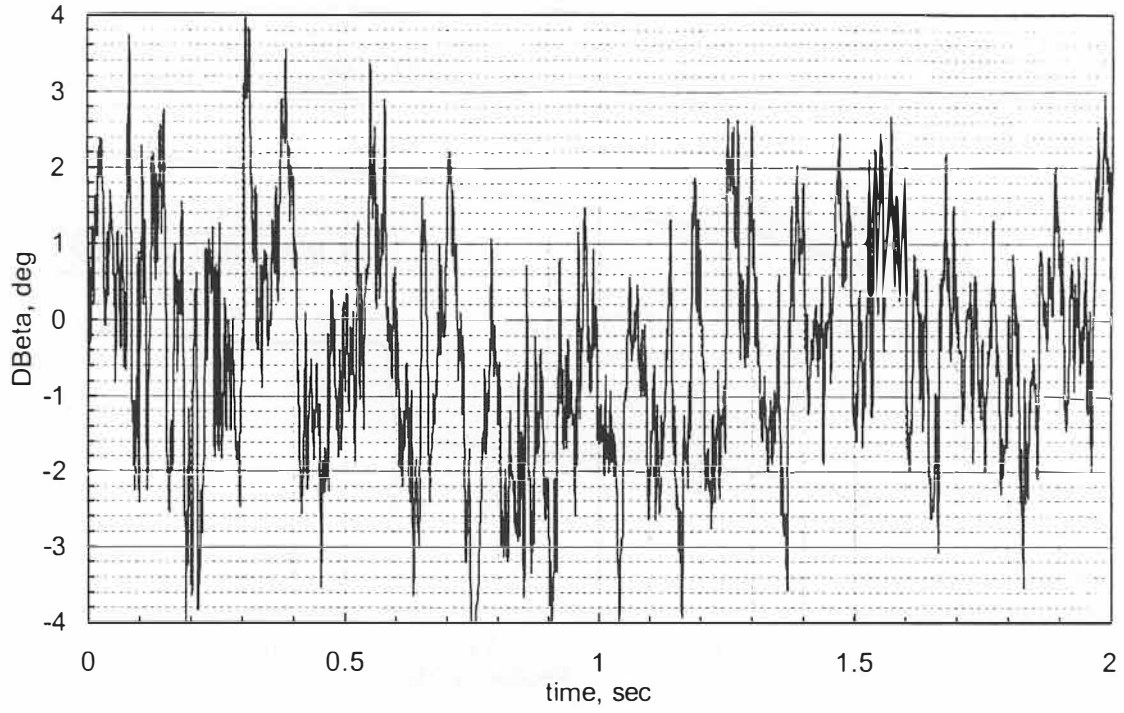


a) Cumulative Turbulence Intensity, * - Actual Variance of Timewise Signal

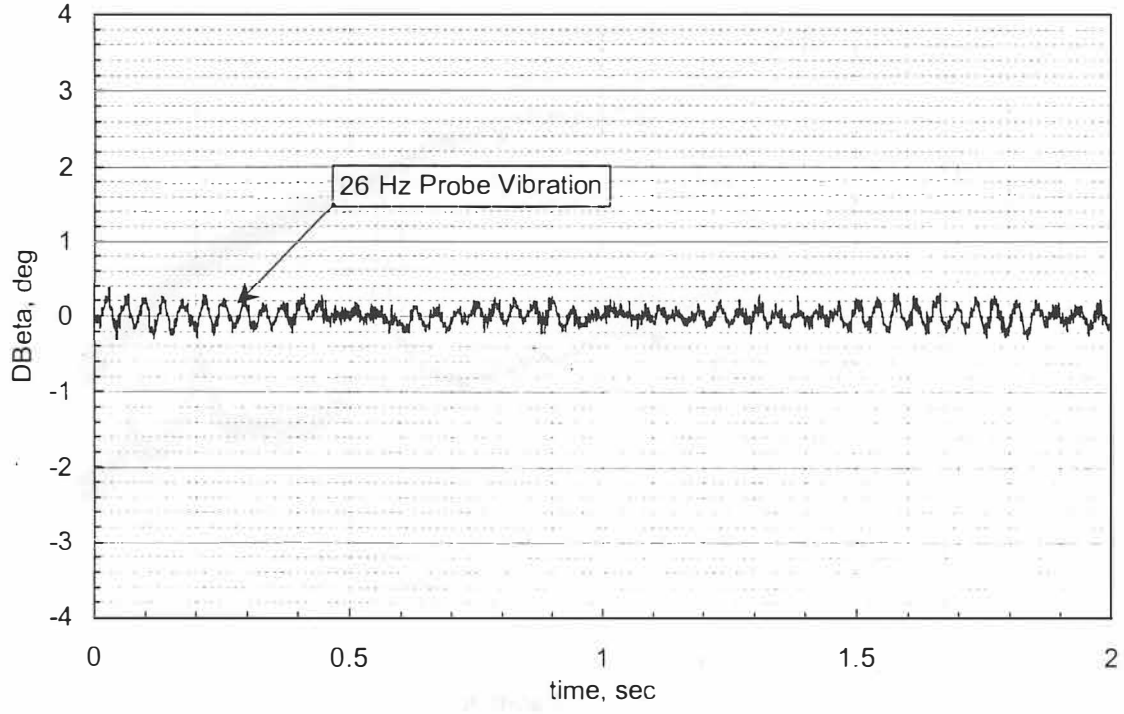


b) Power Spectral Density, df = 0.12 Hz.

Figure C-35. Hot Wire Anemometer Spectral Density, v'/U (yaw) at Test Section Center, Configurations C19 and C21.

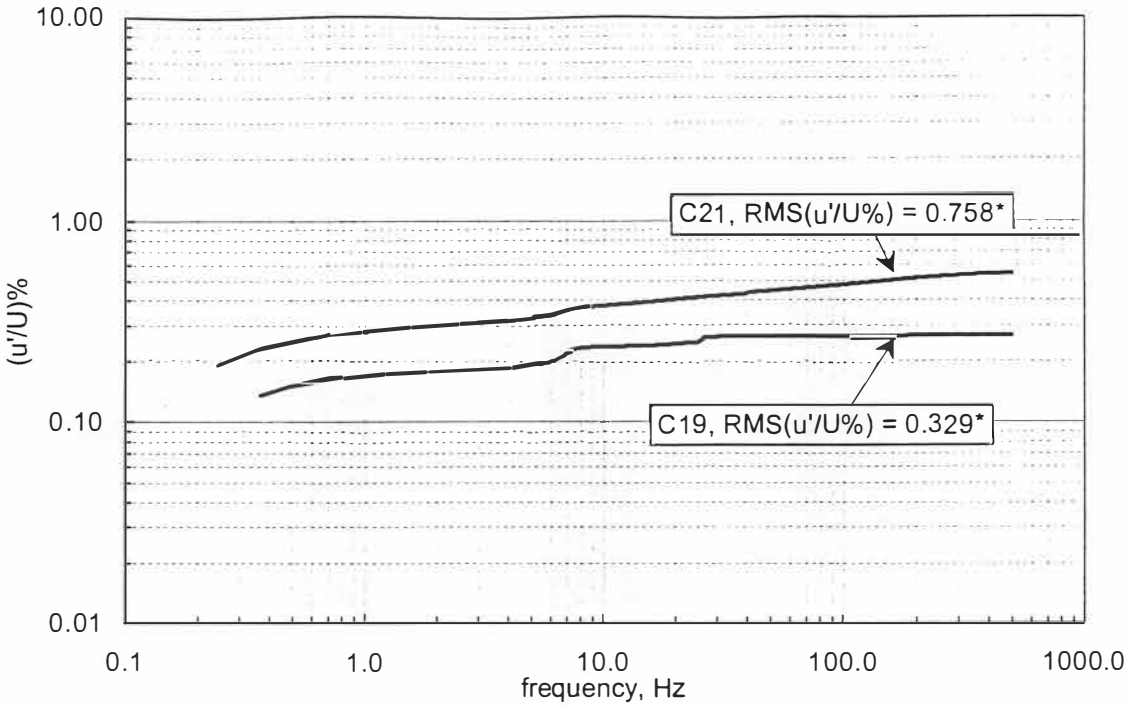


a) Configuration C21, RMS(DBeta) = 1.46 deg

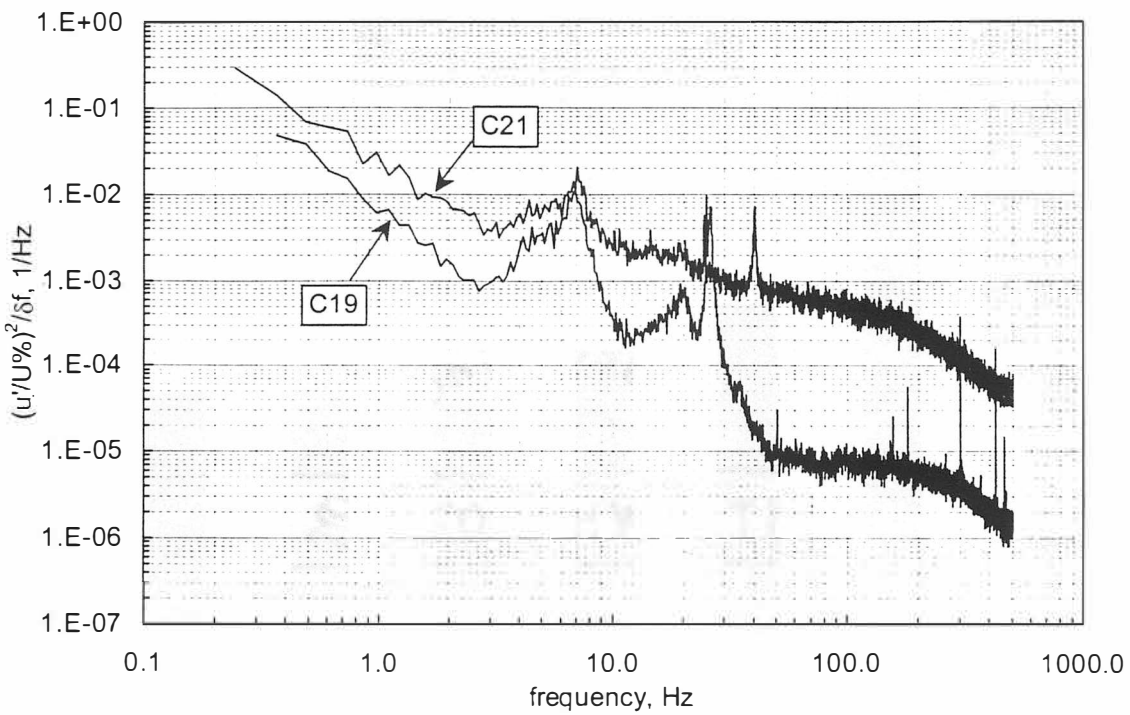


b) Configuration C19, RMS(DBeta) = 0.12 deg

Figure C-36. Hot Wire Anemometer Yaw Angle Time Trace at Test Section Center, Configurations C21 and C19.



a) Cumulative Turbulence Intensity, * - Actual Variance of Timewise Signal



b) Power Spectral Density, df = 0.12 Hz.

Figure C-37. Hot Wire Anemometer Spectral Density, u'/U at Test Section Center, Configurations C19 and C21.

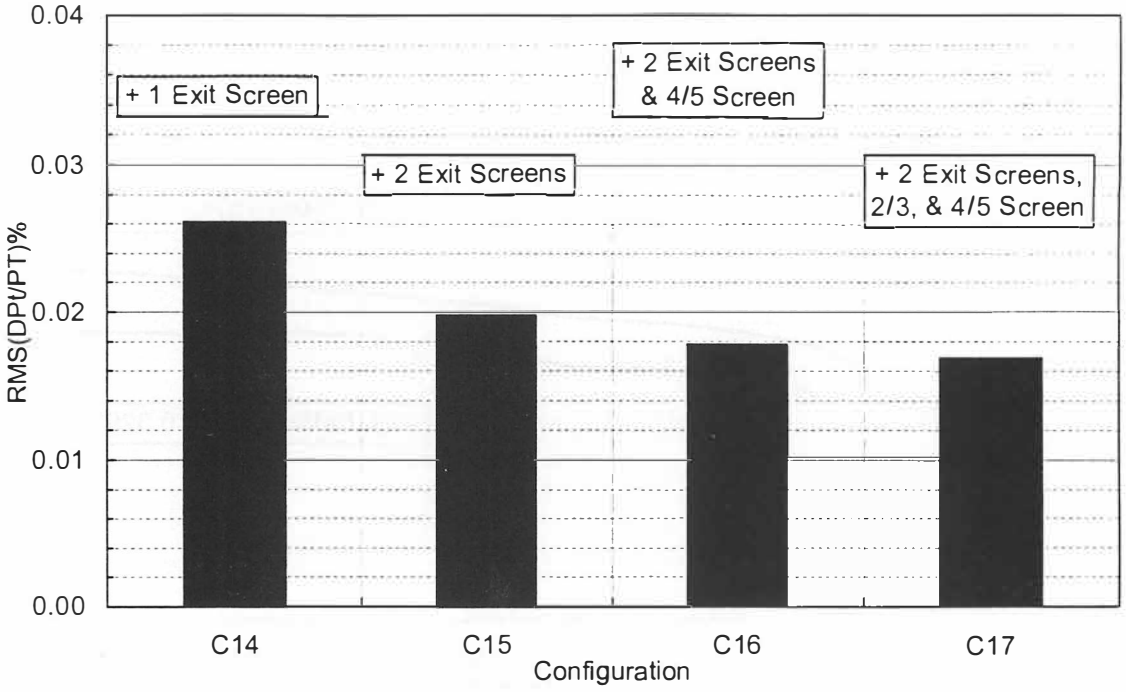


Figure C-38. Temporal High Response Total Pressure Fluctuation in Core Region, Corner 3 and Swirl Vanes Removed.

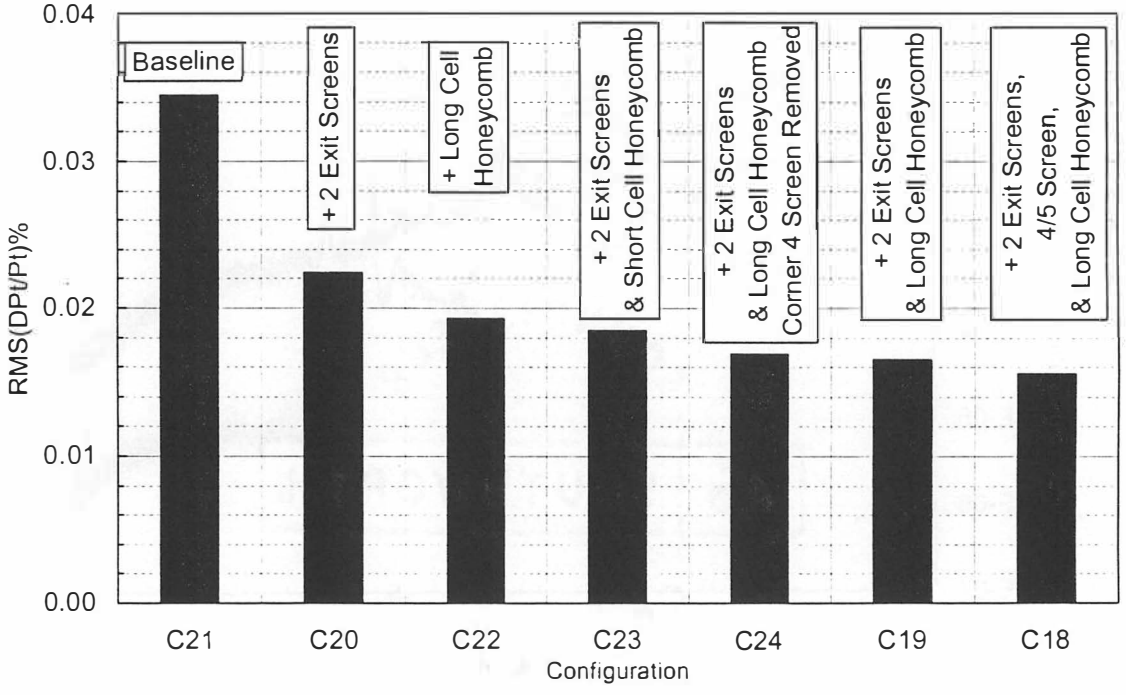
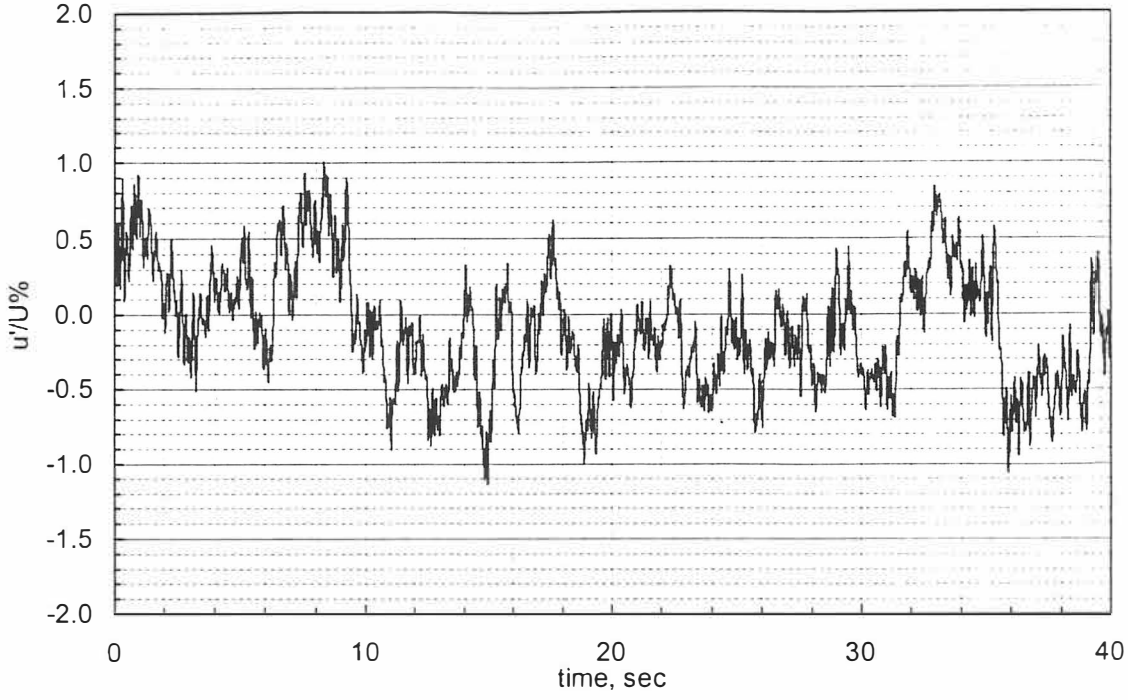
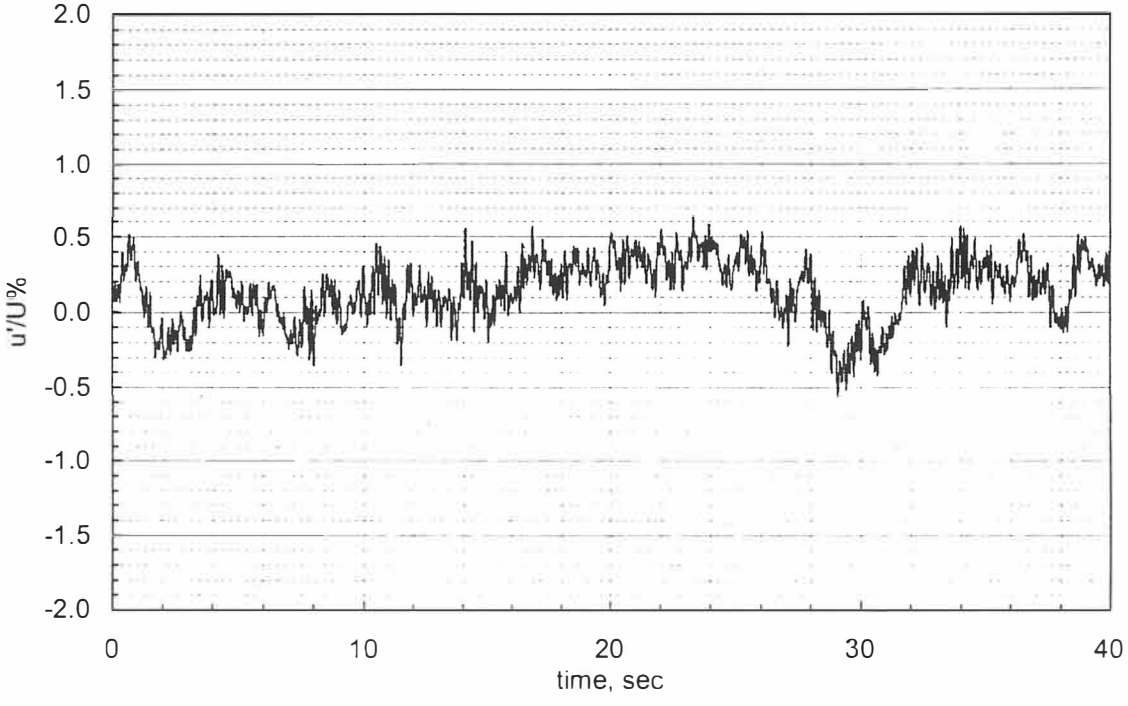


Figure C-39. Temporal High Response Total Pressure Fluctuation in Core Region, Corner 3 and Swirl Vanes Installed.

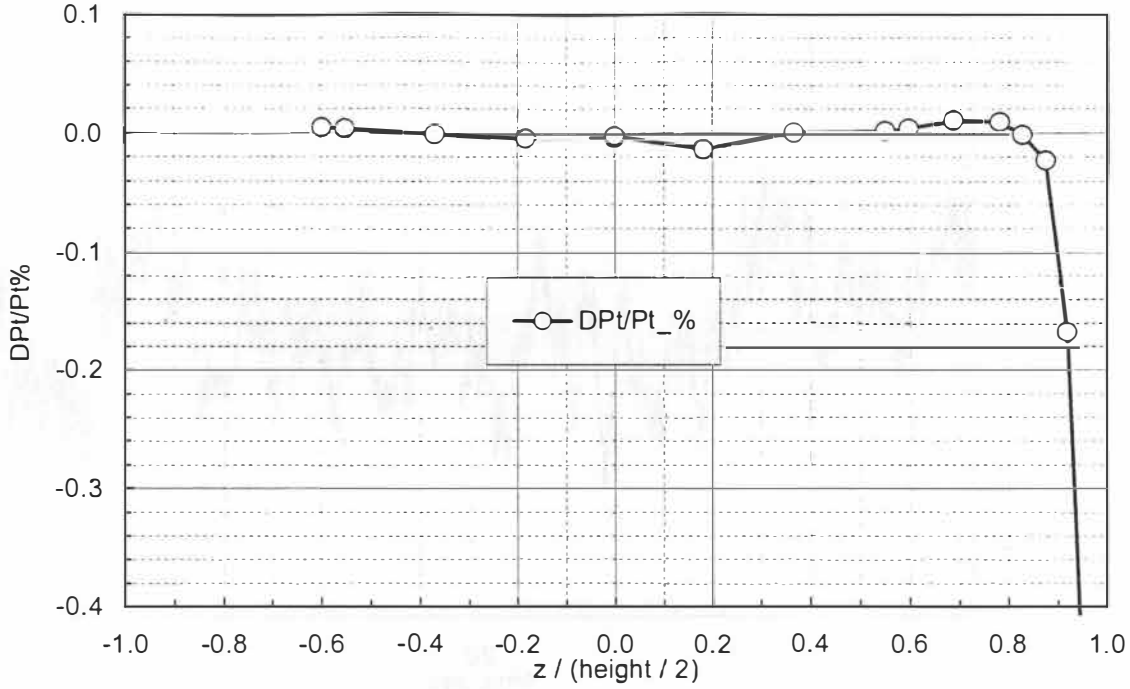


a) Configuration C21, RMS(u'/U)% = 0.45

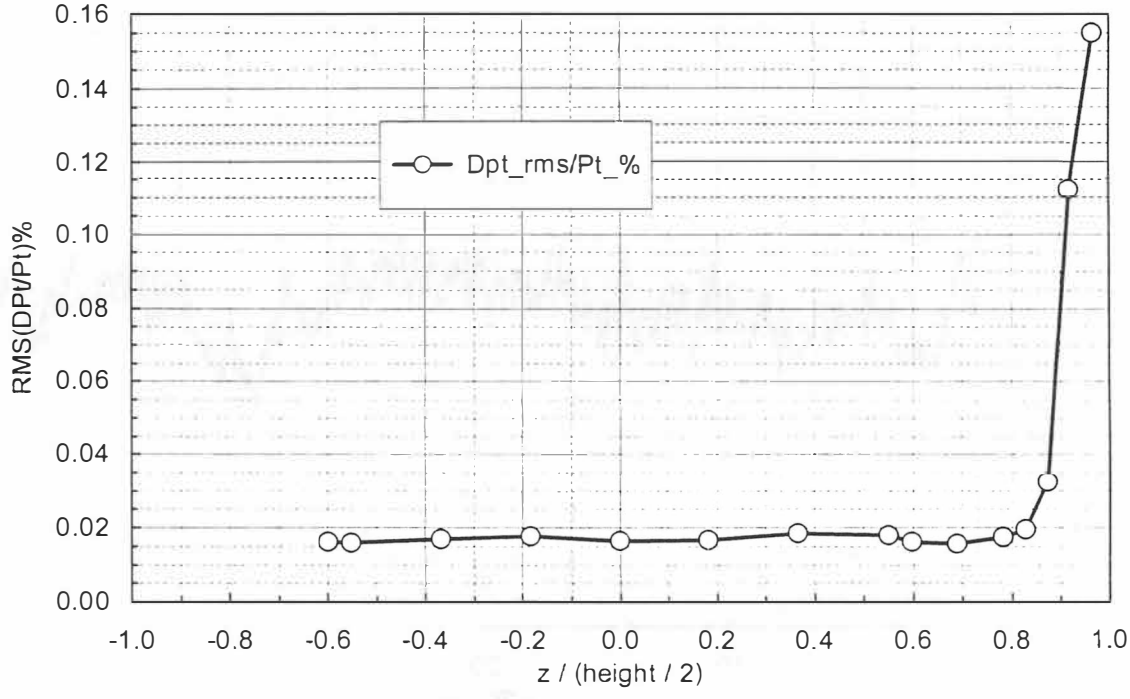


b) Configuration C19, RMS(u'/U)% = 0.28

Figure C-40. High Response Probe Calculated Turbulence Intensity Time Trace at Test Section Center, Configurations C21 and C19.

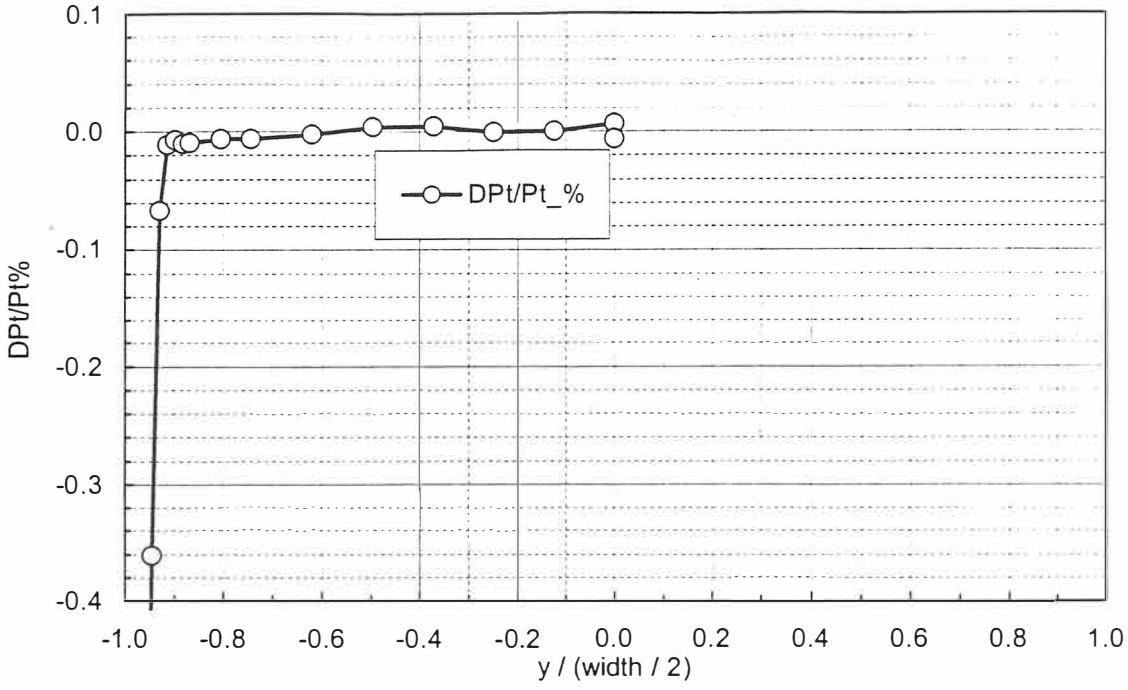


a) Total Pressure Profile

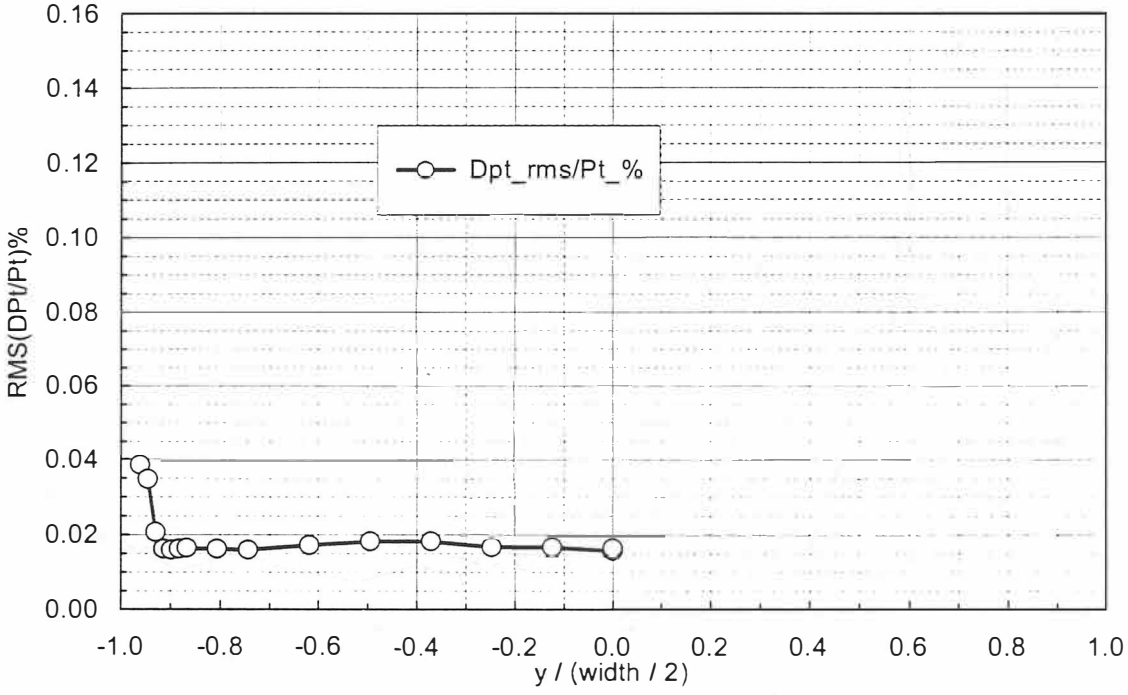


b) Temporal RMS Profile.

Figure C-41. High Response Probe Profiles on Test Section Vertical Centerline, Configuration C24.

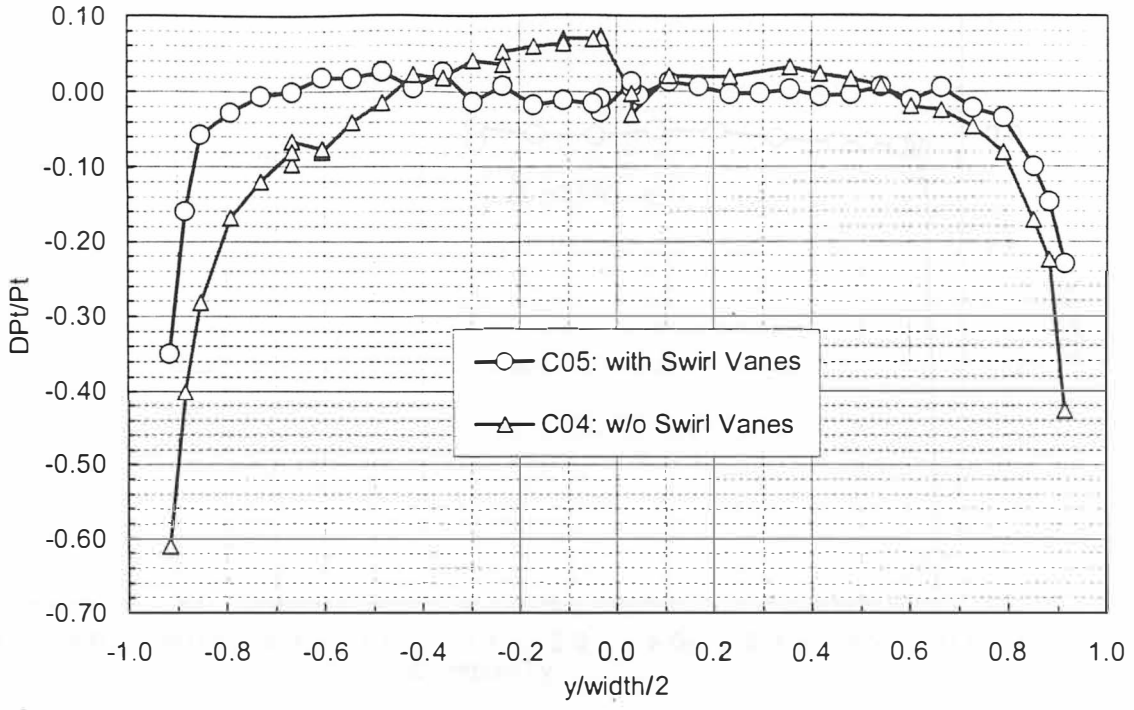


a) Total Pressure Profile

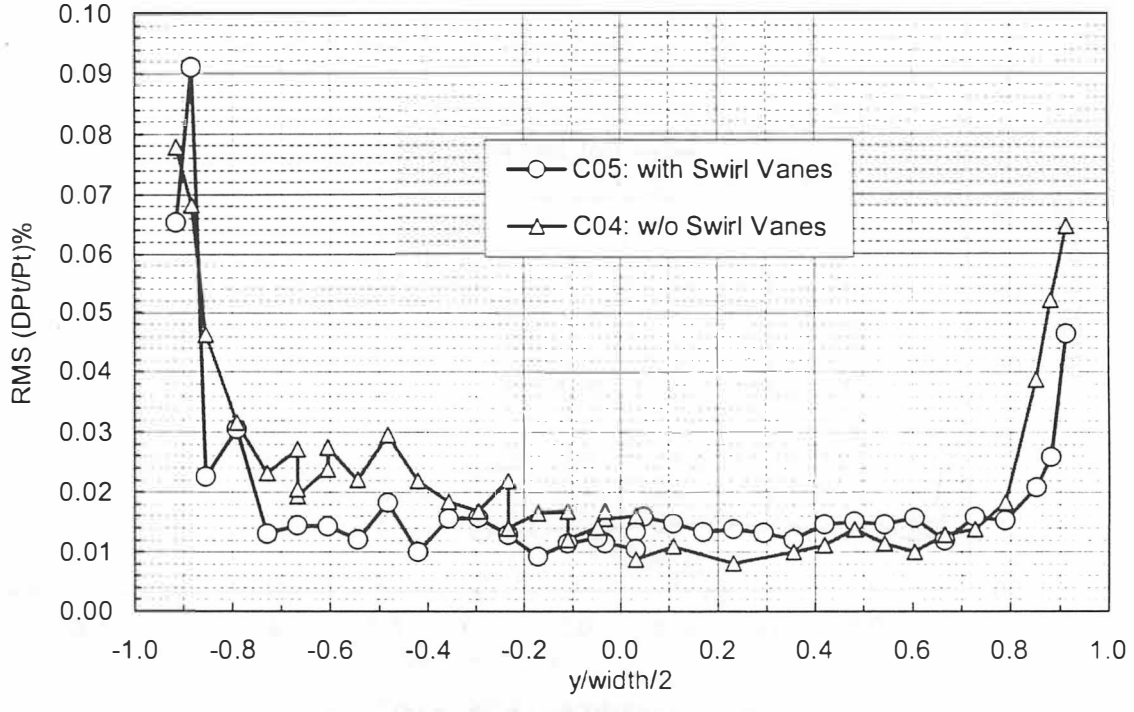


b) Temporal RMS Profile.

Figure C-42. High Response Probe Profiles on Test Section Horizontal Centerline, Configuration C24.

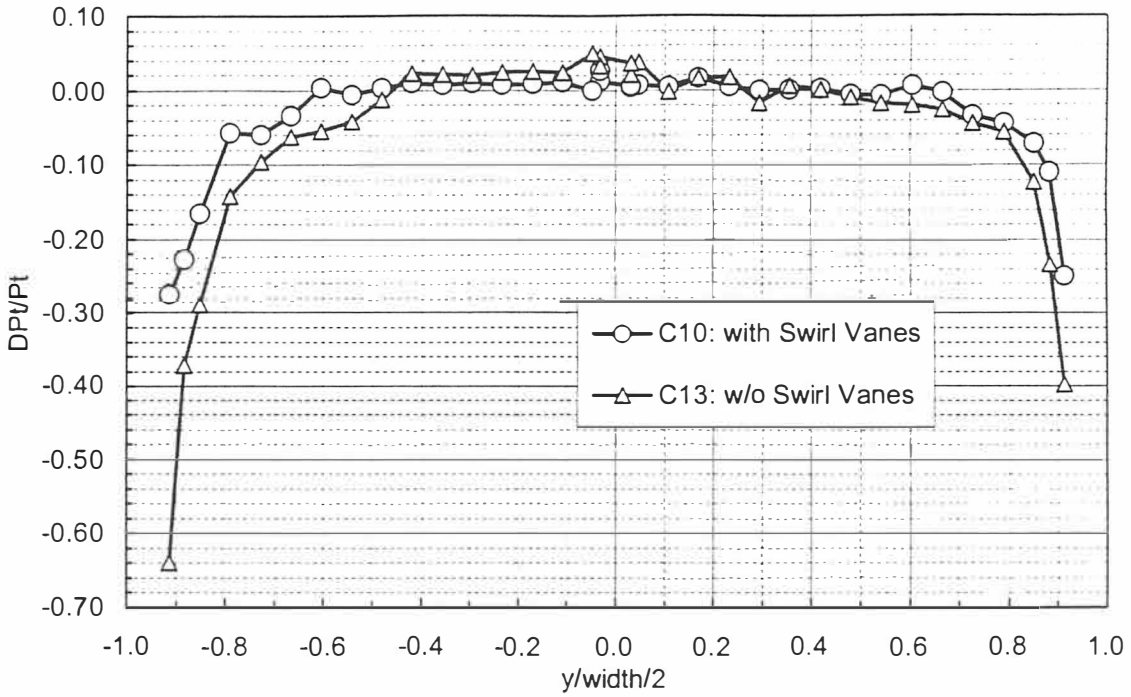


a) Total Pressure Profile

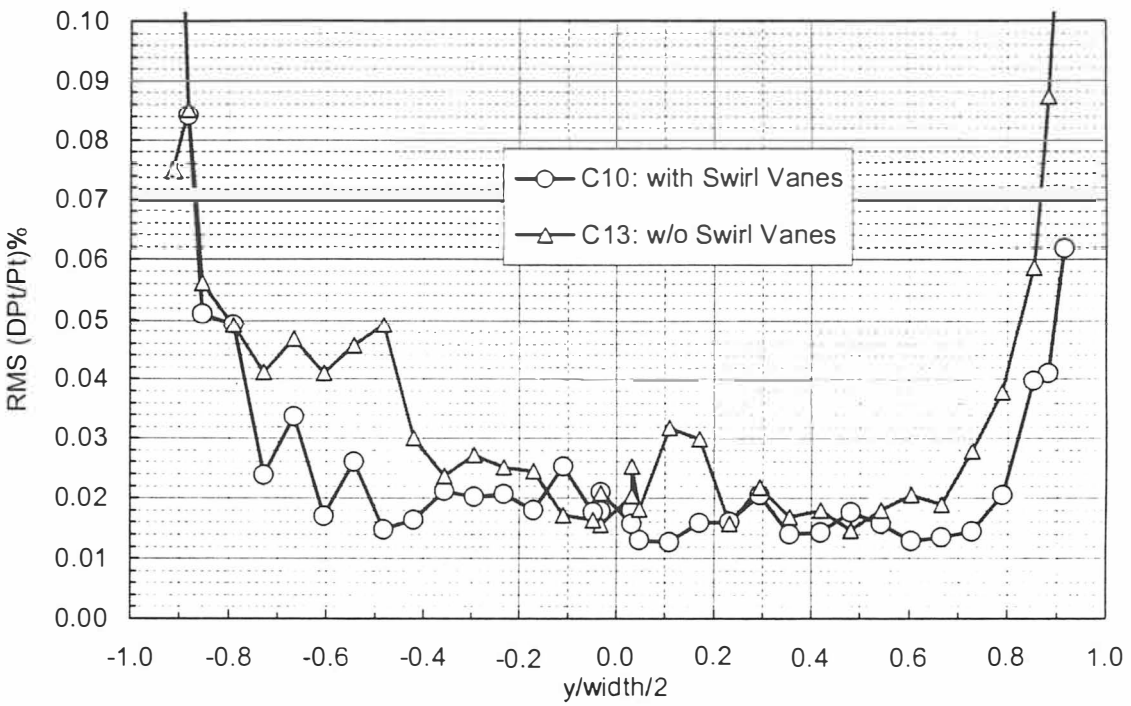


b) Temporal RMS Profiles

Figure C-43. Test Section Total Pressure & RMS Profiles, Corner 3 Installed: C05 (with swirl vanes) & C04 (without swirl vanes)

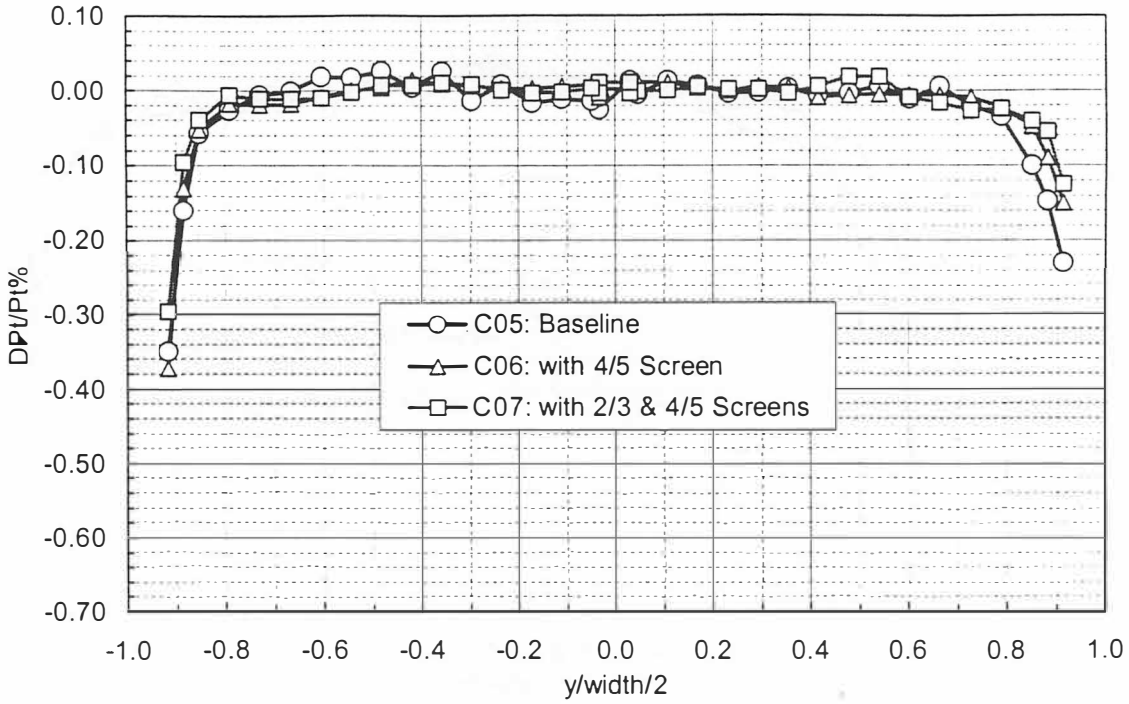


a) Total Pressure Profile

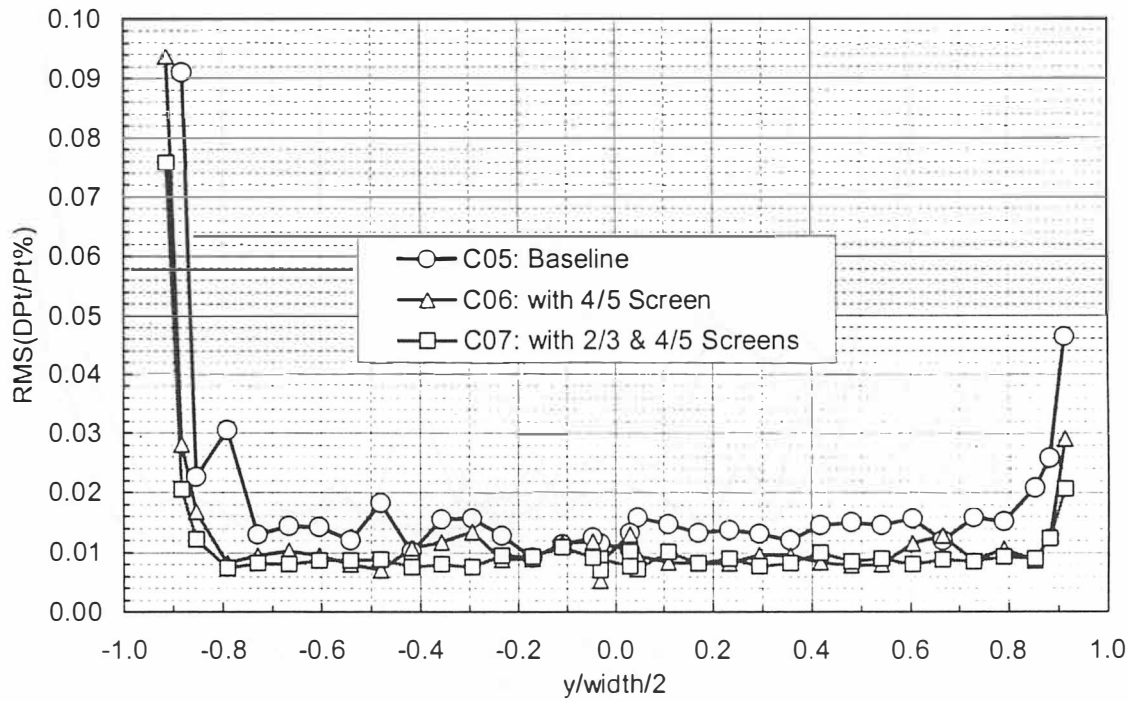


b) Temporal RMS Profiles

Figure C-44. Test Section Total Pressure & RMS Profiles, Corner 3 Removed: C10 (with swirl vanes) & C13 (without swirl vanes)

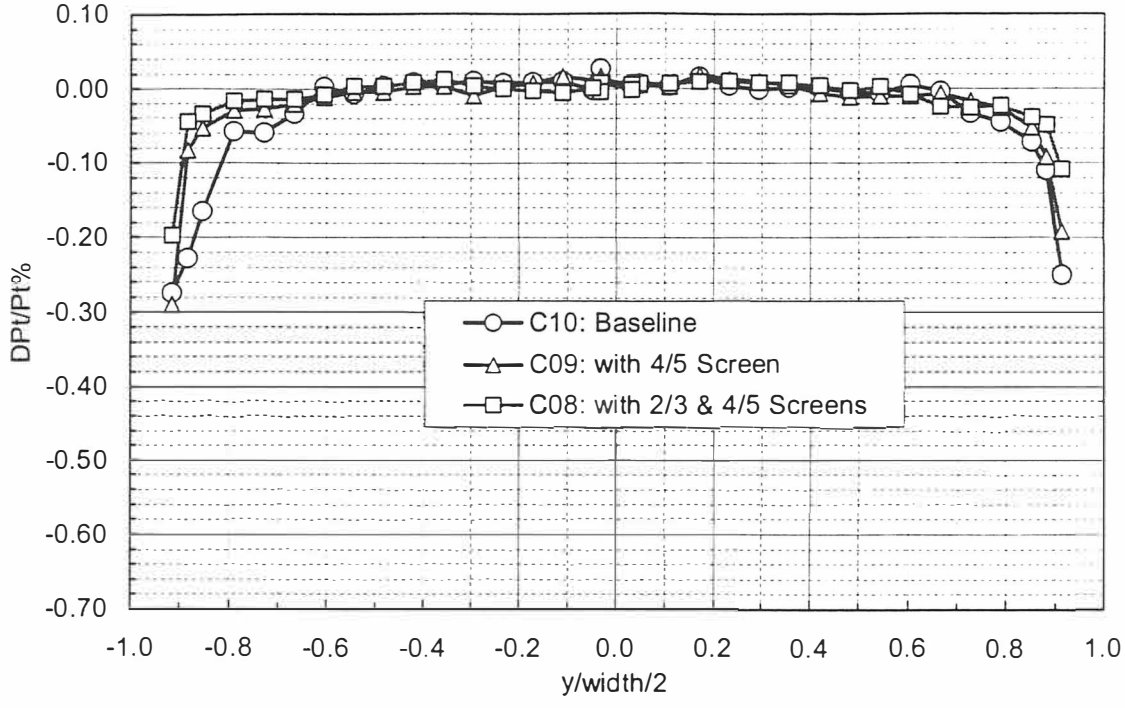


a) Total Pressure Profile

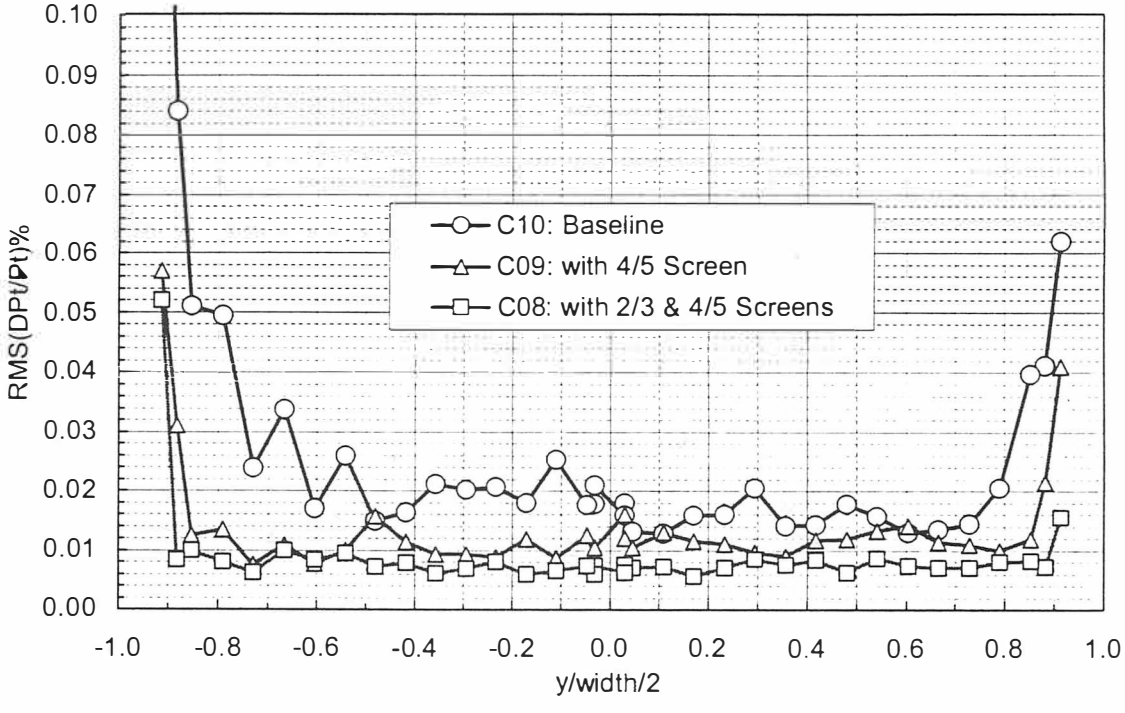


b) Temporal RMS Profiles

Figure C-45. Test Section Total Pressure & RMS Profiles, Corner 3 Installed: C05 (baseline), C06 (with 4/5 screen), & C07 (with 4/5 & 2/3 screens)

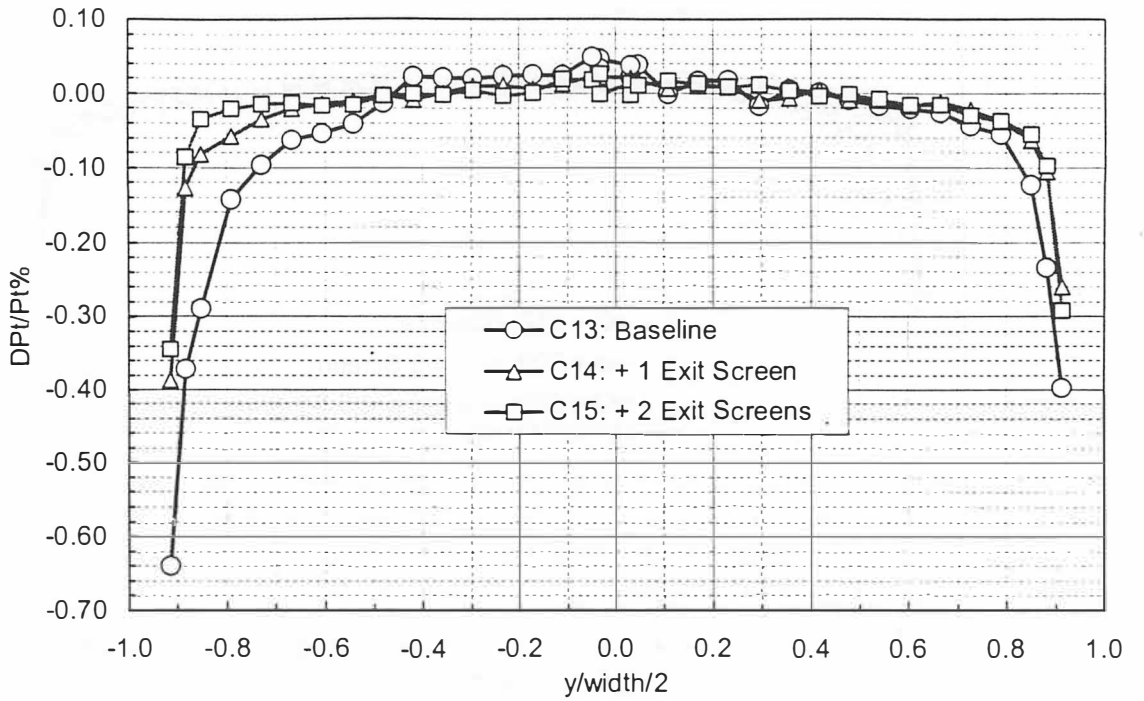


a) Total Pressure Profile

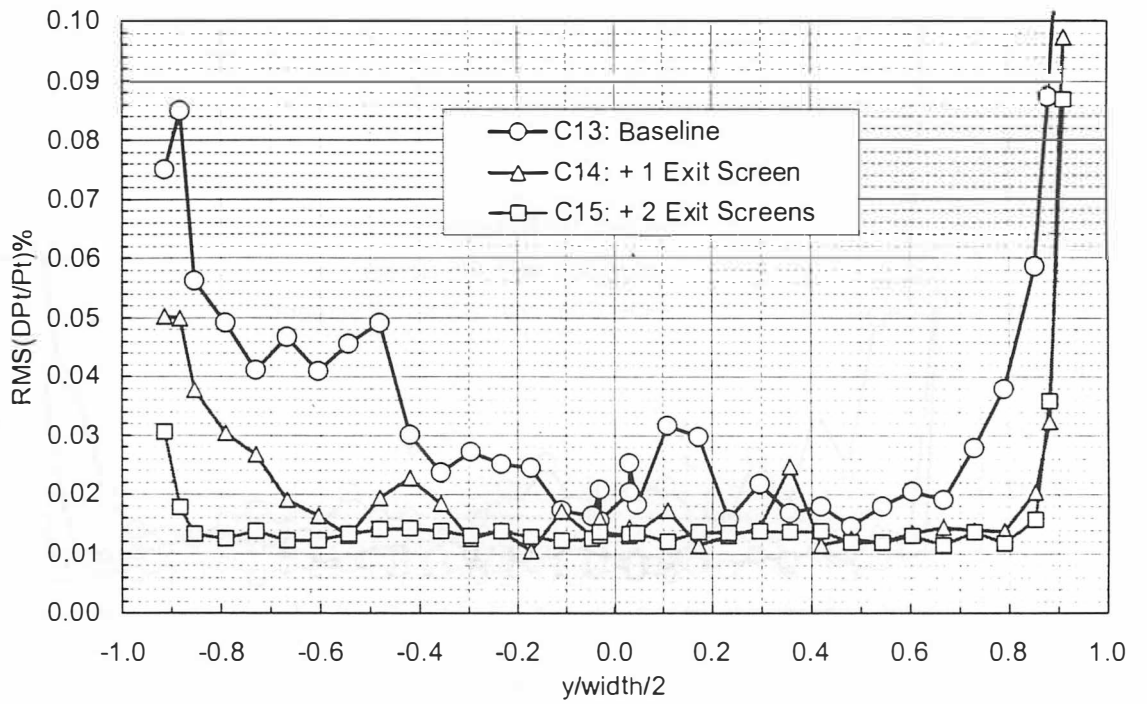


b) Temporal RMS Profiles

Figure C-46. Test Section Total Pressure & RMS Profiles, Corner 3 Removed: C10 (baseline), C09 (with 4/5 screen), & C08 (with 4/5 & 2/3 screens)

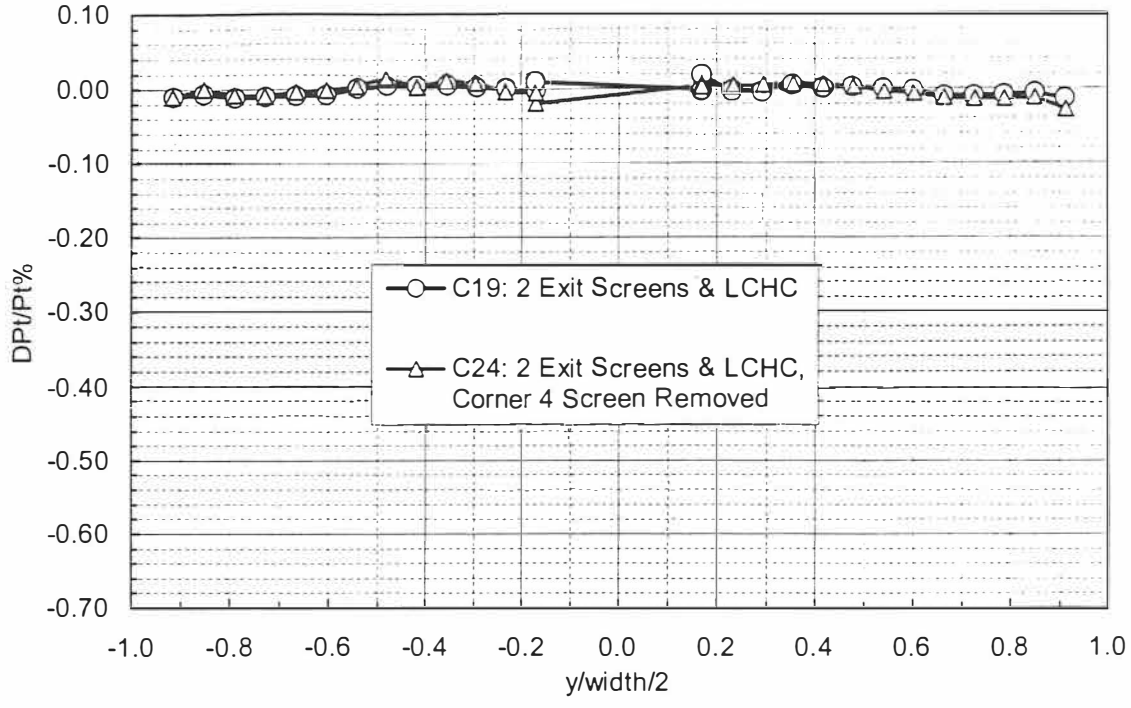


a) Total Pressure Profile

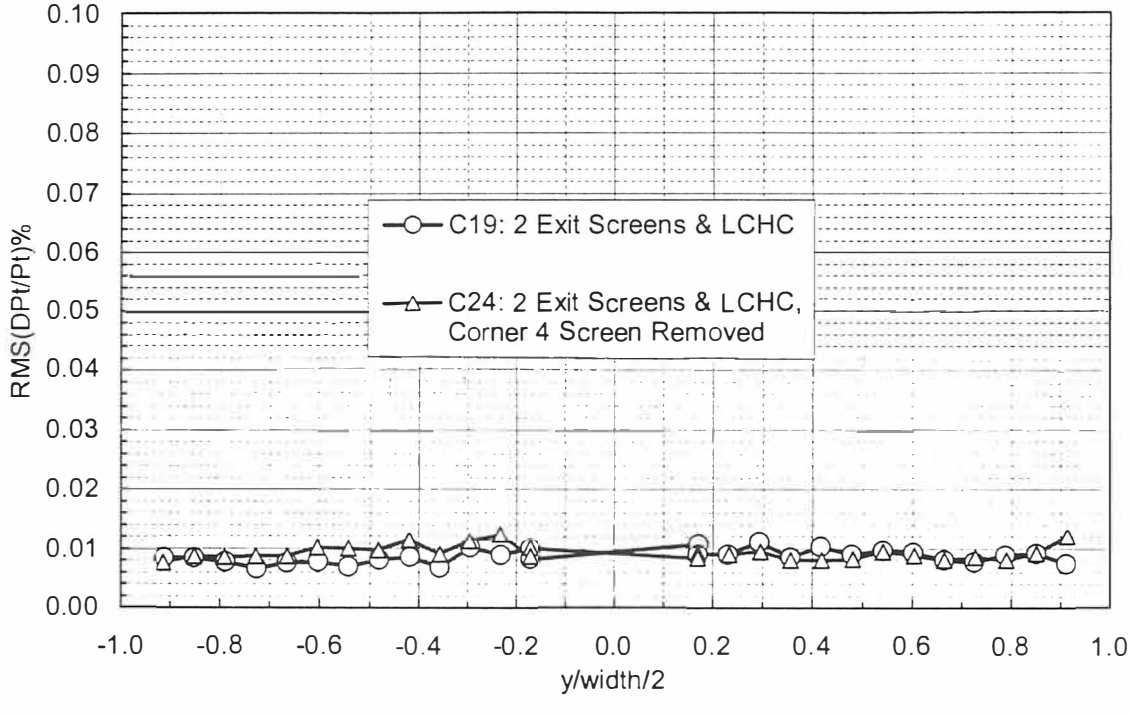


b) Temporal RMS Profiles

Figure C-47. Test Section Total Pressure & RMS Profiles, Corner 3 and Swirl Vanes Removed C13 (baseline), C14 (one exit screen), & C15 (two exit screens)

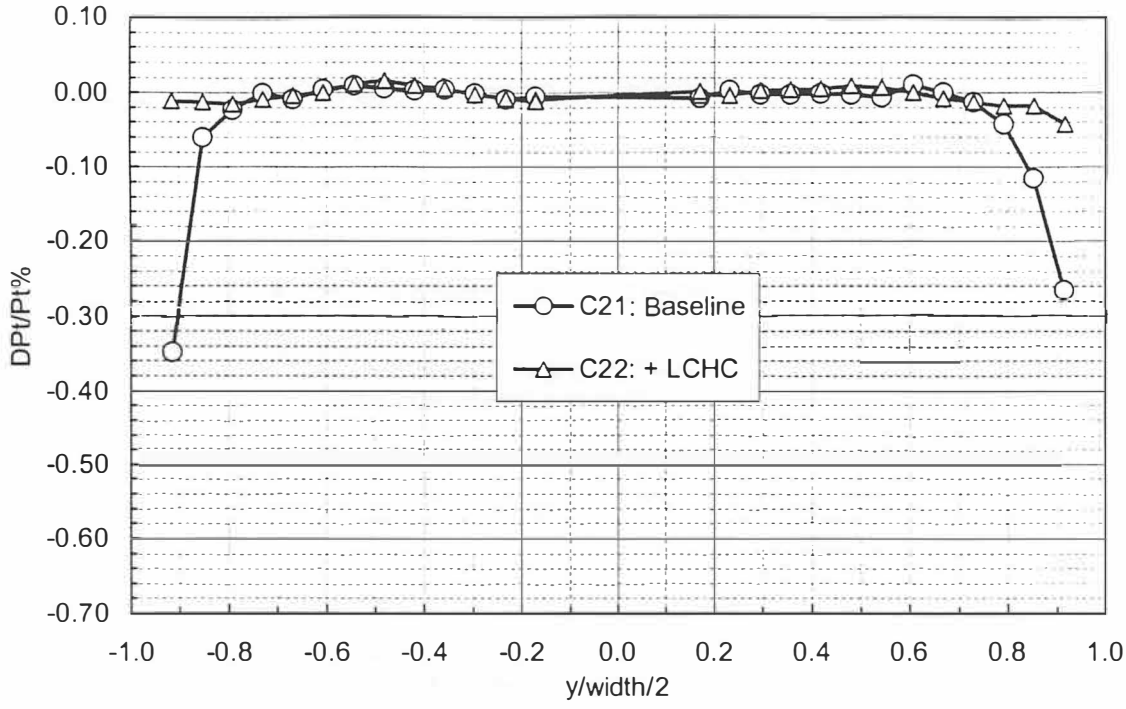


a) Total Pressure Profile

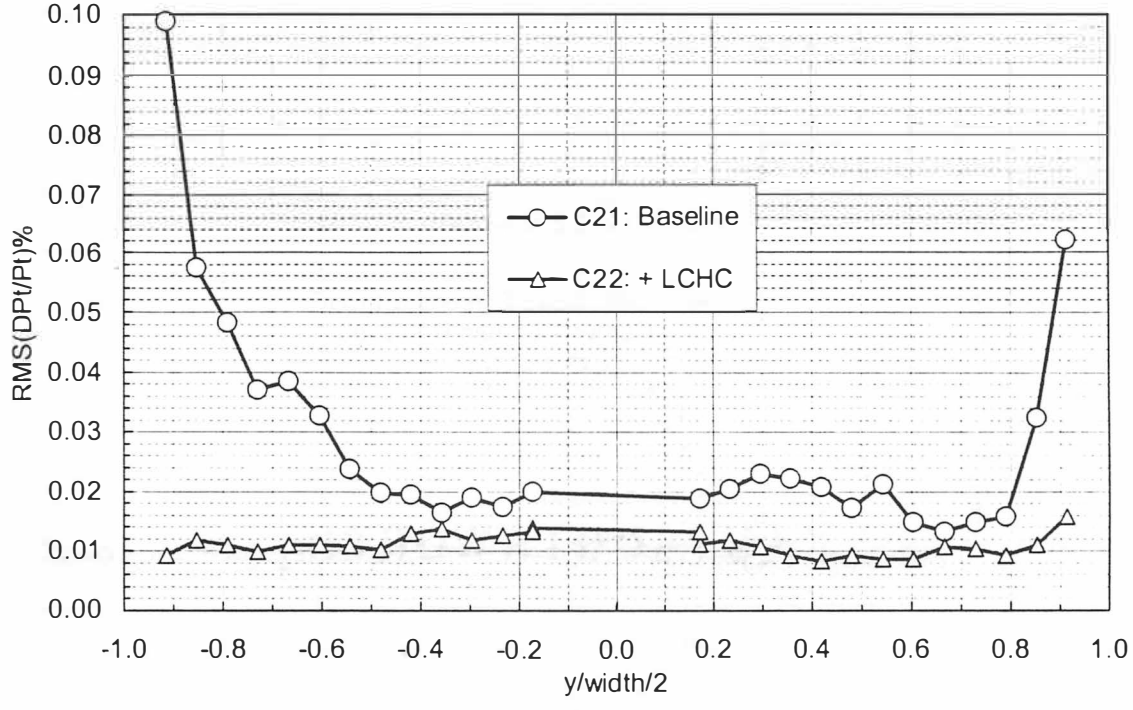


b) Temporal RMS Profiles

Figure C-48. Test Section Total Pressure & RMS Profiles, C19 (with C4 screen) & C24 (without C4 screen).

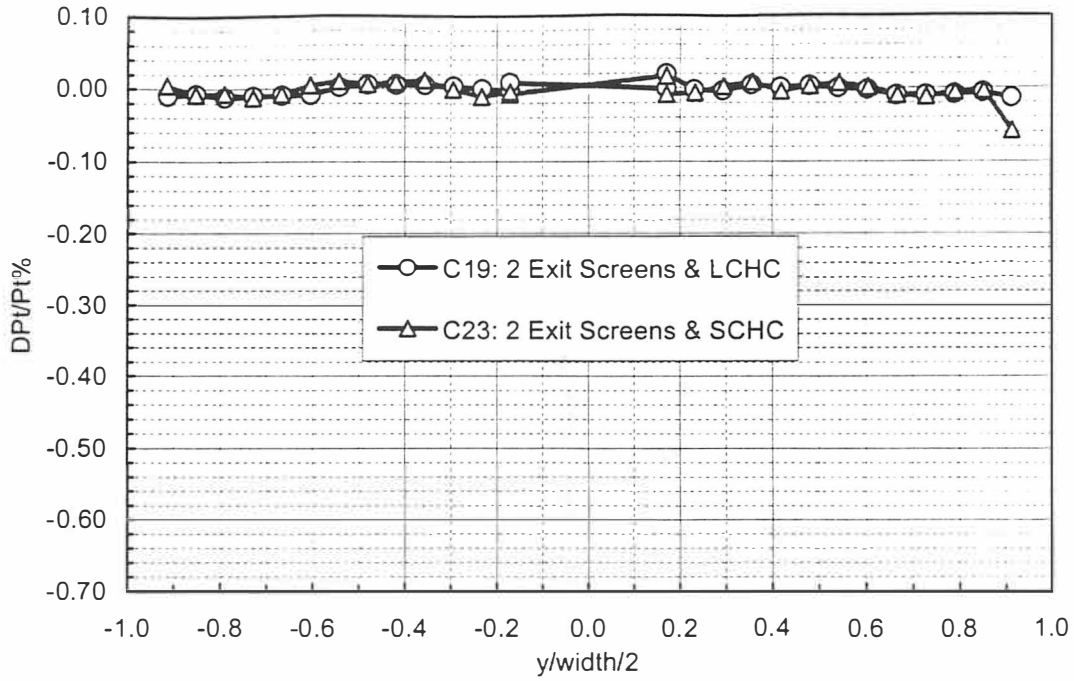


a) Total Pressure Profile

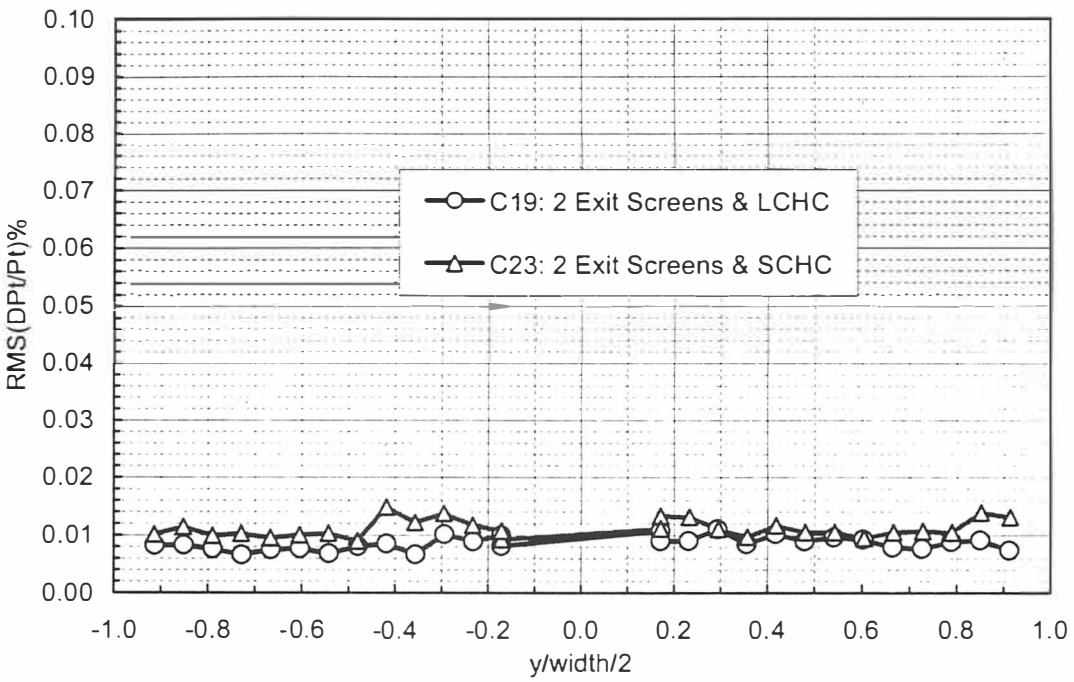


b) Temporal RMS Profiles

Figure C-49. Test Section Total Pressure & RMS Profiles, C21 (Baseline) & C22 (Long Cell Honeycomb).



a) Total Pressure Profile



b) Temporal RMS Profiles

Figure C-50. Test Section Total Pressure & RMS Profiles, C19 (Long Cell Honeycomb) & C23 (Short Cell Honeycomb).

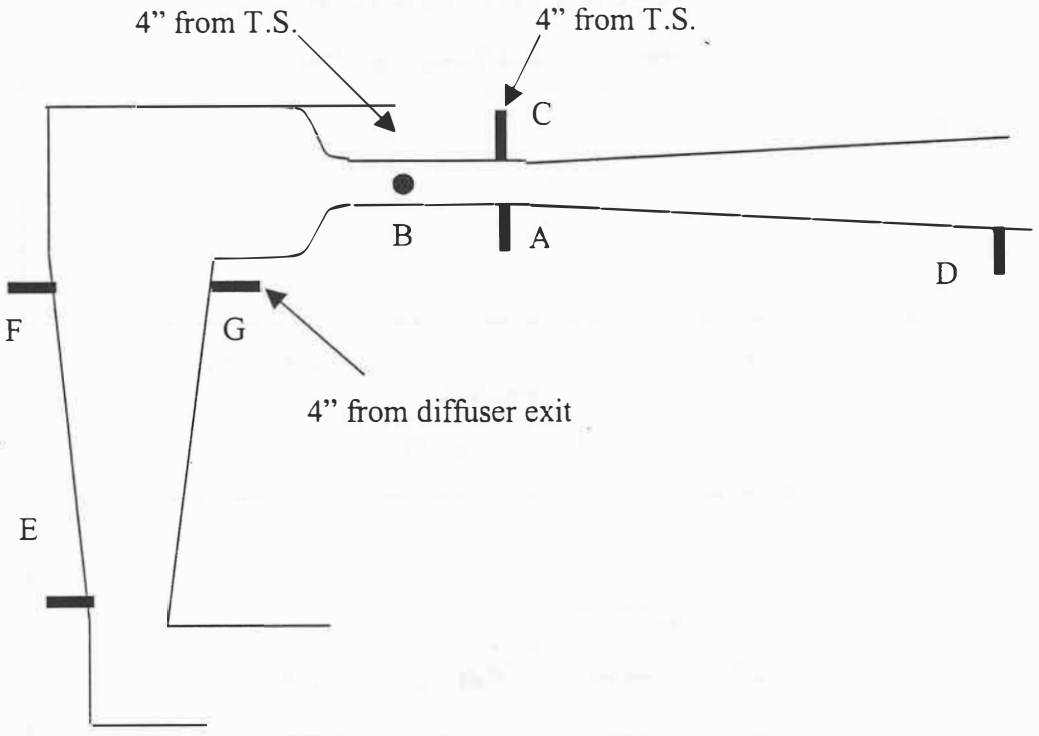
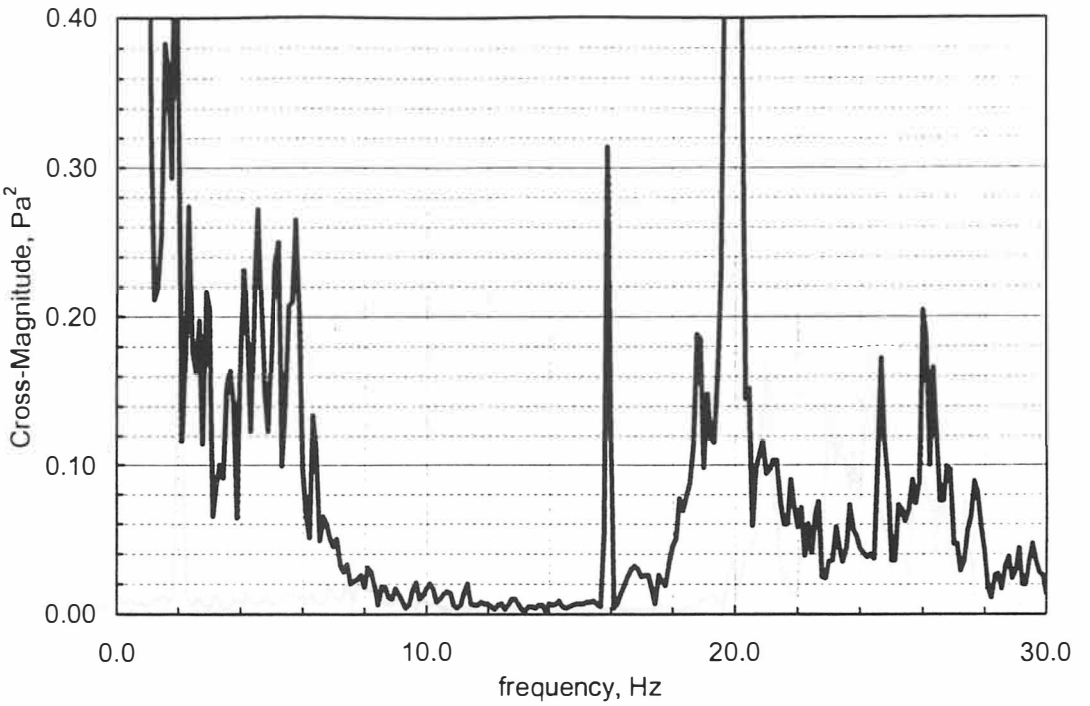
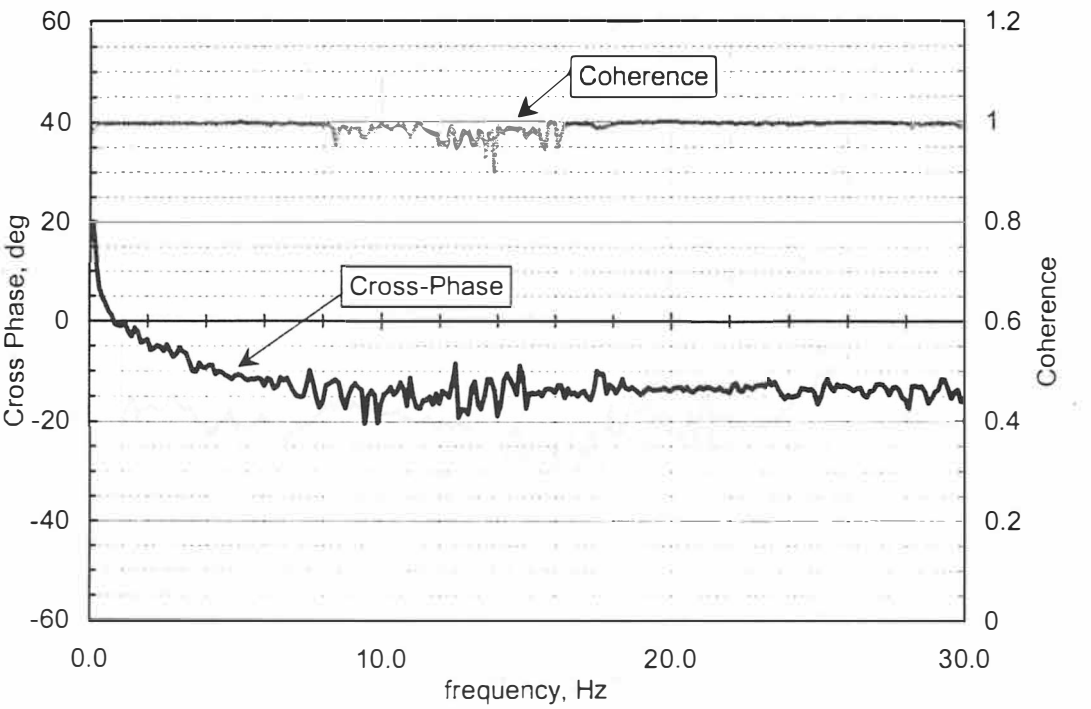


Figure C-51. Layout of Acoustic Instrumentation.

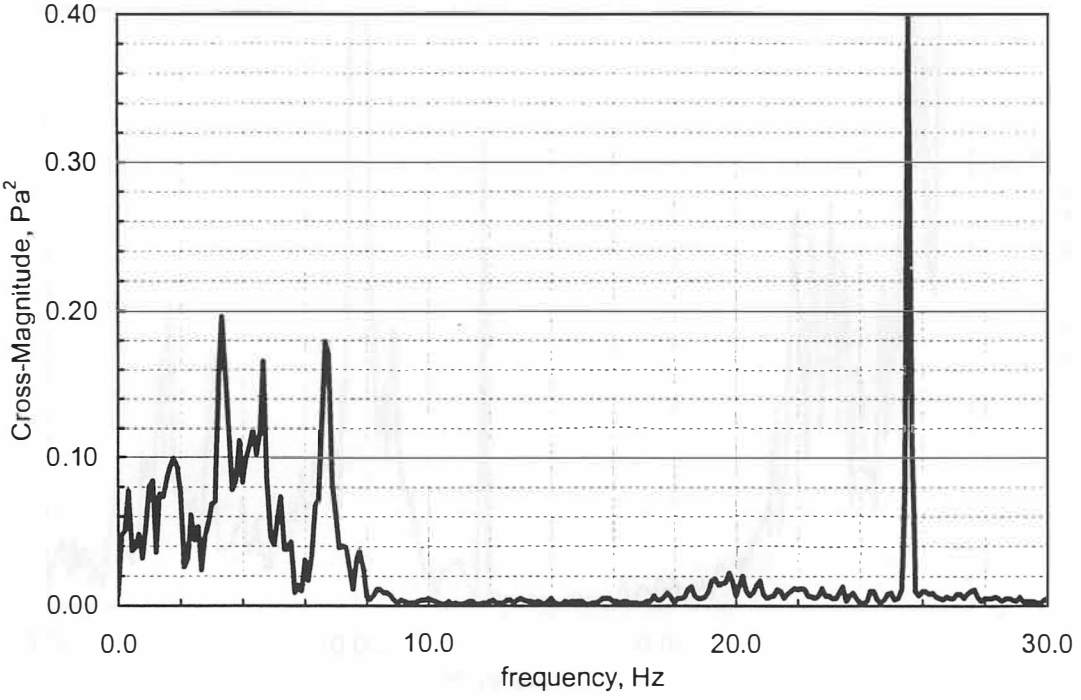


a) Cross-Magnitude

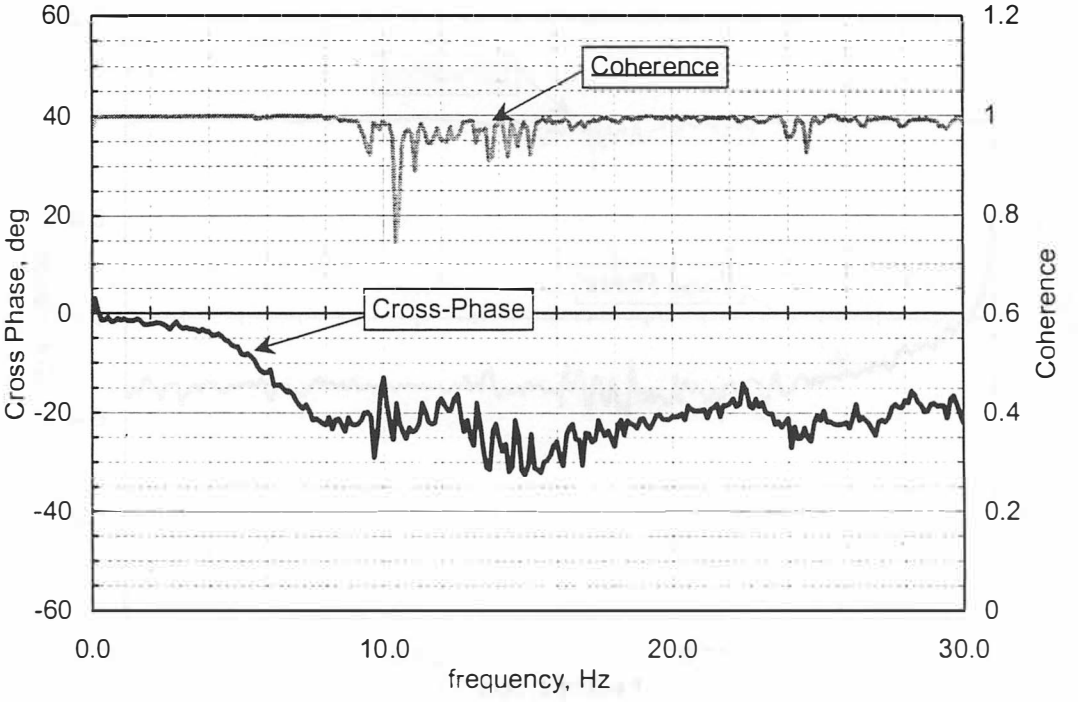


b) Cross-Phase and Coherence

Figure C-52. Cross-Magnitude, Phase, and Coherence, Microphone Locations A & B, Setup A.

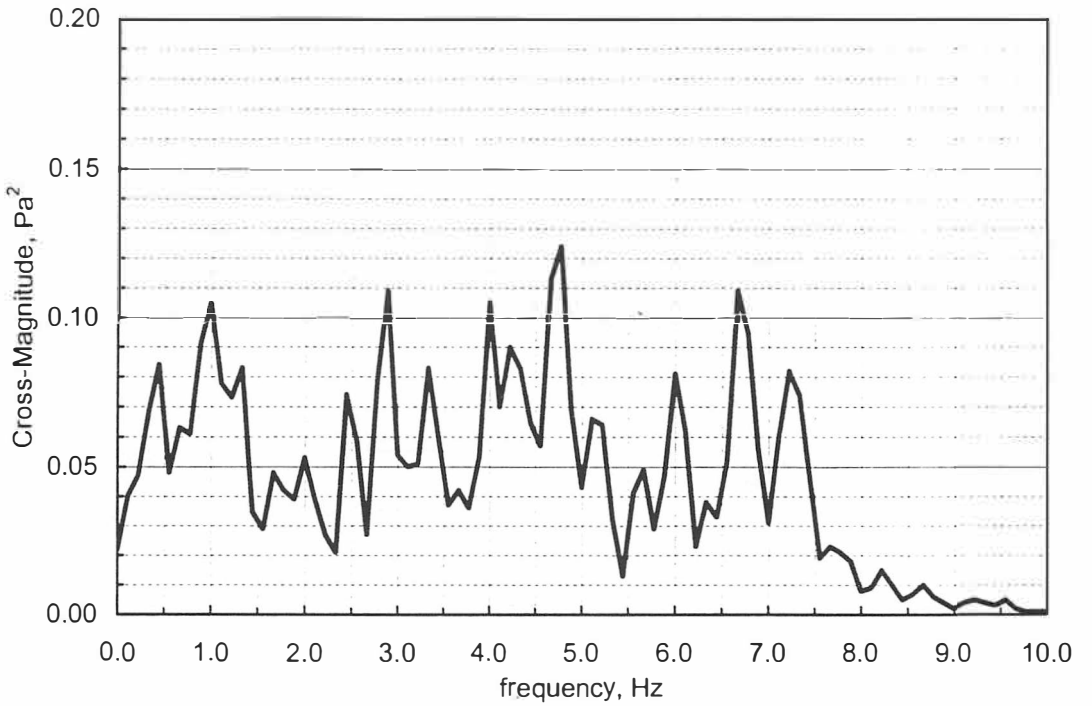


a) Cross-Magnitude

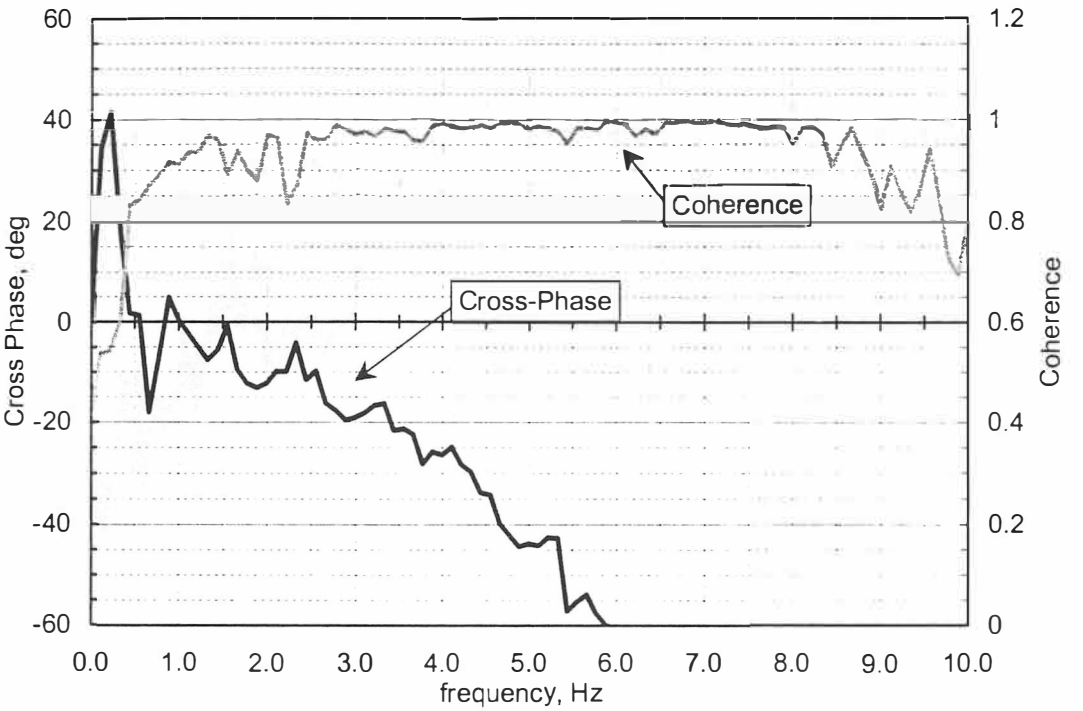


b) Cross-Phase and Coherence

Figure C-53. Cross-Magnitude, Phase, and Coherence, Microphone Locations A & B, Configuration C19.

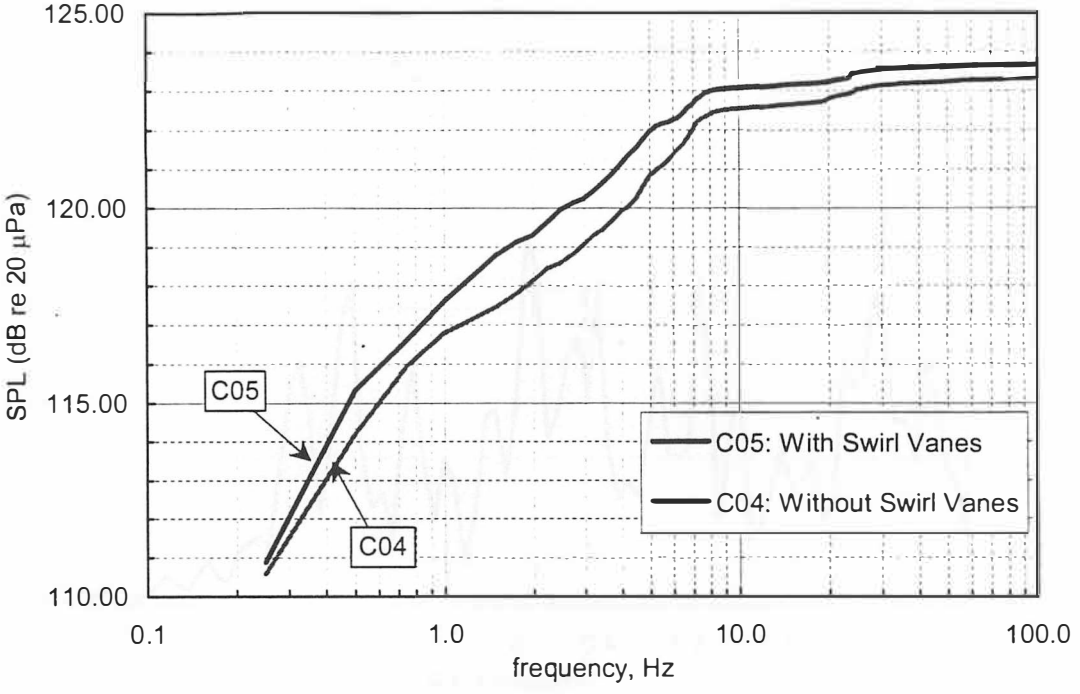


a) Cross-Magnitude

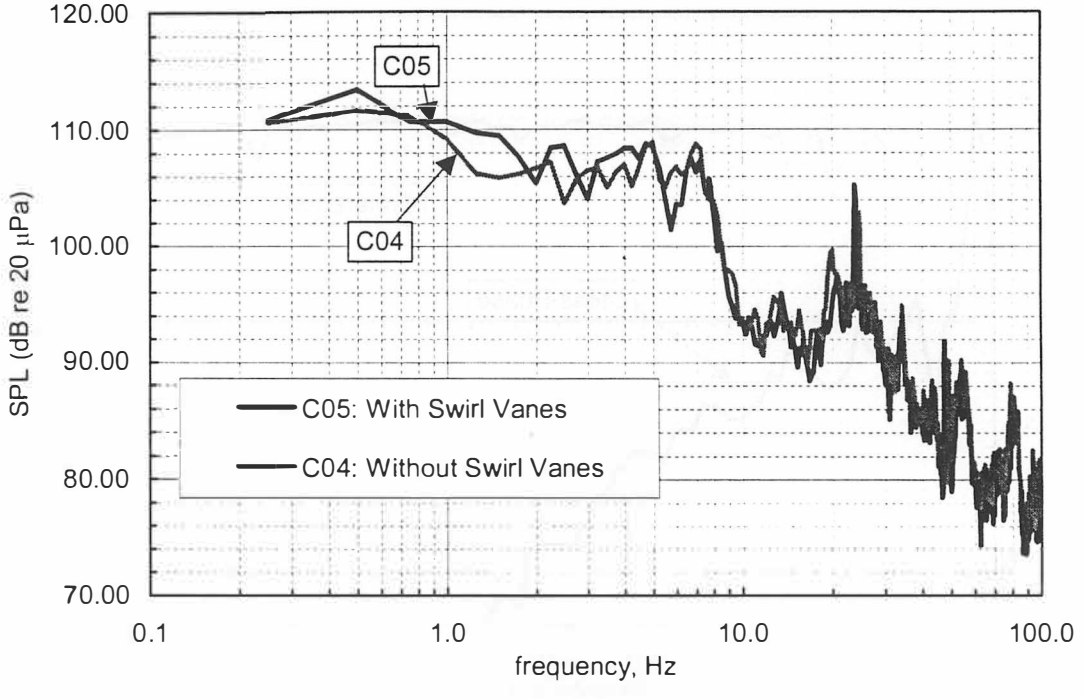


b) Cross-Phase and Coherence

Figure C-54. Cross-Magnitude, Phase, and Coherence, Microphone Locations A & E, Configuration C19.

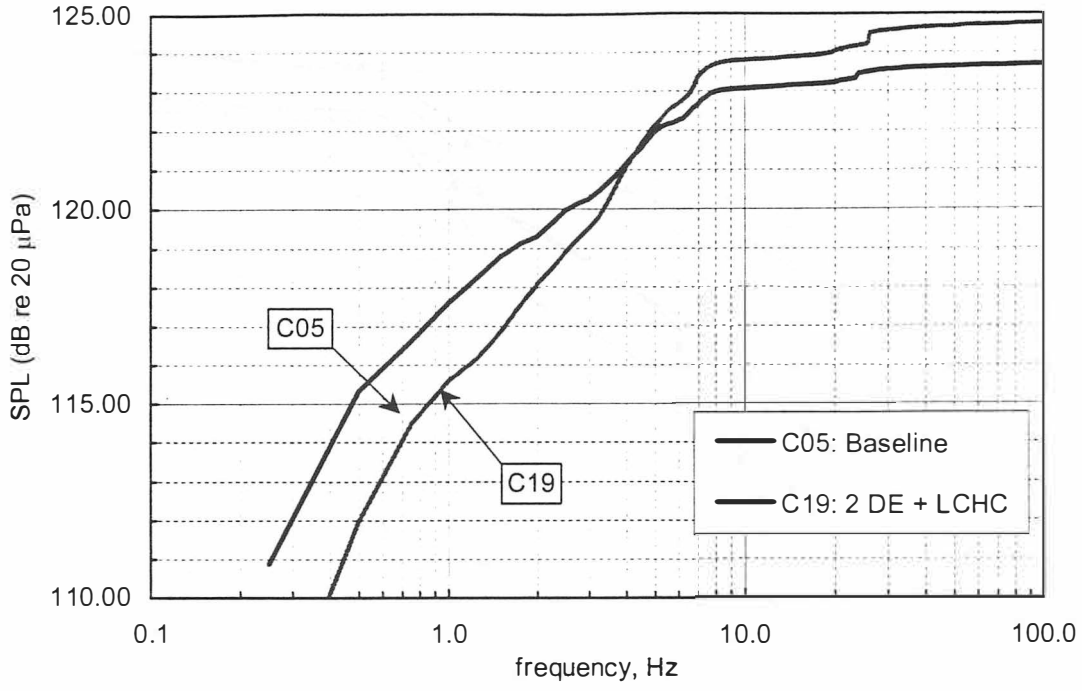


a) Cumulative Sound Energy

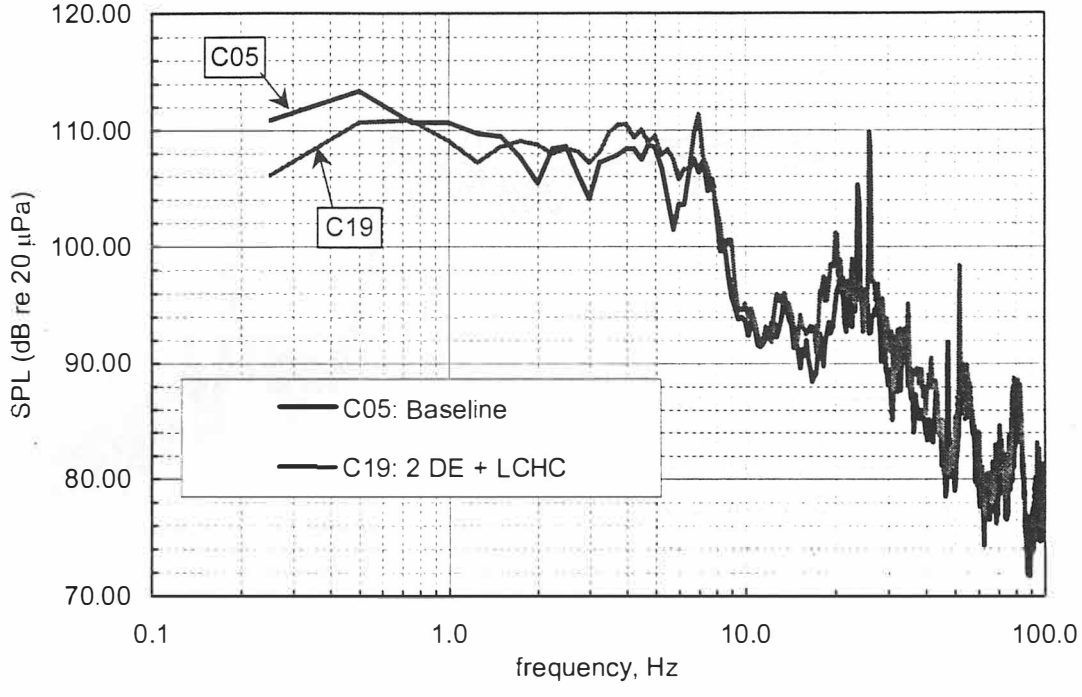


b) Sound Power Spectra, Bandwidth = 0.25 Hz

Figure C-55. Cumulative Sound Power and Power Spectra from Acoustic Data in Test Section Floor, Configurations C05 (with swirl vanes) and C04 (without swirl vanes) .

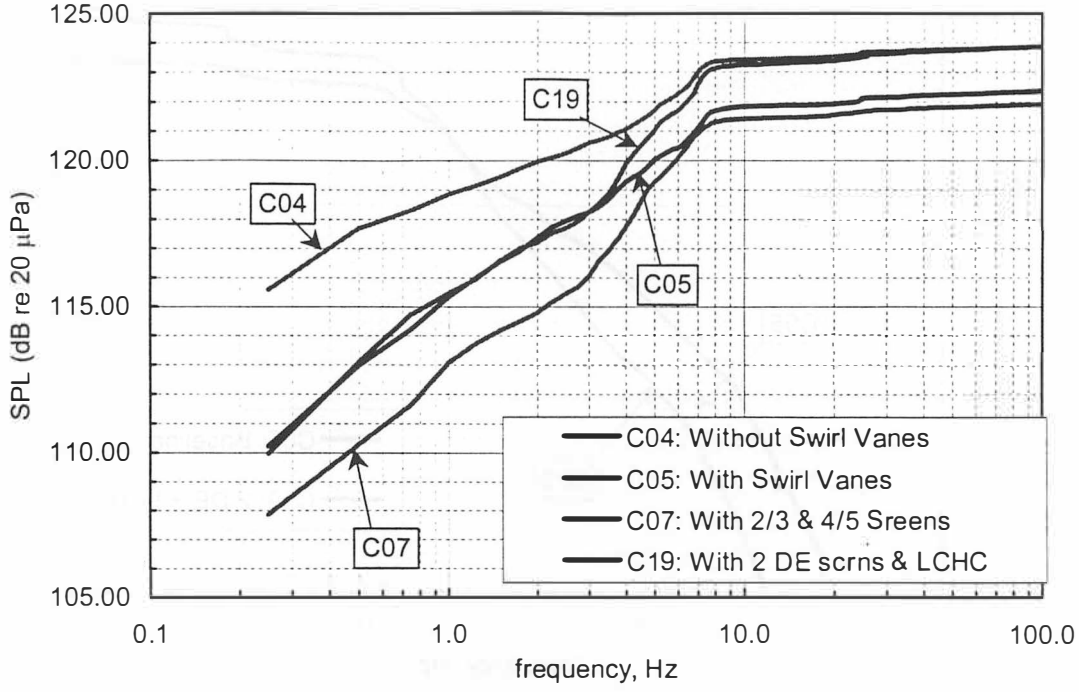


a) Cumulative Sound Energy

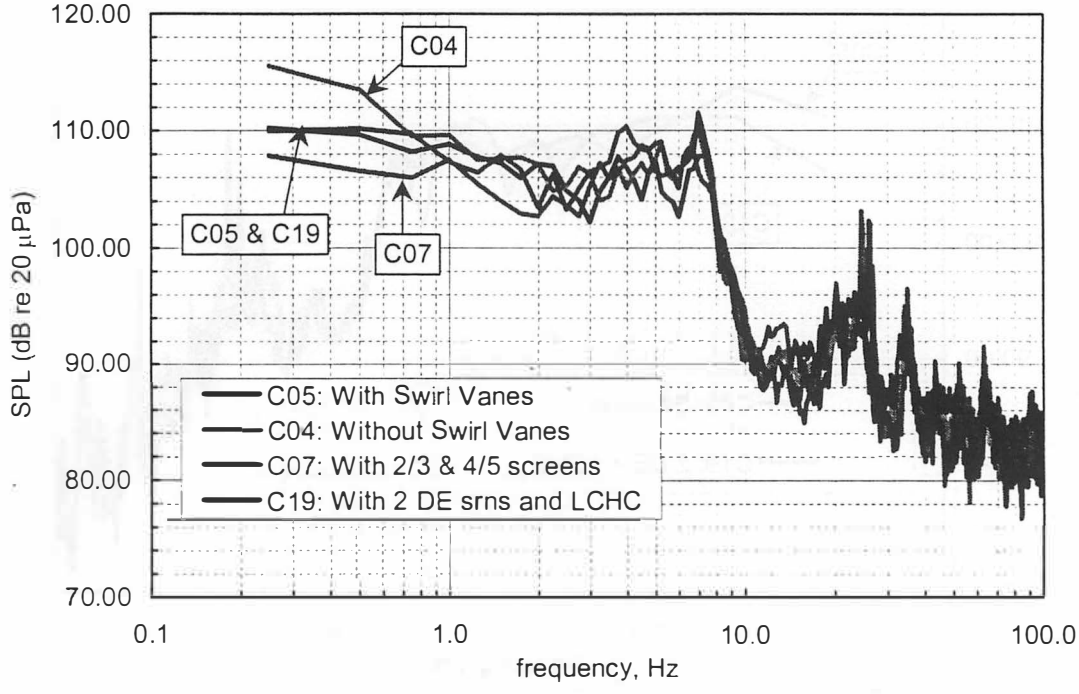


b) Sound Power Spectra, Bandwidth = 0.25 Hz

Figure C-56. Cumulative Sound Power and Power Spectra from Acoustic Data in Test Section Floor, Configurations C05 (baseline) and C19 (two diffuser exit screens and long cell honeycomb) .

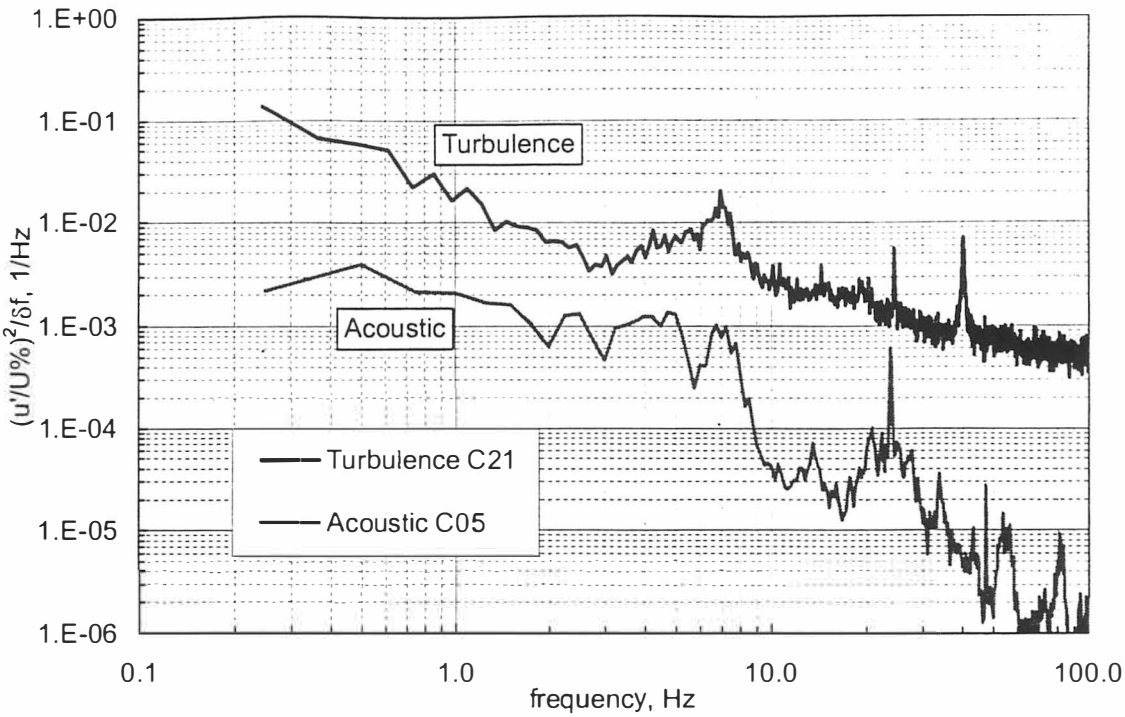


a) Cumulative Sound Energy

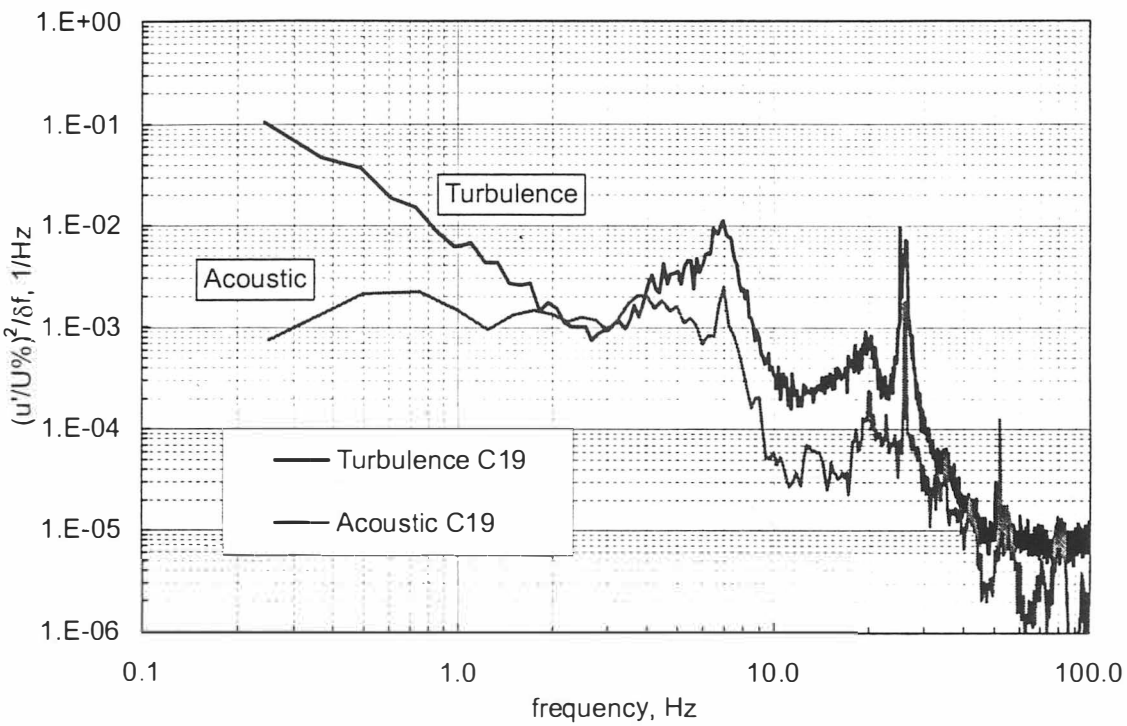


b) Sound Power Spectra, Bandwidth = 0.25 Hz

Figure C-57. Cumulative Sound Power and Power Spectra from Acoustic Data at the Cross-Leg Diffuser Exit, Configurations C04, C05, C07, & C19.

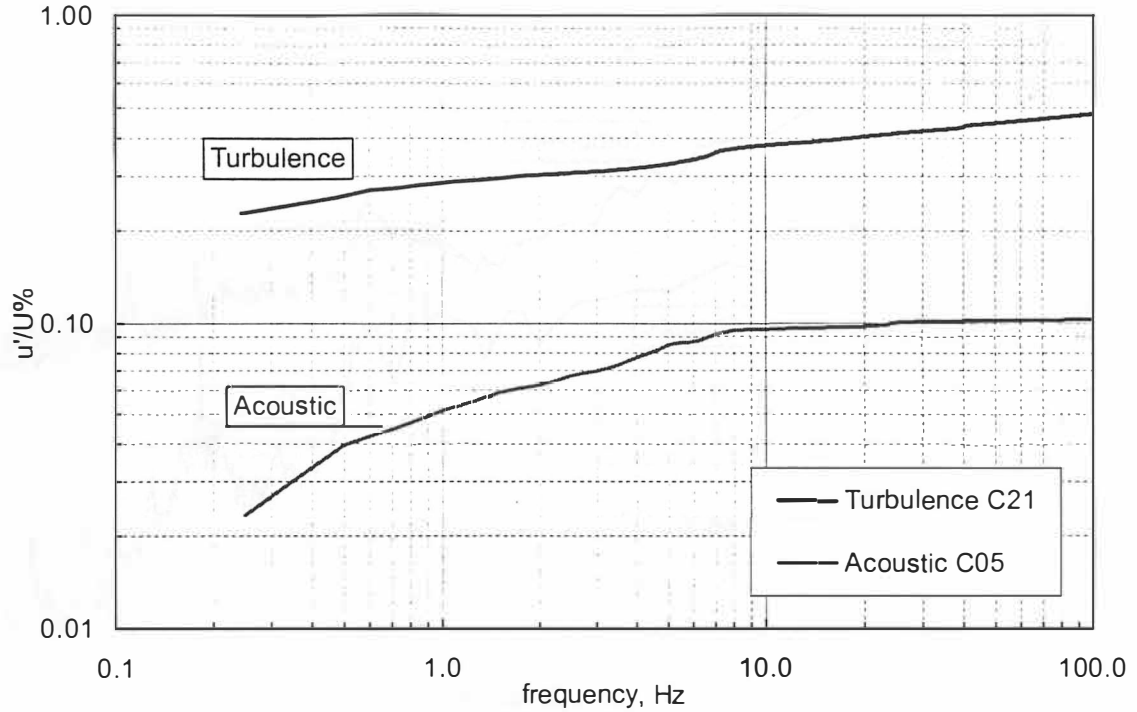


a) Baseline Configurations

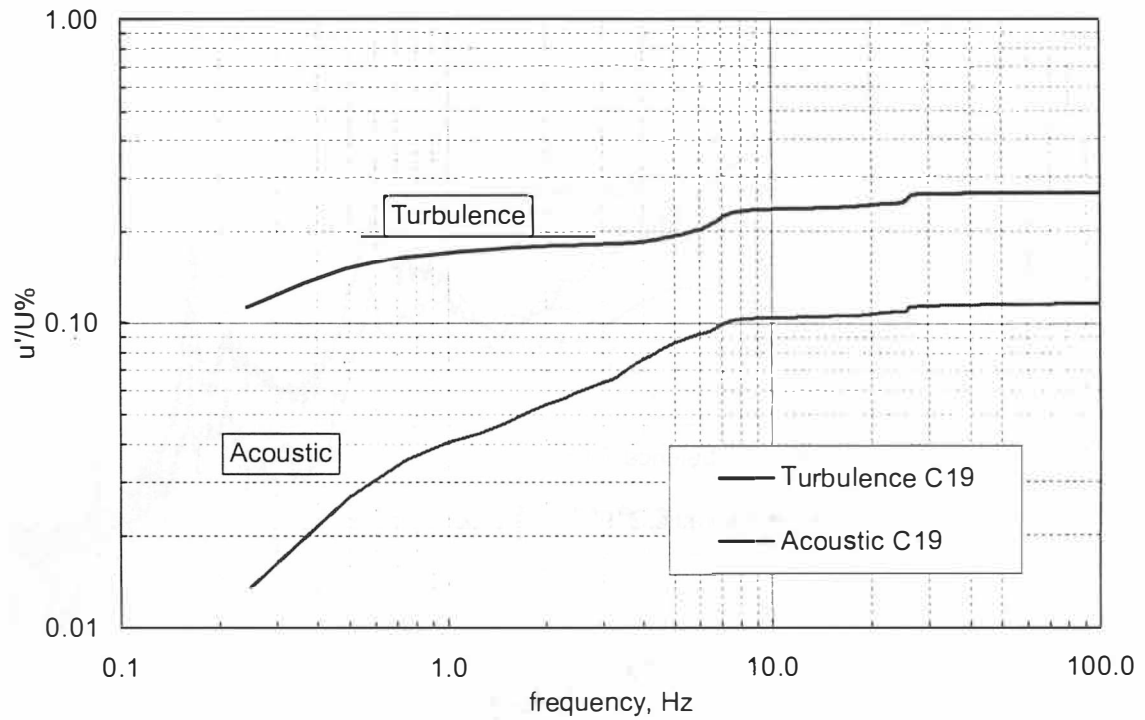


b) Configuration C19

Figure C-58. Power Spectral Density Comparison of Acoustic and Hot Wire Data, Baseline Configuration (C05 & C21) and C19.



a) Baseline Configurations



b) Configuration C19

Figure C-59. Cumulative Turbulence Intensity Comparison of Acoustic and Hot Wire Data, Baseline Configuration (C05 & C21) and C19.

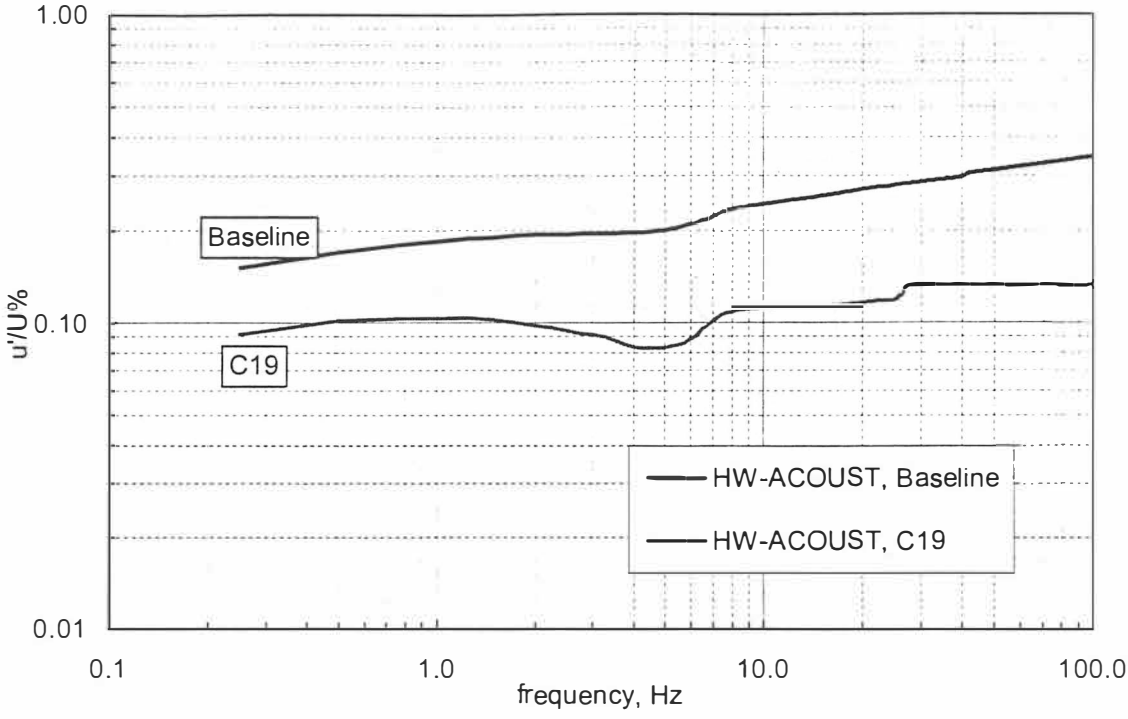
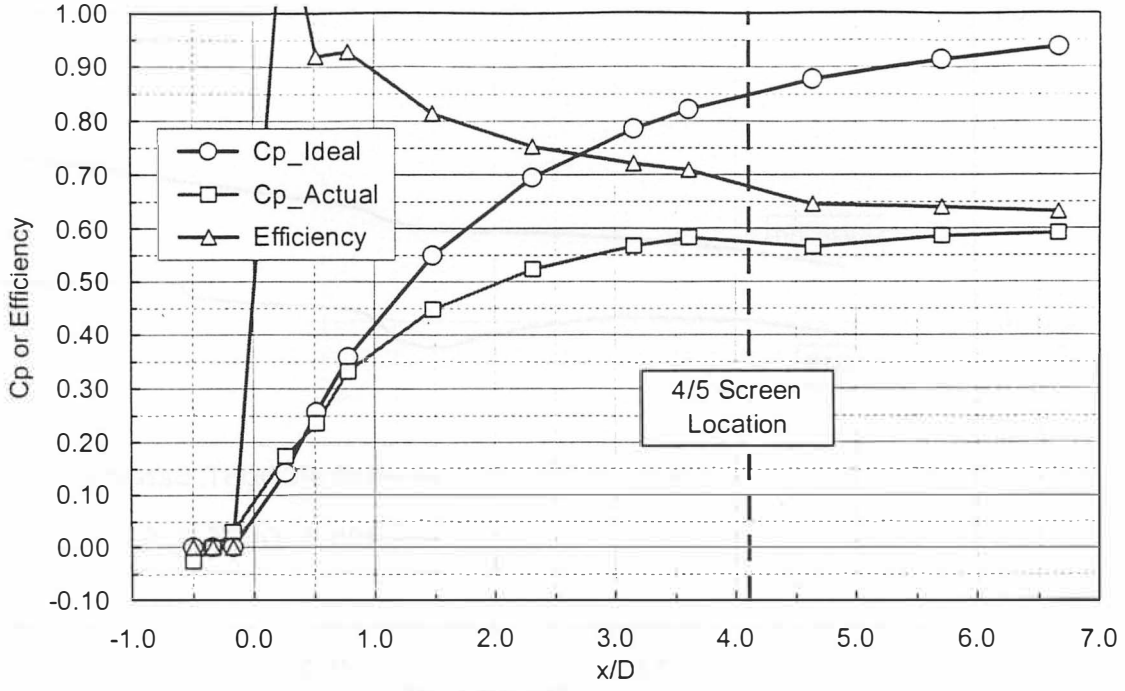
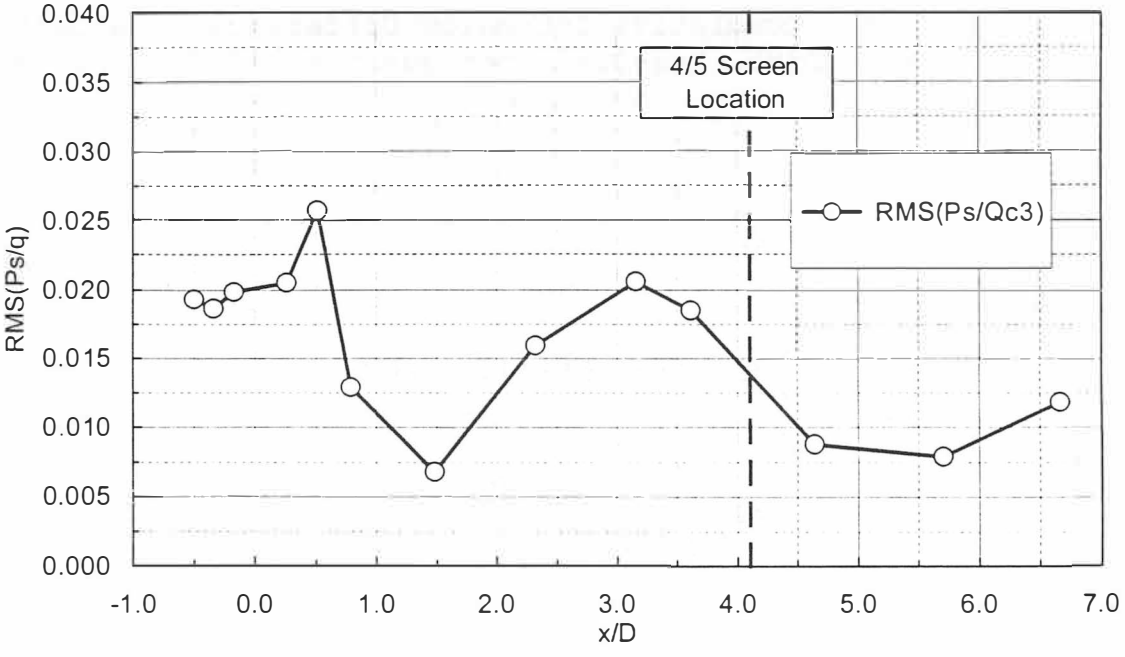


Figure C-60. Cumulative Intensity Difference of Acoustic and Hot Wire Data, Baseline Configuration (C05 & C21) and C19.

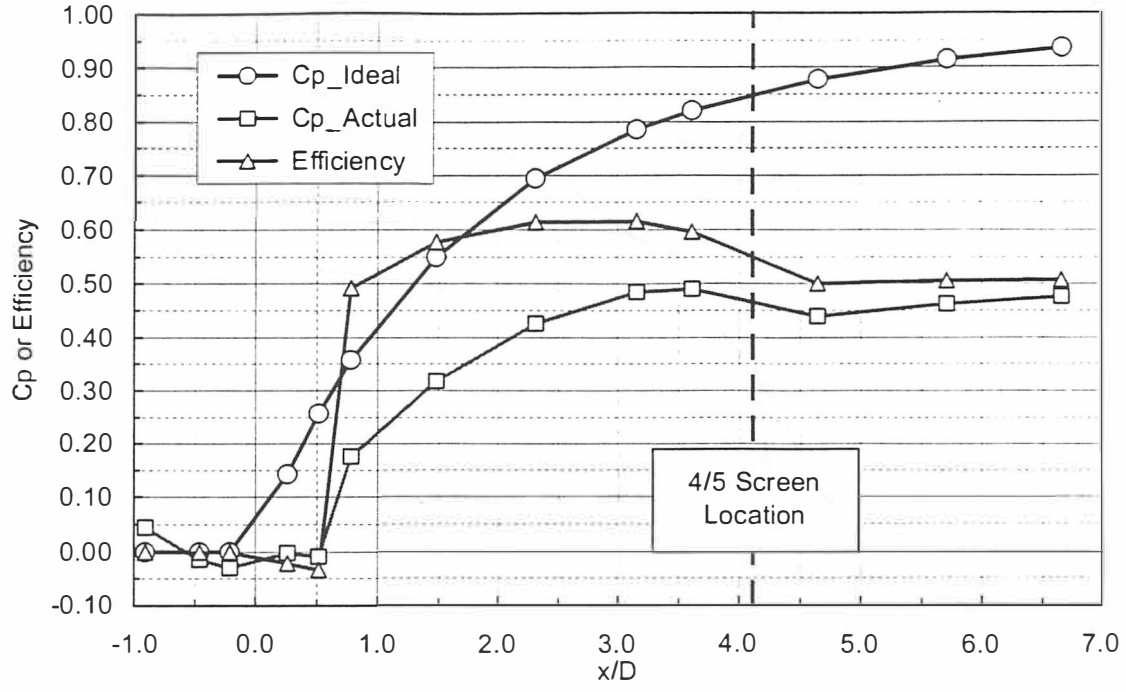


a) Cross-Leg Diffuser Cp Distribution

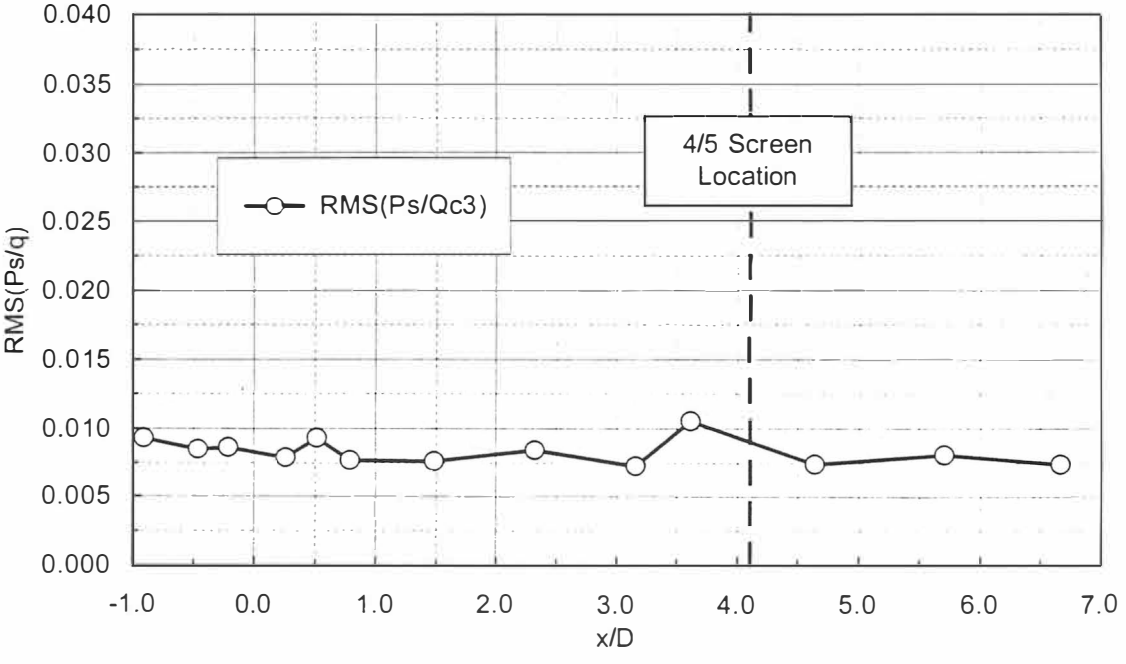


b) Cross-Leg Diffuser Static Pressure Fluctuation Distribution

Figure C-61. Cross-Leg Diffuser Pressure Coefficient and Temporal Fluctuation Distributions, Corner 3 Removed, 4/5 Screen Installed (configuration C17).

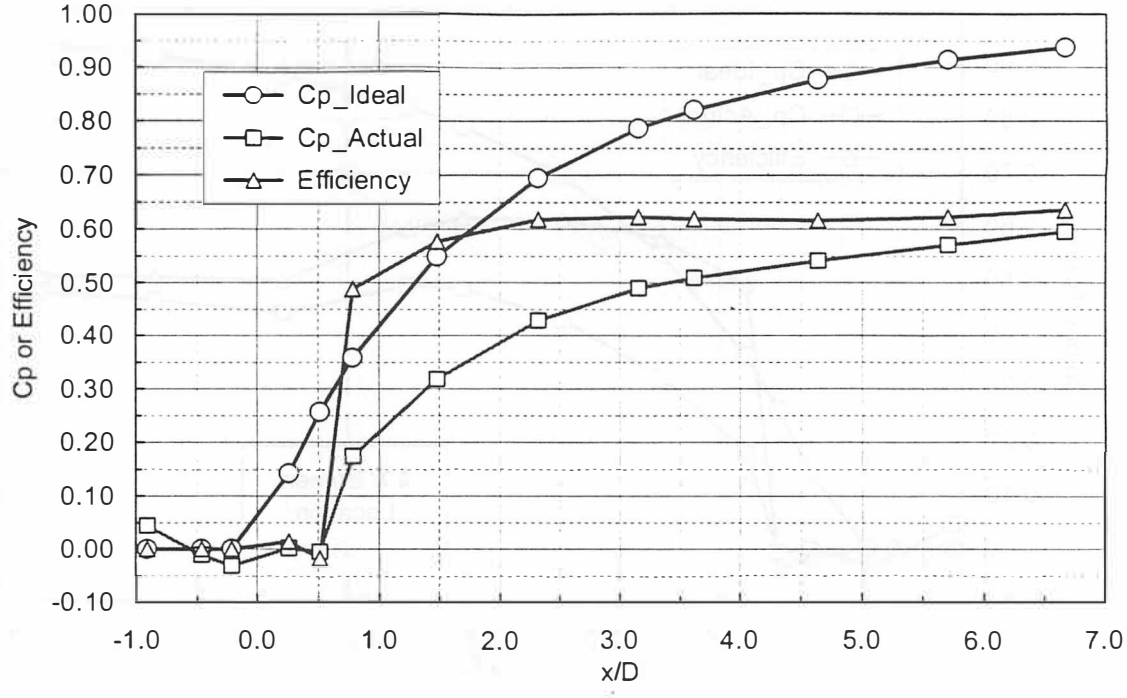


a) Cross-Leg Diffuser Cp Distribution

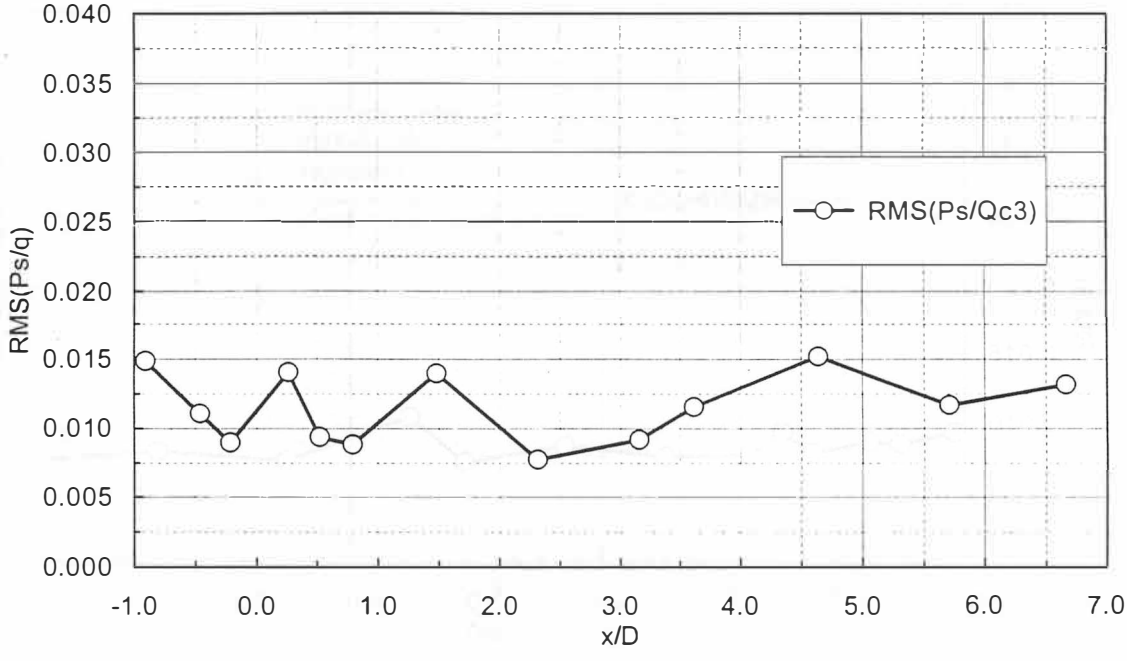


b) Cross-Leg Diffuser Static Pressure Fluctuation Distribution

Figure C-62. Cross-Leg Diffuser Pressure Coefficient and Temporal Fluctuation Distributions, Corner 3, Swirl Vanes, 4/5 Screen Installed (configuration C18).

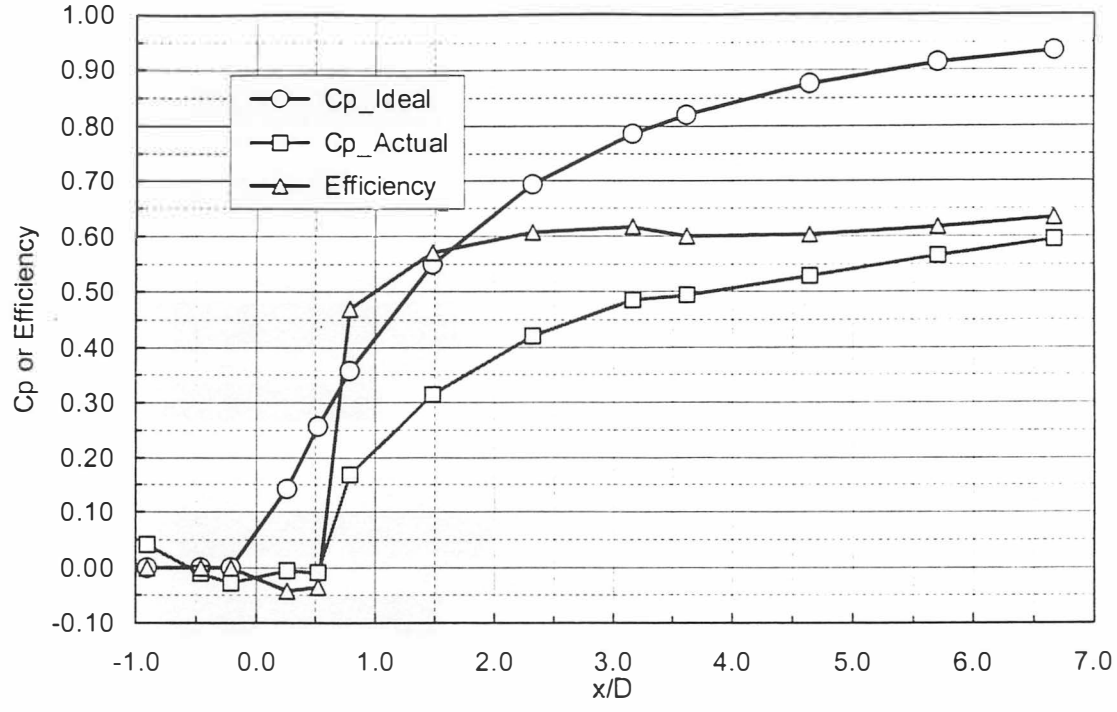


a) Cross-Leg Diffuser Cp Distribution

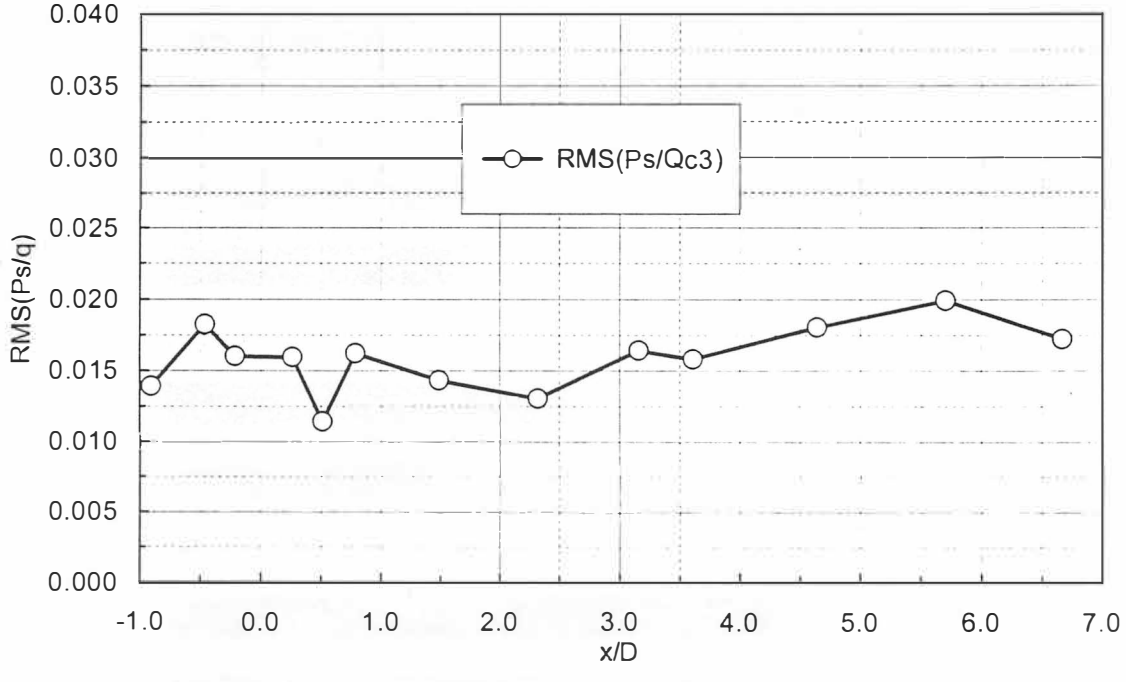


b) Cross-Leg Diffuser Static Pressure Fluctuation Distribution

Figure C-63. Cross-Leg Diffuser Pressure Coefficient and Temporal Fluctuation Distributions, 2 Exit Screens and Long Cell Honeycomb Installed (configuration C19).



a) Cross-Leg Diffuser Cp Distribution



b) Cross-Leg Diffuser Static Pressure Fluctuation Distribution

Figure C-64. Cross-Leg Diffuser Pressure Coefficient and Temporal Fluctuation Distributions, Baseline Configuration C21

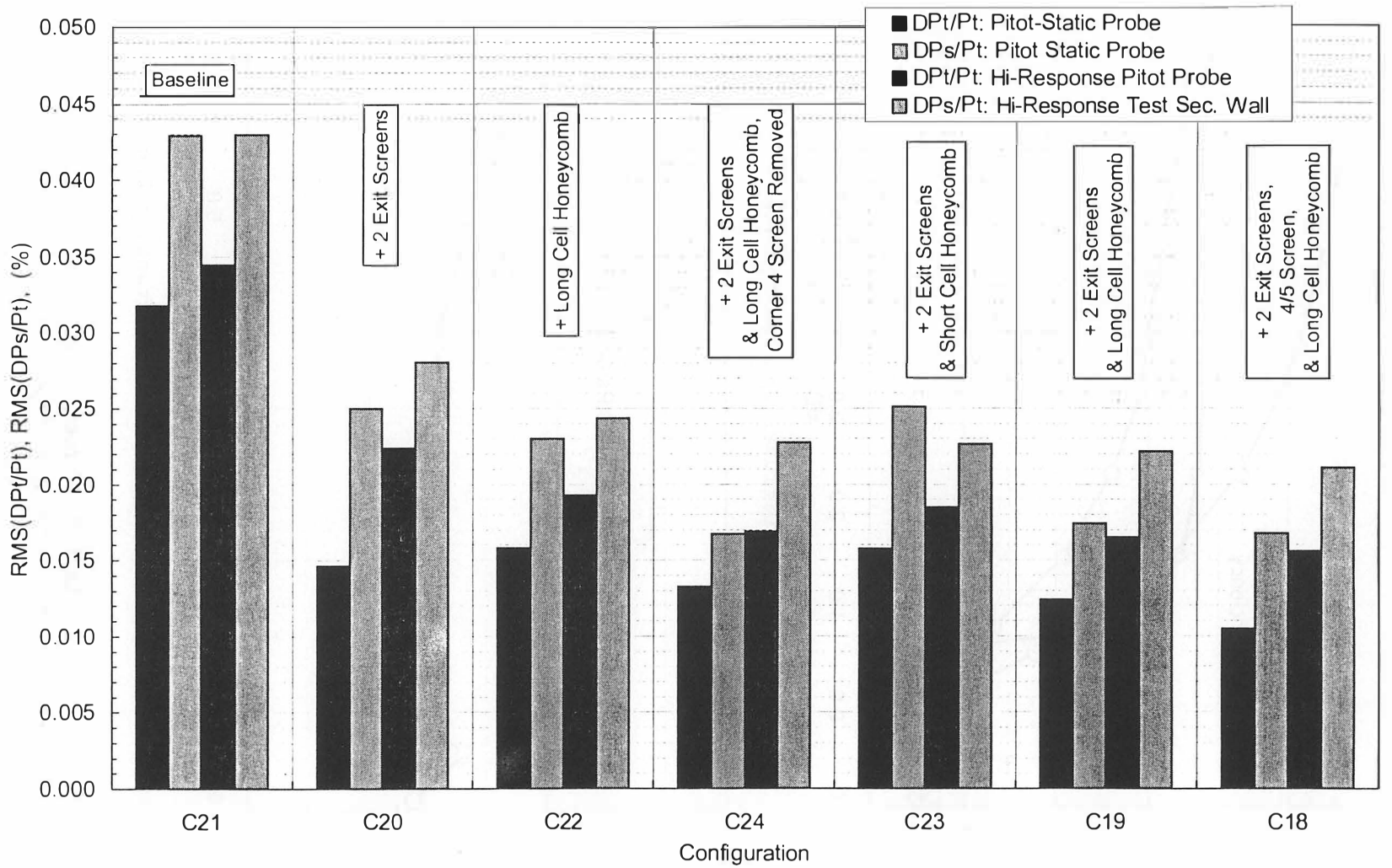


Figure C-65. The Effect of Flow Conditioners on Test Section RMS Temporal Fluctuations of Total and Static Pressure

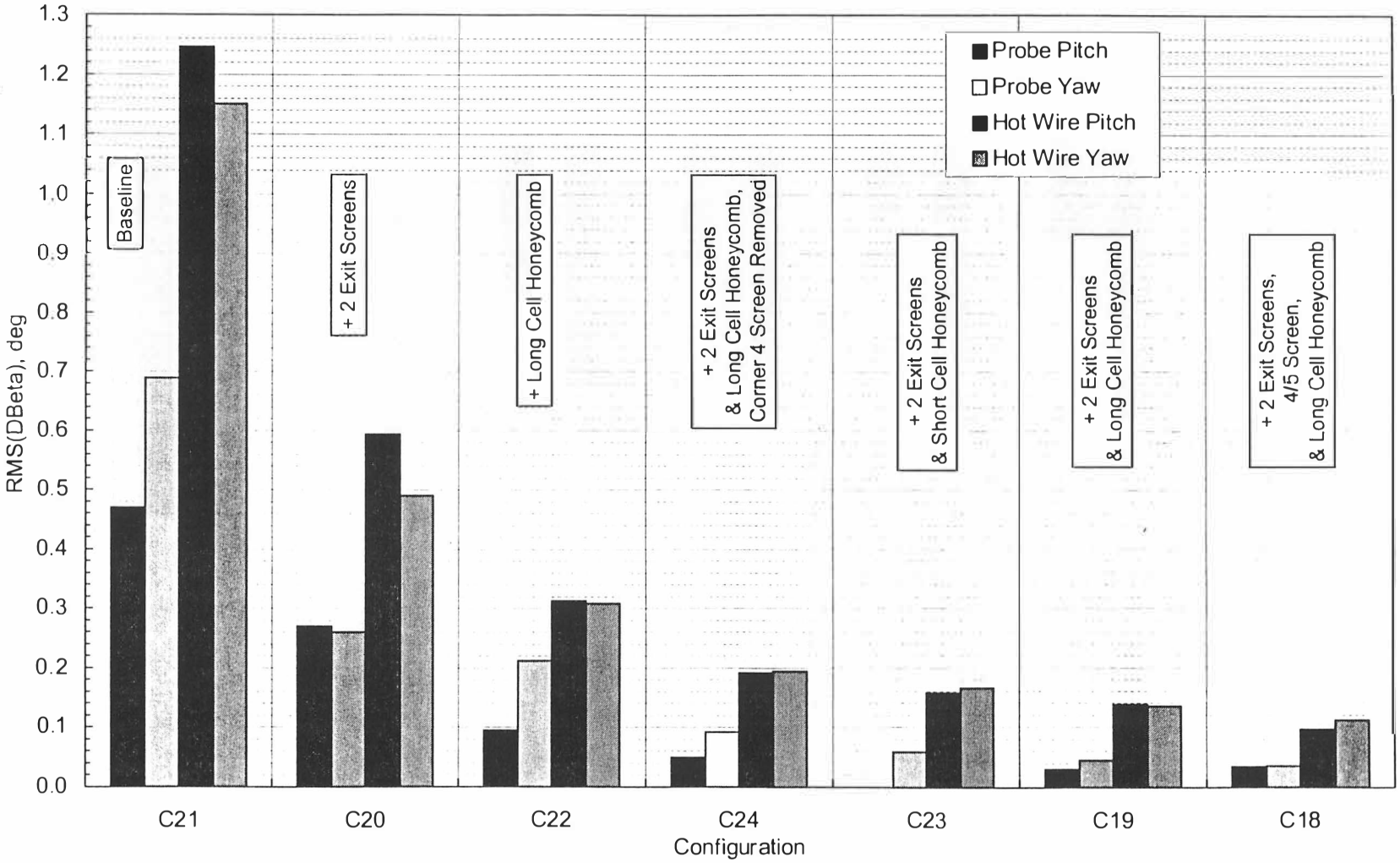


Figure C-66. Effect of Flow Conditioners on the RMS Temporal Fluctuation in Flow Angle of the Flow Angularity Probe and Hot Wire Anemometer.

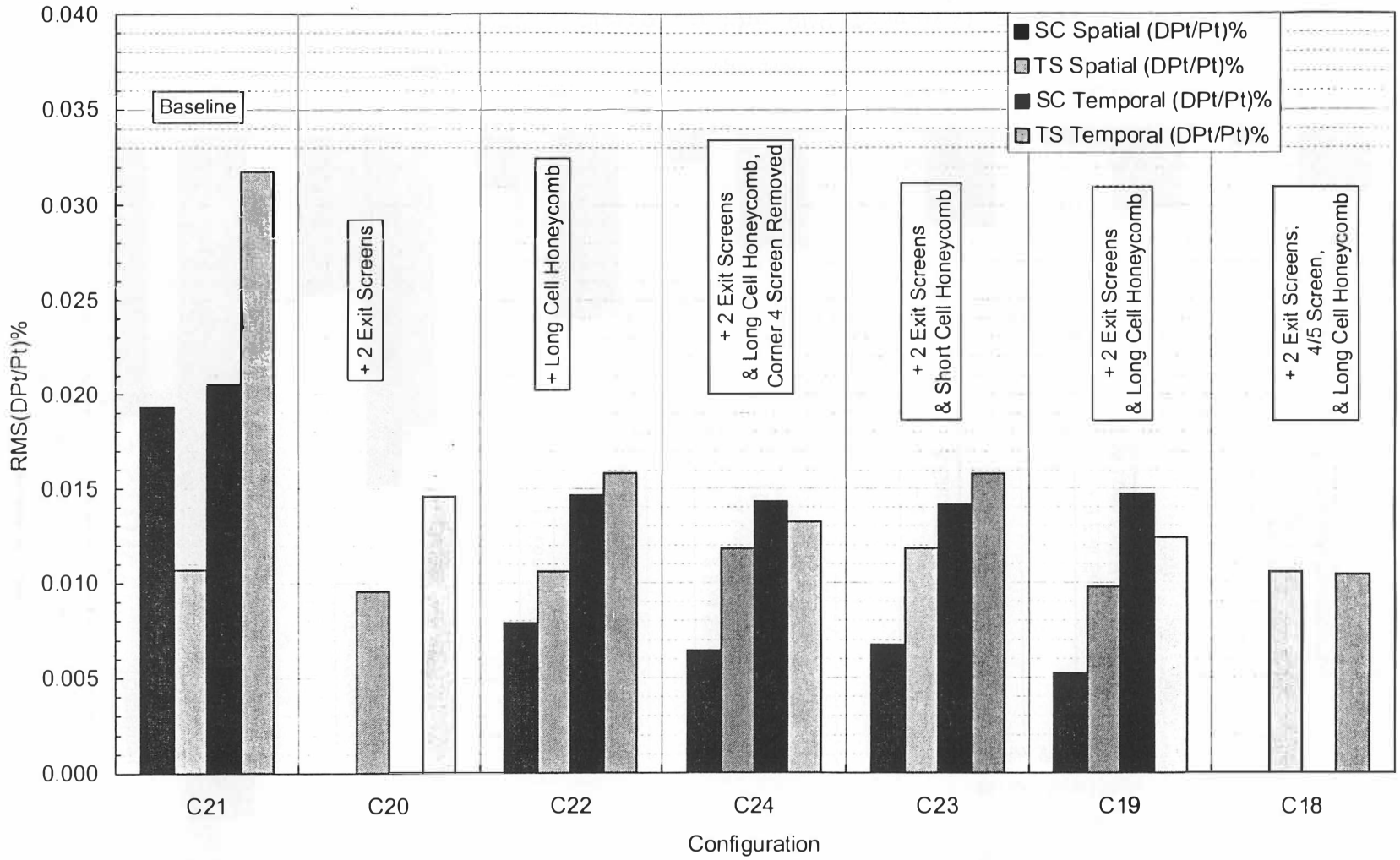


Figure C-67. Stilling Chamber and Test Section Core Region Total Pressure Spatial Distribution and Temporal Fluctuation Summary.

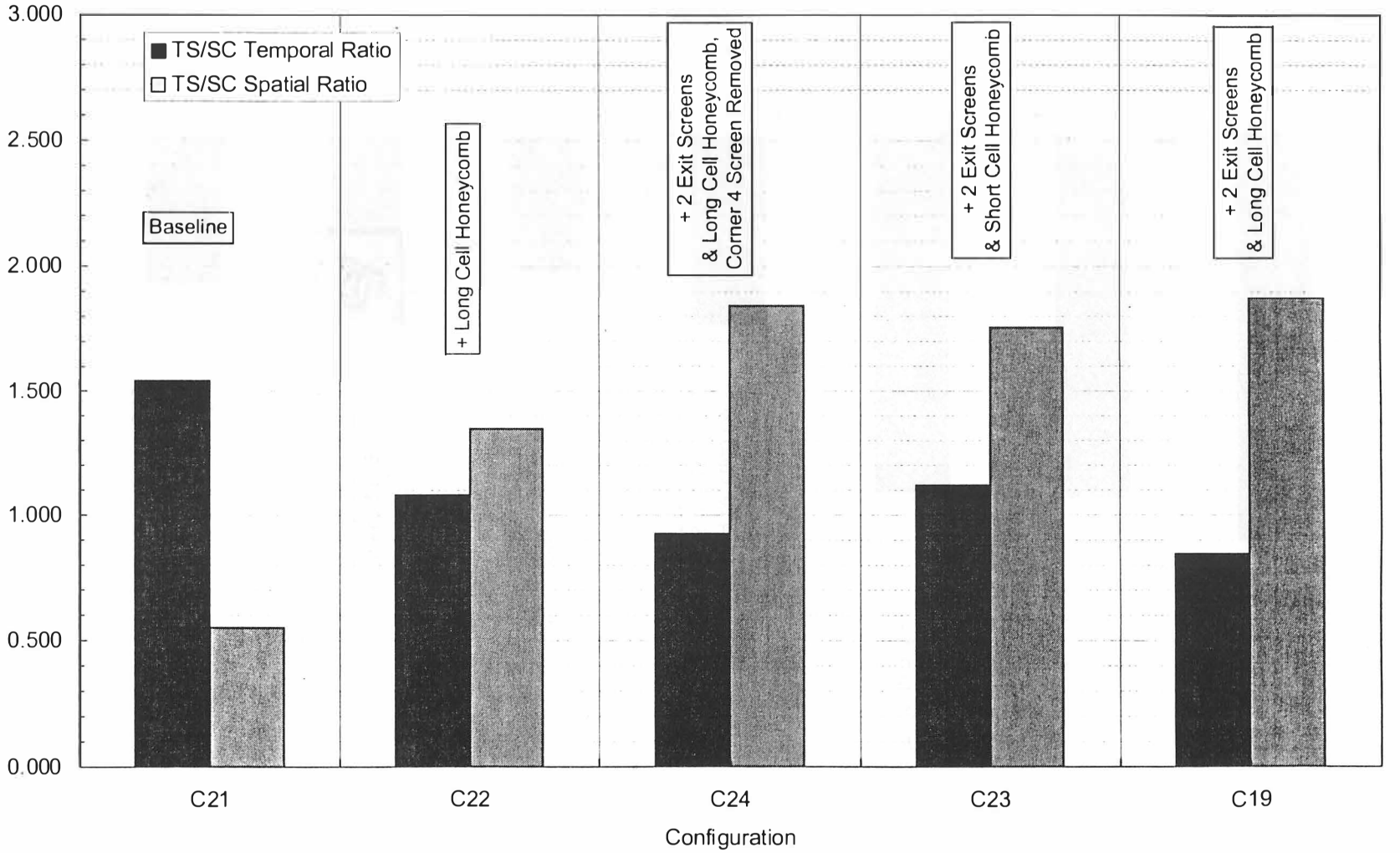


Figure C-68. Test Section to Stilling Chamber Core Region Total Pressure Spatial Distribution and Temporal Fluctuation Ratios.

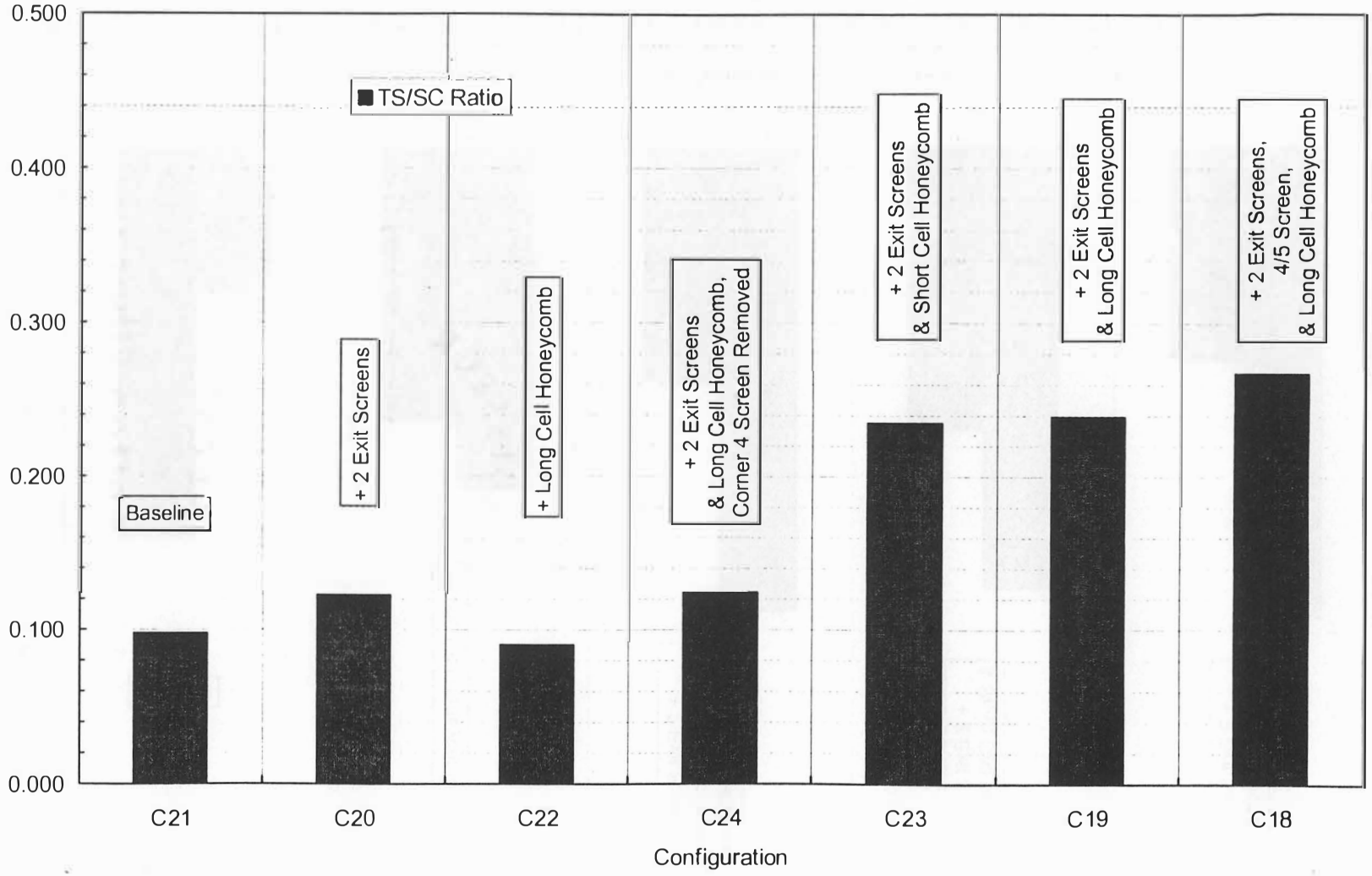


Figure C-69. Test Section to Stilling Chamber Core Region Axial Turbulence (u'/U) Temporal Fluctuation Ratios.

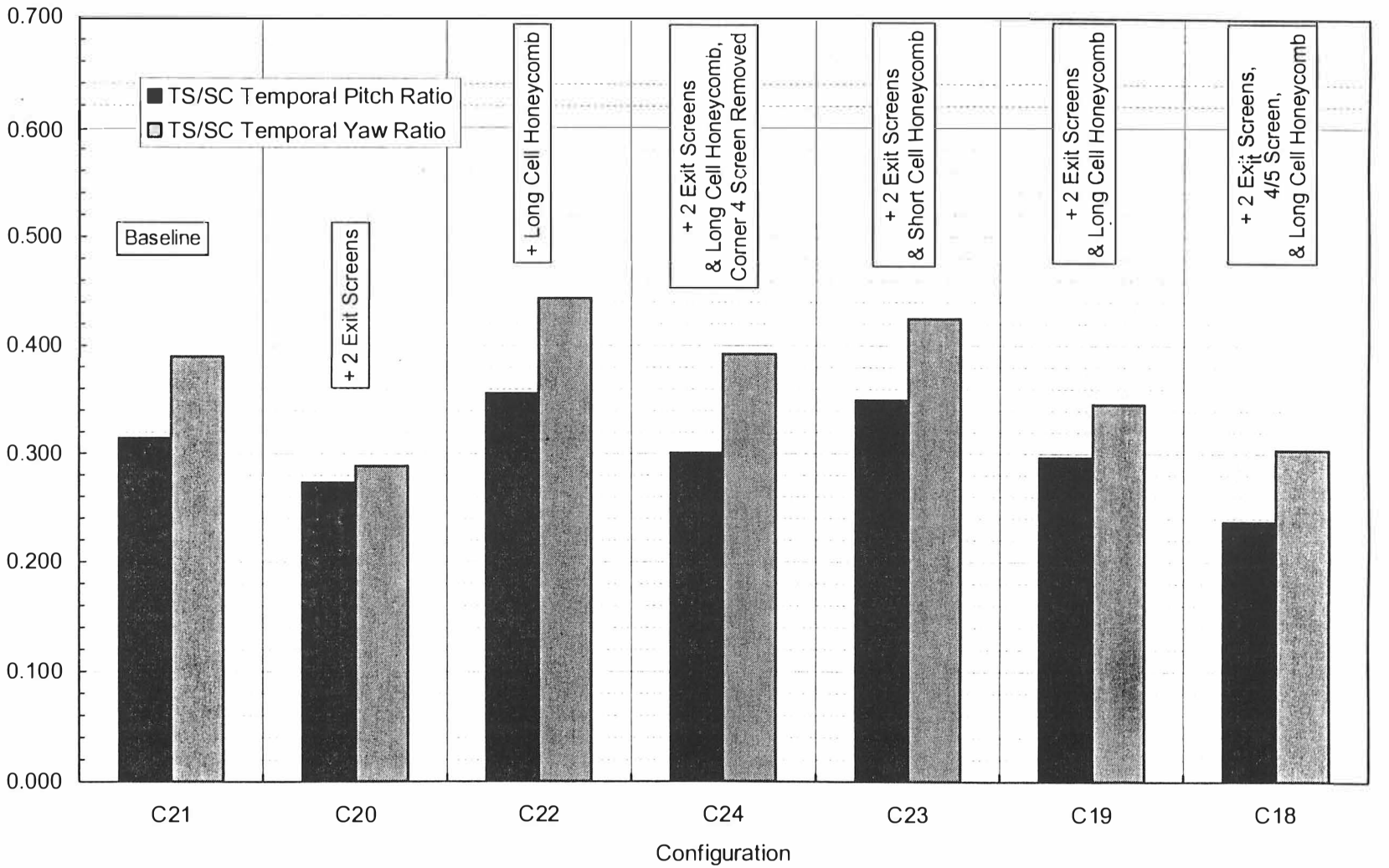


Figure C-70. Test Section to Stilling Chamber Core Region Yaw (w'/U) and Pitch (v'/U) Angle Temporal Fluctuation Ratios.

APPENDIX D

DERIVATION OF AXIAL TURBULENCE AND COMPRESSOR POWER EQUATIONS

DERIVATION OF AXIAL TURBULENCE APPROXIMATION IN TERMS OF TOTAL AND STATIC PRESSURE VARIATION

For isentropic compressible flow, the total and static pressure can be related as follows:

$$\frac{p_t}{p} = \left(1 + \frac{\gamma - 1}{2} M^2\right)^{\frac{\gamma}{\gamma - 1}}$$

where:

p_t	Total pressure
p	Static pressure
γ	Specific heat ratio
M	Mach number

Take the log of both sides.

$$\ln(p_t) - \ln(p) = \frac{\gamma}{\gamma - 1} \ln\left(1 + \frac{\gamma - 1}{2} M^2\right)$$

Differentiate:

$$\frac{\delta p_t}{p_t} - \frac{\delta p}{p} = \frac{\gamma}{\gamma - 1}\left(\frac{\gamma - 1}{2} 2M\delta M\right) \frac{1}{1 + \frac{\gamma - 1}{2} M^2}$$

$$\frac{1}{\gamma M^2}\left(\frac{\delta p_t}{p_t} - \frac{\delta p}{p}\right) = \frac{1}{1 + \frac{\gamma - 1}{2} M^2} \frac{\delta M}{M} \qquad \text{(D1-1)}$$

Now take the log of the mach number equation and differentiate:

$$M = \frac{u}{a}$$

where: M Mach number

u Fluid velocity

a Speed of Sound in Fluid

$$\ln(M) = \ln(u) - \ln(a)$$

$$\frac{\delta M}{M} = \frac{\delta u}{u} - \frac{\delta a}{a} \qquad \text{(D1-2)}$$

Recall the speed of sound equation $a = (\gamma RT)^{1/2}$

Where: a sound speed

R Gas constant of fluid

T Static Temperature

Now substitute the isentropic compressible flow relation for total and static temperature into the sound speed equation:

$$\frac{T_t}{T} = \left(1 + \frac{\gamma - 1}{2} M^2\right) \qquad a = \left(\frac{\gamma R T_t}{1 + \frac{\gamma - 1}{2} M^2}\right)^{1/2}$$

Where: T_t Total Temperature

Now take the log and differentiate:

$$\ln(a) = \frac{1}{2}\left[\ln(\gamma R T_t) - \ln\left(1 + \frac{\gamma - 1}{2} M^2\right)\right]$$

$$\frac{\delta a}{a} = \frac{1}{2}\left[\frac{\delta\gamma}{\gamma} + \frac{\delta R}{R} + \frac{\delta T_t}{T_t} - \left(\frac{\gamma-1}{2} 2M\delta M\right)\frac{1}{1+\frac{\gamma-1}{2}M^2}\right]$$

If γ, R, and T_t are assumed to be constant, the above equation reduces to:

$$\frac{\delta a}{a} = \frac{-(\gamma-1)M^2}{2\left(1+\frac{\gamma-1}{2}M^2\right)}\frac{\delta M}{M} \qquad \text{(D1-3)}$$

Now substitute equation D-3 into D-2:

$$\frac{\delta M}{M} = \frac{\delta u}{u} + \frac{(\gamma-1)M^2}{2\left(1+\frac{\gamma-1}{2}M^2\right)}\frac{\delta M}{M}$$

$$\frac{\delta M}{M} = \left(1+\frac{\gamma-1}{2}M^2\right)\frac{\delta u}{u} \qquad \text{(D1-4)}$$

Now substitute equation D-4 into D-1

$$\frac{\delta u}{u} = \frac{1}{\gamma M^2}\left(\frac{\delta p_t}{p_t} - \frac{\delta p}{p}\right) \qquad \text{(D1-5)}$$

Equation D-5 is valid for isentropic compressible flow with constant total temperature and specific heats.

DERIVATION OF COMPRESSOR POWER IMPACT EQUATION

Assume that the total power consumed by the wind tunnel circuit is given by:

$$\dot{E} = \frac{\dot{m} c_p T_{to}}{\eta} \left[\lambda^{\frac{\gamma-1}{\gamma}} - 1 \right] \qquad \text{(D2-1)}$$

where:

$\dot{E}$	Power
$\dot{m}$	Mass flow rate
c_p	Fluid specific heat
T_{to}	Total temperature at compressor inlet
η	Compressor efficiency
λ	Compressor pressure ratio
γ	Fluid specific heat ratio

Assume that the changes in these parameters are small (eg., $\delta\lambda/\lambda << 1$). Then we can use the differential form of equation D2-1 to evaluate the percentage change in power caused by increasing the backleg loss coefficient. First take the log of equation D2-1 and differentiate.

$$\ln(\dot{E}) = \ln(\dot{m}) + \ln(T_{to}) + \ln(c_p) - \ln(\eta) + \ln\left(\lambda^{\frac{\gamma-1}{\gamma}} - 1 \right) \qquad \text{(D2-2)}$$

$$\frac{\delta\dot{E}}{\dot{E}} = \frac{\delta\dot{m}}{\dot{m}} + \frac{\delta T_{to}}{T_{to}} + \frac{\delta c_p}{c_p} - \frac{\delta\eta}{\eta} + \frac{\gamma-1}{\gamma} \frac{\lambda^{\frac{\gamma-1}{\gamma}}}{\lambda^{\frac{\gamma-1}{\gamma}} - 1} \frac{\delta\lambda}{\lambda} \qquad \text{(D2-3)}$$

Assume that the testleg (stilling chamber to compressor inlet) is not affected by the addition of a loss element upstream and that stilling chamber conditions are held constant.

Then: $$\frac{\delta \dot{m}}{\dot{m}} = \frac{\delta T_{to}}{T_{to}} = \frac{\delta c_p}{c_p} = 0$$

Also, assume that the compressor efficiency does not change, so $\delta\eta/\eta = 0$.

With these assumptions, equation D2-3 reduces to:

$$\frac{\delta \dot{E}}{\dot{E}} = \frac{\gamma - 1}{\gamma} \frac{\lambda^{\frac{\gamma-1}{\gamma}}}{\lambda^{\frac{\gamma-1}{\gamma}} - 1} \frac{\delta\lambda}{\lambda} \qquad \text{(D2-4)}$$

The next step is to relate $\delta\lambda/\lambda$ to changes in the backleg loss coefficient. To do this the differential rise in total pressure across the compressor must be split into testleg and backleg components as follows:

$$p_{tc2} - p_{tc1} = (p_{tc2} - p_{tsc}) + (p_{tsc} - p_{tc1}) \qquad \text{(D2-5)}$$

where:
- p_{tc1} Compressor inlet total pressure
- p_{tc2} Compressor exit total pressure
- p_{tsc} Stilling chamber total pressure

Define the testleg and backleg loss coefficients as:

$$K_{TL} = \frac{p_{to} - p_{tc1}}{q_{sc}} \quad \text{and} \quad K_{BL} = \frac{p_{tc2} - p_{to}}{q_{sc}} \qquad \text{(D2-6 and 7)}$$

where: q_{sc} Stilling chamber dynamic pressure

Now substitute (D2-6 and 7) into (D2-5) and divide through by p_{tc1}:

$$\frac{p_{tc2}}{p_{tc1}} = 1 + \frac{q_{sc}}{p_{tc1}}\left(K_{BL} - K_{TL}\right) \qquad \text{(D2-8)}$$

Let $\lambda_T = \frac{p_{to}}{p_{tc1}}$ and $\lambda_c = \frac{p_{tc2}}{p_{tc1}}$

Then $$\lambda_c = 1 + \lambda_T \frac{q_{sc}}{p_{to}}\left(K_{BL} - K_{TL}\right) \qquad \text{(D2-9)}$$

The testleg pressure ratio, λ_T, and q_{sc}/p_{to} are taken to be functions of test section mach number only.

Define a reference state corresponding to conditions before the backleg loss coefficient is changed:

$$\lambda_c^o = 1 + \lambda_T \frac{q_{sc}}{p_{to}}\left(K_{BL}^o - K_{TL}\right) \qquad \text{(D2-10)}$$

Subtract equation D2-10 from D2-9.

$$\lambda_c - \lambda_c^o = \lambda_T \frac{q_{sc}}{p_{to}} \left(K_{BL} - K_{BL}^o \right) \qquad \text{(D2-11)}$$

So,
$$\frac{\delta\lambda}{\lambda} = \frac{\lambda_c - \lambda_c^o}{\lambda_c^o} = \frac{\lambda_T}{\lambda_c^o} \frac{q_{sc}}{p_{to}} \left(K_{BL} - K_{BL}^o \right) \qquad \text{(D2-12)}$$

Now, substitute equation D2-12 into D2-4:

$$\frac{\delta \dot{E}}{\dot{E}} = \frac{\gamma - 1}{\gamma} \frac{\lambda_c^{o\frac{\gamma-1}{\gamma}}}{\lambda_c^{o\frac{\gamma-1}{\gamma}} - 1} \frac{\lambda_T}{\lambda_c^o} \frac{q_{sc}}{p_{to}} \left(K_{BL} - K_{BL}^o \right) \qquad \text{(D2-13)}$$

Now, assuming incompressible flow in the backleg (subsonic portion of tunnel) evaluate K_{BL} & K_{BL}^o:

$$p_{tc2} - p_{to} = \sum K_i q_i \qquad K_{BL}^o q_{sc} = \sum K_i q_i$$

$$K_{BL}^o = \frac{1}{q_{sc}} \sum K_i q_i \qquad K_{BL}^o = \sum K_i \left(\frac{A_{sc}}{A_i} \right)^2$$

Add a new loss element at station k:

$$K_{BL} = K_{tk} \left(\frac{A_{sc}}{A_k} \right)^2 + \sum K_i \left(\frac{A_{sc}}{A_i} \right)^2$$

So,
$$K_{BL} - K_{BL}^o = K_{tk} \left(\frac{A_{sc}}{A_k} \right)^2 \qquad \text{(D2-14)}$$

Substitute equation D2-14 into D2-13:

$$\frac{\delta \dot{E}}{\dot{E}} = \frac{\gamma - 1}{\gamma} \frac{\lambda_c^{o\,\frac{\gamma-1}{\gamma}}}{\lambda_c^{o\,\frac{\gamma-1}{\gamma}} - 1} \frac{\lambda_T \, q_{sc}}{\lambda_c^o \, p_{t0}} K_{tk} \left(\frac{A_{sc}}{A_k} \right)^2$$

VITA

Grady Pike Saunders was born in Tullahoma, TN on March 25, 1975. He graduated from Tullahoma High School in 1993. From there, he went to the University of Tennessee, Chattanooga and received a B.S in mechanical engineering with emphases in mechanics and the thermal sciences. He is currently employed by the Advanced Technology Segment of Sverdrup Technology, Inc. in Tullahoma, TN.